ANALYSIS OF FREQUENCY SELECTIVE SURFACES
ON CHIRAL SLAB

A Ph. D. THESIS

in

Electrical and Electronics Engineering

University of Gaziantep

By

Ahmet Oğuzhan KOCA

March, 1997

Approval of the Graduate School of Nartural and Applied Sciences
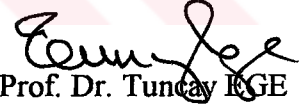
Assoc. Prof. Dr. Ali Rıza TEKİN

Director

I certify that I have read this thesis and that in my opinion it is fully adequate, in scope and quality, as a dissertation for degree of Doctor of Philosophy.

Prof. Dr. Tuncay EGE

Chairman of the Department

I certify that I have read this thesis and that in my opinion it is fully adequate, in scope and quality, as a dissertation for the degree of Doctor of Philosophy.
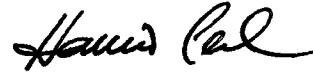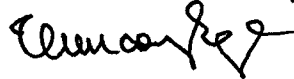
Prof. Dr. Tuncay EGE

Supervisor

Examining Committee in Charge :

Prof. Dr. A. Hamit SERBEST (Chairman)

Prof. Dr. Tuncay EGE

Prof. Dr. Sadettin ÖZYAZICI

ABSTRACT

ANALYSIS OF FREQUENCY SELECTIVE SURFACES ON CHIRAL SLAB

KOCA, Ahmet Oğuzhan

Ph. D. in Electrical and Electronics Engineering

Supervisor : Prof. Dr. Tuncay EGE

March 1997, 225 pages

In this thesis a new type Frequency Selective Surface (FSS), named Chiro-FSS, is analysed. A Chiro-FSS is comprised of two dimensional infinite periodic array of conducting elements printed on an isotropic chiral slab. The spectral characteristics of Chiro-FSS consisting of various geometries of conducting elements are examined in detail.

In the analysis, the modal technique which is employed in the analysis of FSS printed on a dielectric substrate (conventional FSS) is used, since the existence of the isotropic chiral slab does not alter the transversal nature of the problem. In a chiral medium only left circularly polarised (LCP) and right circularly polarised (RCP) plane waves can propagate. Therefore the transversal components of the scattered electric and magnetic fields are expressed as the infinite sums of LCP and RCP, TE and TM Floquet modes propagating in the chiral slab and in the surrounding medium, respectively. These Floquet modes also satisfy the periodicty requirements imposed by the geometry. Boundary conditions combined with the orthogonal property of the Floquet modes over a single unit cell leads to an integral equation for the unknown current density induced

on a conducting element by the incident plane wave. The resulting integral equation is then solved by Method of Moments (MOM), thereby expressing the current distribution on a conducting element by suitable basis functions. Upon finding the unknown current coefficients by means of matrix inversion, the reflection and transmission coefficients of the Chiro-FSS are computed.

Computed resuts of the reflection and transmission characteritics of five different type of Chiro-FSS comprised of conducting elements shaped as, narrow strips, cross dipoles, circular rings, square loops and square patches are presented.

ÖZET

CHİRAL DİLİM ÜZERİNE YERLEŞTİRİLMİŞ FREKANS SEÇİCİ YÜZEYLERİN ANALİZİ

KOCA, Ahmet Oğuzhan

Doktora Tezi, Elektrik ve Elektronik Mühendisliği

Tez Yöneticisi : Prof. Dr. Tuncay EGE

Mart 1997, 225 sayfa

Bu tezde Chiro-FSY adı verilen yeni bir tür frekans seçici yüzeyin (FSY) analizi yapılmıştır.Chiro-FSY, izotropik chiral dilim üzerine yerleştirilen sonsuz iki boyutlu iletken eleman dizinlerinden oluşmaktadır. Değişik geometrilere sahip iletken elemanlardan oluşturulan Chiro-FSY'lerin spektral karakteristikleri detaylı bir şekilde incelenmiştir.

İzotropik chiral dilim problemin enine yapısını değiştirmediğinden dolayı, dielektrik dilim üzerine yerleştirilen FSY'lerin analizinde uygulanan Modal analiz tekniği, Chiro-FSY'lerin analizinde de kullanılmıştır. Bir chiral ortamda sadece sağ el ve sol el polarizasyonlu düzlemsel dalgalar propagasyon yapabilmektedir. Bu yüzden saçılan elektrik ve manyetik alanların enine bileşenleri chiral dilim içinde sağ el ve sol el dairesel polarizasyonlu, çevreleyen ortamda ise TE ve TM Floquet modları olarak ifade edilmişlerdir.Bu Floquet modlar geometrinin yüklediği periyodlu olma gerekliliğini de sağlamaktadırlar. Bir birim hücre üzerinde Floquet modlarının dikgen özelliğinin sınır şartları ile birleştirilmesi, gelen düzlemsel dalganın bir iletken eleman üzerinde oluşturduğu bilinmeyen akım yoğunluğu cinsinden bir integral denklemini verir. Bir

v

iletken elemanın üzerindeki akım yoğunluğu uygun temel fonksiyonlar ile ifade edilerek sonuçta elde edilen integral denklemi Moment Metodu ile çözülür.Bilinmeyen akım katsayıları matriks evirmesiyle bulunduktan sonra Chiro-FSY'lerin yansıtma ve geçirgenlik katsayıları hesaplanmıştır.

Dar şerit, çapraz dipol, dairesel halka, kare halka ve kare yama şeklindeki iletken elemanlardan oluşturulan Chiro-FSY'lerin yansıtma ve geçirgenlik karakteristikleri sunulmuştur.

Anahtar Kelimeler : frekans seçici yüzeyler, chiral.

ACKNOWLEDGEMENT

TABLE OF CONTENTS

LIST OF FIGURES

Page

CHAPTER 1

INTRODUCTION

1.1   Introduction to Electromagnetic Chirality

Since the early part of the nineteenth century, the concept of chirality has played
an increasingly important role in a variety of fields such as chemistry, optics, particle
physics and more recently in electromagnetics.

Chirality is a geometric notation that refers to the handedness of an object. The
word 'chiral' comes from the old Greek word 'chira' meaning 'hand'. A chiral object is,
by definition, a body that can not be brought into congruence with its mirror image by
translation and/or rotation. In other words, such a body lacks bilateral symmetry, and can
not be superposed on its mirror image. An object of this sort has the property of
handedness and is said to be either right or left handed. An object that is not chiral, is
called achiral.

In 1811 Arago [1] discovered that quartz cyrstals rotate the plane of polarisation
of linearly polarised light, giving rise to a new phenomenon which was named 'optical
activity'. Shortly thereafter, in 1815, experimentation by Biot [2] on the plates of quartz
put in evidence the dependence of optical activity on the light wavelength. Fresnel [3],
in 1822, conjectured that a linearly polarised light travelling along the axis of a cyrstal
of quartz, is divided into circularly rays of opposite handedness and unequal phase
velocities. Behind the cyrstal, the two rays combined resulting in a linearly polarised
plane wave whose plane of polarisation is rotated with respect to the plane of
polarisation of the incident wave. Pasteur [4] postulated that molecules of optically active

1

materials are three-dimensional chiral structure and chirality or handedness of these molecules causes optical activity.

The phenomenon of wave interaction with chiral objects began to attract attention in the electromagnetics' community with the simple but illuminating microwave experiments of Lindman [5] which were anologous to the optical experiments performed in the nineteenth century. They devised a macroscopic model for the phenomenon by using microwave instead of light, and wire helicies instead of chiral molecules. The results demonstrated that a collection of helicies of a given handedness would rotate the plane of polarisation of a linearly polarised wave in one direction while collection of helicies of opposite handedness would rotate the plane of polarisation in the opposite direction. In 1979, a macroscopic model for the interaction of electromagnetic waves with chiral structures was presented by a theoretical couterpart to the experimentally devised model of Lindman [6].

Even if, the isotropic chiral medium is modelled hypotetically, behaviour of electromagnetic waves in chiral medium and its applications have been investigated during the last decade.

BASSIRI et. al. [6] studied on dyadic Green's function and dipole radiation in chiral media. They have expressed the dyadic Green's function for a sourceof finite spatial extent in an unbounded, lossless chiral medium. The Green's function involves two spherical waves which place in evidence that the medium supports double-mode propagation. In the case of a dipole antenna, found that the chirality of the ambi ent medium increases the wave impedance of the medium, and the radiation resistance of the dipole, but has no effect on the directivity of the radiaton. The dominant effect of chirality is the change it produces in the state of polarisation of the dipole's feed.

LAKHTAKIA et. al. [8] devised a procedure based on T matrix method to study the electromagnetic response of nonspherical chiral and dielectric (lossy) objects exposed to an arbitrary incident field. The plane wave scattering and absorption characteristics of lossy dielectric, assymmetric scatterers (spheres, prolate and oblate spheroid) with and without chiral properties are examined at frequencies above 50 GHz. They conclude that, the chiral spheres are the most effective objects in retarding the

2

progress of an incident plane wave regardless of its polarisations.

PELET et. al. [9] proposed a new type of wave guiding structure, named chirowaveguide, consisting of cylindirical waveguides filled with homogenous isotropic chiral materials. It was shown that the Helmholtz equation for the longitudinal components of the electric and magnetic fields in chirowaveguides are always coupled and consequently in these waveguides invidual transverse electric (TE) and transverse magnetic (TM) or transverse electromagnetic (TEM) modes can not be supported. A paralle plate chirowaveguide was analysed in detail and the corresponding dispersion relation, cut-off frequencies, propagating and evanescent modes are obtained. It was shown that there are pairs of bifurcated modes with common cut-off frequencies and differing propagation constant.

BASSIRI et. al. [10] analyzed the reflection from and transmission through a semi-infinite chiral medium by obtaining the Fresnel equations in terms of parallel and perpendicular polarised modes. The conditions were obtained for the total internal reflection of the incident wave from the interface and for the existence of the Brewster angle. The effects of chirality on the polarisation and the intensity of the reflected wave from the chiral half space were discussed. The propagation of electromagnetic waves through an infinite slab of chiral medium was formulated for oblique incidence and solved analytically for the case of normal incidence.

LAKHTAKIA et. al. [11] extended the field equations, Huygen's principle, integral equations and theorems for radiation and scattering of electromagnetic waves in isotropic chiral media. Vector and scalar potentials, the mathematical expression of Huygen's principle, as applicable to chiral media, was derived and employed to set up a scattering formalism and to establish the theorems for forward scattering of plane wave.

GUIRE et. al. [12] described preparetion of chiral dielectric composite slab that contains a random distribution of miniature helices having right and left handedness. The reflection properties of the metal backed samples were measured with free space systems using a pair of spot focusing antennas.

JAGGARD et. al. [13] investigated the electromagnetic properties of a structure that is both chiral and periodic using coupled mode equations. The periodicity was

described by a sinusoidal perturbation of the permittivity, permeability and chiral admittance. The couple mode equations derived from physical cosiderations were used to examine the reflected and transmitted field.

SAADOUN et. al [14] discussed a conceptional idea for a reciprocal phase shifter using chiral materials. This phase shifter, named chiro-phase shifter, consists of a general cylindrical waveguide in which a thin chiral rod is inserted longitudinally. The perturbation technique was employed to analyse the effects of the chiral rod's parameters on propagation constant of guided modes theoretically. A simple expression relating the relative change of propagation constant to other relevant quantities such as polarisation characteritics of unperturbated guided modes, material parameters of the chiral rod and location of the rod was presented.The circular metallic chiro-pahes shifter was discussed in some details.

1.2 Frequency Selective Surfaces - FSS

Frequency selective surfaces are the structures whose reflection and transmission characteristics vary with the frequency of the incoming wave. There are two types of FSSs. The first type comprised of periodic arrays of conducting patches and the second one is formed by periodically perforated screens. FSSs can be supported by a slab or in freestanding form. The first structure is referred as capacitive FSS and behaves as a solid reflector over a specific frequency band whereas the second one is referred as inductive FSS and transparent over a frequency band. In other words, FSSs exhibits bandpass or bandstop spectral characteristics depending on their geometry.

Historically, the understanding of the underlying physics of FSS has directly evolved from the investigation of diffraction gratings in optics which are used to decompose a beam of non-monochromatic light into its spectral orders. This filtering process, as well as, the diffraction grating itself, was discovered by Rittenhouse [15]. The phonemenon described by Rittenhause is also fundamental to any screen consisting of periodically placed conducting patches or perforated screens. The change of structure in two dimensions increases the complexity in understanding and analysing the

4

screen. The shape of each element (either patch or aperture within an array of periodic cell) as well as the spacing between them, contributes to the form of the scattered fields which exhibits resonances as the wavelength is varied i.e., the fields will either be totally reflected or transmitted for patch or aperture screens, respectively, at a specific wavelength. Resonaces in genaral occur when the size of the element is an integer number of the half wavelengths with the infinite array of elements modifying the spectral response from what it would be if it were isolated. At wavelengths past the first resonance, the higher order modes begin to scattering energy at regular angles and as the wavelength is further decreased, repeated resonances occur. Therefore the highest allowable operation frequency in the spectrum for an efficient use of FSSs must be less than the frequency at which the higher order modes start to propagate into distance. Spectral response of a FSS depends also on element spacing, thickness and constitutive parameters of the backing material that may be part of the screen.

In general two different approaches have been used to analyse the scattering of a plane wave by a FSS. First is based on physical considerations of the structure and leads to an equivalent circuit representation of the grid with capacitive and inductive elements obtained by studying a simpler one-dimensional structure. This method however is limited to freestanding grids illuminated by a normally incident plane wave and is accurate near the resonance frequency [17] and [18]. Because it is a scalar model, no information about the cross-polarisation characteristics can be obtained. The second approach is the modal analysis technique which enables to predict the scattering of plane waves by a FSS in freestanding form or even backed an isotropic material, for arbitrary polarisation and angle of incidence. This powerful approach has been applied by Montgomery [18] in order to obtain a rigorous solution to the problem of scattering of a plane wave by an infinite periodic array of thin conductors arranged periodically along any two skewed coordinates printed on a dielectric. In the modal analysis technique, the transverse components of the scattered fields are expanded into a set of two dimensional Floquet space harmonics within an unit cell. Application of appropriate boundary conditions combined with the orthogonal property of the Floquet modes over a single unit cell leads to a Fredholm type integral eqaution of the first kind in terms of the

unknown current density induced on the metallic scatterers. This integral equation can then be reduced to a matrix equation by employing the Method of Moment (MOM) in which the unknown current density is expanded into a set of orthogonal functions.

In general, there are two categories of basis functions used to represent the unknown current density in the context of MOM; entire domain and sub-domain basis functions. The entire domain functions are used to express the unknowns are defined all over the unit cell and tailored for the specific geometry of the region over which the unknown is being expanded. Examples for which the entire domain functions have been succesfully applied include dipole, square patch, circular ring, circular patch, cross etc. An important advantage of using entire domain type of basis functions is that the size of the resulting matrix equation obtained is usually smaller than that for the sub-domain functions. Thus it becomes possible to solve problems dealing with electrically large structures which could otherwise be difficult to using sub-domain functions. On the other hand, for treating FSS comprised of arbitrarily shaped patches and screens with finite conductivity, sub-domain type basis functions have been found to be more versatile, albeit at an increased cost in computation time.

The applications of Frequency Selective Surfaces are many and varied. In microwave region of the electromagnetic spectrum, frequency selective properties of periodic screens are exploited to make efficient use of reflector antennas. As shown in Figure 1.1, a FSS is placed betweeen two feeds which radiate at different frequencies, and the main reflector. The screen is designed to provide total reflection over the operating band of feed one, but total transmission over the band of feed two. Hence, in this configuration, two independent feeds may share the same reflector antenna simultaneously. Similar configuration have been used in satellite communication systems [19], [20].

Another example of the exploitation of the frequency selective property of periodic screens in the microwave region is the in application in radome design [21]. In this case the screen is tuned to provide a bandpass transmission characteristics at the operating frequency of the antenna. At the out-of-band frequencies, the screen is made essentially totally reflecting.
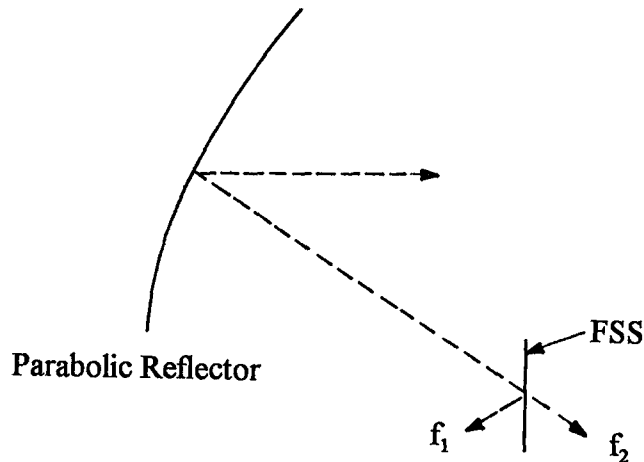
Figure 1.1   Reflector antenna system using frequency selective surface.

In the far-infrared region, periodic screens are used as beam splitters and as mirror for improving the pumping efficiency in molecular lasers [22], [23], [24]. In a laser, the cavity mirror used can be constructed from a FSS such that it is totally reflecting at the wavelength of the energy used to pump the cavity, and partially transmitting at the lasing wavelength. Since no energy used in optically pumping the laser is lost at the mirror; the efficiency of the system increases.

In the near-infrared and visible portion of the spectrum periodic screns have also been proposed as solar selective surfaces to aid in the collection of solar energy [25]. A screen can be designed such that it is essentially transparent in the frequncy band where the solar cells are most efficient and is reflecting at frequencies outside this band. Millimeter and submillimeter wave applications include, in interferometers [26], in detectors [27], in phase shifters [28], frequency doublers [29], in polarisers[30], and artificial dielectrics [31]. In some applications in order to achive the desired spectral characteristics cascaded configurations of these screens are employed [32], [33].

More recently the following researhes are focused on the interesting applications of FSS have been presented. WU et. al. [34] presented theoretical and experimental results for a multi band frequency selective surface with multiring patch elements.

7

Theoretical analysis was based on mode-matching technique. In the design, the size and thus the spacing of the circular ring elements are reduced by the dielectric loading effect to avoid grating lobes at the high end of the frequency spectrum. This dielectric loading effect was accomplished by placing very high dielectric constant on one side of the frequency selective screen or by loading the screen on both sides with relatively low dielectric constant material.

CHANG et. al. [35] dicussed the experimental results of the frequency selective surfaces printed on ferrite substrate. Biasing the ferrite substrate with dc magnetic field changes the permeability, which in turn changes the spectral characteristics of the frequency selective surfaces so that resonance frequency may be continuously varied or the surface may be switched from full reflection case to total transmission case. This surface is expected to find applications in waveguide filters, RCS reduction techniques and reconfigurable antenna systems.

ZHANG et. al. [36] performed experimental studies on quasi-optical millimeter wave band pass filters using high -T_c superconducting films on a substrate. Transmitted power through the filter was investigated in the 75 GHz to 110 GHz frequency range at temperature ranging from 15 K to 300 K. Measurements of high -T_c superconductors were compared with similar filters fabricated using gold. At 15 K and 92 GHz, an improvement of 75% in the quality factor of the superconductor filter was obtained compared with that of a filter made of gold. At lower frequencies, the superconducting filters offers more than an order of magnitude improvement in quality factor over gold filters where the surface resistivity dependens on the square root of frequency. This was the first experimental observation that high -T_c superconductors can be used as quasi-optical, high performance frequency selective surfaces.

KASTNER et. al. [37] accomplished on an iterative anlaysis of finite sized planar frequency selective surfaces with rectangular patches or perforations without the benefit of the assumption that the structure has infinite periodicity. This, in turn, requires the handling of a large number of unknowns and made it diffucult to solve the problem using conventional matrix methods. Two different iteration approaches, spectral iteration technique and conjugate gradient iteration algoritm, were discussed in solving the finite

frequency selective surface problem.

CAROGLANIAN et. al. [38] investigated for determining the forward scattered field from a generally shaped inductive frequency selective surface with nonplanar illumination by applying Locally Planar Technique (LPT) . The effects of nonplanar incident field were determined by comparing the LPT, results with a series of experiments with feed source placed at varying distances from the planar frequency selective surface. The limitations of the LPT model due to surface curvature was also investigated and compared with that obtained by an experimental study using a set of hyperbolic cylinders of different curvatures.

In this study, the scattering of a plane wave of arbitrary polarisation and incidence from a two dimensional infinte periodic array of perfectly conducting elements printed on an isotropic chiral slab is analysed.

The analysis is based on Modal techniques. The complexity of the problem does not permit us to obtain the solution analytically. Therefore a numerical solution to the problem will be obtained employing Method of Moment after application of the Floquet type boundary conditions to the field at the boundaries. The reflection and transmission characteristics of the Chiro-FSSs comprised of various conducting element geometries, such as narrow strips, cross dipoles, circular rings, square loops and rectangular patches will then be presented in detail.

Next chapter is devoted to a brief review of Maxwell's equations and behaviour of electromagnetic waves in an isotropic chiral medium. Solution to wave equation in the case of chiral medium yields double mode propagation. That is, a right and a left circularly polarised waves having unequal wavenumbers can travel within such a medium.

In Chapter III , a full wave analysis of scattering of a electromagnetiic plane wave with arbitrary polarisation and angle of incidence from a doubly periodic infinite array of thin perfectly conducting patches are analysed. Analysis method is based on Modal Analysis Technique and Method of Moments (MOM) combined with the Floquet Theorem.the reflection and transmission coefficients are obtained for these type of surfaces after solving the integral equation which is obtained by applying the boundary conditions for the unknown induced current density on the conducting elements, the

reflection and transmission coefficients are obtained for these type of surfaces.

Computed results of reflection and transmission characteristics for five different types of chiro-frequency selective surfaces (comprised of narrow strips, circular rings, crosses dipoles, square loops and rectangular patches) are presented in Chapter IV. Dependence of polarisation and angle of incidence of the incident plane wave on spectral response of each type chiro-frequency selective surface is also investigated. On the other hand, effects of chirality and constitutive parameters of the slab are examined for various type of array configuration and spacing are investigated and presented in this chapter too.

The conlusions that are reached, for the chiro-frequency selective surfaces are given in the last chapter.

CHAPTER 2

CHIRAL MEDIUM

2.1 Maxwell's Equations

The fundamental equations for electromagnetic wave theory were established by Maxwell in 1873 and experimentally verified by Hertz in 1888. Since then electromagnetic theory has played an important role in the development of many applications. Einstein's theory of relativity in 1905 further assert the rigorousness and elengance of Maxwell's theory. As a well-established scientific disciplines, this sophisticated theoretical structure embodies many principles and concepts which serve as a fundamental rules of nature and vital links to other scientific disciplines.

In three-dimensional notation, Maxwell's equations are,

$$\vec{\nabla} \times \vec{E}(r,t) + \frac{\partial \vec{B}(r,t)}{\partial t} = 0 \tag{2-1}$$

$$\vec{\nabla} \times \vec{H}(r,t) - \frac{\partial \vec{D}(r,t)}{\partial t} = \vec{J}(r,t) \tag{2-2}$$

$$\vec{\nabla} \cdot \vec{D}(r,t) = \rho(r,t) \tag{2-3}$$

$$\vec{\nabla} \cdot \vec{B}(r,t) = 0 \tag{2-4}$$

11

where E, H, B, D, J and ρ are the real functions of position and time. Equation (2-1) is Faraday's induction law, (2-2) is the generalised Ampere's circuit law, (2-3) and (2-4) are Gauss law for electric and magnetic fields. Taking the divergence of (2-2) and introducing into (2-4) following equation is obtained.

$$\vec{\nabla} \cdot \vec{J}(r,t) + \frac{\partial \rho\,(r,t)}{\partial t} = 0 \qquad\qquad (2\text{-}5)$$

which is the continuity equation. Regarding (2-5) as a fundamental equation, it is obvious that, it can be used to derive (2-4) by taking the divergence of (2-1) which gives that the divergence of B is constant or independent of time. Such a constant if not zero, than implies the existence of magnetic monopole similar to free electric charges. Since magnetic monopoles do not exist, this constant must be zero. This term leads to (2-3).

Maxwell's equations are fundamental laws governing the behaviour of electromagnetic fields in free space and in any media. We have so far no references to the various material properties that provide connections to other disciplines of physics such as plasma physics, quantum mechanics, solid state physics, etc. all of which interact in one way or another with electromagnetic fields. From the electromagnetic point of view, it is interested that how electromagnetic fields behave in the presence of media, whether the wave reflected, refracted or scattered. Thus we shall characterise material by so-called constitutive relations that can be classifed according to the various properties of the media.

The necessity of using constitutive relations to supplement the Maxwell's equations is clear from the following mathematical observations. Let us examine the Maxwell's equations for the number of unknown quantities. There are a total twelve scalar unknowns for the field components. It is already known that (2-3) and (2-4) are not independent, they can be derived from (2-1), (2-2) and (2-5). The independent equations are (2-1) and (2-2) which constitute six scalar equations. Thus we need six more scalar equations. These are the constitutive relations which relate D to E and B and H to E and B, respectively.

Constitutive relations in the most general form can be written as,

$$c\vec{D} = P.\vec{E} + cL.\vec{B} \qquad (2\text{-}6)$$

$$\vec{H} = M.\vec{E} + cQ.\vec{B} \qquad (2\text{-}7)$$

where c is the speed of light in free space and P,Q,L and M are 3×3 matricies. Their elements are called constitutive parameters. Equations (2-6) and (2-7) can be written in the matrix form.

$$\begin{bmatrix} cD \\ H \end{bmatrix} = U \begin{bmatrix} E \\ cB \end{bmatrix} \qquad (2\text{-}8)$$

with

$$U = \begin{bmatrix} P & L \\ M & Q \end{bmatrix}$$

U is a 6×6 constitutive matrix which has the dimension of admittance. According to the functional dependence of U, any media can be classified as,

i) Inhomegenous if U is a function of space coordinates,

ii) Nonstationary if U is a function of time,

iii) Time-dispersive if U is a function of time derivative,

iv) Spatial-dispersive if U is a function of spatial derivativies,

v) Nonlinear if U is a function of electromagnetic fields.

The constitutive relations can be expressed in the form of D and B as a function of E and H and vice versa.

$$\begin{bmatrix} D \\ B \end{bmatrix} = \frac{1}{c} \begin{bmatrix} P - L.Q^{-1} & L.Q^{-1} \\ - Q^{-1}.M & Q^{-1} \end{bmatrix} \begin{bmatrix} E \\ H \end{bmatrix} \qquad (2\text{-}9)$$

or

13

$$\begin{bmatrix} E \\ H \end{bmatrix} - c \begin{bmatrix} P^{-1} & -P^{-1}.L \\ M.P^{-1} & Q - M.^{-1}L \end{bmatrix} \begin{bmatrix} D \\ B \end{bmatrix} \qquad (2\text{-}10)$$

In the definition of the constitutive relations, the constitutive matricies L and M relate the electric and magnetic fields. When L and M are not identically zero, the medium is bianisotropic. When there is no coupling between electric and magnetic fields (i.e. L=M=0) then the medium is anisotropic. When P=cεI and Q=(1/εμ)I with I denoting the 3×3 unit matrix the medium is isotropic.

2.2 Wave Propagation in Chiral Medium

It has been shown that in the case of a chiral medium, modelled by randomly oriented and uniformly distributed, lossless, short wire helicies, the set of the constitutive relations for the time harmonic field are in the following form [39] (with the suppressed time convention of $e^{j\omega t}$),

$$\vec{D} - \epsilon \vec{E} - j\xi\vec{B} \qquad (2\text{-}11)$$

$$\vec{H} - -j\xi\vec{E} + \frac{1}{\mu}\vec{B} \qquad (2\text{-}12)$$

where ϵ, μ and ξ are real constants representing the permittivity, permeability and the chirality admittance of the medium, respectively.

As evident from these constitutive relations, the displacement vector D inside a chiral medium not only depends on E but also on B. Similarly, the magnitude of the magnetic field vector H depends on both B and E. This is due to the special configuration of the model of the object, the short metallic helix. Explicitly, when an electromagnetic wave illuminates this medium and the object therein the electric fields induces current in tthe straight portion of the helix, and by continuity these current must also flow in

14

circular portion of the object. The current in the straight portion contributes to the electric dipole moment of the object while the currents in the circular portion contributes to its magnetic dipole moment. In a complementary manner, the incident magnetic field induces currents in the circular portion and by its continuity in the straight portion. Thus, also the magnetic field contributes to both electric and magnetic dipole moments of the object. From this physical argument, the extra parameter ξ (real number) in constitutive relations (2-11) and (2-12), is an indication of the degree of chirality of the medium.

Consider the time harmonic form of the Maxwell's equations ($e^{j\omega t}$ time convention suppressed) for source free region.

$$\vec{\nabla} \times \vec{E} = -j\omega\vec{B} \qquad (2\text{-}12)$$

$$\vec{\nabla} \times \vec{H} = j\omega\vec{D} \qquad (2\text{-}13)$$

$$\vec{\nabla}.\vec{D} = 0 \qquad (2\text{-}14)$$

$$\vec{\nabla}.\vec{B} = 0 \qquad (2\text{-}15)$$

Using above equations and the constitutive relations given in (2-11) and (2-12) on can obtain following relations.

$$\vec{\nabla} \times \vec{E} = -j\omega\mu\vec{H} + \omega\mu\xi\vec{E} \qquad (2\text{-}17)$$

$$\vec{\nabla} \times \vec{H} = j\omega(\epsilon + \mu\xi^2)\vec{E} + \omega\mu\xi\vec{H} \qquad (2\text{-}18)$$

Taking the curl of (2-17) and introducing (2-18) and vice versa leads to the following wave equations for electric and magnetic fields,

$$\vec{\nabla} \times \vec{\nabla} \times \vec{E} - 2\omega\mu\xi\vec{\nabla} \times \vec{E} - k^2\vec{E} = 0 \qquad (2\text{-}19)$$

15

$$\vec{\nabla} \times \vec{\nabla} \times \vec{H} - 2 \omega \mu \xi \vec{\nabla} \times \vec{H} - k^2 \vec{H} = 0 \qquad (2\text{-}20)$$

where $k^2 = \omega^2 \mu \epsilon$.

Now assume that, an electric field of a plane wave propagating in the +z direction in an unbounded, source free isotropic chiral medium and let the electric field be in the following form.

$$\vec{E} = (A \vec{a}_x + B \vec{a}_y) e^{\gamma z} \qquad (2\text{-}21)$$

where A and B are real or complex constants to be determined and γ is the propagation constant. Substitution of (2-21) into (2-19) yields $A^2 + B^2 = 0$ or $A = \pm jB$.

For B= -jA, Equation (2-21) represents a Right Circularly Polarised (RCP) wave and corresponding wavenumber γ_{RCP} is,

$$\gamma_{RCP} = -j \, k_R = -j [\, \omega \mu \xi + \sqrt{\omega^2 \mu \epsilon + (\omega \mu \xi)^2} \,] \qquad (2\text{-}22)$$

For B= +jA, (2-21) represents a Left Circularly Polarised (LCP) wave and corresponding wavenumber γ_{LCP} is,

$$\gamma_{LCP} = -j \, k_L = -j [\, -\omega \mu \xi + \sqrt{\omega^2 \mu \epsilon + (\omega \mu \xi)^2} \,] \qquad (2\text{-}23)$$

Hence, for a plane wave propagating in an unbounded isotropic chiral medium, there exist two bulk eigenmodes of propagation. These are right circularly and left circularly polarised plane waves with unequal wavenumbers k_R and k_L respectively.

Equation (2-22) and (2-23) place in evidence the double-mode propagation in a chiral medium which is called polarisation birefringence. Here a right circularly polarised wave propagates through the medium with a phase velocity $v_R = w/k_R$ and a left circularly polarised wave propagates with a phase velocity $v_L = w/k_L$ which is different from v_R. As a result, a linearly polarised wave can not traverse this medium without changing its polarisation, giving rise to optical activity as shown in Figure.2.1.

Optical activity is referred as the rotation of the plane of polarisation by a medium. Here in an isotropic chiral slab, a linearly polarised wave is divided into two circularly polarised waves of opposite handedness and unequal phase velocities. Behind the slab,

16

the two rays combine to result a linearly polarised wave whose plane of polarisation is rotated with respect to that of the incident wave. Optical activity in an isotropic chiral medium differs from the phenomenon of Faraday rotation in, say, magnetoplasma or in a ferrite by the fact that the eigenwaves (RCP and LCP) are independent of the direction of propagation whereas the latter is not.
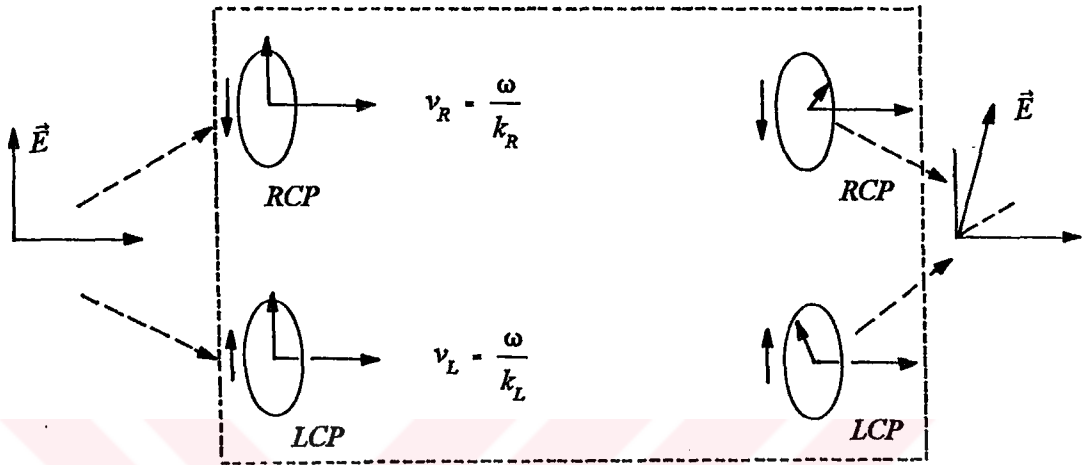
Figure 2.1   Optical acticity

When k_R and k_L are complex quantities, the two eigenmodes experience unequal attenuation in addition to dissimilar phase velocities. This referred to as circular dichroism and shown in Figure. 2.2
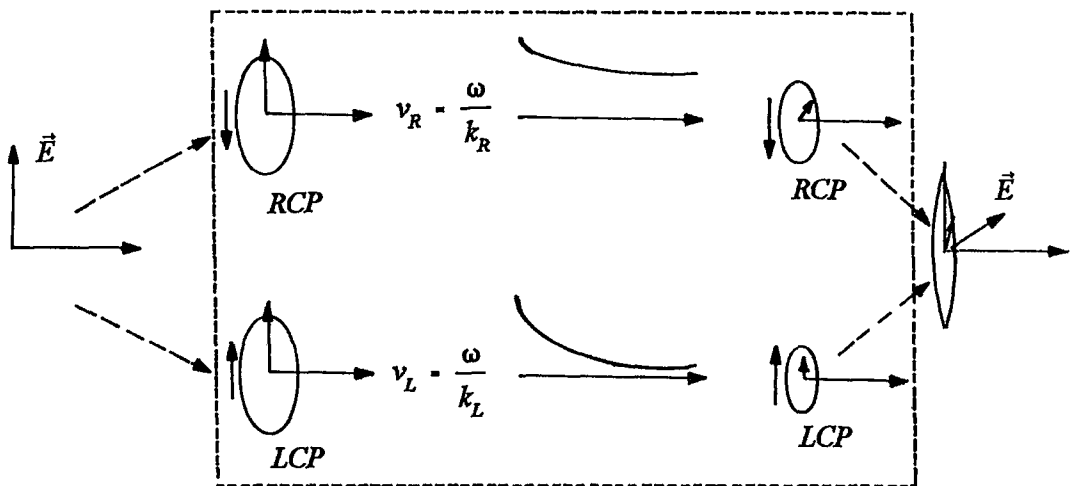
Figure 2.2   Circular dichroism

17

Circular dichroism which refer to a change of the polarisation ellipticity of waves by a medium. Here in an isotropic chiral slab, a linearly polarised wave is divided into RCP and LCP waves with unequal attenuation. Behind the slab, the two waves combine to give an elliptically polarised wave.

The amount of rotation or attenuation depends on the distance travelled in the medium and on the difference between the two wavenumbers which is an indication of degree of chirality given by ξ. Also note that as the chirality of the medium disappears, i.e., $\xi \rightarrow 0$, the chiral wave equation (2-19), (2-20) approaches to that of the conventional Helmholtz Equation and two unequal wavenumbers approach the single wavenumber $k^2 = \omega^2 \mu_0 \epsilon$.

The problem of reflection and refraction of electromagnetic waves at an achiral-chiral interface has attracted the attention of many reseachers in recent years. It has been shown that when a monochromatic plane wave is obliquely incident upon a boundary between achiral an isotropic chiral medium, it splits into two transmitted waves proceeding into the chiral medium, and a reflected wave propagating back into the achiral medium as depeicted in Figure. 2.3
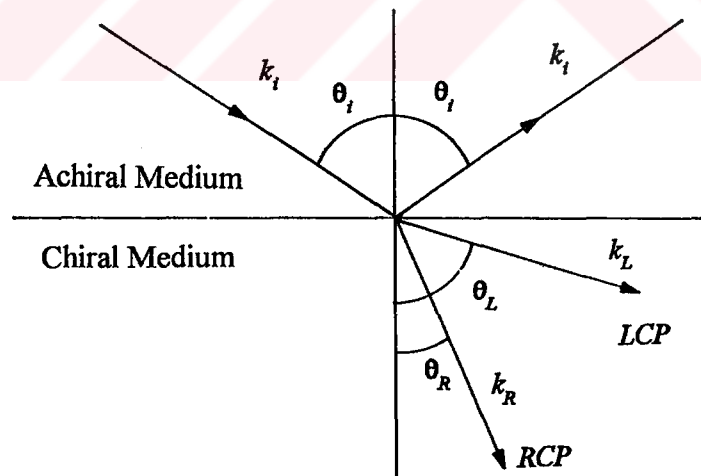
Figure 2.3   Reflection and refraction at an achiral-chiral interface

18

The two transmitted waves inside the isotropic chiral medium, are being a RCP and a LCP plave wave with associated wavenumbers and unequal phase velocities. Therefore the Snell's law has been written for the angles as,

$$k_i \sin \theta_i - k_R \sin \theta_R - k_L \sin \theta_L \qquad \theta_i - \theta_r \qquad (2\text{-}24)$$

where θ_R and θ_L are angles of refraction for RCP and LCP waves respectively; k_i is the wavenumber of the incident wave, θ_i is the angle of incidence and θ_r is the angle of reflection. The Fresnell equation, total internal reflection, the Brewster angle for an achiral-chiral interface has been extensively studied and novel results have reported in the literature [40],[41].

CHAPTER 3

FREQUENCY SELECTIVE SURFACES LOADED BY AN ISOTROPIC CHIRAL SLAB

3.1 Floquet Theorem

Consider a periodic structure lying on the xy plane of the three dimensional absolute cartesian system and has periodicty b in x direction and d in y direction in a source free region. The scalar Helmholtz equation with harmonic dependence of $e^{j\omega t}$ is,

$$(\nabla^2 + k^2)\,\psi(x,y,z) = 0 \tag{3-1}$$

where k is the wavenumber, $k^2 = \omega^2 \mu \epsilon$. If the direction of propagation is along the +z axis, a solution to the homogenous wave equation will be of the form.

$$\psi(x,y,z) = e^{-j\gamma z}\,\Phi(x,y) \tag{3-2}$$

Then Equation(3-1) becomes

$$\left(\frac{\partial^2}{\partial x^2} + \frac{\partial^2}{\partial y^2} + (k^2 - \gamma^2)\right)\,\Phi(x,y) = 0 \tag{3-3}$$

$$\phi(x,y) = f(x)\cdot g(y) \tag{3-4}$$

Assuming that,and using the seperation of variables technique, the partial differential equation (3-3) can be written as two ordinary differential equations:

20

$$\left(\frac{d^2}{dx^2} + k_x^2\right).f(x) = 0$$

$$\left(\frac{d^2}{dy^2} + k_y^2\right).g(y) = 0$$

(3-5)

here the seperation constants k_x and k_y are related through the following equation.

$$k^2 = k_x^2 + k_y^2 + \gamma^2$$

(3-6)

However recalling that the structure is periodic in the x and y directions the solution must also be periodic according to the Floquet Theorem . Thus if f(x) and g(y) are to represent the waves propagating in x and y directions, respectively, it is necessary that,

$$f(x + b) = e^{-jk_{x0}b}.f(x)$$

(3-7)

$$g(y + d) = e^{-jk_{y0}d}.g(y)$$

(3-8)

where b and d are the periodicities in the x and y directions respectively. This is possible if,

$$f(x) = e^{-jk_{x0}x}.F_p(x)$$

(3-9)

$$g(y) = e^{-jk_{y0}y}.G_p(y)$$

(3-10)

where $F_p(x)$ and $G_p(y)$ are the periodic functions of x with period b and function of y with period d, respectively. Therefore $F_p(x)$ and $G_p(y)$ can be expanded into a Fourier series;

$$F_p(x) = \sum_{p=-\infty}^{\infty} A_p\, e^{-j\frac{2\pi}{b}px}$$

(3-11)

21

$$G_p(y) = \sum_{q=-\infty}^{\infty} B_p\, e^{-j\frac{2\pi}{d}qy} \qquad (3\text{-}12)$$

Substituting (3-11) and (3-12) into (3-9) and (3-10) one can obtain.

$$f(x) = \sum_{p=-\infty}^{\infty} A_p\, e^{-j(k_{x0} + \frac{2\pi}{b}p)x} \qquad (3\text{-}13)$$

$$g(y) = \sum_{q=-\infty}^{\infty} B_q\, e^{-j(k_{y0} + \frac{2\pi}{d}q)y} \qquad (3\text{-}14)$$

Therefore the solution to (3-2) can be written as,

$$\psi(x,y,z) = \sum_{p=-\infty}^{\infty} \sum_{q=-\infty}^{\infty} C_{pq}\, e^{-j(k_{x0} + \frac{2\pi}{b}p)x}\, e^{-j(k_{y0} + \frac{2\pi}{d}q)y}\, e^{-j\gamma_{pq}z} \qquad (3\text{-}15)$$

where $C_{pq} = A_{pq} B_{pq}$ and

$$\gamma_{pq}^2 = k^2 - (k_{x0} + \frac{2\pi}{b}p)^2 - (k_{y0} + \frac{2\pi}{d}q)^2 \qquad (3\text{-}16)$$

The constants k_{x0} and k_{y0} are equal to the wavenumbers in the x and y direction of the incident wave.

Now consider a periodic structure along the skewed (nonorthogonal) coordinates η_1 and η_2 as shown in Figure 3.1. Without loss of generality, the η_1 axis is choosen to coincide with the x axis and η_2 axis makes an angle, α, with respect to the x axis. Then the element location is now defined by two indicies p and q as,

$$\vec{P}_{pq} = pb\hat{\eta}_1 + qd\hat{\eta}_2 \qquad (3\text{-}17)$$

where η_1 and η_2 are unit vectors along η_1 and η_2 axes, while b and d represent the periodicities of the two dimensional structure along η_1 and η_2, respectively. A basic unit cell now has the shape of a parallelogram as depicted.

22
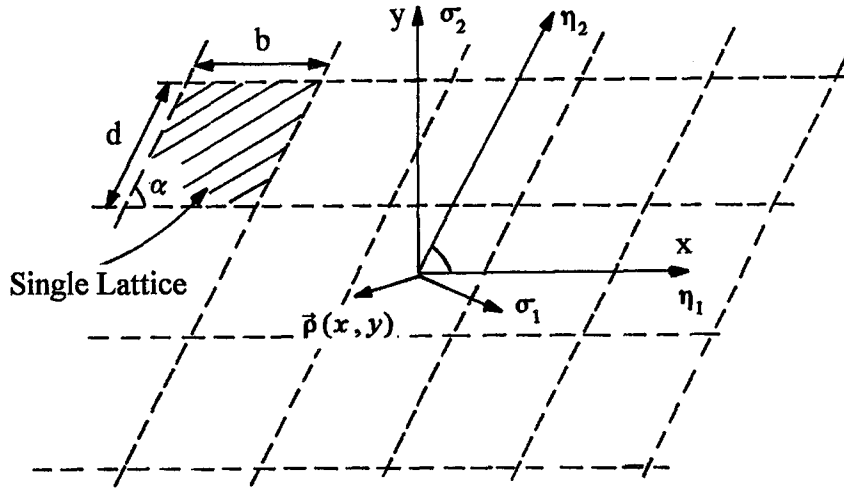
Figure 3.1   Lattice geometry

The lattice described by the vectors η_1 and η_2 will be referred as direct lattice. The vectors η_1 and η_2 may also be written interms of cartesian ones as follows.

$$\begin{bmatrix} \vec{\eta}_1 \\ \vec{\eta}_2 \end{bmatrix} = \begin{bmatrix} 1 & 0 \\ \cos\alpha & \sin\alpha \end{bmatrix} \begin{bmatrix} \vec{a}_x \\ \vec{a}_y \end{bmatrix} \tag{3-18}$$

Now assume that one may also define another set of vectors σ_1 and σ_2 called reciprocal lattice vectors such that,

$$\vec{\sigma}_i \cdot \vec{\eta}_k = \delta_{ik} = \begin{pmatrix} 1 & i = k \\ 0 & i \neq k \end{pmatrix} , i = k = 1,2,.. \tag{3-19}$$

writing σ_1 and σ_2 in terms of cartesian components.

$$\begin{aligned} \vec{\sigma}_1 &= \vec{a}_x \sigma_{11} + \vec{a}_y \sigma_{12} \\ \vec{\sigma}_2 &= \vec{a}_x \sigma_{21} + \vec{a}_y \sigma_{22} \end{aligned} \tag{3-20}$$

Introducing (3-18) and (3-19) into (3-20), the following relations are obtained.

$$\vec{\eta}_1 \cdot \vec{\sigma}_1 = 1 = \delta_{11}$$

$$\vec{\eta}_1 \cdot \vec{\sigma}_2 = 1 = \sigma_{21} \cos\alpha + \sigma_{22} \sin\alpha$$

$$\vec{\eta}_2 \cdot \vec{\sigma}_1 = 0 = \sigma_{11} \cos\alpha + \sigma_{12} \sin\alpha$$

$$\vec{\eta}_2 \cdot \vec{\sigma}_2 = 0 = \delta_{21}$$

23

Consequently one can deduce,

$$\sigma_{11} = 1 \quad , \quad \sigma_{12} = -\frac{\cos \alpha}{\sin \alpha} = -\frac{1}{\tan \alpha}$$

$$\sigma_{21} = 1 \quad , \quad \sigma_{22} = -\frac{1}{\sin \alpha}$$

(3-21)

Therefore reciprocal lattice vector will be

$$\vec{\sigma}_1 = \vec{a}_x - \cot \alpha \; \vec{a}_y$$

$$\vec{\sigma}_2 = \vec{a}_x - \mathrm{cosec} \; \alpha \; \vec{a}_y$$

(3-22)

Note that according to the given definition σ_1 and σ_2 are orthogonal to η_2 and η_1 respectively.

Now consider a periodic function $F(x,y)$ in the direct lattice such that it has the same values at points defined by the vectors.

$$\vec{p}(x,y) = \vec{p}(x,y) + nb \; \vec{\eta}_1 + md \; \vec{\eta}_2$$

(3-23)

where n and m are integers. Using the η_1 and η_2 instead of x and y respectively, in which case

$$\vec{p}(x,y) = x \vec{a}_x + y \vec{a}_y$$

(3-24)

becomes

$$\vec{p}(\eta_1,\eta_2) = \eta_1 \vec{\eta}_1 + \eta_2 \vec{\eta}_2$$

(3-25)

That is, $p(x,y)$ is represented by its η_1 and η_2 components along the unit vectors η_1 and η_2. Thus a new function $f(\eta_1,\eta_2)$ with periods b and d in η_1 and $,\eta_2$ are obtained. This periodic function can be expressed in a double Fourier series as,

$$f(\eta_1,\eta_2) = \sum_{p=-\infty}^{\infty} \sum_{q=-\infty}^{\infty} H_{pq} \; e^{-j\frac{2\pi}{b}p \; \eta_1} \; e^{-j\frac{2\pi}{d}q \; \eta_2}$$

(3-26)

Remembering that $\sigma_1 \perp \eta_2$ and $\sigma_2 \perp \eta_1$, η_1 and η_2 can be expressed interms of reciprocal

24

lattice vectors as follows.

$$\vec{\sigma}_1 \cdot \vec{p} = (\vec{\sigma}_1 \cdot \vec{\eta}_1)\eta_1 + (\vec{\sigma}_1 \cdot \vec{\eta}_2)\eta_2 = \eta_1$$

$$\vec{\sigma}_2 \cdot \vec{p} = (\vec{\sigma}_2 \cdot \vec{\eta}_1)\eta_1 + (\vec{\sigma}_2 \cdot \vec{\eta}_2)\eta_2 = \eta_2$$

(3-27)

Thus (3-26) can be rearranged as,

$$f(x,y) = \sum_{p=-\infty}^{\infty} \sum_{q=-\infty}^{\infty} H_{pq} e^{-j\frac{2\pi}{b}p(\vec{\sigma}_1 \cdot \vec{p})} e^{-j\frac{2\pi}{d}q(\vec{\sigma}_2 \cdot \vec{p})}$$

(3-28)

or in terms of x, y and α.

$$f(x,y) = \sum_{p=-\infty}^{\infty} \sum_{q=-\infty}^{\infty} H_{pq} e^{-j\frac{2\pi}{b}p(x - y\cot\alpha)} e^{-j\frac{2\pi}{d}q(y\csc\alpha)}$$

(3-29)

where

$$\eta_1 = \vec{\sigma}_1 \cdot \vec{p} = x - y\cot\alpha$$

$$\eta_2 = \vec{\sigma}_2 \cdot \vec{p} = y\csc\alpha$$

(3-30)

Thus for the periodic structure shown in Figure 3.1 a complete set of solution given by (3-15) to the scalar wave equation can be written as.

$$\psi = \sum_{p=-\infty}^{\infty} \sum_{q=-\infty}^{\infty} A_{pq} e^{-j(k_{\eta_1} + \frac{2\pi}{b}p)\eta_1} e^{-j(k_{\eta_2} + \frac{2\pi}{d}q)\eta_2} e^{-j\gamma_{pq}z}$$

(3-31)

where k_{η_1} and k_{η_2} are the wavenumbers along η_1 and η_2 axis respectively. That is ,

$$k_{\eta_1} = \vec{\eta}_1 \cdot \vec{k} = \vec{a}_x \cdot \vec{k} = k\sin\theta\cos\phi$$

(3-32)

$$k_{\eta_2} = \vec{\eta}_2 \cdot \vec{k} = (\cos\alpha\,\vec{a}_x + \sin\alpha\,\vec{a}_y) \cdot \vec{k}$$

$$= k(\sin\theta\cos\phi\cos\alpha + \sin\theta\sin\phi\sin\alpha)$$

(3-33)

where

$$\vec{k} = k \sin \theta \cos \phi \, \vec{a}_x + k \sin \theta \sin \phi \, \vec{a}_y + k \cos \theta \, \vec{a}_z \qquad (3\text{-}34)$$

Therefore (3-31) can also be written as.

$$\psi = \sum_{p=-\infty}^{\infty} \sum_{q=-\infty}^{\infty} A_{pq} \, e^{-j(k_{x0} + \frac{2\pi}{b}p)x} \, e^{-j(k_{y0} - \frac{2\pi}{b\tan\alpha}p + \frac{2\pi}{d\sin\alpha}q)y} \, e^{-j\gamma_{pq}z} \qquad (3\text{-}35)$$

where

$$\gamma_{pq}^2 = k^2 - (k_{x0} + \frac{2\pi}{b}p)^2 - (k_{y0} - \frac{2\pi}{b\tan\alpha}p + \frac{2\pi}{d\sin\alpha}q)^2 \qquad (3\text{-}36)$$

Now let su define the two vectors k_1 and k_2 as,

$$\vec{k}_1 = \frac{2\pi d}{A}\vec{\eta}_2 \times \vec{a}_z$$

$$= \frac{2\pi d}{A}(\cos\alpha\,\vec{a}_x + \sin\alpha\,\vec{a}_y) \times \vec{a}_z \qquad (3\text{-}37)$$

and

$$\vec{k}_2 = \frac{2\pi b}{A}\vec{a}_z \times \vec{a}_x$$

$$= \frac{2\pi}{d\sin\alpha}\vec{a}_y \qquad (3\text{-}38)$$

where A is the area of the unit cell, A= b.d.sinα
and so,

$$(p\vec{k}_1 + q\vec{k}_2)\cdot\vec{\rho} = \frac{2\pi p}{b}x + (\frac{2\pi q}{d\sin\alpha} - \frac{2\pi p}{b\tan\alpha})y \qquad (3\text{-}39)$$

Substituting (3-39) into (3-35) yields

$$\psi = \sum_{p=-\infty}^{\infty} \sum_{q=-\infty}^{\infty} A_{pq} \, e^{-j(k_{x0}x + k_{y0}y)} \, e^{-j(p\vec{k}_1 + p\vec{k}_2)\cdot\vec{\rho}} \, e^{-j\gamma_{pq}z} \qquad (3\text{-}40)$$

26

or

$$\psi = \sum_{p=-\infty}^{\infty} \sum_{q=-\infty}^{\infty} A_{pq} \, e^{-j\vec{k}_{Tpq}\cdot\vec{\rho}} \, e^{-j\gamma_{pq}z} \qquad (3\text{-}41)$$

where

$$\vec{k}_{Tpq} = \vec{k}_T + p\,\vec{k}_1 + q\,\vec{k}_2$$
$$= (k_{x0} + \frac{2\pi}{b}p)\,\vec{a}_x + (k_{y0} - \frac{2\pi}{b\tan\alpha}p + \frac{2\pi}{d\sin\alpha}q)\,\vec{a}_y \qquad (3\text{-}42)$$

with $k_{x0} = k.\sin\theta\,\cos\phi$ and $k_{y0} = k.\sin\theta\,\sin\phi$, and

$$\gamma_{pq}^2 = k^2 - \vec{k}_{Tpq}\cdot\vec{k}_{Tpq} \qquad (3\text{-}43)$$

3.2 Modal Fields in Achiral (Dielectric) and Chiral Medium

Consider a linearly polarised plane wave propagating in an arbitrary direction specified by the spherical angles θ and ϕ as shown in Figure 3.2.
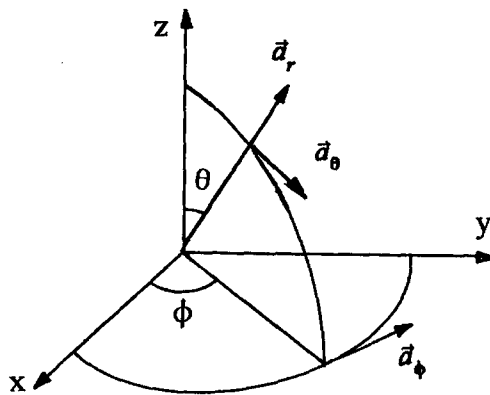
Figure 3.2   Propagation vector

Let the electric field be polarised in $\vec{a}_u$ direction. Therefore the eelectric field vector can

27

be written in the following form

$$\vec{E} = E_0 \, \vec{a}_u \, e^{-jk\,\vec{a}_r \cdot \vec{r}} \tag{3-44}$$

where $\vec{a}_u$ (unit vector) is perpendicular to $\vec{a}_r$ which specifies the direction of propagation. More explicitly one can write (3-44) as,

$$\vec{E} = E_0 (\cos \beta \, \vec{a}_\phi + \sin \beta \, \vec{a}_\theta) \, e^{-jk_x x} \, e^{-jk_y y} \, e^{-j\gamma z} \tag{4-45}$$

where,

$$k_x = k \sin \theta \cos \phi$$

$$k_y = k \sin \theta \sin \phi$$

$$\gamma = \sqrt{k^2 - k_x^2 - k_y^2} = k \cos \theta$$

$$\vec{r} = x \, \vec{a}_x + y \, \vec{a}_y + z \, \vec{a}_z$$

$$\vec{a}_r = \sin \theta \cos \phi \, \vec{a}_x + \sin \theta \sin \phi \, \vec{a}_x + \cos \theta \, \vec{a}_z$$

$$\vec{a}_\theta = \cos \theta \cos \phi \, \vec{a}_x + \cos \theta \sin \phi \, \vec{a}_x - \sin \theta \, \vec{a}_z$$

$$\vec{a}_\phi = - \sin \phi \, \vec{a}_x + \cos \phi \, \vec{a}_y$$

If $\beta = 90°$, then the magnetic field associated to the electric field has no z component, so it represents a TM_z wave.

$$\vec{E}^{TM} = E_0 \, \vec{a}_\theta \, e^{-jk\,\vec{a}_r \cdot \vec{r}} \tag{3-46}$$

Associated magnetic field,

$$\vec{H}^{TM} = E_0 \, \frac{k}{\omega \mu} \, \vec{a}_\phi \, e^{-jk\,\vec{a}_r \cdot \vec{r}} \tag{3-47}$$

Now let us define,

$$\vec{k}_T = \sin\theta\cos\phi\,\vec{a}_x + \sin\theta\sin\phi\,\vec{a}_y$$

$$\vec{r}_T = x\,\vec{a}_x + y\,\vec{a}_y$$

$$\gamma = \sqrt{k^2 - |\vec{k}_T|^2} \tag{3-48}$$

$$Y = \sqrt{\frac{\epsilon}{\mu}}$$

using (3-48) and rearranging (3-46) and (3-47) the electric field and associated magnetic field can be written as,

$$\vec{E}^{TM} = E_0 \frac{\gamma}{k} \left(\frac{\vec{k}_T}{|\vec{k}_T|} - \frac{k}{\gamma} |\vec{k}_T| \vec{a}_z \right) e^{-j\vec{k}_T \cdot \vec{r}_T} e^{-j\gamma z} \tag{3-49}$$

$$\vec{H}^{TM} = E_0 \frac{\gamma}{k} \vec{a}_z \times \frac{\vec{k}_T}{|\vec{k}_T|} e^{-j\vec{k}_T \cdot \vec{r}_T} e^{-j\gamma z} \tag{3-50}$$

The transverse components of the fields can be written as,

$$\vec{E}_t^{TM} = E^{TM} \psi_{TM} e^{-j\gamma z} \tag{3-51}$$

$$\vec{H}_t^{TM} = \vec{a}_z \times Y^{TM} E^{TM} \psi_{TM} e^{-j\gamma z} \tag{3-52}$$

$$E^{TM} = E_0 \frac{\gamma}{k}$$

$$Y^{TM} = Y \frac{k}{\gamma}$$

$$\psi_{TM} = \vec{u}_{TM} e^{-j\vec{k}_T \cdot \vec{r}_T}$$

$$\vec{u}_{TM} = \frac{\vec{k}_T}{|\vec{k}_T|}$$

where

29

If $\beta = 0°$ the electric field vector has no z component therefore it represents TE_z waves.

$$\vec{E}^{TE} = E_0 \, \vec{a}_\phi \, e^{-jk\,\vec{a}_r \cdot \vec{r}} \tag{3-53}$$

and associated magnetic field is,

$$\vec{H}^{TE} = E_0 \, \frac{k}{\omega \, \mu} \, (- \cos \theta \cos \phi \, \vec{a}_x + \cos \theta \sin \phi \, \vec{a}_y + \sin \theta \, \vec{a}_z) \, e^{-jk\vec{a}_r \cdot \vec{r}} \tag{3-54}$$

Using the defintions given in (3-48) the electric and magnetic field vectors can be rearranged in the following form.

$$\vec{E}^{TE} = E_0 \, (\, \vec{a}_z \times \frac{\vec{k}_T}{|\vec{k}_T|} \,) \, e^{-j\vec{k}_T \cdot \vec{r}_T} \, e^{-j\gamma z} \tag{3-55}$$

$$\vec{H}^{TE} = E_0 \frac{\gamma}{k} \, (\, \vec{a}_z \times \vec{a}_z \times \frac{\vec{k}_T}{|\vec{k}_T|} + \frac{k}{\gamma} \, |\vec{k}_T| \, \vec{a}_z \,) \, e^{-j\vec{k}_T \cdot \vec{r}_T} \, e^{-j\gamma z} \tag{3-56}$$

The transverse components of the above fields can therefore be expressed in more implicit form as,

$$\vec{E}_t^{TE} = E^{TE} \, \vec{\psi}_{TE} \, e^{-j\gamma z} \tag{3-57}$$

$$\vec{H}_t^{TE} = \vec{a}_z \times Y^{TE} \, E^{TE} \, \vec{\psi}_{TE} \, e^{-j\gamma z} \tag{3-58}$$

where

30

$$E^{TE} = E_0$$

$$Y^{TE} = Y\frac{\gamma}{k}$$

$$\vec{\Psi}_{TE} = \vec{u}_{TE}\, e^{-j\vec{k}_T \cdot \vec{r}_T}$$

$$\vec{u}_{TE} = \vec{a}_z \times \frac{\vec{k}_T}{|\vec{k}_T|}$$

It has been already known that left hand circularly (LCP) polarised plane wave is an eigenwave in an isotropic chiral medium. A LCP plane wave propagating in an isotropic chiral medium can be written as,

$$\vec{E}^{LCP} = E_L\,(\,\vec{a}_\theta + j\,\vec{a}_\phi\,)\, e^{-j k_L \vec{a}_r \cdot \vec{r}} \tag{3-59}$$

and associated magnetic field can be obtained by substituting (3-59) into (2-15). The transverse components of the electric and magnetic field vectors of a LCP plane wave in chiral medium are expressed in the following form.

$$\vec{E}_t^{LCP} = (\,E_L^{TM}\,\vec{u}_{TM} + j\,E_L^{TE}\,\vec{u}_{TE}\,)\, e^{-j\vec{k}_T \cdot \vec{r}_T}\, e^{-j\gamma_L z} \tag{3-60}$$

$$\vec{H}_t^{LCP} = \vec{a}_z \times (\,Y_L^{TM}\,E_L^{TM}\,\vec{u}_{TM} + j\,Y_L^{TE}\,E_L^{TE}\,\vec{u}_{TE}\,)\, e^{-j\vec{k}_T \cdot \vec{r}_T}\, e^{-j\gamma_L z} \tag{3-61}$$

where

$$E_L^{TM} = E_L\,\frac{\gamma_L}{k_L} \qquad\qquad E_L^{TE} = E_L$$

$$Y_L^{TM} = Y_s\,\frac{k_L}{\gamma_L} \qquad\qquad Y_L^{TE} = Y_s\,\frac{\gamma_L}{k_L}$$

$$Y_s = \frac{k_s}{\omega\mu} \qquad\qquad k_s = \omega\mu\xi + k_L$$

$$\gamma_L = \sqrt{k_L^2 - |\vec{k}_T|^2}$$

31

Right hand circularly polarised (RCP) plane wave is the other eigenwave which can propagate in an isotropic chiral medium. A right circularlt polarised plane wave propagating in chiral medium in an arbitrary direction can be expressed as,

$$\vec{E}^{RCP} = E_L (\vec{a}_\theta - j \vec{a}_\phi) \, e^{-jk_R \vec{a}_r \cdot \vec{r}} \tag{3-62}$$

Corresponding magnetic field can be obtained by introducing (3-62) into (2-15) and transverse components of the fields can be written in the following form.

$$\vec{E}_t^{RCP} = (E_R^{TM} \vec{u}_{TM} - j E_R^{TE} \vec{u}_{TE}) \, e^{-j\vec{k}_T \cdot \vec{r}_T} \, e^{-j\gamma_R z} \tag{3-63}$$

$$\vec{H}_t^{RCP} = \vec{a}_z \times (Y_R^{TM} E_R^{TM} \vec{u}_{TM} - j Y_R^{TE} E_R^{TE} \vec{u}_{TE}) \, e^{-j\vec{k}_T \cdot \vec{r}_T} \, e^{-j\gamma_R z} \tag{3-64}$$

where

$$E_R^{TM} = E_R \, \frac{\gamma_R}{k_R} \qquad\qquad E_R^{TE} = E_R$$

$$Y_R^{TM} = Y_s \, \frac{k_R}{\gamma_R} \qquad\qquad Y_R^{TE} = Y_s \, \frac{\gamma_R}{k_R}$$

$$Y_s = \frac{k_s}{\omega \mu} \qquad\qquad k_s = \omega \mu \xi + k_R$$

$$\gamma_R = \sqrt{k_R^2 - |\vec{k}_T|^2}$$

3.3. Formulation of the Problem

Consider a frequency selective surface comprising of the two dimensional infinite array of thin conducting elements printed on an isotropic chiral slab having thickness of d as depicted in Figure 3.3. Conducting elements have the periodicities of d_1 and d_2 in the direction of skewed axes η_1 and η_2 respectively. Without loss of genarility η_1 axis is assumed to have the same direction of the x axis of the absolute cartesian system.

32
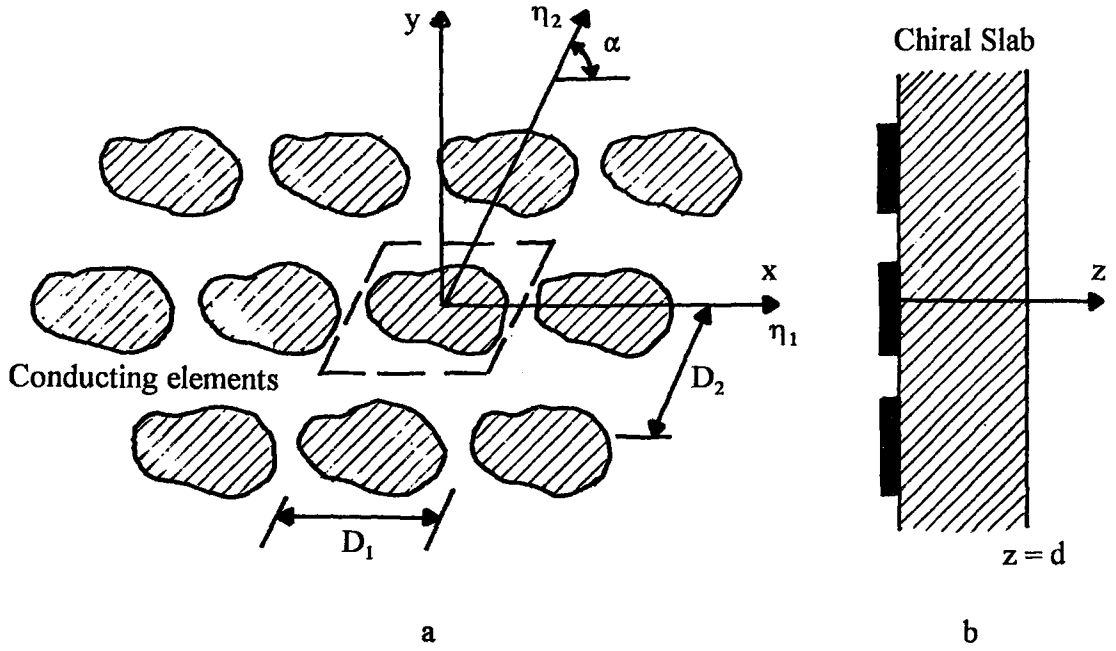
Figure 3.3   Geometry of a Chiro-FSS, a) Top view, b) Side view

Even in the presence of the chiral slab the transversal nature of the scattering problem is still preserved due owing to isotropic property of the chiral slab. This allows us to use the modal analysis technique that is frequently applied in the analysis of FSS backed by a dielectric slab [18]. On the other hand, due to periodicity of the structure, electric and magnetic field components are to be expressed in terms of the two dimensional Floquet space harmonics. Since a plane wave can always be decomposed into a combination of E and H polarized waves corresponding to the zero order TE and TM Floquet modes with respect to the normal of the surface. Therefore the transverse components of the incident fields can be expressed as :

$$\vec{E}_{inc} = \sum_{m=1}^{2} E_0^{(m)} e^{-j \Upsilon_{00} z} \vec{\Psi}_{m00} \qquad (3\text{-}65)$$

$$\vec{H}_{inc} = \vec{a}_z \times \sum_{m=1}^{2} Y_{00}^{(m)} E_0^{(m)} e^{-j \Upsilon_{00} z} \vec{\Psi}_{m00} \qquad (3\text{-}66)$$

The fields scattered by the chiral slab in the absence of the scaterers contain only zero order Floquet modes and are expressed in three regions (i.e., z<0, 0<z<d, d<z);

For z<0

$$\vec{E}_r = \sum_{m=1}^{2} (J)^{m-1} E_r^{(m)} e^{j\gamma_{00}z} \vec{\psi}_{m00} \tag{3-67}$$

$$\vec{H}_r = - a_z \times \sum_{m=1}^{2} (J)^{m-1} Y_{00}^{(m)} E_r^{(m)} e^{j\gamma_{00}z} \vec{\psi}_{m00} \tag{3-68}$$

For 0<z<d (inside the chiral slab)

Fields propagating in +z direction,

$$\vec{E}_c^{+} = \sum_{m=1}^{2} (J)^{m-1} [A_{L00}^{(m)} e^{-j\gamma_{L00}z} + (-1)^{m-1} A_{R00}^{(m)} e^{-j\gamma_{R00}z}] \vec{\psi}_{m00} \tag{3-69}$$

$$\vec{H}_c^{+} = a_z \times \sum_{m=1}^{2} (J)^{m-1} [Y_{L00}^{(m)} A_{L00}^{(m)} e^{-j\gamma_{L00}z} +$$
$$(-1)^{m-1} Y_{R00}^{(m)} A_{R00}^{(m)} e^{-j\gamma_{R00}z}] \vec{\psi}_{m00} \tag{3-70}$$

Fields propagating in -z direction,

$$\vec{E}_c^{-} = \sum_{m=1}^{2} (-j)^{m-1} [B_{L00}^{(m)} e^{j\gamma_{L00}z} + (-1)^{m-1} B_{R00}^{(m)} e^{j\gamma_{R00}z}] \vec{\psi}_{m00} \tag{3-71}$$

$$\vec{H}_c^{-} = - a_z \times \sum_{m=1}^{2} (-j)^{m-1} [Y_{L00}^{(m)} B_{L00}^{(m)} e^{j\gamma_{L00}z} +$$
$$(-1)^{m-1} Y_{R00}^{(m)} B_{R00}^{(m)} e^{j\gamma_{R00}z}] \vec{\psi}_{m00} \tag{3-72}$$

for z>d

$$\vec{E}_t = \sum_{m=1}^{2} (J)^{m-1} E_{t00}^{(m)} e^{-j\gamma_{00}(z-d)} \vec{\psi}_{m00} \tag{3-73}$$

34

$$\vec{H}_t = \vec{a}_z \times \sum_{m=1}^{2} (j)^{m-1} Y_{00}^{(m)} E_{t00}^{(m)} e^{-j\gamma_{00}(z-d)} \Psi_{m00} \qquad (3\text{-}74)$$

where

$$\Psi_{mpq} = \frac{1}{\sqrt{A}} e^{-j\vec{k}_{Tpq} \cdot \vec{r}_T} \vec{u}_{mpq}$$

$$(3\text{-}75)$$

$$p = q = 0, \pm 1, \pm 2,\ldots \qquad m = 1 \ (TM \ Modes) \ , \ m = 2 \ (TE \ Modes)$$

$$\vec{K}_{Tpq} = \vec{k}_T + p\vec{k}_1 + q\vec{k}_2$$

$$\vec{k}_T = k \sin \theta \cos \phi \ \vec{a}_x + k \sin \theta \sin \phi \ \vec{a}_y$$

$$\vec{k}_1 = -\frac{2\pi}{A} \vec{a}_z \times \vec{d}_2 \qquad \vec{k}_2 = \frac{2\pi}{A} \vec{a}_z \times \vec{d}_1$$

$$\vec{u}_{1pq} = \frac{\vec{k}_{Tpq}}{|\vec{k}_{Tpq}|} \qquad \vec{u}_{2pq} = \vec{a}_z \times \vec{u}_{1pq}$$

$$\gamma_{pq} = \begin{cases} \sqrt{k^2 - |\vec{k}_{Tpq}|^2} & k^2 > |\vec{k}_{Tpq}|^2 \\ \\ -j\sqrt{|\vec{k}_{Tpq}|^2 - k^2} & k^2 < |\vec{k}_{Tpq}|^2 \end{cases}$$

$$\gamma_{L,Rpq} = \begin{cases} \sqrt{k_{L,R}^2 - |\vec{k}_{Tpq}|^2} & k_{L,R}^2 > |\vec{k}_{Tpq}|^2 \\ \\ -j\sqrt{|\vec{k}_{Tpq}|^2 - k_{L,R}^2} & k_{L,R}^2 < |\vec{k}_{Tpq}|^2 \end{cases}$$

$$A_{Lpq}^{(m)} = (\frac{Y_s}{Y_{Lpq}^{(1)}})^{2-m} A_{Lpq} \qquad\qquad A_{Rpq}^{(m)} = (\frac{Y_s}{Y_{Rpq}^{(1)}})^{2-m} A_{Rpq}$$

$$B_{Lpq}^{(m)} = (\frac{Y_s}{Y_{Lpq}^{(1)}})^{2-m} B_{Lpq} \qquad\qquad B_{Rpq}^{(m)} = (\frac{Y_s}{Y_{Rpq}^{(1)}})^{2-m} B_{Rpq}$$

35

$$k_R = \omega \mu_c \xi + k_s \qquad\qquad k_L = -\omega \mu_c \xi + k_s$$

$$k = \omega \sqrt{\mu \epsilon} \qquad\qquad k_s = \sqrt{\omega^2 \mu_c \epsilon_c + (\omega \mu_c \xi)^2}$$

$$A = |\vec{d}_1 \times \vec{d}_2| \quad \text{Area of an unit cell}$$

$$\vec{d}_1, \vec{d}_2 \quad \text{Unit vectors}$$

$$\vec{r}_T = x \vec{a}_x + y \vec{a}_y$$

$$Y_{Lpq}^{(1)} = Y_s \frac{k_L}{\gamma_{Lpq}} \qquad\qquad Y_{Rpq}^{(1)} = Y_s \frac{k_R}{\gamma_{Rpq}}$$

$$Y_{Lpq}^{(2)} = Y_s \frac{\gamma_{Lpq}}{k_L} \qquad\qquad Y_{Rpq}^{(2)} = Y_s \frac{\gamma_{Rpq}}{k_R}$$

$$Y_{pq}^{(1)} = Y \frac{k}{\gamma_{pq}} \qquad\qquad Y_{pq}^{(2)} = Y \frac{\gamma_{pq}}{k}$$

$$Y = \sqrt{\frac{\epsilon}{\mu}} \qquad\qquad Y_s = \frac{k_s}{\omega \mu_c}$$

where ϵ, μ and ϵ_c, μ_c are the permittivity and permeability of the surounding medium and chiral slab respectively.

Matching the tangential electric and magnetic fields on the boundaries at z=0 and z=d the modal coefficients of the reflected and transmitted fields in the absence of the scatterers are obtained in terms of the magnitude of the incident field.

$$E_r^{(m)} = A_{L00}^{(m)} + (-1)^{m-1} A_{R00}^{(m)} +$$
$$(-1)^{m-1} B_{L00}^{(m)} + B_{R00}^{(m)} - (j)^{1-m} E_0^{(m)} \tag{3-76}$$

$$E_t^{(m)} = A_{L00}^{(m)} e^{-j\gamma_{L00}d} + (-1)^{m-1} A_{R00}^{(m)} e^{-j\gamma_{R00}d} +$$

$$(-1)^{m-1} B_{L00}^{(m)} e^{j\gamma_{L00}d} + B_{R00}^{(m)} e^{j\gamma_{R00}d}$$

(3-77)

where

$$\begin{bmatrix} B_{Lpq}^{(m)} \\ B_{Rpq}^{(m)} \end{bmatrix} = \begin{bmatrix} r_{LLpq}^{(m)} & r_{LRpq}^{(m)} \\ r_{RLpq}^{(m)} & r_{RRpq}^{(m)} \end{bmatrix} \begin{bmatrix} A_{Lpq}^{(m)} \\ A_{Rpq}^{(m)} \end{bmatrix}$$

(3-78)

$$\begin{bmatrix} A_{Lpq} \\ A_{Rpq} \end{bmatrix} = \frac{1}{\Delta A_{pq}} \begin{bmatrix} A_{1pq} & A_{2pq} \\ A_{3pq} & A_{4pq} \end{bmatrix} \begin{bmatrix} 2 Y_{pq}^{(1)} E_0^{(1)} \\ j2 Y_{pq}^{(2)} E_0^{(2)} \end{bmatrix}$$

(3-79)

$$\Delta A_{pq} = A_{1pq} A_{4pq} - A_{2pq} A_{3pq}$$

$$r_{LLpq}^{(1)} = r_{LLpq}^{(2)} = r_{LLpq} \qquad\qquad r_{RRpq}^{(1)} = r_{RRpq}^{(2)} = r_{RRpq}$$

(3-80)

$$r_{LRpq}^{(m)} = \left(\frac{Y_{Rpq}^{(m)}}{Y_{Lpq}^{(m)}} \right)^{m-2} r_{LRpq} \qquad\qquad r_{RLpq}^{(m)} = \left(\frac{Y_{Lpq}^{(m)}}{Y_{Rpq}^{(m)}} \right)^{m-2} r_{RLpq}$$

$$r_{LLpq} = \left(\frac{S_{1pq} + S_{2pq}}{\Delta_{pq}} \right) e^{-2j\gamma_{Lpq}d} \qquad\qquad r_{RRpq} = \left(\frac{S_{1pq} - S_{2pq}}{\Delta_{pq}} \right) e^{-2j\gamma_{Rpq}d}$$

(3-81)

$$r_{LRpq} = \frac{2 Y_{Rpq}^{(2)} S}{\Delta_{pq}} e^{-j(\gamma_{Lpq} + \gamma_{Rpq})d} \qquad\qquad r_{RLpq} = \frac{2 Y_{Lpq}^{(2)} S}{\Delta_{pq}} e^{-j(\gamma_{Lpq} + \gamma_{Rpq})d}$$

$$S - Y^2 - Y_s^2$$

$$S_{1pq} - (Y_s^2 + Y^2)(Y_{Rpq}^{(2)} - Y_{Lpq}^{(2)})$$

$$S_{2pq} - 2\,Y_{Rpq}^{(2)}(Y_{Rpq}^{(1)}\,Y_{pq}^{(2)} - Y_{Lpq}^{(2)}\,Y_{pq}^{(1)})$$

$$\Delta_{pq} - (Y_s^2 + Y_{Lpq}^{(2)}\,Y_{pq}^{(1)})\,(Y_{Rpq}^{(2)} + Y_{pq}^{(2)}) + (Y_s^2 + Y_{Rpq}^{(2)}\,Y_{pq}^{(1)})\,(Y_{Lpq}^{(2)} + Y_{pq}^{(2)})$$

$$A_{1pq} - -(Y_{Rpq}^{(2)} + Y_{pq}^{(2)}) + (Y_{Lpq}^{(2)} - Y_{pq}^{(2)})r_{LRpq}^{(2)} - (Y_{Rpq}^{(2)} - Y_{pq}^{(2)})r_{RRpq}^{(2)}$$

$$A_{2pq} - \frac{Y_s}{Y_{Rpq}^{(1)}}\{(Y_{Rpq}^{(1)} + Y_{pq}^{(1)}) - (Y_{Lpq}^{(1)} - Y_{pq}^{(1)})r_{LRpq}^{(1)} - (Y_{Rpq}^{(1)} - Y_{pq}^{(1)})r_{RRpq}^{(1)}\}$$

$$A_{3pq} - -(Y_{Lpq}^{(2)} + Y_{pq}^{(2)}) + (Y_{Rpq}^{(2)} - Y_{pq}^{(2)})r_{RLpq}^{(2)} - (Y_{Lpq}^{(2)} - Y_{pq}^{(2)})r_{LLpq}^{(2)}$$

$$A_{4pq} - -\frac{Y_s}{Y_{Lpq}^{(1)}}\{(Y_{Lpq}^{(1)} + Y_{pq}^{(1)}) - (Y_{Rpq}^{(1)} - Y_{pq}^{(1)})r_{RLpq}^{(1)} - (Y_{Lpq}^{(1)} - Y_{pq}^{(1)})r_{LLpq}^{(1)}\}$$

On the other hand, the scattered fields radiated by the current induced on the scatteres contain higher order Floquet modes as well and can be expressed in three regiong (i.e., z<0, 0<z<d, d<z) as in the following form.

for z<0

$$\vec{E}_1 - \sum_{m-1}^{2}\sum_{p}\sum_{q} (j)^{m-1}\,E_{1pq}^{(m)}\,e^{j\gamma_{pq}z}\,\vec{\Psi}_{mpq} \qquad (3\text{-}82)$$

38

$$\vec{H}_1 = -\vec{a}_z \times \sum_{m-1}^{2} \sum_p \sum_q (j)^{m-1} Y_{pq}^{(m)} E_{1pq}^{(m)} e^{j\gamma_{pq}z} \psi_{mpq} \qquad (3\text{-}83)$$

for z<0<d,

$$\vec{E}_2^+ = \sum_{m-1}^{2} \sum_p \sum_q (j)^{m-1} [A_{SLpq}^{(m)} e^{-j\gamma_{Lpq}z} +$$
$$(-1)^{m-1} A_{SRpq}^{(m)} e^{-j\gamma_{Rpq}z}] \psi_{mpq} \qquad (3\text{-}84)$$

$$\vec{E}_2^- = \sum_{m-1}^{2} \sum_p \sum_q (-j)^{m-1} [B_{SLpq}^{(m)} e^{j\gamma_{Lpq}z} + (-1)^{m-1} B_{SRpq}^{(m)} e^{j\gamma_{Rpq}z}] \psi_{mpq} \qquad (3\text{-}86)$$

$$\vec{H}_2^- = -\vec{a}_z \times \sum_{m-1}^{2} \sum_p \sum_q (-j)^{m-1} [Y_{Lpq}^{(m)} B_{SLpq}^{(m)} e^{j\gamma_{Lpq}z} +$$
$$(-1)^{m-1} Y_{Rpq}^{(m)} B_{SRpq}^{(m)} e^{j\gamma_{Rpq}z}] \psi_{mpq} \qquad (3\text{-}87)$$

$$\vec{H}_2^+ = \vec{a}_z \times \sum_{m-1}^{2} \sum_p \sum_q (j)^{m-1} [Y_{Lpq}^{(m)} A_{SLpq}^{(m)} e^{-j\gamma_{Lpq}z} +$$
$$(-1)^{m-1} Y_{Rpq}^{(m)} A_{SRpq}^{(m)} e^{-j\gamma_{Rpq}z}] \psi_{mpq} \qquad (3\text{-}85)$$

for z>d

$$\vec{E}_3 = \sum_{m-1}^{2} \sum_p \sum_q (j)^{m-1} E_{3pq}^{(m)} e^{-j\gamma_{pq}(z-d)} \psi_{mpq} \qquad (3\text{-}88)$$

$$\vec{H}_3 = \vec{a}_z \times \sum_{m-1}^{2} \sum_p \sum_q (j)^{m-1} Y_{pq}^{(m)} E_{3pq}^{(m)} e^{-j\gamma_{pq}(z-d)} \psi_{mpq} \qquad (3\text{-}89)$$

These scattered fields due to induced current must satisfy the following boundary conditions:

39

1 - Tangential electric and magnetic fields are continuous at z=d

2 - Tangential electric field is continuous at z=0

3 - Tangential magnetic field is discontinuous at z=0 by an amount equal to J(x',y')

These boundary conditions combined with the orthogonality of the Floquet modes over a single periodic cell, lead to the equations in which the magnitude of the scattered fields in regions, z<0 and d<d, are expressed in terms of unknown current density induced J(x',y') as follows,

$$E_{1pq}^{(m)} - A_{SLpq}^{(m)} + (-1)^{m-1} A_{SRpq}^{(m)} + (-1)^{m-1} B_{SLpq}^{(m)} + B_{SRpq}^{(m)}$$

(3-90)

$$E_{3pq}^{(m)} - A_{SLpq}^{(m)} e^{-j\gamma_{Lpq} d} + (-1)^{m-1} A_{SRpq}^{(m)} e^{-j\gamma_{Rpq} d} +$$

$$(-1)^{m-1} B_{SLpq}^{(m)} e^{j\gamma_{Lpq} d} + B_{SRpq}^{(m)} e^{j\gamma_{Rpq} d}$$

(3-91)

where

$$\begin{bmatrix} B_{SLpq}^{(m)} \\ B_{SRpq}^{(m)} \end{bmatrix} - \begin{bmatrix} r_{LLpq}^{(m)} & r_{RLpq}^{(m)} \\ r_{LRpq}^{(m)} & r_{RRpq}^{(m)} \end{bmatrix} \begin{bmatrix} A_{SLpq}^{(m)} \\ A_{SRpq}^{(m)} \end{bmatrix}$$

(3-92)

$$A_{SLpq}^{(m)} - (\frac{Y_s}{Y_{Lpq}^{(1)}})^{2-m} A_{SLpq} \qquad\qquad A_{SRpq}^{(m)} - (\frac{Y_s}{Y_{Rpq}^{(1)}})^{2-m} A_{SRpq}$$

$$B_{SLpq}^{(m)} - (\frac{Y_s}{Y_{Lpq}^{(1)}})^{2-m} B_{SLpq} \qquad\qquad B_{SRpq}^{(m)} - (\frac{Y_s}{Y_{Rpq}^{(1)}})^{2-m} B_{SRpq}$$

$$\begin{bmatrix} A_{SLpq} \\ A_{SRpq} \end{bmatrix} - \frac{1}{\Delta A_{spq}} \begin{bmatrix} A_{S1pq} & A_{S2pq} \\ A_{S3pq} & A_{S4pq} \end{bmatrix} \begin{bmatrix} I_{1pq} \\ jI_{2pq} \end{bmatrix}$$

(3-93)

40

$$A_{S1pq} = -A_{1pq} \qquad A_{S2pq} = A_{2pq} \qquad A_{S3pq} = -A_{3pq} \qquad A_{S4pq} = A_{4pq}$$

$$\Delta A_{Spq} = A_{S1pq} A_{S4pq} - A_{S2pq} A_{S3pq}$$

$$I_{mpq} = \frac{1}{\sqrt{A}} \iint \vec{J}(x',y') \cdot e^{j\vec{k}_{Tpq} \cdot \vec{r}_{T''}} \vec{u}_{mpq} \, dx' \, dy' \tag{3-94}$$

The primed variables denote the local coordinate variables on the conducting elements and asterix (*) denotes the complex conjugate..

The only remaining boundary conditions is that the total tangential electric field are to be vanished over the perfect conductor. That is,

$$\vec{E}_{INC}(x',y',0) + \vec{E}_r(x',y',0) + \vec{E}_1(x',y',0) = 0 \tag{3-95}$$

or using Equation(3-67), (3-76) and (3-82), the last boundary condition can be expressed explicitly as

$$\sum_{m=1}^{2} (E_0^{(m)} + (j)^{m-1} E_r^{(m)}) \, \Psi_{m00} = -\sum_{m=1}^{2} \sum_p \sum_q (j)^{m-1} E_{1pq}^{(m)} \, \Psi_{mpq} \tag{3-96}$$

Using (3-90) and (3-93),

$$B_{SLpq}^{(m)} = \Omega_{1pq}^{(m)} I_{1pq} + \Omega_{2pq}^{(m)} I_{2pq}$$

$$\tag{3-97}$$

$$B_{SRpq}^{(m)} = \Omega_{3pq}^{(m)} I_{1pq} + \Omega_{4pq}^{(m)} I_{2pq}$$

where

$$\Omega_{1pq}^{(m)} = r_{LLpq}^{(m)} \left(\frac{Y_s}{Y_{Lpq}^{(1)}}\right)^{2-m} u_{1pq} + r_{RLpq}^{(m)} \left(\frac{Y_s}{Y_{Rpq}^{(1)}}\right)^{2-m} u_{3pq} \tag{3-98}$$

41

$$\Omega_{2pq}^{(m)} - r_{LLpq}^{(m)} \left(\frac{Y_s}{Y_{Lpq}^{(1)}}\right)^{2-m} u_{2pq} + r_{RLpq}^{(m)} \left(\frac{Y_s}{Y_{Rpq}^{(1)}}\right)^{2-m} u_{4pq} \qquad (3\text{-}99)$$

$$\Omega_{3pq}^{(m)} - r_{LRpq}^{(m)} \left(\frac{Y_s}{Y_{Lpq}^{(1)}}\right)^{2-m} u_{1pq} + r_{RRpq}^{(m)} \left(\frac{Y_s}{Y_{Rpq}^{(1)}}\right)^{2-m} u_{3pq} \qquad (3\text{-}100)$$

$$\Omega_{4pq}^{(m)} - r_{LRpq}^{(m)} \left(\frac{Y_s}{Y_{Lpq}^{(1)}}\right)^{2-m} u_{2pq} + r_{RRpq}^{(m)} \left(\frac{Y_s}{Y_{Rpq}^{(1)}}\right)^{2-m} u_{4pq} \qquad (3\text{-}101)$$

with $u_{ipq} = A_{sipq}/\Delta A_{spq}$, $i=1, 2, 3, 4$.

The magnitude of the scattered field due to induced current density can be written as,

$$E_{1pq}^{(m)} - z_{1pq}^{(m)} I_{1pq} + z_{2pq}^{(m)} I_{2pq} \qquad (3\text{-}102)$$

or in more explicit form.

$$E_{1pq}^{(m)} - z_{1pq}^{(m)} \frac{1}{\sqrt{A}} \int\int_{Unit\ Cell} \vec{J}(x',y') \cdot \vec{\Psi}_{1pq}^* \, dx' \, dy' +$$

$$z_{2pq}^{(m)} \frac{1}{\sqrt{A}} \int\int_{Unit\ Cell} \vec{J}(x',y') \cdot \vec{\Psi}_{2pq}^* \, dx' \, dy' \qquad (3\text{-}103)$$

where * denotes the complex conjugate and

$$z_{1pq}^{(m)} - \left(\frac{y_s}{Y_{Lpq}^{(1)}}\right)^{2-m} u_{1pq} + (-1)^{m-1} \left(\frac{y_s}{Y_{Rpq}^{(1)}}\right)^{2-m} u_{3pq} +$$

$$(-1)^{m-1} \Omega_{1pq}^{(m)} + \Omega_{3pq}^{(m)} \qquad (3\text{-}104)$$

$$z_{2pq}^{(m)} - \left(\frac{y_s}{Y_{Lpq}^{(1)}}\right)^{2-m} u_{2pq} + (-1)^{m-1} \left(\frac{y_s}{Y_{Rpq}^{(1)}}\right)^{2-m} u_{4pq} +$$

$$(-1)^{m-1} \Omega_{2pq}^{(m)} + \Omega_{4pq}^{(m)} \qquad (3\text{-}105)$$

42

Using Equation(3-91) and (3-93) the megnitude of the transmitted field due to induced current can be expressed as,

$$E_{3pq}^{(m)} = s_{1pq}^{(m)} I_{1pq} + s_{2pq}^{(m)} I_{2pq}$$ (3-106)

where

$$s_{1pq}^{(m)} = (\frac{y_s}{Y_{Lpq}^{(1)}})^{2-m} u_{1pq} e^{-j\gamma_{Lpq}} + (-1)^{m-1} (\frac{y_s}{Y_{Rpq}^{(1)}})^{2-m} u_{3pq} e^{-j\gamma_{Rpq}} +$$
$$(-1)^{m-1} \Omega_{1pq}^{(m)} e^{j\gamma_{Lpq}} + \Omega_{3pq}^{(m)} e^{j\gamma_{Rpq}}$$ (3-107)

$$s_{2pq}^{(m)} = (\frac{y_s}{Y_{Lpq}^{(1)}})^{2-m} u_{2pq} e^{-j\gamma_{Lpq}} + (-1)^{m-1} (\frac{y_s}{Y_{Rpq}^{(1)}})^{2-m} u_{4pq} e^{-j\gamma_{Rpq}} +$$
$$(-1)^{m-1} \Omega_{2pq}^{(m)} e^{j\gamma_{Lpq}} + \Omega_{4pq}^{(m)} e^{j\gamma_{Rpq}}$$ (3-108)

Therefore Equation (3-109) becomes,

$$\sum_{m=1}^{2} (E_0^{(m)} + (j)^{m-1} E_r^{(m)}) \Psi_{m00} =$$
$$- \sum_{m=1}^{2} \sum_{p} \sum_{q} (j)^{m-1} [z_{1pq}^{(m)} I_{1pq} + z_{2pq}^{(m)} I_{2pq}] \Psi_{mpq}$$ (3-109)

Equation (3-109) is a Fredholm type integral equation of the first kind for the unknown current density induced on a metallic scatterer within an unit cell. Numerical solution to this equation is obtained by applying the Method of Moment. For this, first the unknown function (induced current density) is to be expressed as a finite sum of orthogonal functions which are suitable to the geometry of the metallic scatterers. Therefore, let us assume that the unknown current density can be expressed as,

43

$$\vec{J}(x',y') - \sum_{n=0}^{n=N} \alpha_n \vec{I}_n(x',y') \qquad (3\text{-}110)$$

where α_n is the unknown coefficients. I_n are complete and orthogonal functions over a conducting element and N is a finite number.

Substituting Equation (3-104) and (3-105) into Equation (3-103) yields,

$$E_{1pq}^{(m)} - \sum_{n=1}^{N} \alpha_n [\ z_{1pq}^{(m)}\ <I_n, \dot{\Psi}_{1pq}> \ + \ z_{2pq}^{(m)}<I_n, \dot{\Psi}_{2pq}> \ ] \qquad (3\text{-}111)$$

where

$$<I_n, \dot{\Psi}_{mpq}> - \frac{1}{\sqrt{A}} \int\int_{Unit\ Cell} \vec{I}(x',y') \cdot \dot{\Psi}_{mpq}\ dx'\ dy' \qquad (3\text{-}112)$$

Substituting Equation (3-112) into Equation (3-111) yields,

$$\sum_{m=1}^{2} (E_0^{(m)} + (j)^{m-1} E_r^{(m)})\ \dot{\Psi}_{m00} -$$

$$\qquad (3\text{-}113)$$

$$- \sum_{n=1}^{N} \alpha_n [\ \sum_{m=1}^{2} \sum_p \sum_q (j)^{m-1}\ [z_{1pq}^{(m)}\ <I_n,\dot{\Psi}_{1pq}> \ + \ z_{2pq}^{(m)}<I_n,\dot{\Psi}_{2pq}>\ ]\ \dot{\Psi}_{mpq}\ ]$$

Taking the dot product of both sides of the above equation with I_k, k = 1, 2, 3,...N, and then integrating over a single unit cell gives,

$$\sum_{m=1}^{2} (E_0^{(m)} + (j)^{m-1} E_r^{(m)})\ <I_k, \dot{\Psi}_{0pq}> - - \sum_{n=1}^{N} \alpha_n [\ \sum_{m=1}^{2} \sum_p \sum_q$$

$$\qquad (3\text{-}114)$$

$$(j)^{m-1}\ [z_{1pq}^{(m)}\ <I_n,\dot{\Psi}_{1pq}> \ + \ z_{2pq}^{(m)}<I_n,\dot{\Psi}_{2pq}>\ ]\ <I_k,\dot{\Psi}_{mpq}>\ ]$$

Equation (3-114) is the desired marix equation to be solved for the unknown coefficients α_n. Upon finding the unknown coefficients by matrix inversion, the total reflected field from the chiro-frequency selective surface can be expressed as,

44

$$\vec{E}^{ref} = \sum_{m=1}^{2} (j)^{m-1} E_r^{(m)} e^{j \gamma_{00} z} \Psi_{m00} + \sum_{m=1}^{2} \sum_{p} \sum_{q} (j)^{m-1} E_{1pq}^{(m)} e^{j \gamma_{pq} z} \Psi_{mpq} \qquad (3\text{-}115)$$

In a similar manner, the transmitted field is expressed using Equation (3-74) and (3-91) in the following form.

$$\vec{E}^{trans} = \sum_{m=1}^{2} (j)^{m-1} E_t^{(m)} e^{-j \gamma_{00} (z-d)} \Psi_{m00} +$$

$$\sum_{m=1}^{2} \sum_{p} \sum_{q} (j)^{m-1} E_{3pq}^{(m)} e^{-j \gamma_{pq} (z-d)} \Psi_{mpq} \qquad (3\text{-}116)$$

The distant scattered fields consist of only zero order TM and TE Floquet modes. Therefore in the numerical results to follow only the coefficients for the zero order harmonics (p = q = 0) are calculated. Note that the scattered fields contain only the propagating Floquet modes. However, while computing the coefficients of the current density induced the higher order evanescent modes must be included since they are necessary for satisfying the boundary conditions.

45

CHAPTER 4

ANALYSIS OF VARIOUS CHIRO-FREQUENCY SELECTIVE SURFACES

The theoretical background and the formulation for analysing the two dimensional infinite periodic array of conducting elements having an arbitrary shape loaded by an isotropic chiral slab has already been presented in previous chapters. In this chapter the spectral characteristics of the Chiro-FSSs comprised of different geometries; narrow strips, cross dipoles, circular rings, square loops and rectangular patches are examined. For each configuration the unknown currenty density are expressed by suitable entire domain basis functions. Effects of conducting element shape, array configuration, dielectric constant, thickness and chirality admittance of the chiral slab, polarisation and angle of incidence of the incoming wave on the reflection and transmission characteristics are analysed.

In order to check the vaidity of the computed results, the standard necessary check of conservation of power ($P_{inc} = P_{ref} + P_{trans}$) was made and found to be excellent (error is about ~ 10^{-9}). In the limiting case of zero chirality admittance ($\xi \rightarrow 0$) the chiral slab becomes a conventional dielectric slab. The results corresponding to the free-standing and dielectric loaded FSSs are obtained by setting the value of chirality admittance and/or thickness of the chiral slab to zero in our computer programs. As expected these results were found to agree quite well with the numerical and experimental results given in the literature [41-50]. For each configuration, the convergence of the numerical results have been studied by varying the number of basis functions and Floquet harmonics. In the solution, the relative convergence phenomenon is determined between the number p and q of Floquet modes and those of the unknown

46

current amplitudes, where p and q are the maximum indicies used in the modal expansion of the two dimensional Floquet modes. To ensure that all lower order modes are retained in the applicatin of the boundary condition, maximum values for p and q are choosen in such a way that at least the main contribution of the highest order current function used in the analysis is included within the limits of the integrals which are required to be evaluated in forming the impedance matrix.

4.1. Chiro-FSS Comprised of Narrow Strips

The unit cell geometry of the two dimensional infinite periodic array of perfectly conducting narrow strips printed on an isotropic chiral slab is show in Figure 4.1.1.
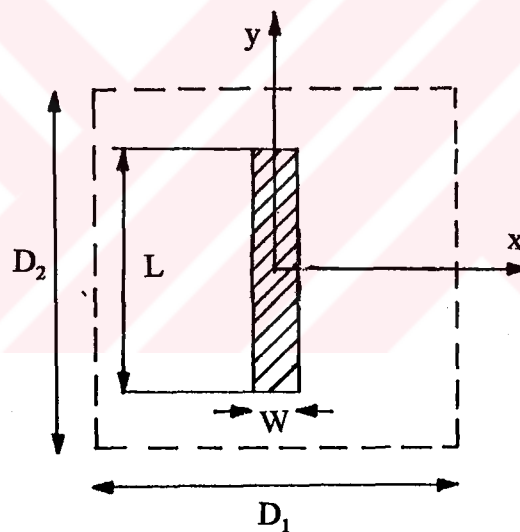
Figure 4.1.1   Unit cell geometry of Chiro-FSS with narrow strips

The unit cell geometry has dimensions d_1 and d_2 along the skew coordinate system variables η_1 and η_2 respectively and α is the angle between the η_1 axis and x axis of the absolute coordinate system and β is the angle between the skewed coordinate axes η_1 and η_2. The narrow strip is located in the unit cell such that the axis of the strip is rotated by an angle of γ with respect to the y axis of the absolute coordinate system. For this gometry the transverse wavenumbers k_{xpq} and k_{ypq} are expressed as,

47

$$k_{xpq} - k\sin\theta\cos\phi + \frac{\sin(\alpha+\beta)}{\sin\beta}\frac{2\pi}{d_1}p - \frac{\sin\alpha}{\sin\beta}\frac{2\pi}{d_2}q \tag{4-1}$$

$$k_{ypq} - k\sin\theta\sin\phi - \frac{\cos(\alpha+\beta)}{\sin\beta}\frac{2\pi}{d_1}p + \frac{\cos\alpha}{\sin\beta}\frac{2\pi}{d_2}q \tag{4-2}$$

For narrow strip geometry the unknown currnet density induced is assumed to have a component along the y' and can be expressed as,

$$\vec{J} - \sum_{n-1}^{N} a_n \vec{I}_n(x',y') \tag{4-3}$$

where

$$\vec{I}_n - \frac{1}{\sqrt{1-(\frac{2x'}{W})^2}} \begin{bmatrix} \cos \\ \sin \end{bmatrix} (\frac{n\pi y'}{L})\, \vec{a}_{y'} \qquad \begin{bmatrix} n & odd \\ n & even \end{bmatrix} \tag{4-4}$$

where a_n is the unknown constant and the radical term in the denominator is included due to edge singularity.

Now consider the inner product that is used in forming the impedance matrix,

$$<\vec{I}_n, \dot{\Psi}_{mpq}> - \frac{1}{\sqrt{A}} \int_{unitcell}\int \vec{I}_n \cdot e^{j(k_{xpq}x + k_{ypq}y)}\, \vec{u}_{mpq}\, dx'dy' \tag{4-5}$$

Let us change the variables of integration from x, y to x', y' respectively. For this, we need relations between the two coordinate systems. That is,

$$x' - x\cos\gamma - y\sin\gamma$$
$$y' - x\sin\gamma + y\cos\gamma \tag{4-6}$$

or

48

$$x = x'\cos\gamma + y'\sin\gamma$$

$$y = -x'\sin\gamma + y'\cos\gamma \tag{4-7}$$

and the Jacobian is,

$$J(x',y') = \begin{vmatrix} \dfrac{\partial x}{\partial x'} & \dfrac{\partial y}{\partial x'} \\[2ex] \dfrac{\partial x}{\partial y'} & \dfrac{\partial y}{\partial y'} \end{vmatrix} = \begin{vmatrix} \cos\gamma & -\sin\gamma \\ \sin\gamma & \cos\gamma \end{vmatrix} = 1 \tag{4-8}$$

Thus Equation (4-1) can written as,

$$\langle \vec{I}_n, \dot{\Psi}_{mpq} \rangle = \frac{1}{\sqrt{A}} \int_{unit\,cell}\int \vec{I}_n \cdot \vec{u}_{mpq}\, e^{\,J(ux' + vy')}\, dx'dy' \tag{4-9}$$

and

$$\langle \vec{I}_n, \Psi_{mpq} \rangle = \frac{1}{\sqrt{A}} \int_{unit\,cell}\int \vec{I}_n \cdot \vec{u}_{mpq}\, e^{\,-J(ux' + vy')}\, dx'dy' \tag{4-10}$$

where

$$u = k_{xpq}\cos\gamma - k_{ypq}\sin\gamma$$

$$v = k_{xpq}\sin\gamma + k_{ypq}\cos\gamma \tag{4-11}$$

$$\vec{a}_{x'} = \cos\gamma\,\vec{a}_x - \sin\gamma\,\vec{a}_y$$

$$\vec{a}_{y'} = \sin\gamma\,\vec{a}_x + \cos\gamma\,\vec{a}_y \tag{4-12}$$

The unknown current density can be expressed as a sum of cosine (symmetrical) and sine (asymmetrical) functions. For symmetrical current,

$$\vec{I}_n = \frac{a_n}{\sqrt{1 - \left(\dfrac{2x'}{W}\right)^2}} \cos\left(\frac{n\pi y'}{L}\right)\vec{a}_{y'} \qquad n = 1,3,5.. \ (\ n \quad odd\ ) \tag{4-13}$$

49

therefore the inner product given in Equation(4-7) can be written as,

$$\langle \vec{I}_n, \dot{\Psi}_{mpq} \rangle = \frac{1}{\sqrt{A}} \left[(\sin \gamma \, \vec{a}_x + \cos \gamma \, \vec{a}_y) \cdot \vec{u}_{mpq} \right] \frac{W}{4} \pi L J_0(\frac{uW}{2}).$$

$$\left[\frac{\sin(\frac{vL}{2} + \frac{n\pi}{2})}{(\frac{vL}{2} + \frac{n\pi}{2})} + \frac{\sin(\frac{vL}{2} - \frac{n\pi}{2})}{(\frac{vL}{2} - \frac{n\pi}{2})} \right] \tag{4-14}$$

In a similar manner, Equation(4-8) is,

$$\langle \vec{I}_n, \Psi_{mpq} \rangle = \langle \vec{I}_n, \dot{\Psi}_{mpq} \rangle \tag{4-15}$$

and the induced current density expressed by sine terms (asymmetrical),

$$\vec{I}_n = \frac{a_n}{\sqrt{1 - (\frac{2x'}{W})^2}} \sin(\frac{n\pi y'}{L}) \vec{a}_{y'} \qquad n = 2,4,6.. \quad (n \quad even) \tag{4-16}$$

Corresponding inner product is obtaines as,

$$\langle \vec{I}_n, \dot{\Psi}_{mpq} \rangle = \frac{j}{\sqrt{A}} \left[(\sin \gamma \, \vec{a}_x + \cos \gamma \, \vec{a}_y) \cdot \vec{u}_{mpq} \right] \frac{W}{4} \pi L J_0(\frac{uW}{2}).$$

$$\left[\frac{\sin(\frac{vL}{2} - \frac{n\pi}{2})}{(\frac{vL}{2} - \frac{n\pi}{2})} - \frac{\sin(\frac{vL}{2} + \frac{n\pi}{2})}{(\frac{vL}{2} + \frac{n\pi}{2})} \right] \tag{4-17}$$

and

$$\langle \vec{I}_n, \Psi_{mpq} \rangle = - \langle \vec{I}_n, \dot{\Psi}_{mpq} \rangle \tag{4-18}$$

50

4.1.1. Numerical Results of the Chiro-FSS with Narrow Strips

In this section, the numerical results of the reflection and transmission characteristics of Chiro-FSS with narrow strips for various type of configurations are presented. The effects of chirality of the slab, array and conducting element geometry, constitutive parameters and thickness of the slab, polarisation and incidence angle of the excitation fields on the spectral characteristics of the Chiro-FSS comprised of narrow strips are analysed.

The first Chiro-FSS configuration considered is two dimensional infinite arrays of perfectly conducting narrow strips having a length of $L = 9.2$ mm and a width of $W = 0.1$ mm and are arranged in a square lattice $D_1 = D_2 = 10$ mm. The screen is illuminated by a normally incident plane wave of both TE and TM polarisation. The chiral slab is assumed to have a thickness of 5 mm and a dielectric constant of $\epsilon_r = 1.06$. In order to show the effects of chirality admittance of the slab on the spectral characteristics four different values of chirality admittance are choosen, $\xi = 0.0$ (dielectric), 0.0005, 0.0015 and 0.0025 mho.

The reflection and transmission characteristics of the Chiro-FSS with narrow strips versus frequency for TE incidence are shown in Figure 4.1.2. As can be seen from figures, for small values of chirality admittance, say, $\xi=0.0005$, the reflection characteristics of the Chiro-FSS is very similar to the characteristics of the conventional FSS ($\xi= 0.0$) having same design parameters. When the chirality admittance of the slab is increased to 0.0015 and 0.0025 mho more than one resonances (full reflection) are observed. These resonances have more narrow bandwidth than that of the resonance bandwidths of the conventional FSS. It is seen that from figures, almost full transmisions are observed for the cross-polar component (TM) of the transmitted wave through the Chiro-FSS for the high values of chirality admittance, 0.0015 and 0.0025 mho. For small values of chirality admittance the transmission characteristics of the Chiro-FSS exhibits great similarity with the transmission characteristics of the conventional FSS.

When the thickness of the chiral slab of the Chiro-FSS introduced above is reduced

from 5 mm to 4 mm, the radical changes are observed in the reflection and transmission characteristics. Figure 4.2.3 is the plot of variation of the reflection and transmission coefficients versus frequency for the normally incident plane wave of TE polarisation. Note that in this case only two full reflections are obtained for the chirality admittance of 0.0025 mho. The resonance frequencies and the bandwidths associated are affected by the variation in the thickness of the chiral slab.

Next, dielectric constant of the chiral slab having a thickness of 5 mm, is increased from 1.06 to 1.32.The numerical results of the spectral characteristics are depicted in Figure 4.2.4. The effects of variation in the dielectric constant of the chiral slab can be seen by comparing the Figure 4.1.2 and Figure 4.2 4. For both cases the other parameters are same as in the previous example. When the dielectric constant of the chiral slab is increased, the resonance frequencies are shifted to the lower frequencies and more resonances are observed in the reflection characteristics. In the former case (ϵ_r =1.06) the magnitude of the reflection coefficients between adjecent resonances are small compared with the that of the later one (ϵ_r =1.32). In other words small values dielectric consatant provides good isolation between the resonances.

When the screen whose unit cell is shown in Figure 4.1.1, is illuminated by the normally incident plane wave of TM polarisation, no current indduced on the strip. Therefore, in this case the magnitude of the reflection and transmission coefficients are same as the chiral slab having no metallic scatterers. The reflection and transmission characteristics of the 5 mm thick chiral slab having a dielectric constant of 1.06 and 1.32 are given in Figure 4.1.5 and Figure 4.1.6, respectively. Almost full transmission is also obtained for cross-polarised component (TE) for both case.

The second Chiro-FSS configuration considered, has the same design parameters as in the first example except the geometry of the narrow strips. In this structure the two dimensional infinite periodic arrays comprised of narrows strips having a length of L = 8 mm and a width of W=1 mm. The magnitude of the computed reflection and transmission coefficients of this configuration are illustrated in Figure 4.2.6. The screen is illuminated by a normal incidence TE plane wave. Comparision of Figure 4.1.2 and Figure 4.1.7 yields that the resonances frequencies of the this geometry is obtained at

52

higher frequencies and the bandwidths of the resonances are more narrow than the bandwidths of the former case (L=9.2 mm and W=1 mm) for all values of the chirality admittance of the slab, ξ= 0.0 (dielectric), 0.0005, 0.0015 and 0.0025.

The next configuration is the Chiro-FSS comprised of perfectly conducting narrow strips arranged in a triangular lattice ($D_1 = D_2 = 10$ mm, α=60°). The length and the width of the dipoles (narrow strips) are L=9.2 mm and W=1 mm, respectively. The chiral slab is assumed to has a dielectric constant of 1.06 and a thickness of 5 mm. The reflection and transmission characteristice of the Chiro-FSS with triangular lattice are obtained for three different values of chirality admittance of the slab (ξ= 0.0, 0.0015 and 0.0025 mho) when the screen is illimunated by the normally incident TE plane wave. The variation of magnitude of reflection and transmission coefficients (co- and cross-polar) with the frequency are plotted in Figure 4.1.8. By comparing the Figure 4.1.2 and Figure 4.1.8, one can see that, the resonances and spikes between two adjecent resonances are getting more bandwidth as the distance between the dipole are reduced, i.e. triangular lattice geometry is used instead of rectangular array geometry for small value of chirality admittance of the slab. This means that the screen is more reflective compared to the case of triangular lattice geometry. Whereas the resonance bandwidths are unchanged for the chirality admittance of ξ=0.0015 and 0.0025 mho, the bandwidths of the spikes between two adjecent resonance have larger bandwidth. Figure 4.1.9 represents the reflection and transmission characteristics versus frequency of the Chiro-FSS comprised of a 4 mm thick chiral slab for the normal incidence TE plane wave. The other design parameters are assumed to be same as in the previous eaxmple. In this case the resonances obtained have large bandwidth when compared with the previous geometry.

When the plane wave direction of incidence is not normal to the Chiro-FSS, some variations with respect to the normal incidence case are observed in the spectral response. Figure 4.1.10 is the plot of power reflection and transmisson characteristics of the Chiro-FSS having the same design parameters as in Figure 4. 1.2 , but the screen is illuminated by a incident TE plane wave having a ploar angle of θ = 30° and azimuth angle of ϕ =0°. In the co-polar (TE) reflection characteristics much resonances are obtained compared with the normal incidence case for the chirality admittance of the

chiral slab of ξ=0.0015 and 0.0025 mho. Magnitude of the power of the reflected cross-polarised (TM) are relatively very small than the co-polar component (TE) for all values of the chirality admittances. In the transmisson characteristic, still cross-polarised compenent (TM) of the transmitted wave is almost fully transmitted through the Chiro-FSS for high value of chirality admittance. Figure 4.1.11 represents the power reflection and transmission coefficent of the Chiro-FSS which is illuminated by the TM polarised plane vawe with $\theta = 30°$, ϕ =0°. In this case, neither full reflection nor full transmission is obtained in the spectral characteristics of the Chiro-FSS. The most part of the incident power is transmitted through the Chiro-FSS for all values of the chirality admittance.

When the azimuth angle is choosen as ϕ =30° and the polar angle is still $\theta = 30°$ some variations are obtained in both reflection and transmission characteristics of Chiro-FSS illuminated by a TE ploarised plane wave, as depicted in Figure 4.1.12. For this case no resonance (full reflection) is observed for all values of the chirality admittance. But still almost full transmission is achivable for ξ=0.0015 and 0.0025 mho in the transmission charecteristic of the cross-polar (TM) component.

Figure 4.1.13 shows the power reflection and transmission coefficient of the Chiro-FSS due to TM polarised plane wave illumination with the same incidence angles as in the previous case (ϕ =30°, $\theta = 30°$). Both reflection and transmission characteristics of the Chiro-FSS are not affected strongly by changing the azimuth angle ϕ, from 0° to 30°. Still most of the power carried by the incident wave is transmitted for ξ=0.0015 and 0.0025. One should note that, when the Chiro-FSS is illuminated by a TM plane wave, most of the power is transmitted through the screen. For high values of frequency power carried by the cross-polar component, whereas in the lower frequency band power carried by the co-polar component. But in the case of zero chiraliy admittance no cross-polar component exist.

The last example of the reflection and transmission characteristics of the Chiro-FSS having the same design parameters as in the Figure 4.1.2 are obtained for the case of oblique incidence with ϕ =30°, $\theta = 0°$. The spectral characteristic of the Chiro-FSS due to TE plane wave excitation is shown in Figure 4.1.14. As can be seen from the reflection curve presented there is no resonance (full reflection) for both co-polar (TE) and cross-

polar(TM) . But the magnitude of the co-polar component reflected wave is higher than the cross-polar one. In this case it is also possible to obtain almost full transmission for the cross-polarised (TM) component for high value of chirality admittance of the slab.The spectral response of the same Chiro-FSS due to TM illumination is shown in Figure 4.1. 15. One can see that, in the case of TM illumination the reflection and transmission characteristics of the Chiro-FSS are very similar to that of the previous examples.

In the light of the results presented, spectral characteristics of the Chiro-FSS comprised of two dimensional infinite arrays of perfectly conducting narrow strips printed on an isotropic chiral slab, can be summarized as;

- Depending on the value of chirality admittance of the slab, it is possible to obtain more than one resonance (full reflection). In all cases considered the first resonance frequency is shifted slightly to lower frequency band, but the frequencies and the shape of the higher resonance stronly depens on the chirality admittance of the slab.

- Decreasing the thickness of the chiral slab causes some changes such that for the case of more thin chiral slab higher order resonances start to disappear.

-It is seen that, dielectric constant of the chiral slab is another important design parameter of the Chiro-FSS. When the dielectric constant is increased from 1.06 to 1.32 more resonances are obtained in the spectral characteristics.

- When the array geometry is changed from square lattice to tringular lattice configuration, the resonance frequencies are moved to higher frequencies and their bandwidths are increased.

- As in the case of conventional FSS (dielectric backed), decreasing the length of the narrow strips modifies the spectral characteristics such that, the resonances occur at higher frequecies compared with the case of longer dipoles and bandwidths associated to the resonances are increaesd.

- In the case of oblique incidence, resonances can be obtained for only zero azimuth angle for TE illumination. In the other conditions no resonance is obtained for neither TE

nor TM plane wave illumination of the screen. But always almost full transmission is observed for TE incidence and for high value of chirality admittance of the slab.
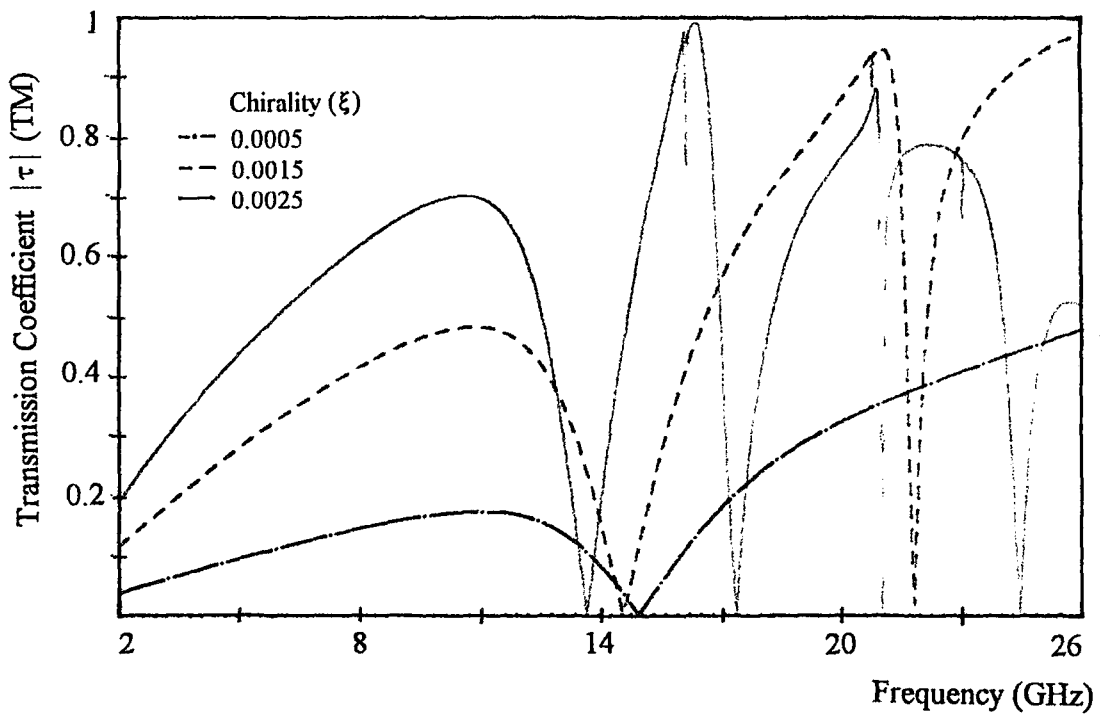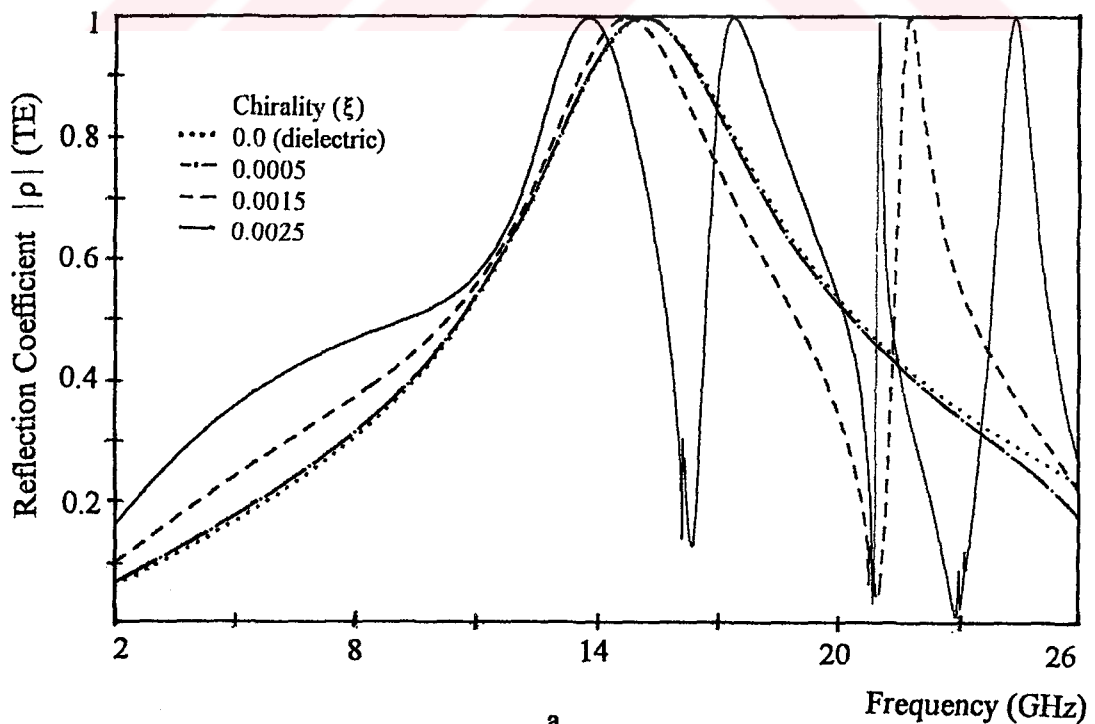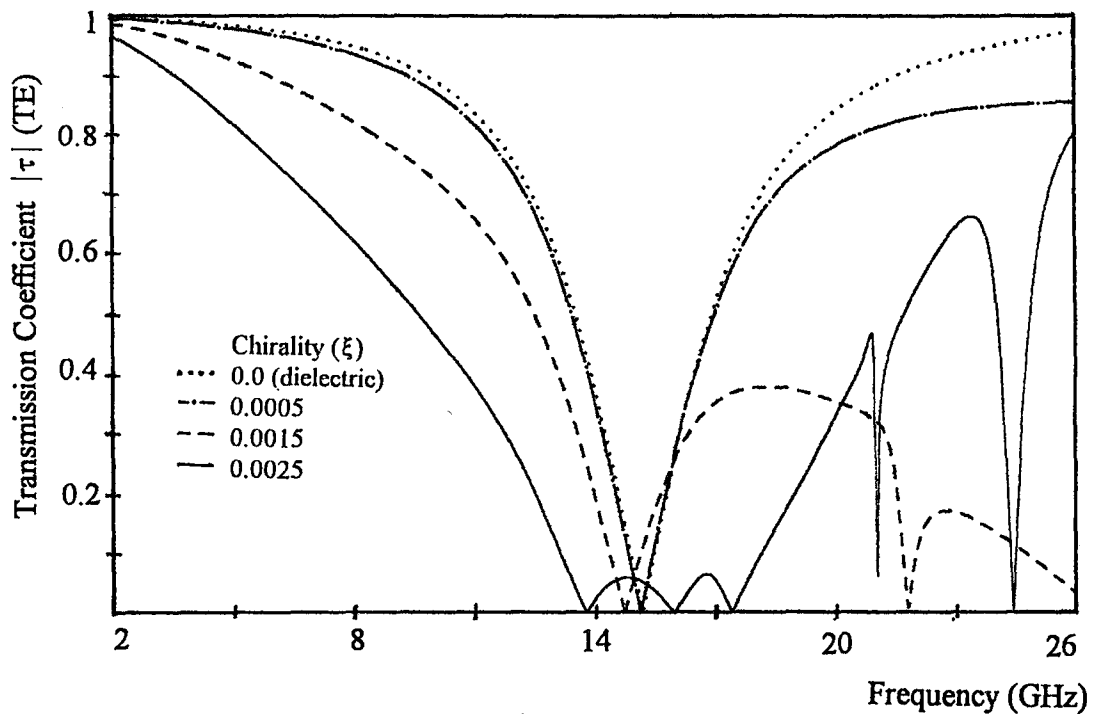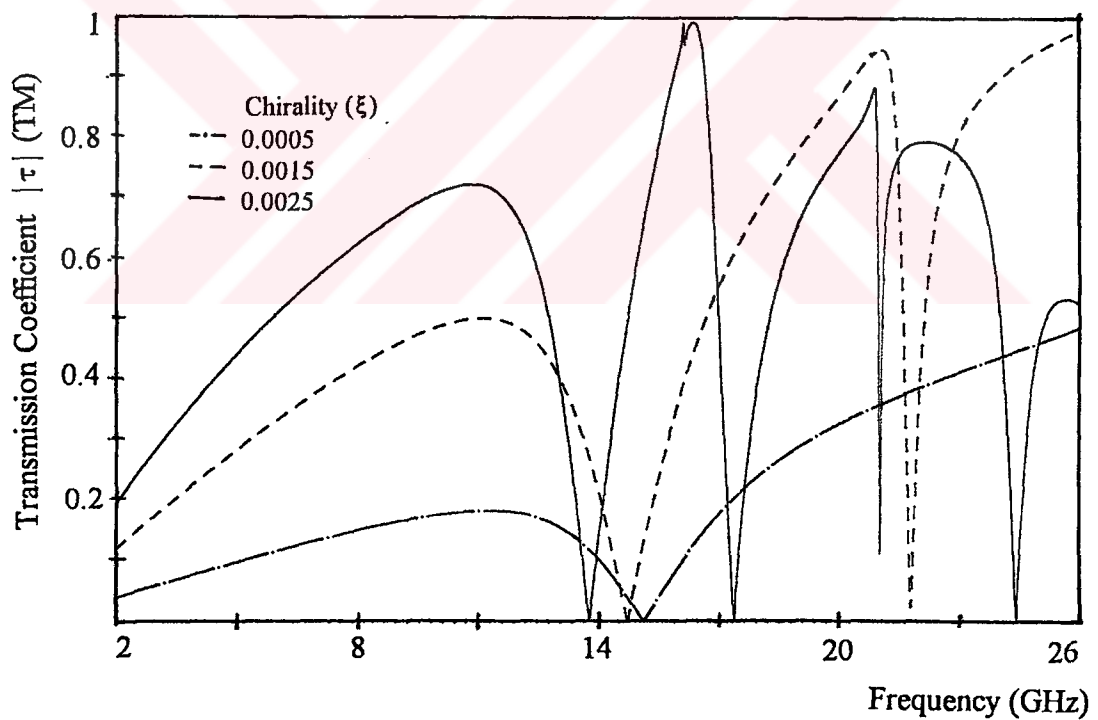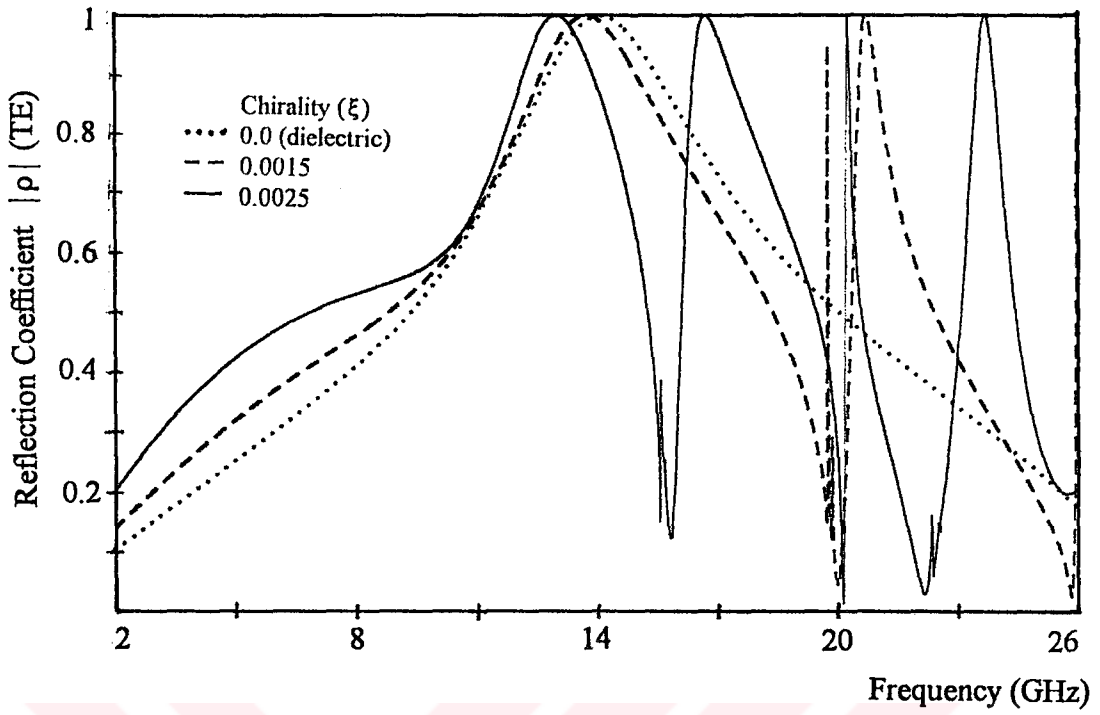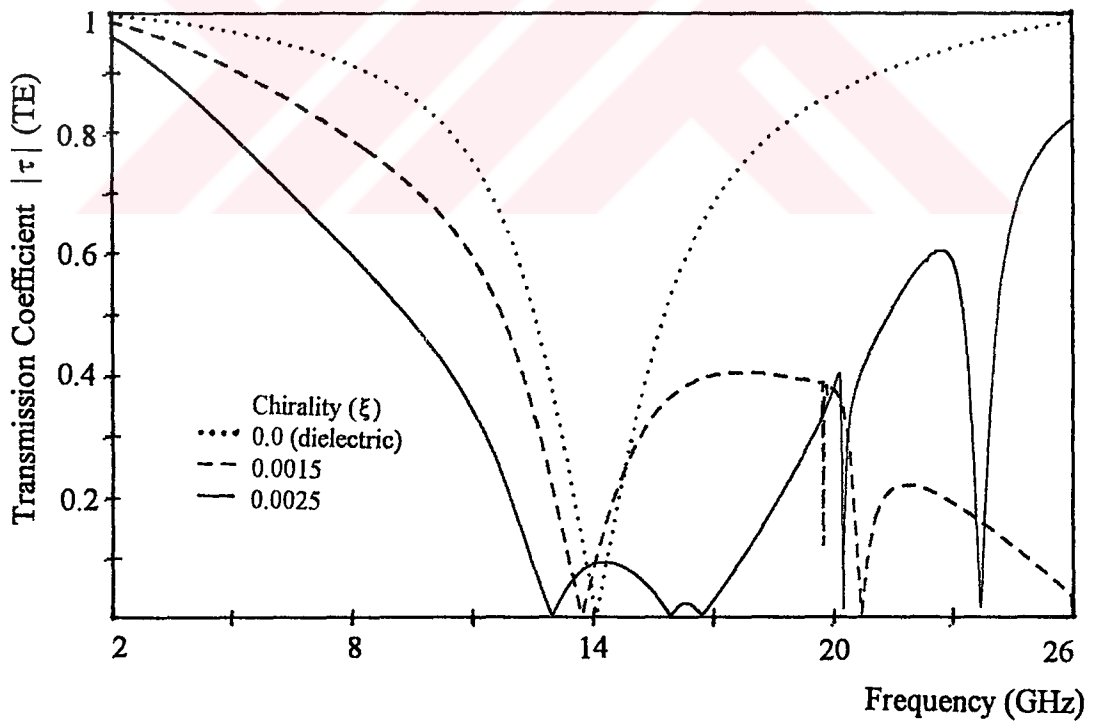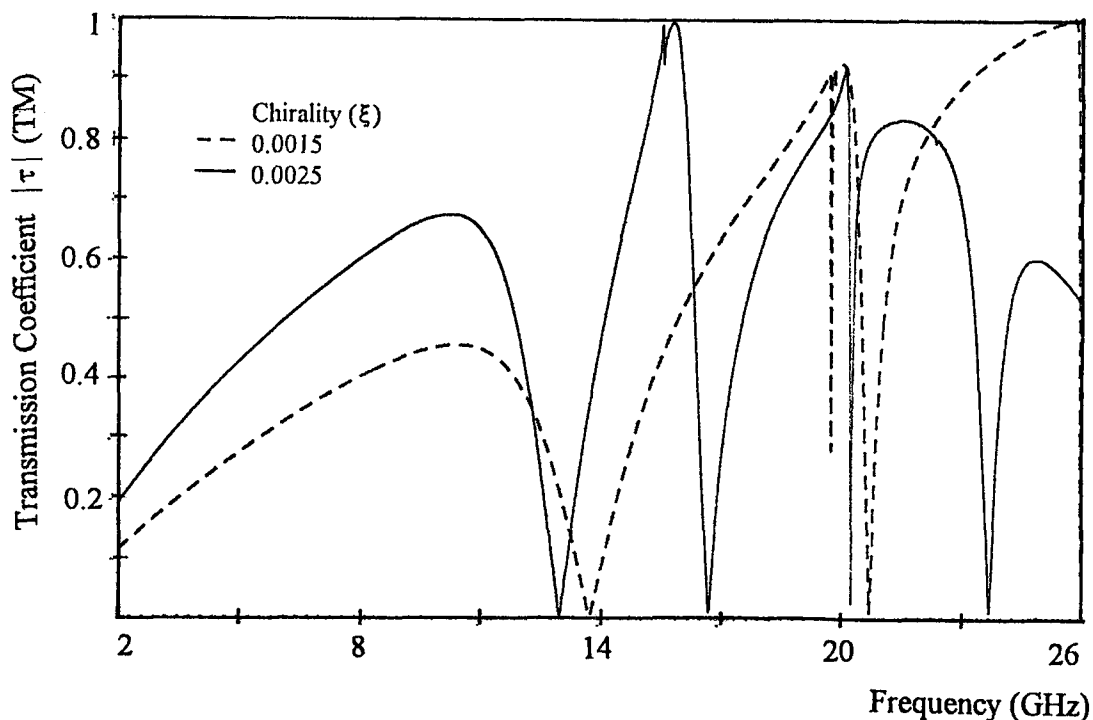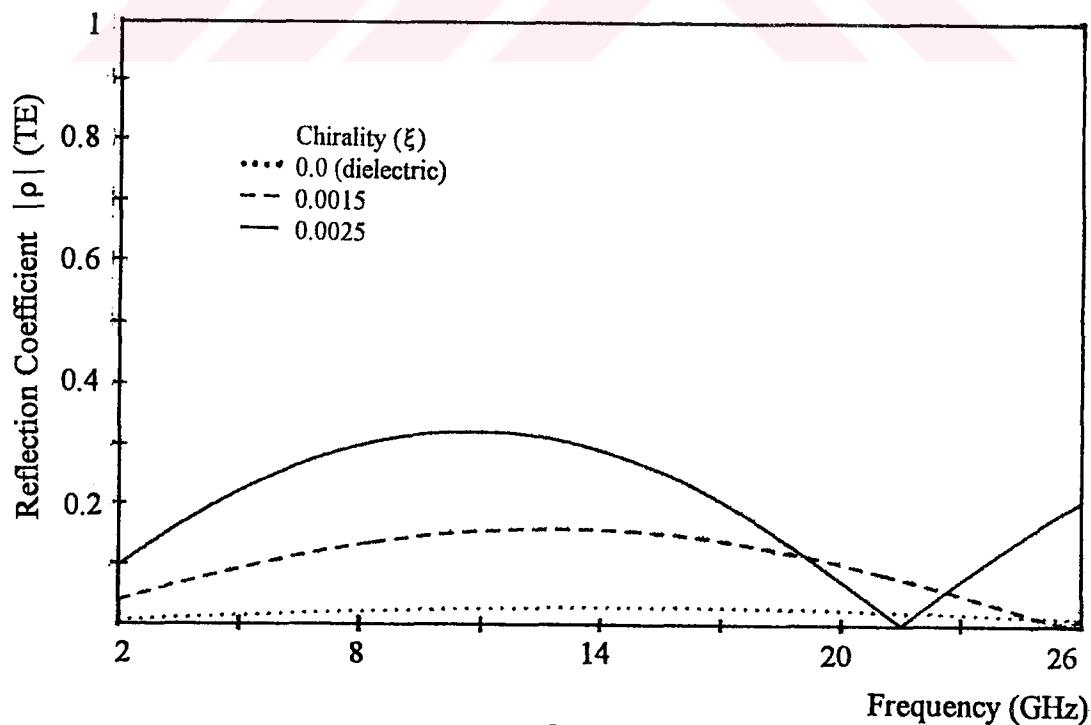
a

b
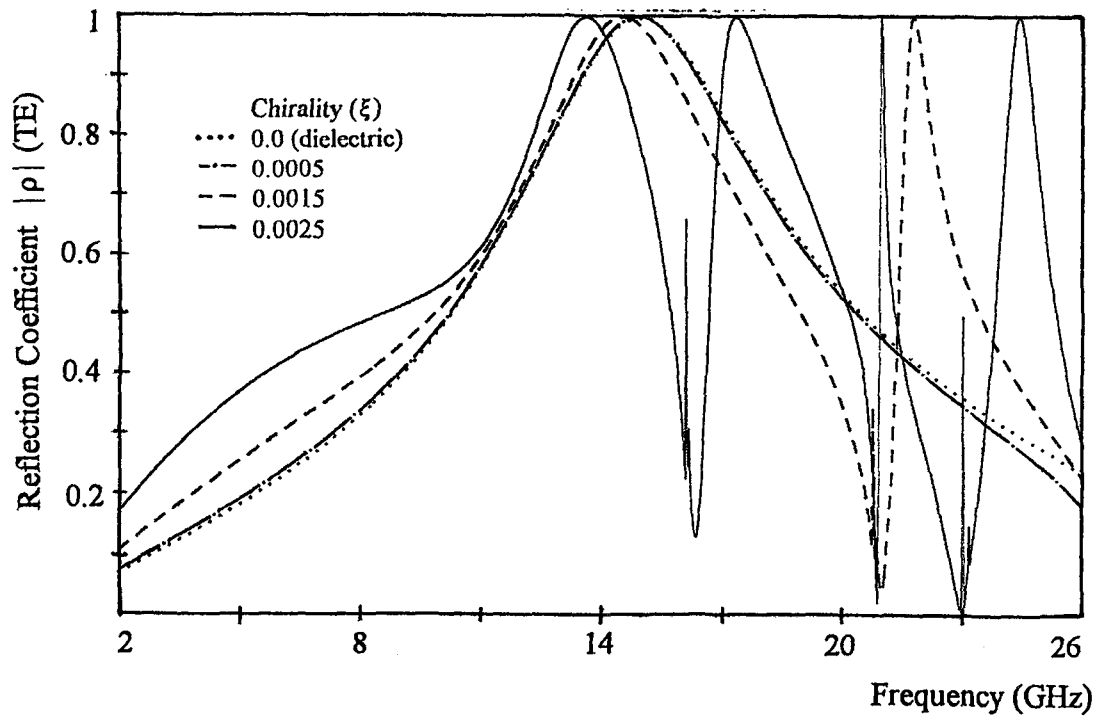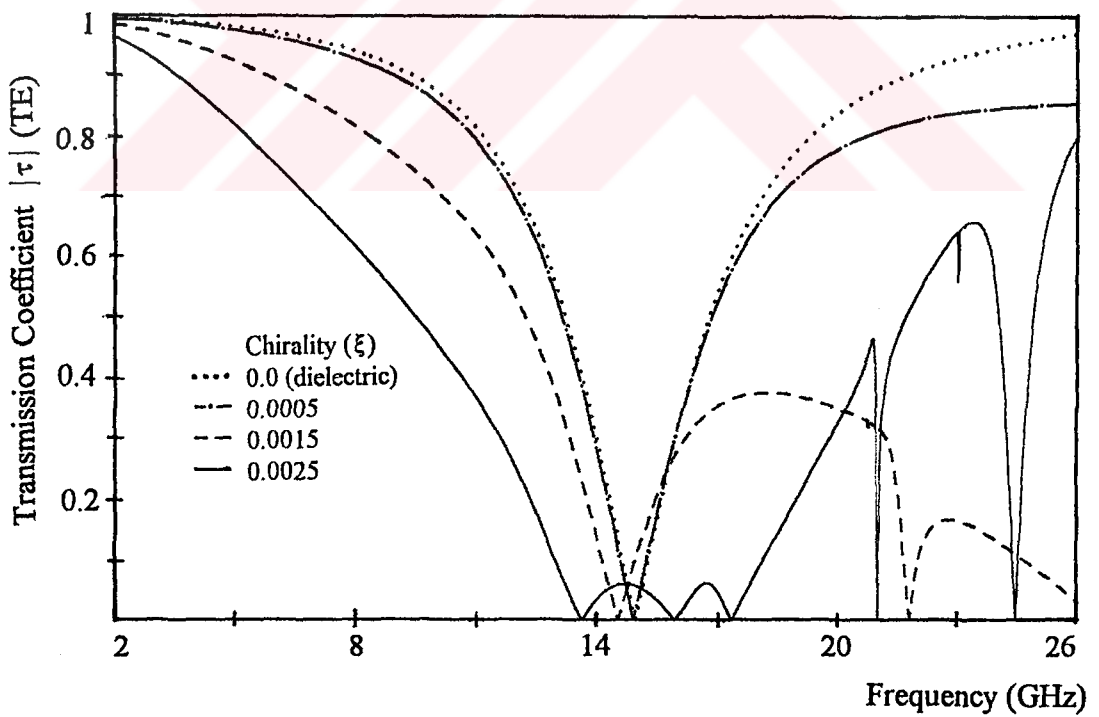
Figure 4.1.2 Spectral characteristics of Chiro-FSS with narrow strips; TE incidence
($\phi = 0°$, $\theta = 0°$), square lattice ($\alpha = 90°$), $D_1 = D_2 = 10$ mm, $L = 9.2$ mm, $W = 1$
mm, $\epsilon_r = 1.06$, $t = 5$ mm. a) Reflection coefficient (TE), b) Transmission
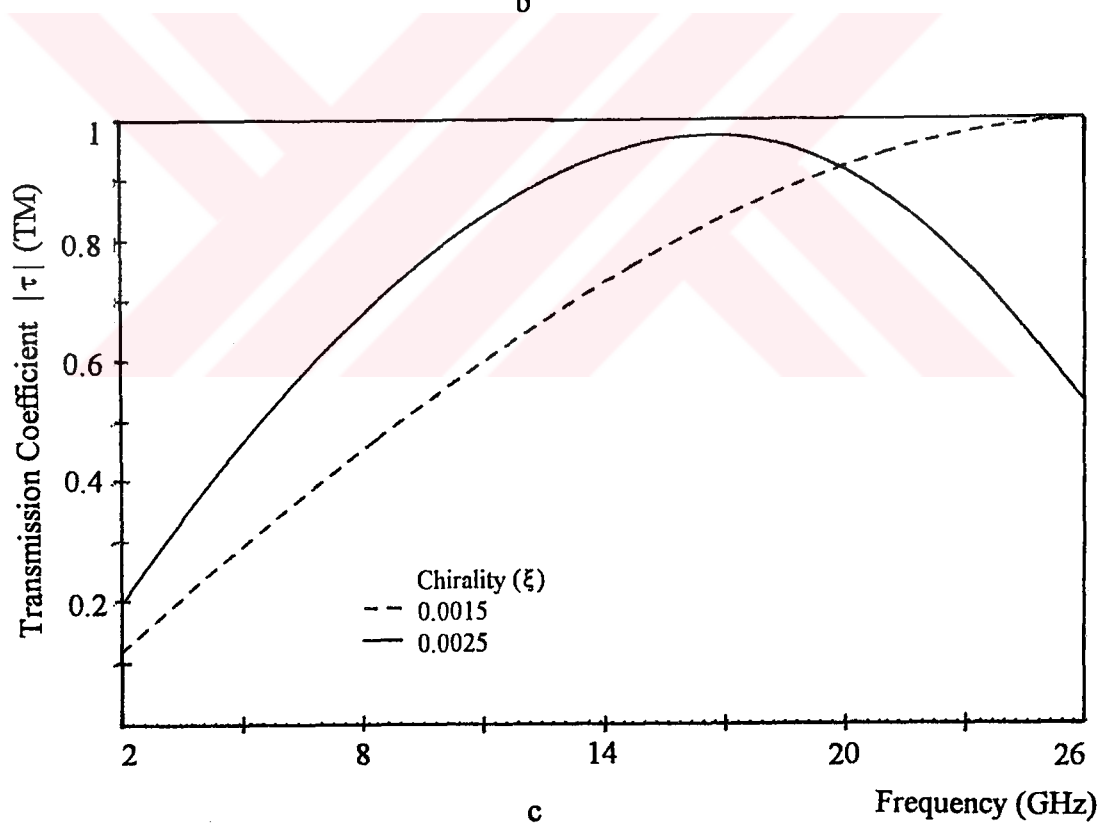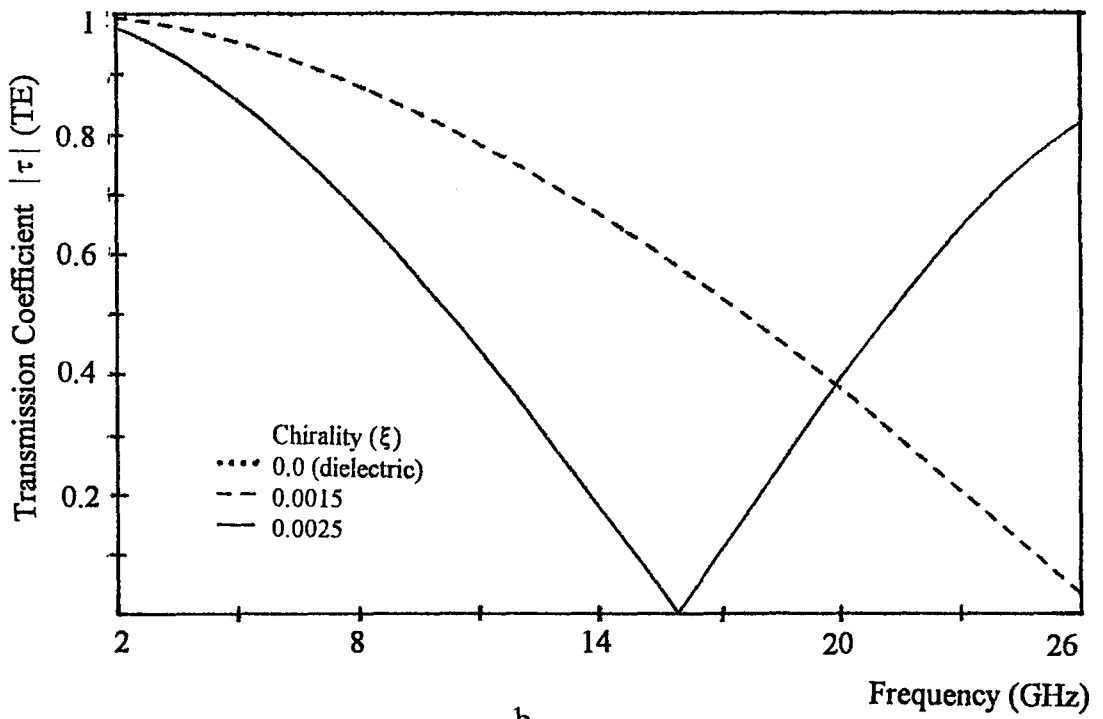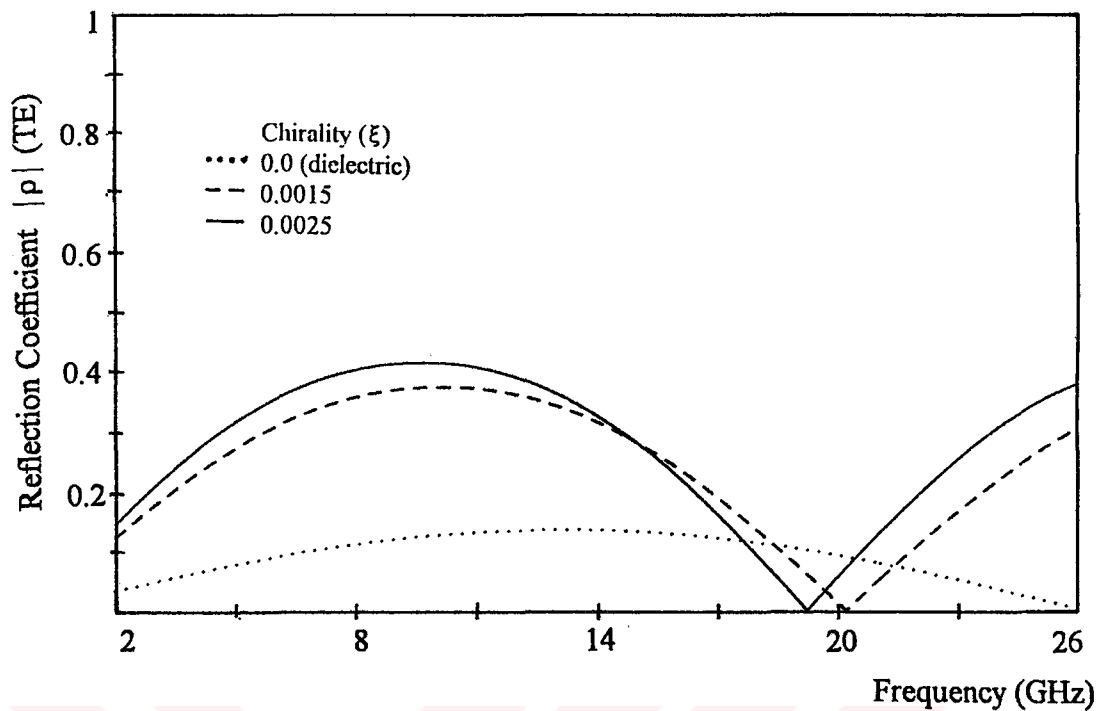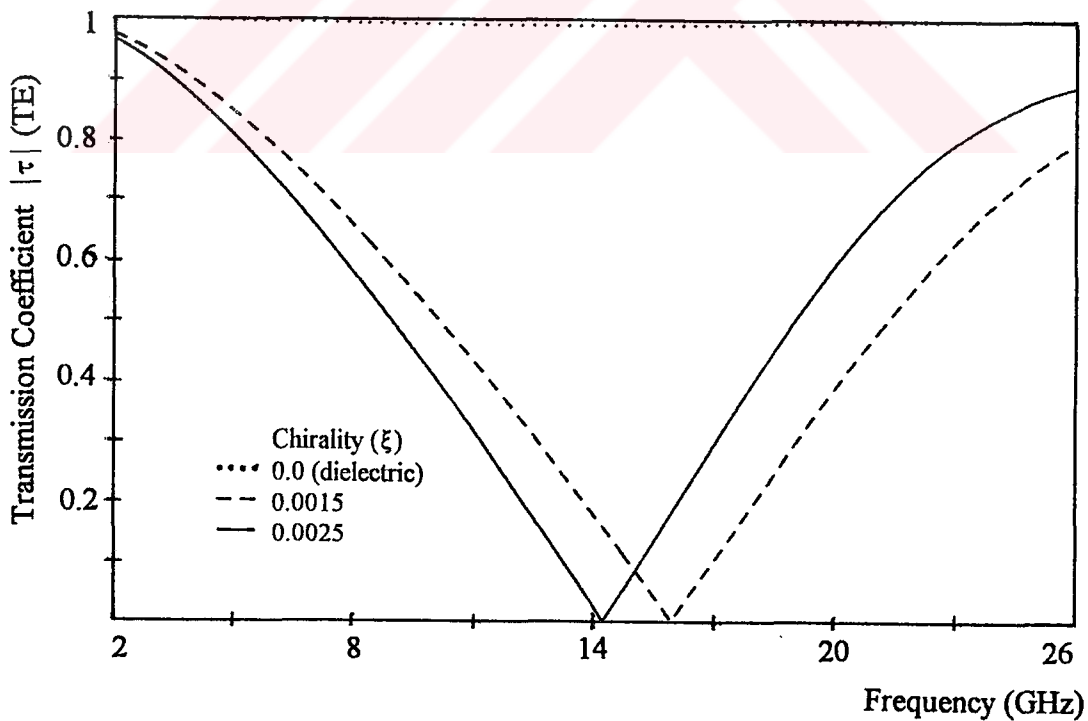coefficient (TE), c) Transmission coefficient (TM).

Figure 4.1.3   Spectral characteristics of Chiro-FSS with narrow strips; TE incidence ($\phi = 0°$, $\theta = 0°$), square lattice ($\alpha = 90°$), $D_1 = D_2 = 10$ mm, $L = 9.2$ mm, $W = 1$ mm, $\epsilon_r = 1.06$, $t = 4$ mm. a) Reflection coefficient (TE), b) Transmission coefficient (TE), c) Transmission coefficient (TM).
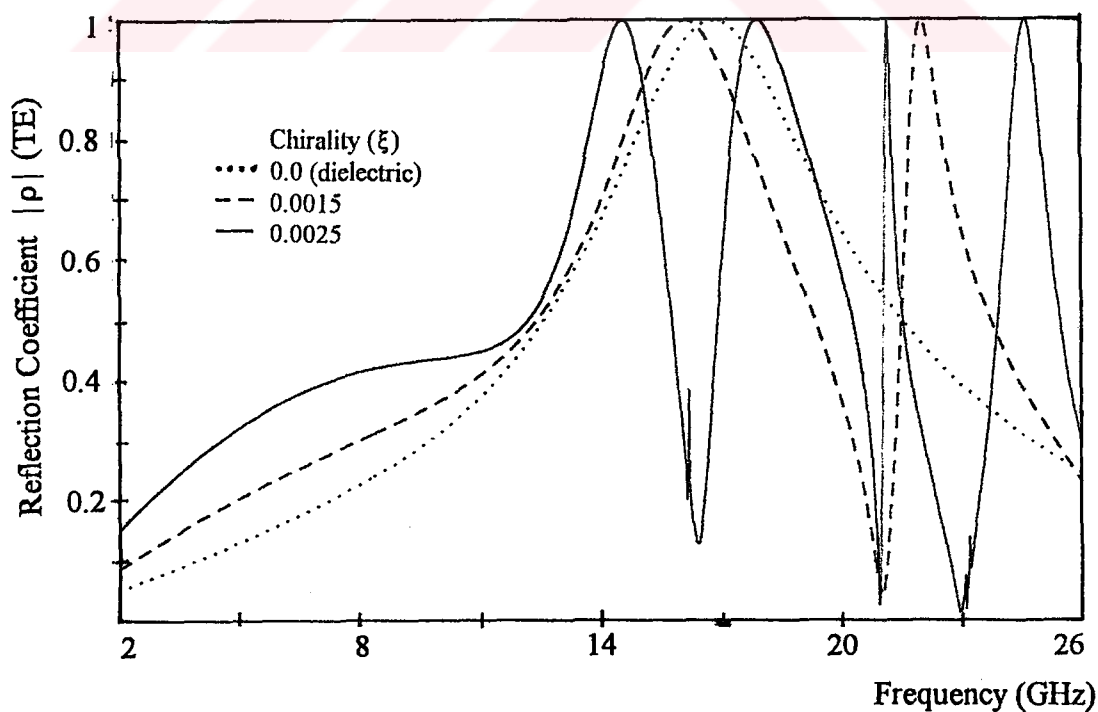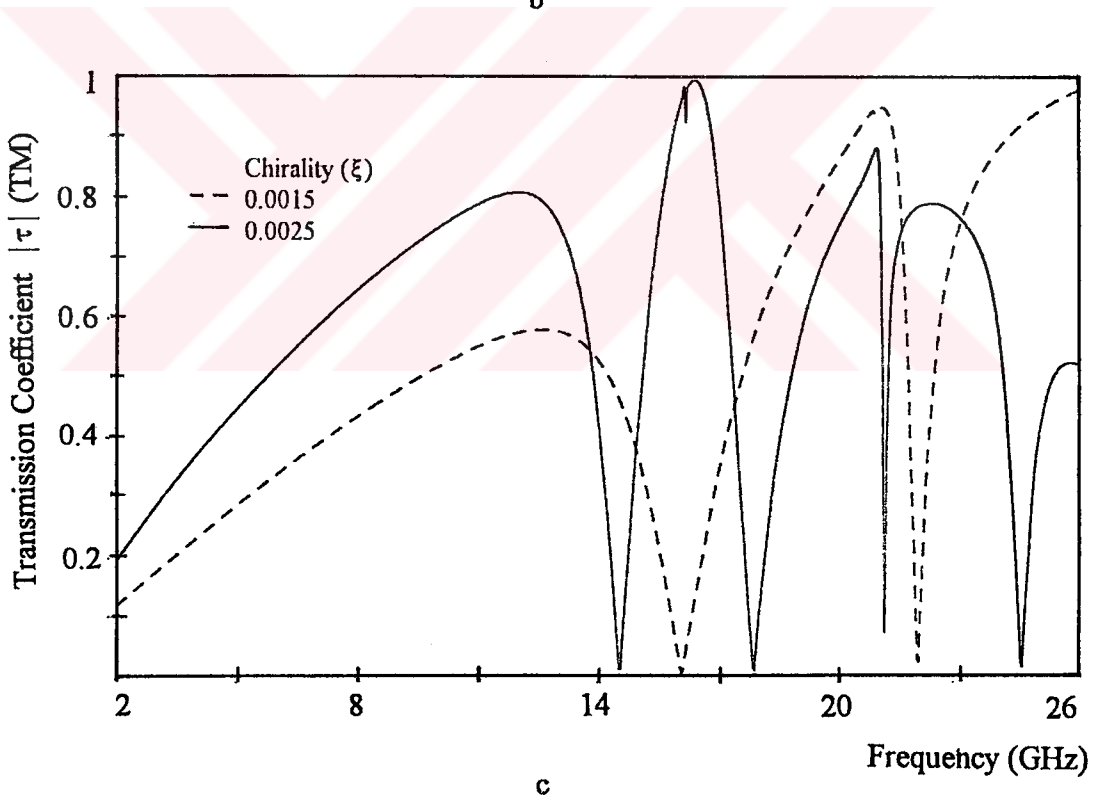
59

a

b

Figure 4.1.4 Spectral characteristics of Chiro-FSS with narrow strips; TE incidence ($\phi = 0°$, $\theta = 0°$), square lattice ($\alpha = 90°$), $D_1 = D_2 = 10$ mm, $L = 9.2$ mm, $W = 1$ mm, $\epsilon_r = 1.32$, $t = 5$ mm. a) Reflection coefficient (TE), b) Transmission coefficient (TE), c) Transmission coefficient (TM).
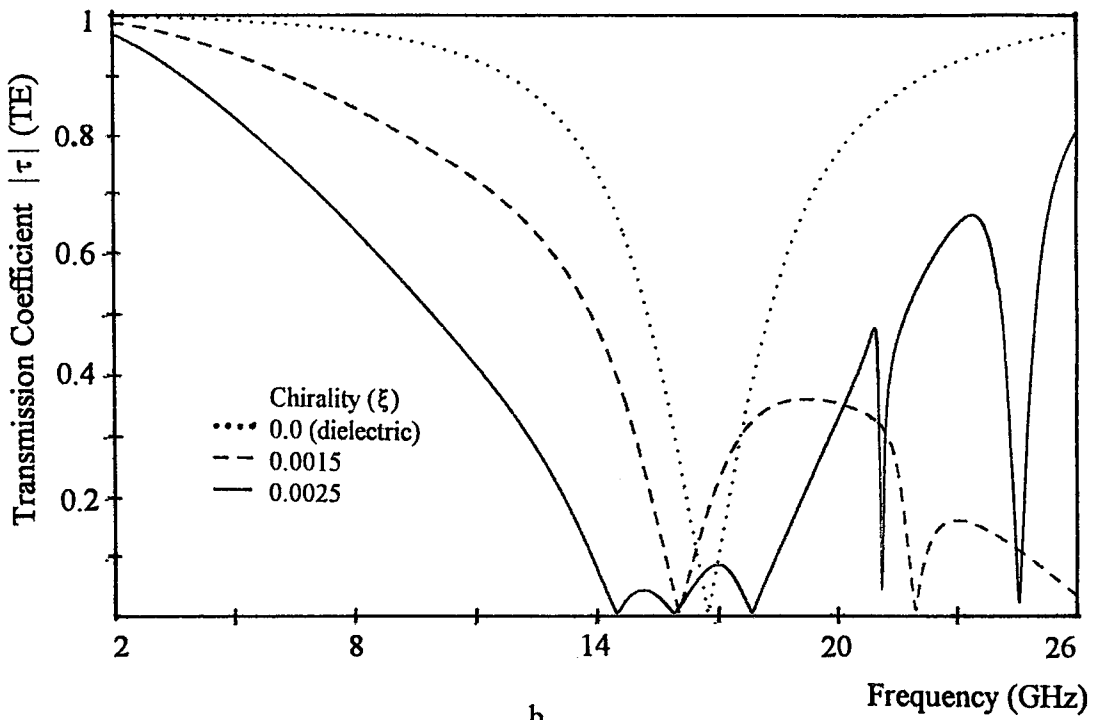
Figure 4.1.5   Spectral chracteristics of a chiral slab; TE incidence ($\phi=0°$, $\theta=0°$), $\epsilon_r=1.06$, t =5 mm. a) Reflection coefficient (TE), b) Transmission coefficient (TE), c) Transmission coefficient (TM).
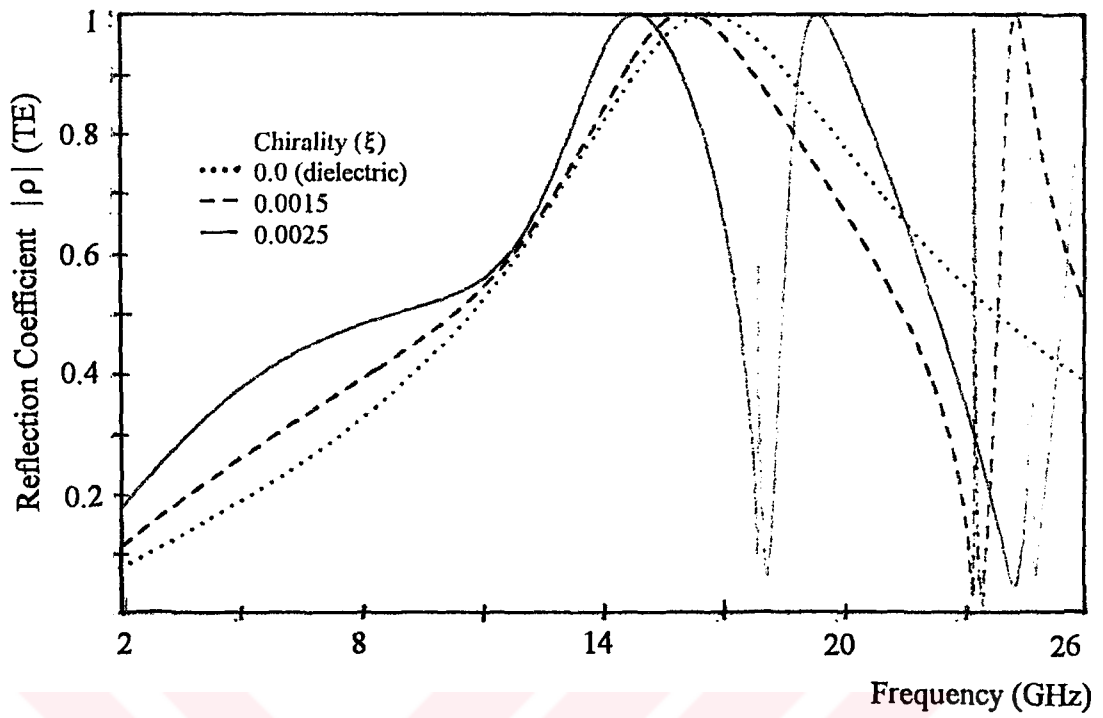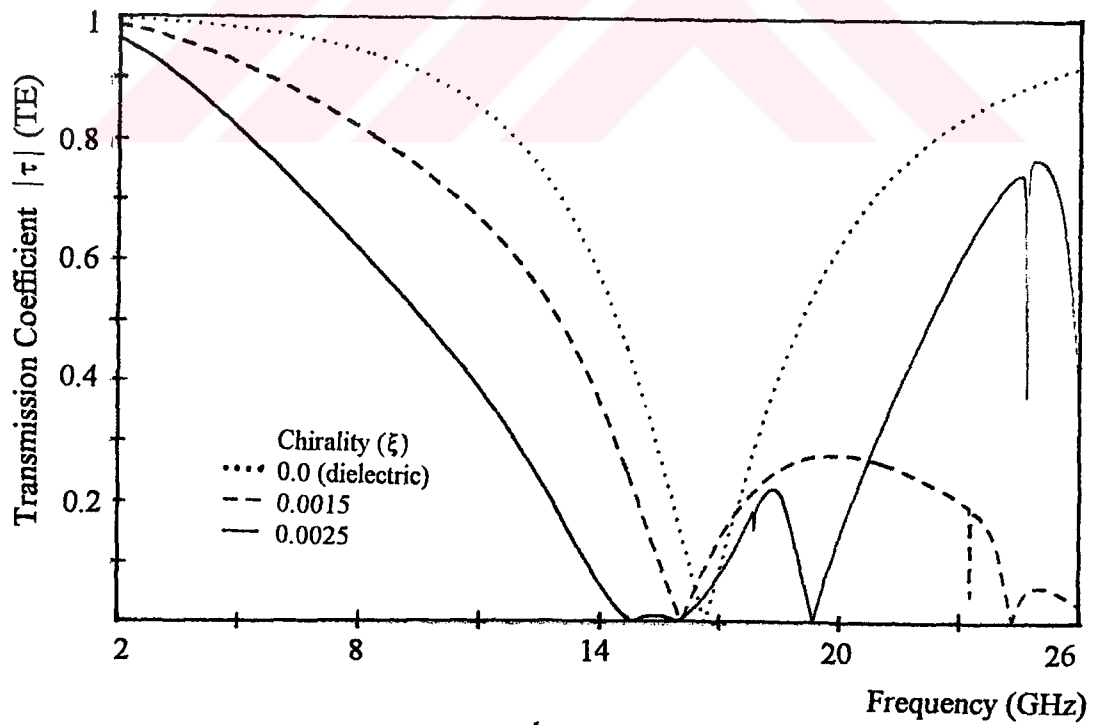
a

b

63
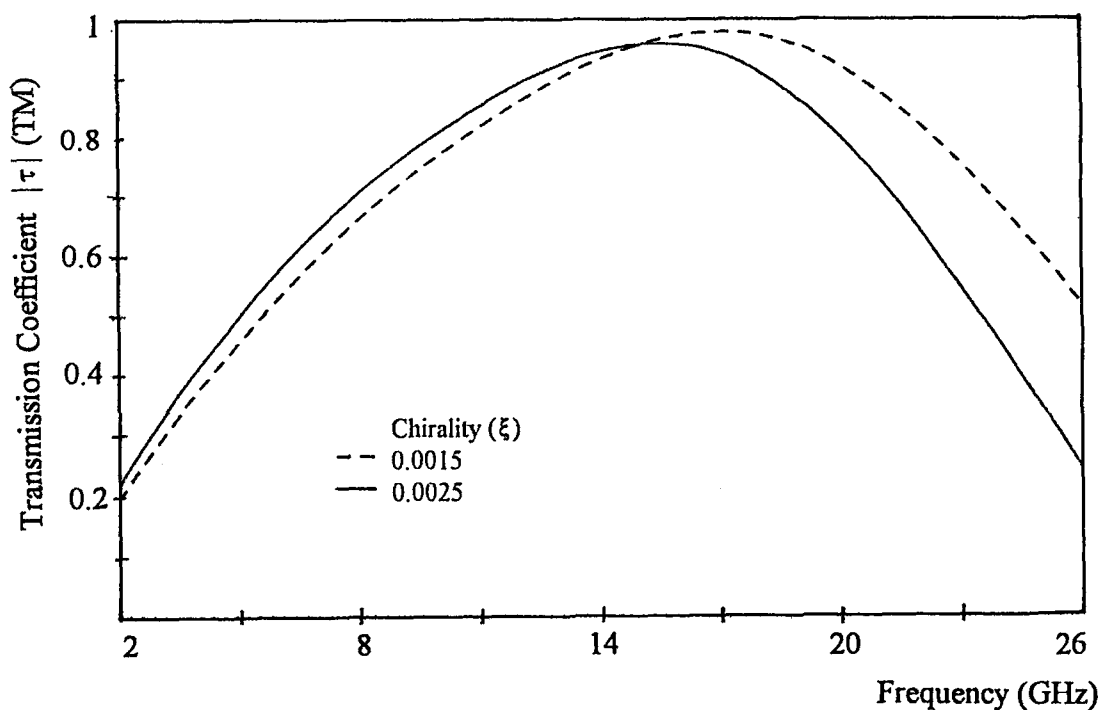
c

Figure 4.1.6   Spectral chracteristics of a chiral slab; TE incidence ($\phi= 0°$, $\theta=0°$), $\epsilon_r=1.32$, t =5 mm. a) Reflection coefficient (TE), b) Transmission coefficient (TE), c) Transmission coefficient (TM).

a

64

Figure 4.1.7 Spectral characteristics of Chiro-FSS with narrow strips; TE incidence
($\phi = 0°$, $\theta = 0°$), square lattice ($\alpha = 90°$), $D_1 = D_2 = 10$ mm, $L = 8$ mm, $W = 1$
mm, $\epsilon_r = 1.06$, $t = 5$ mm. a) Reflection coefficient (TE), b) Transmission
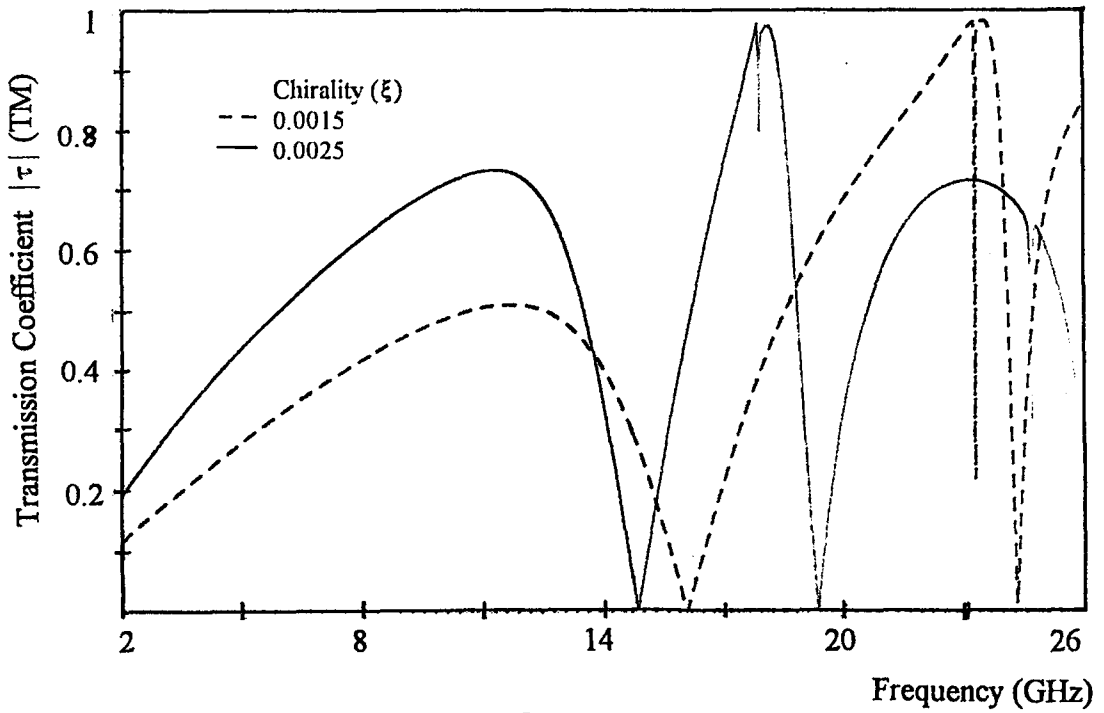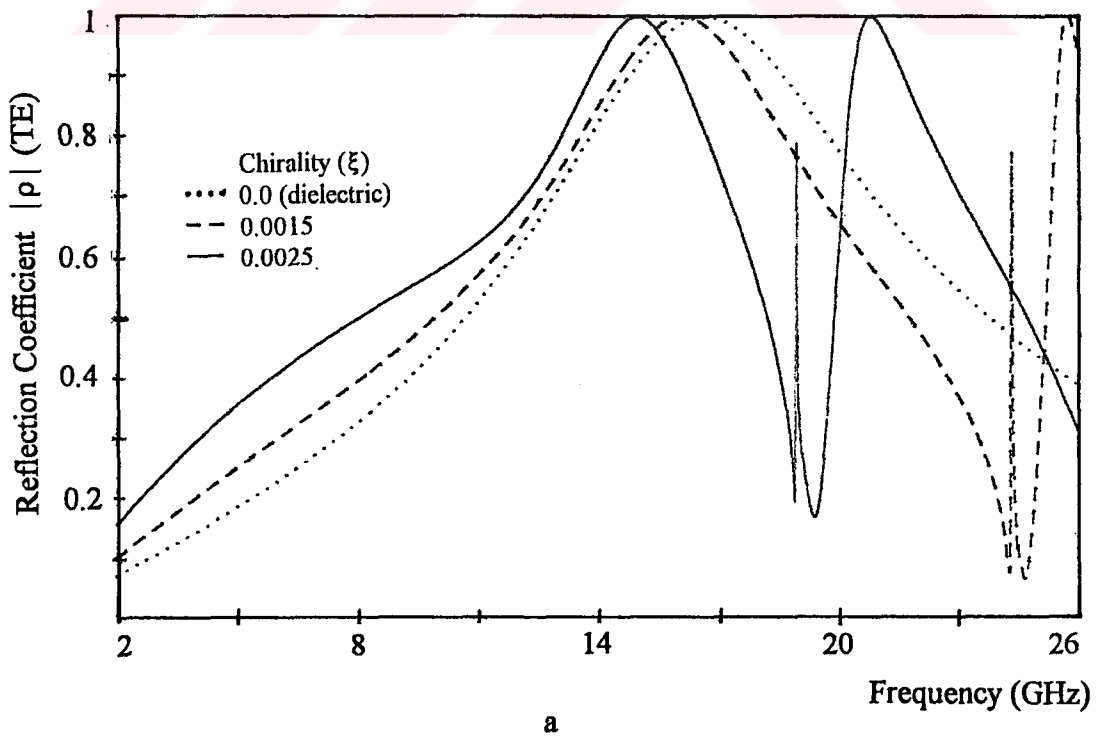coefficient (TE), c) Transmission coefficient (TM).

a

b

Figure 4.1.8   Spectral characteristics of Chiro-FSS with narrow strips; TE incidence
($\phi= 0°$, $\theta=0°$), triangular lattice ($\alpha= 60°$), $D_1=D_2=10$ mm, L=9.2 mm,
W = 1 mm, $\epsilon_r=1.06$, t = 5 mm. a) Reflection coefficient (TE),
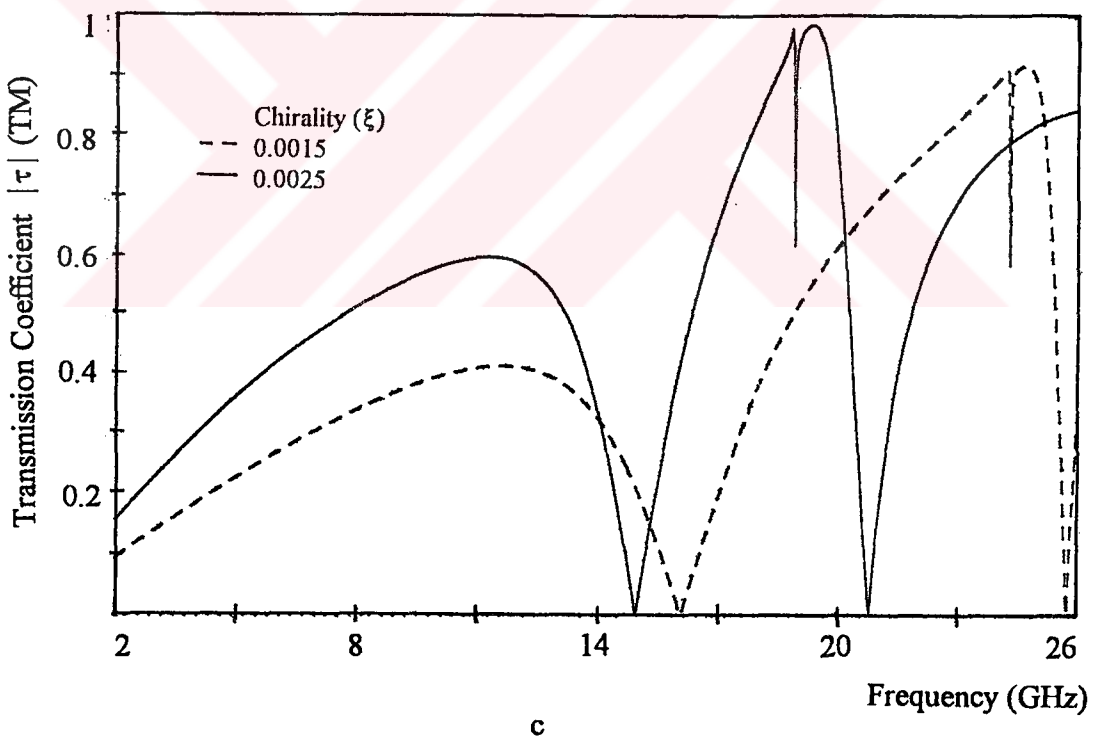b) Transmission coefficient (TE), c) Transmission coefficient (TM).

67

Figure 4.1.9 Spectral characteristics of Chiro-FSS with narrow strips; TE incidence
($\phi = 0°$, $\theta = 0°$), triangular lattice ($\alpha = 60°$), $D_1 = D_2 = 10$ mm, L=9.2 mm,
W = 1 mm, $\epsilon_r = 1.06$, t = 5 mm. a) Reflection coefficient (TE),
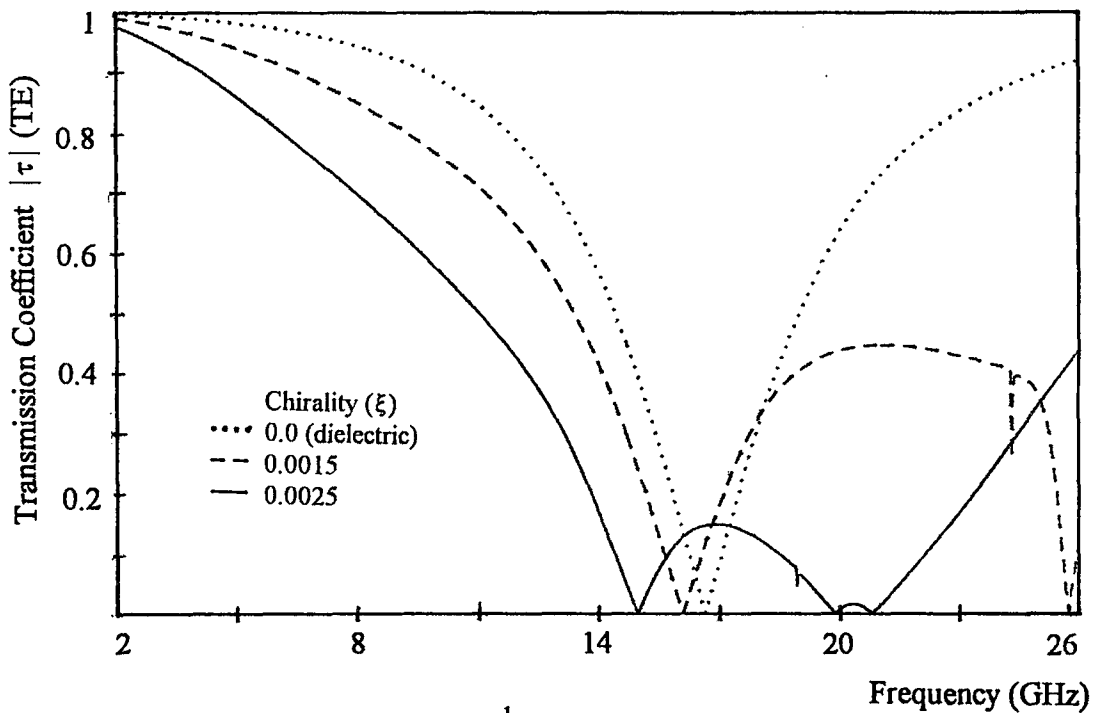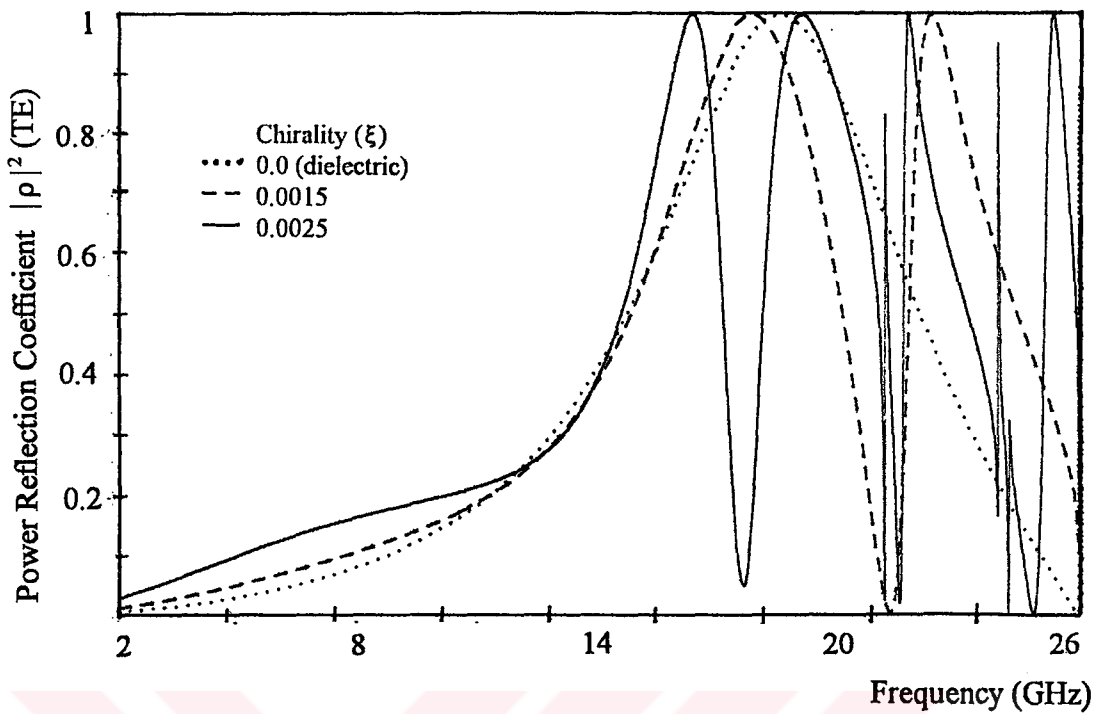b) Transmission coefficient (TE), c) Transmission coefficient (TM).

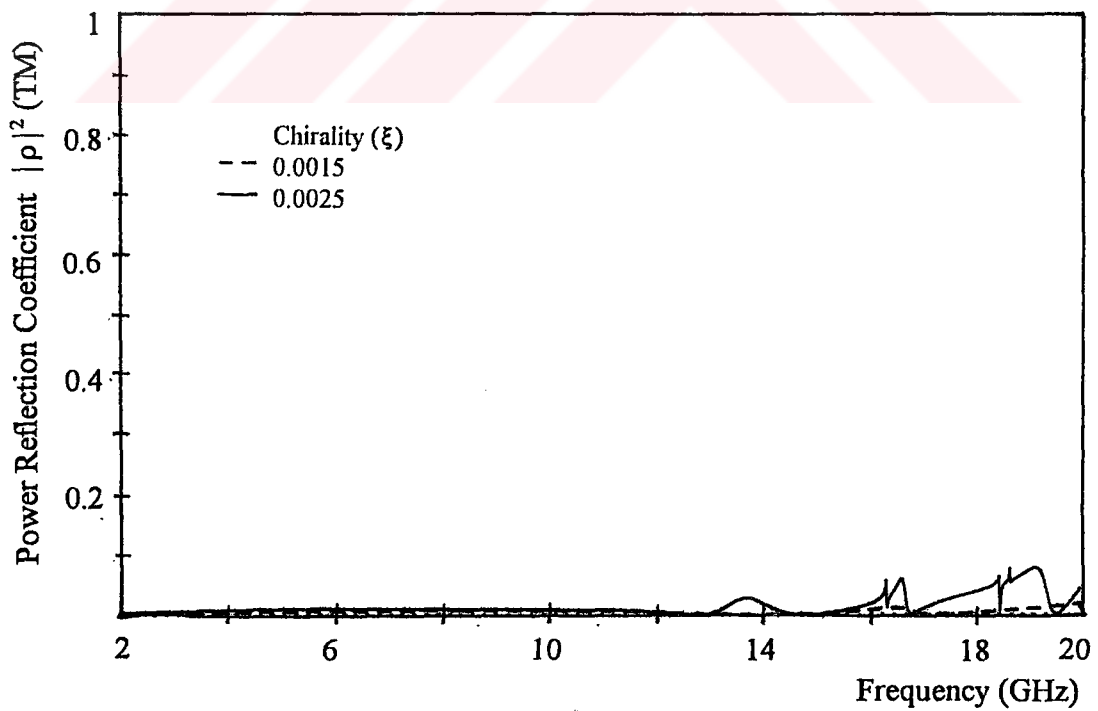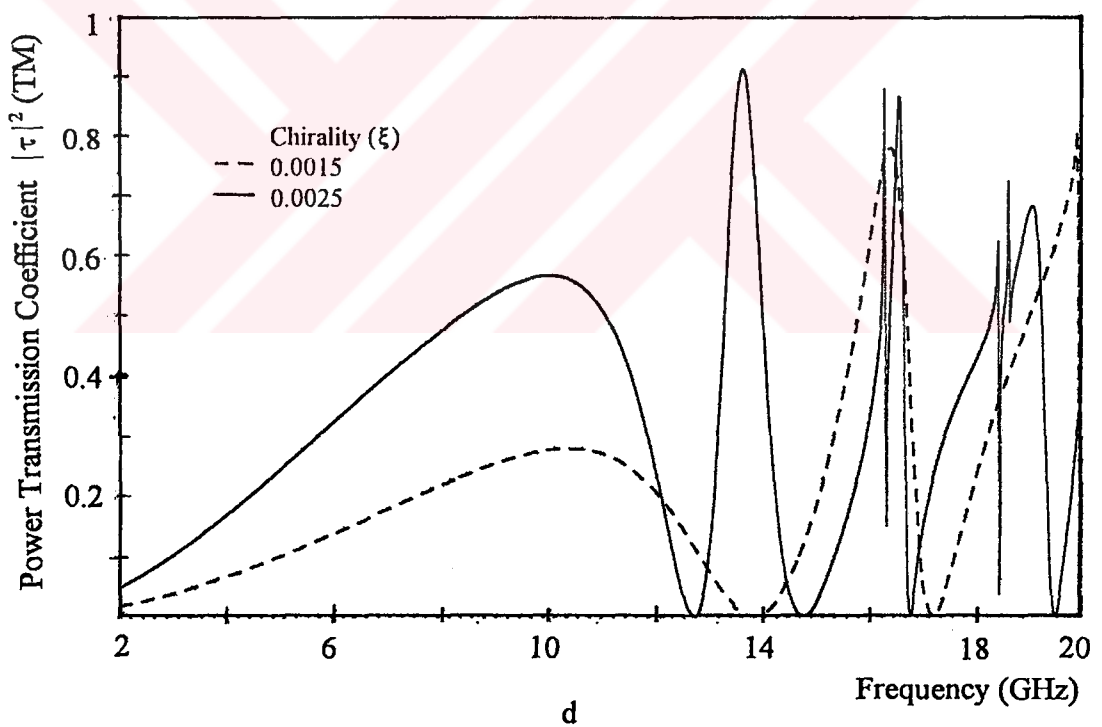Power Reflection Coefficient $|\rho|^2$ (TE)

Chirality (ξ)
······ 0.0 (dielectric)
----- 0.0015
—— 0.0025

Frequency (GHz)

a

Power Reflection Coefficient $|\rho|^2$ (TM)

Chirality (ξ)
----- 0.0015
—— 0.0025

Frequency (GHz)

b

69

Figure 4.1.10 Spectral characteristics of Chiro-FSS with narrow strips; TE incidence

(ϕ= 0°,θ=30°), square lattice (α= 90°), D_1=D_2=10 mm, L=9.2 mm, W=1

mm, ϵ_r=1.06, t = 5mm. a) Power reflection coefficient (TE), b) Power

reflection coefficient (TE), c) Power transmission coefficient (TE),
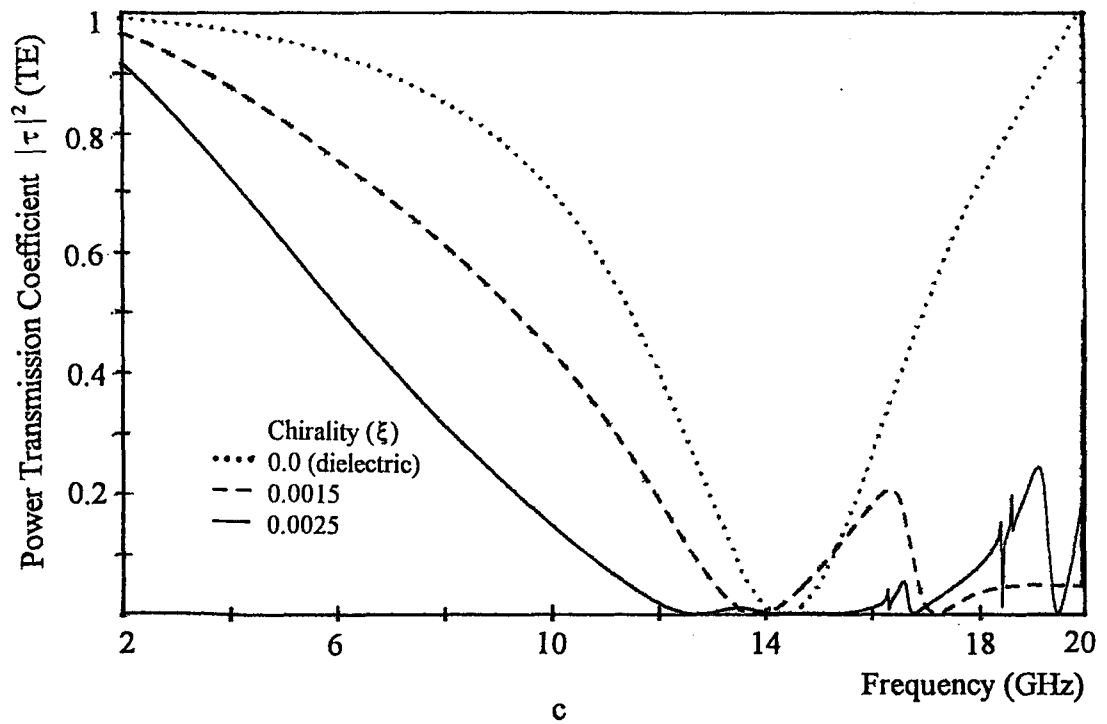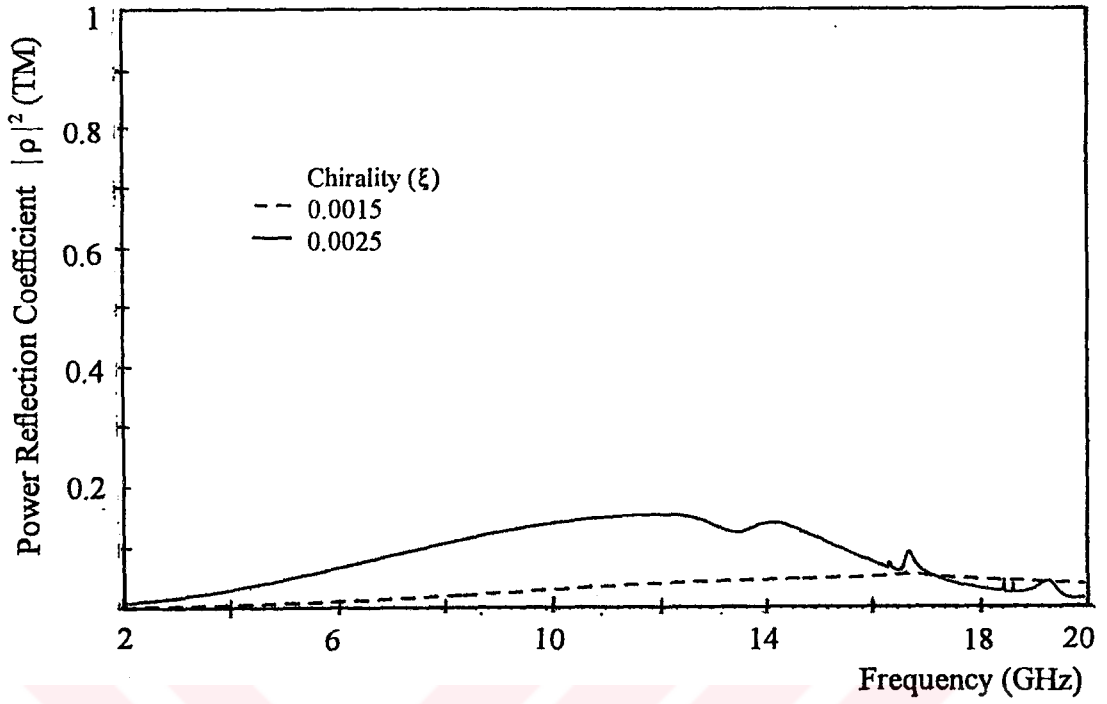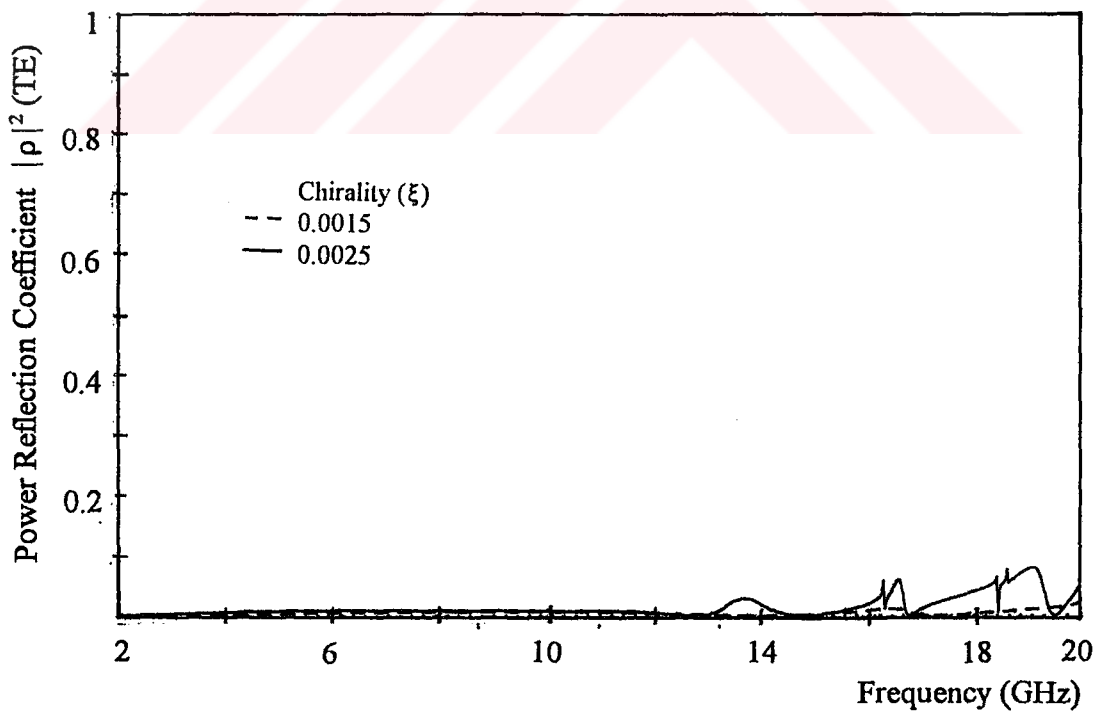
d) Power transmission coefficient (TM).

a

b

Figure 4.1.11 Spectral characteristics of Chiro-FSS with narrow strips; TM incidence (ϕ= 0°,θ=30°), square lattice (α= 90°), D_1=D_2=10 mm, L=9.2 mm, W=1 mm, ϵ_r=1.06, t = 5mm. a) Power reflection coefficient (TE), b) Power reflection coefficient (TM), c) Power transmission coefficient (TE), d) Power transmission coefficient (TM).

72

a

b

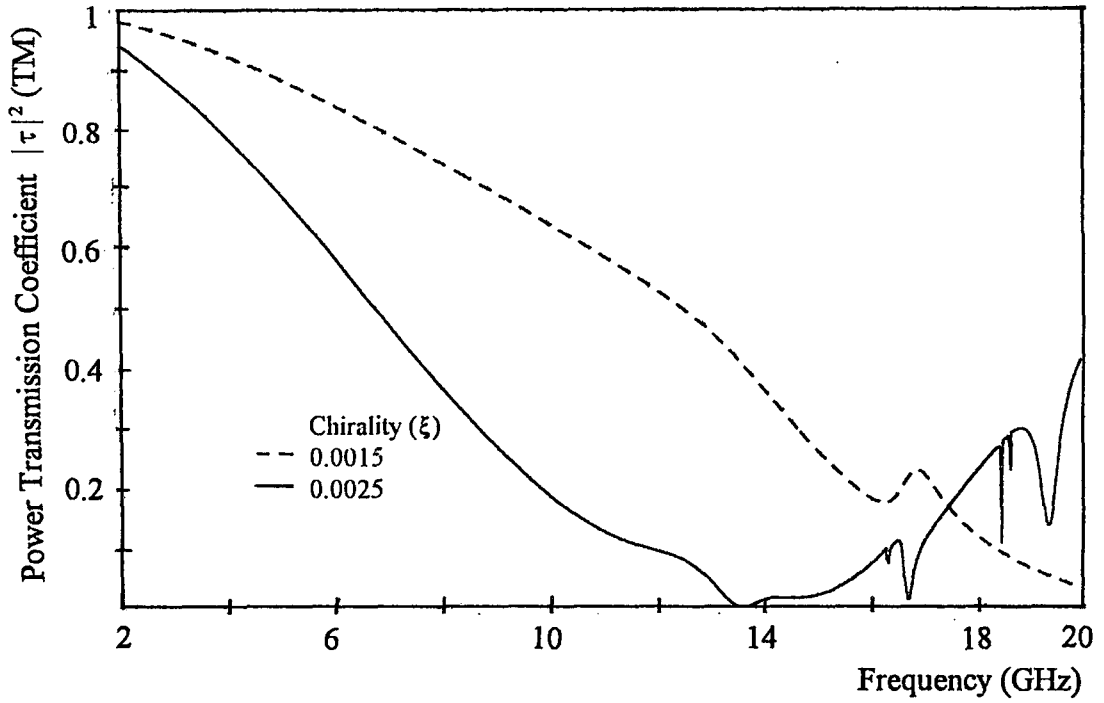Figure 4.1.12   Spectral characteristics of Chiro-FSS with narrow strips; TE incidence

(ϕ=30°,θ=30°), square lattice (α=90°), D_1=D_2=10 mm, L=9.2 mm, W=1

mm, ϵ_r=1.06, t = 5mm. a) Power reflection coefficient (TE), b) Power

reflection coefficient (TM), c) Power transmission coefficient (TE),
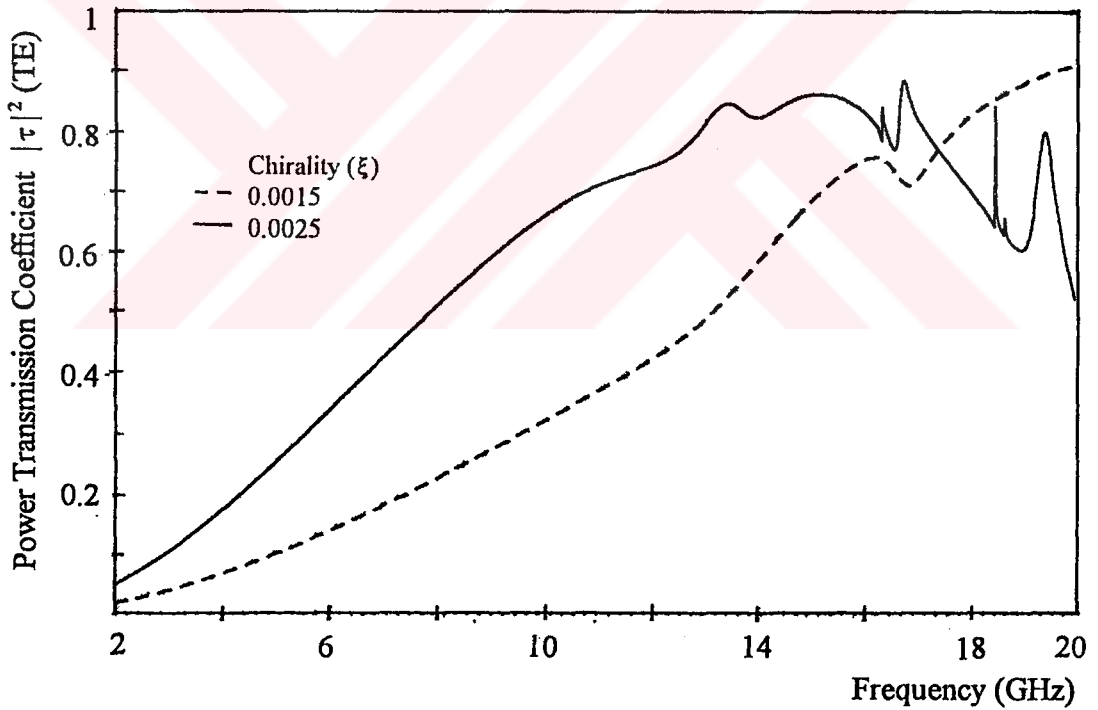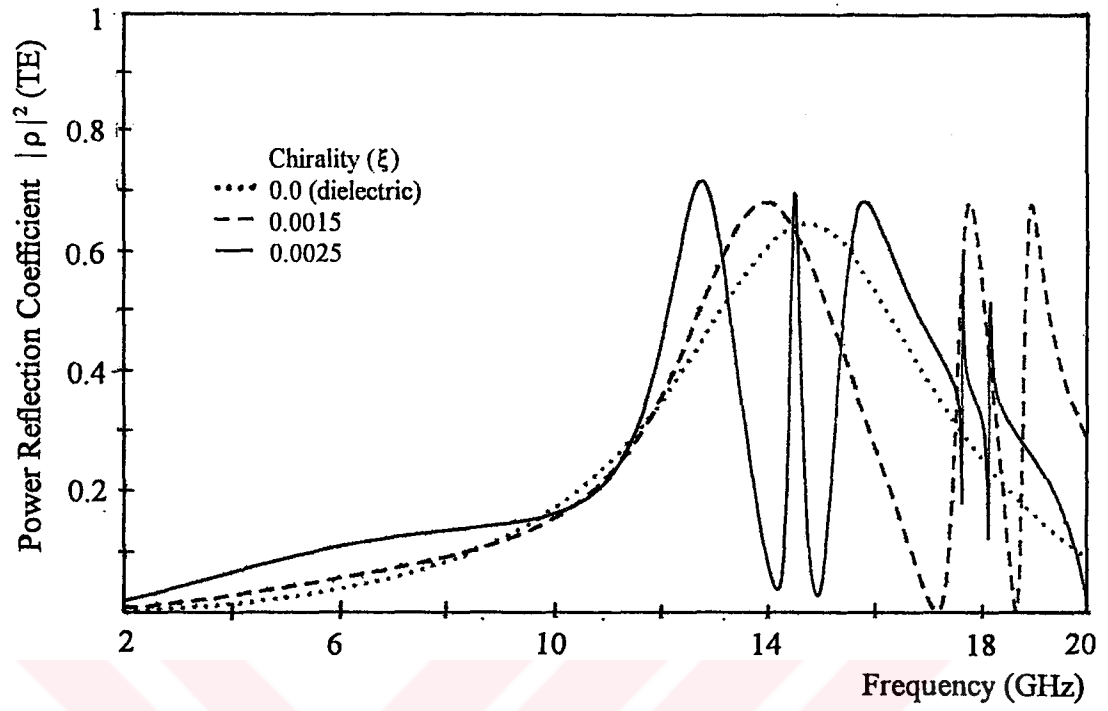
d) Power transmission coefficient (TM).

a

b

75

Figure 4.1.13   Spectral characteristics of Chiro-FSS with narrow strips; TM incidence
($\phi=30°,\theta=30°$), square lattice ($\alpha=90°$), $D_1=D_2=10$ mm, $L=9.2$ mm, $W=1$
mm, $\epsilon_r=1.06$, $t=5$mm. a) Power reflection coefficient (TE), b) Power
reflection coefficient (TM), c) Power transmission coefficient (TE),
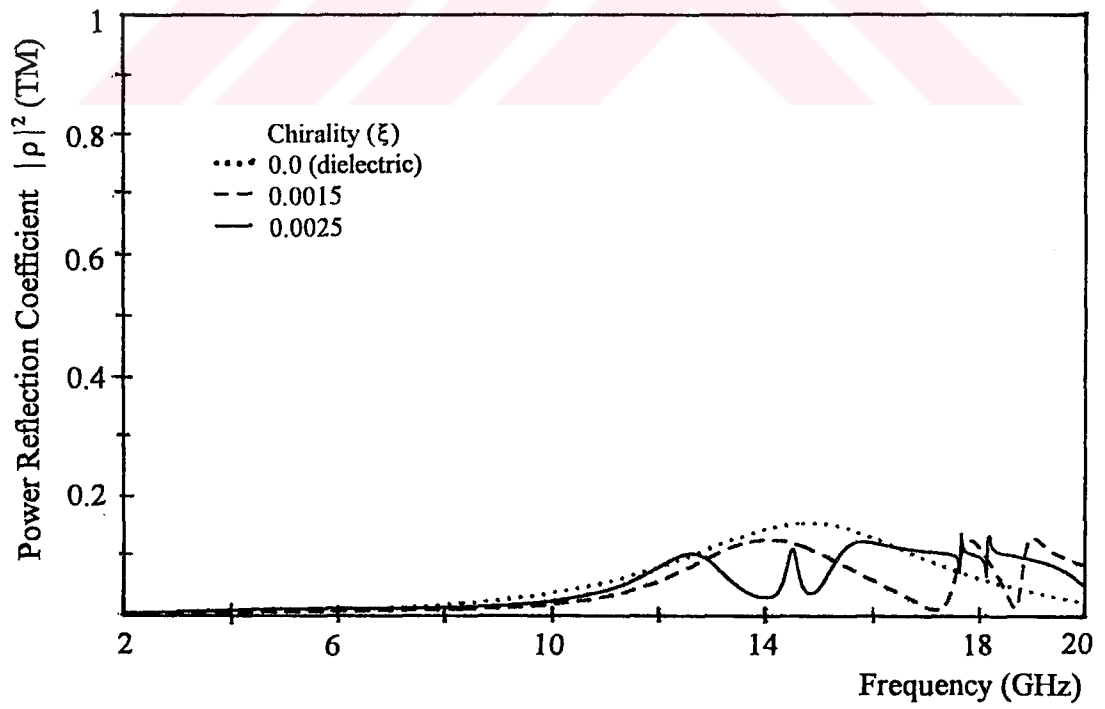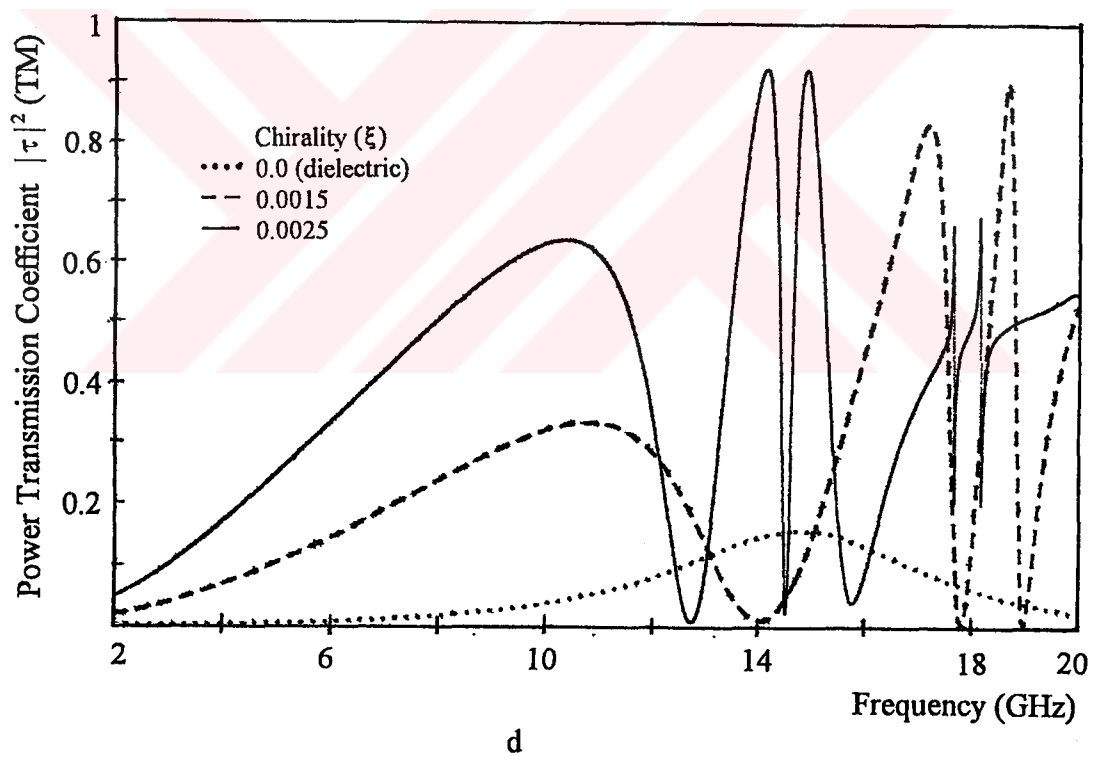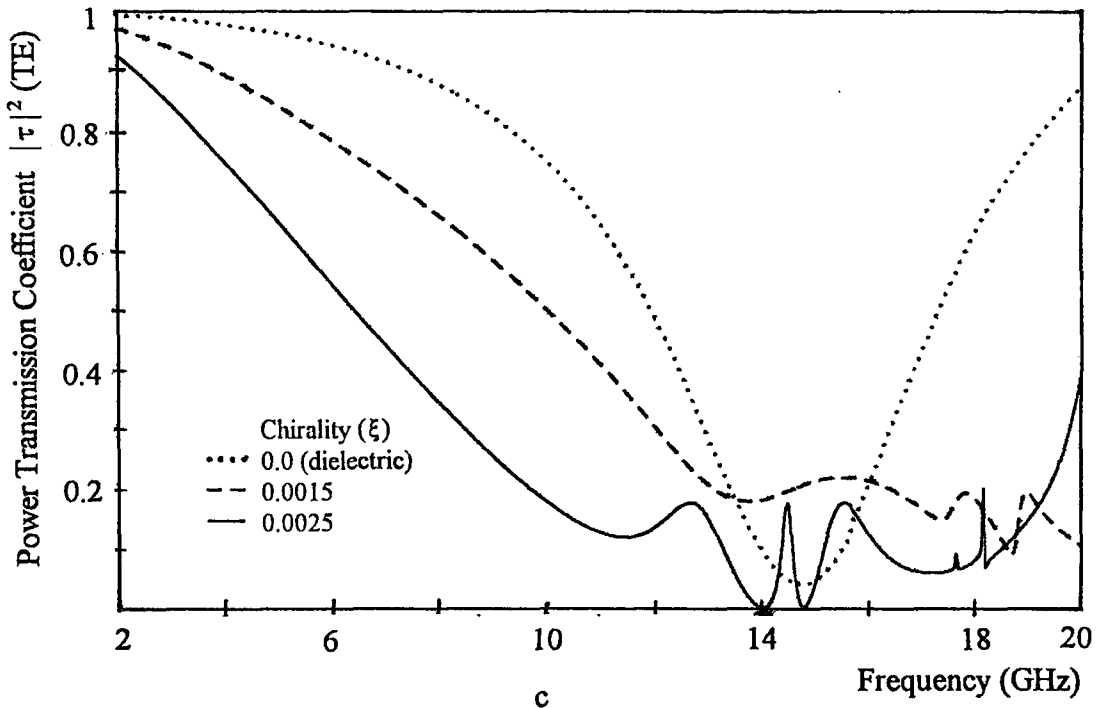d) Power transmission coefficient (TM).

76

a

b

77
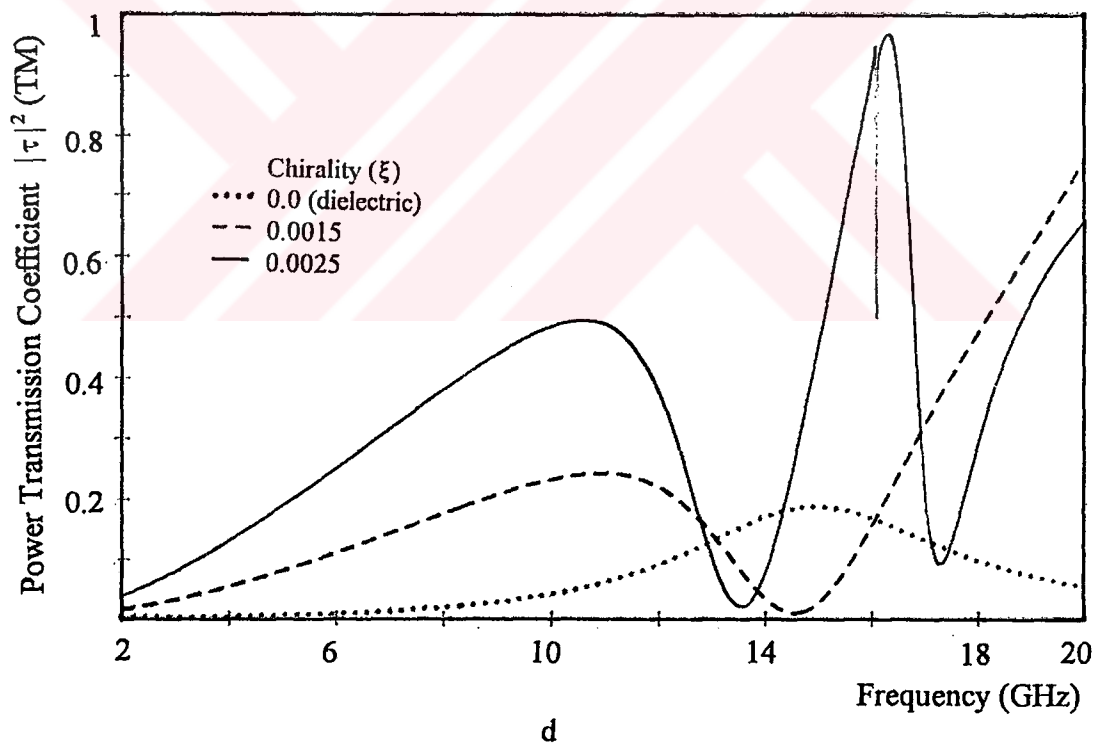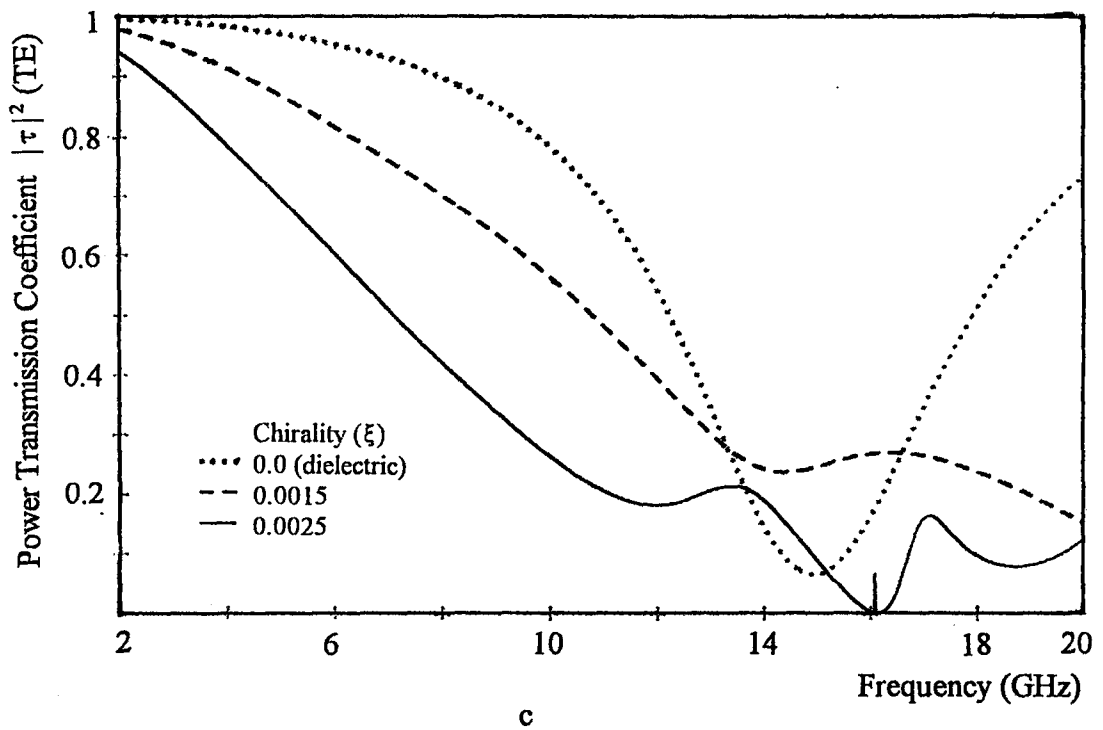
Figure 4.1.14   Spectral characteristics of Chiro-FSS with narrow strips; TE incidence
(ϕ= 30°,θ=0°), square lattice (α= 90°), D_1=D_2=10 mm, L=9.2 mm, W=1
mm, ϵ_r=1.06, t = 5mm. a) Power reflection coefficient (TE), b) Power
transmission coefficient (TE), c) Power transmission coefficient (TM).

78
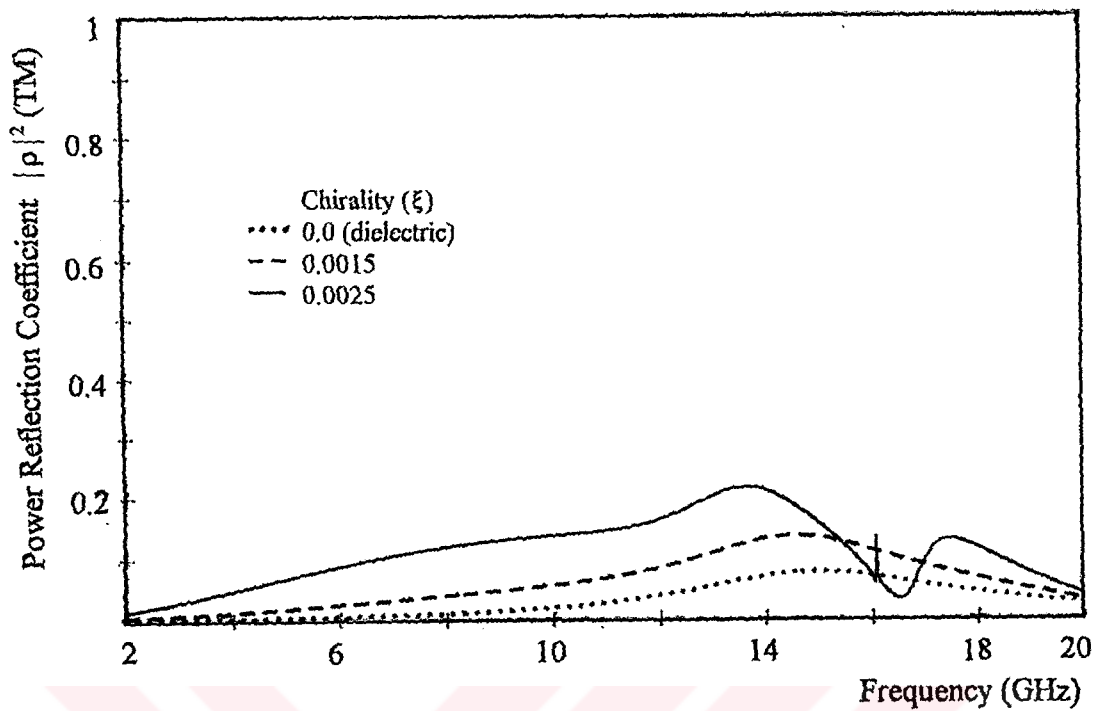
a
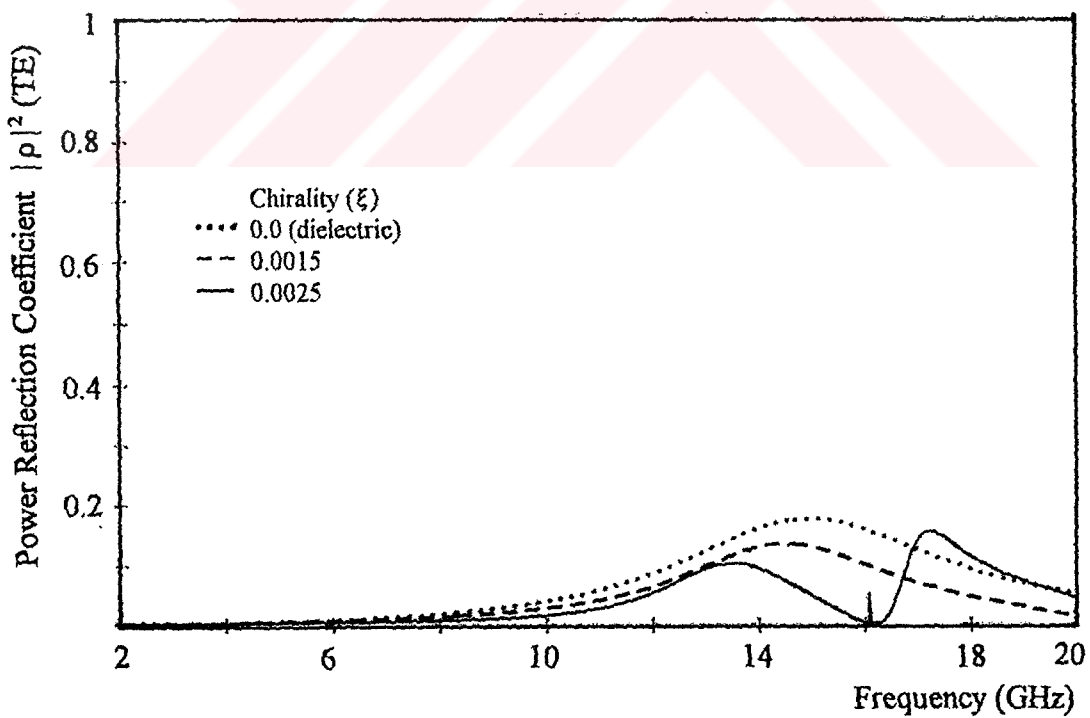
b
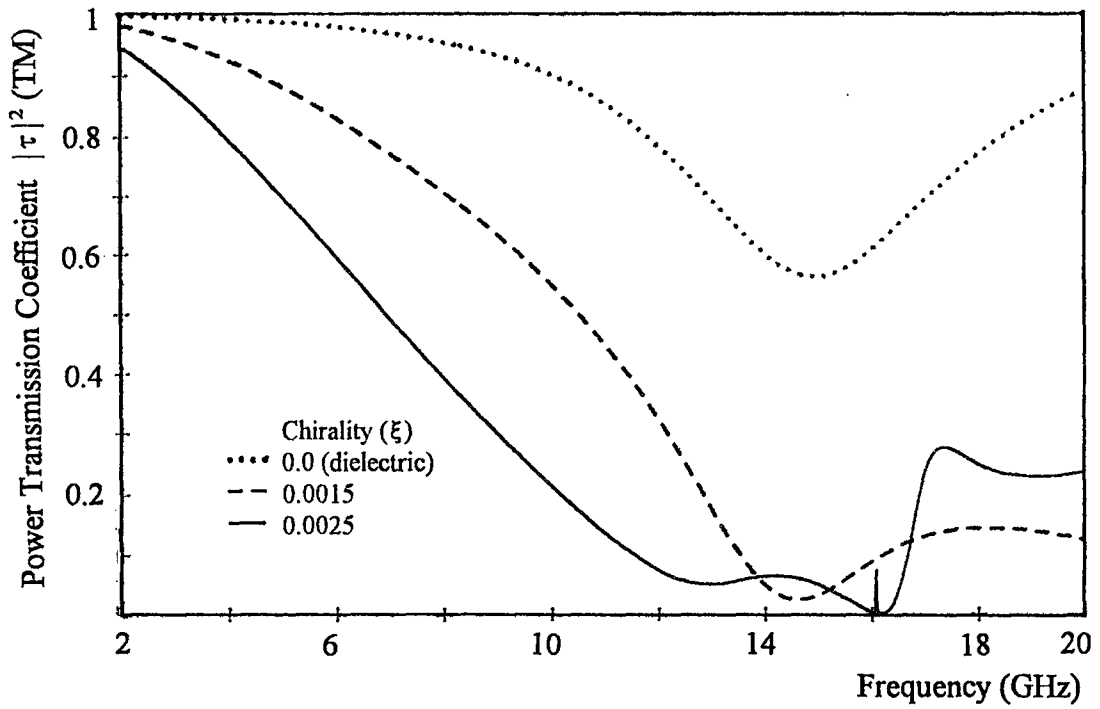
c
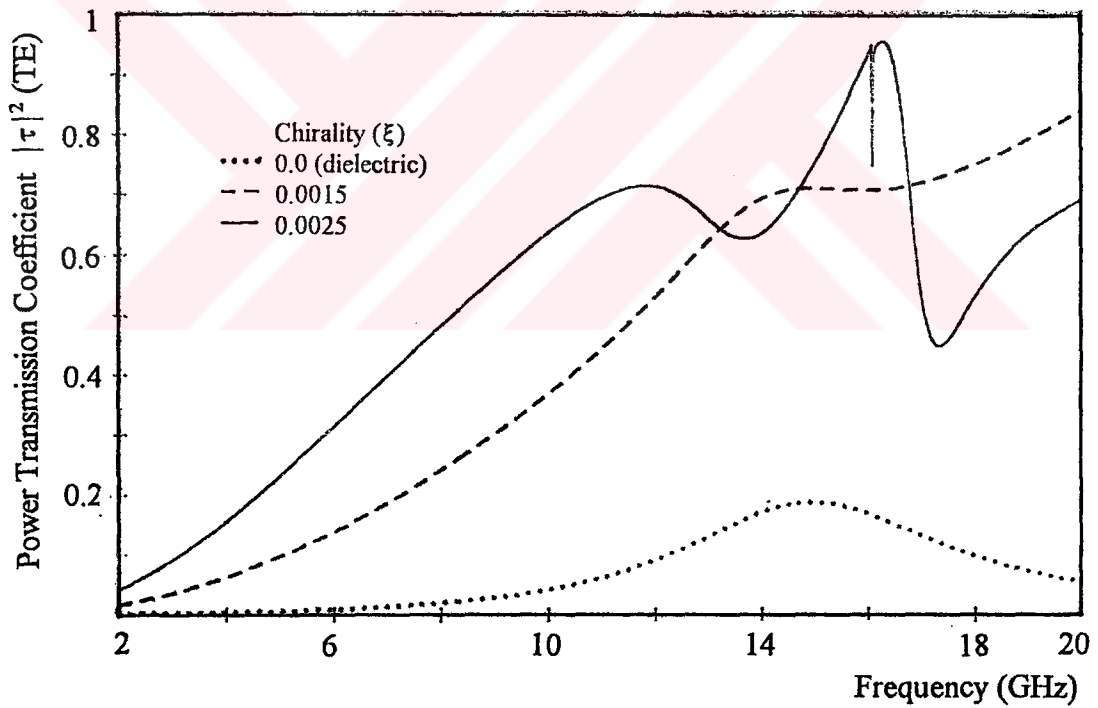
d
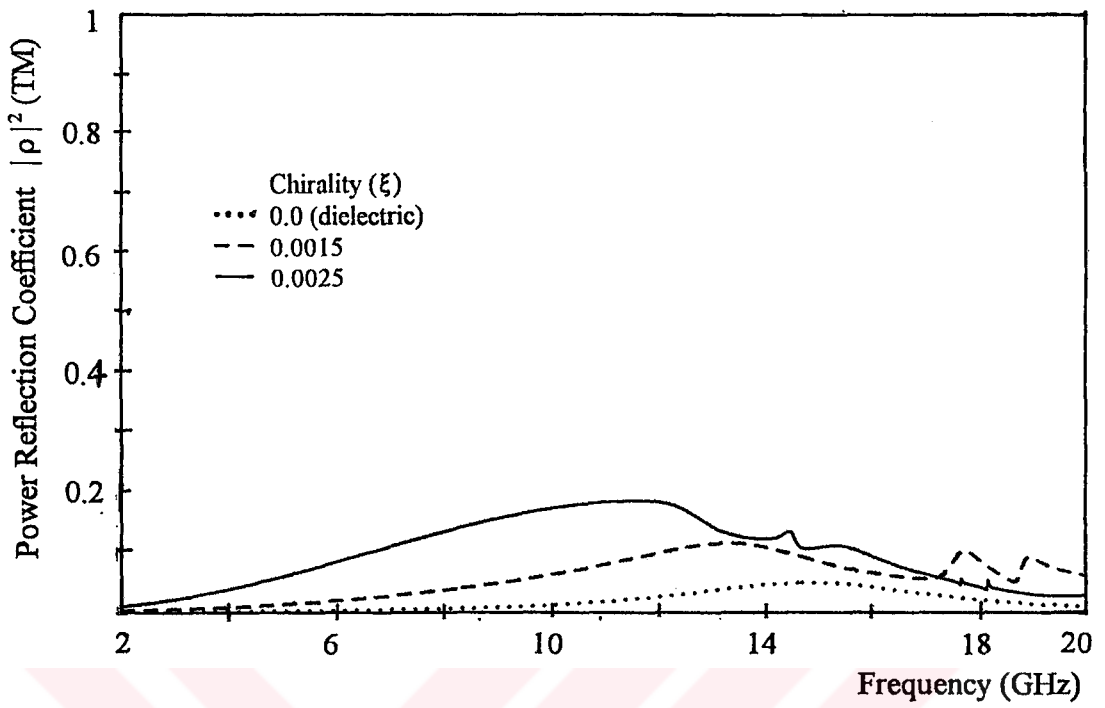
Figure 4.1.15   Spectral characteristics of Chiro-FSS with narrow strips; TM incidence
(ϕ= 30°,θ=0°), square lattice (α= 90°), D_1=D_2=10 mm, L=9.2 mm, W=1
mm, ϵ_r=1.06, t = 5mm. a) Power reflection coefficient (TM), b) Power
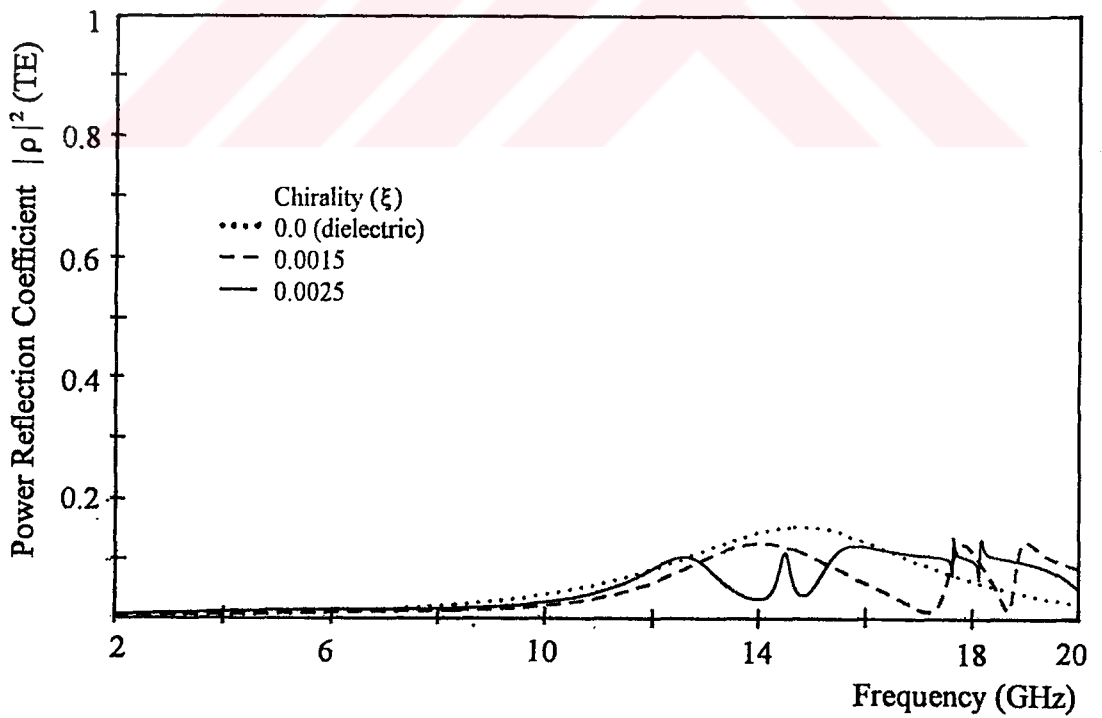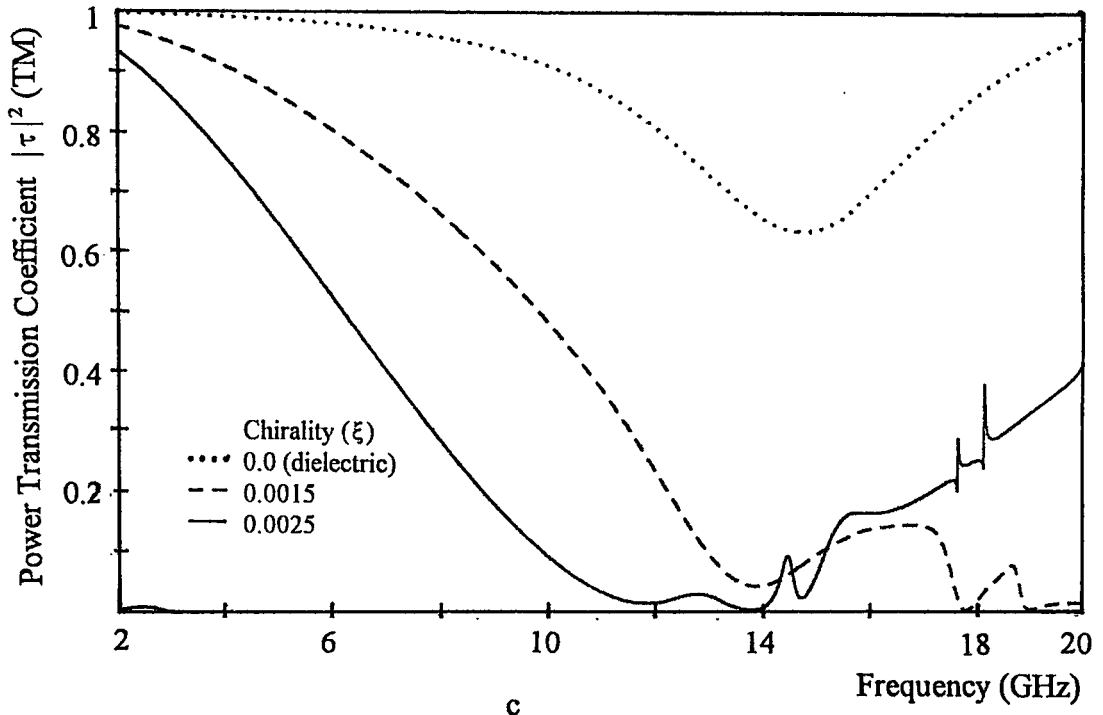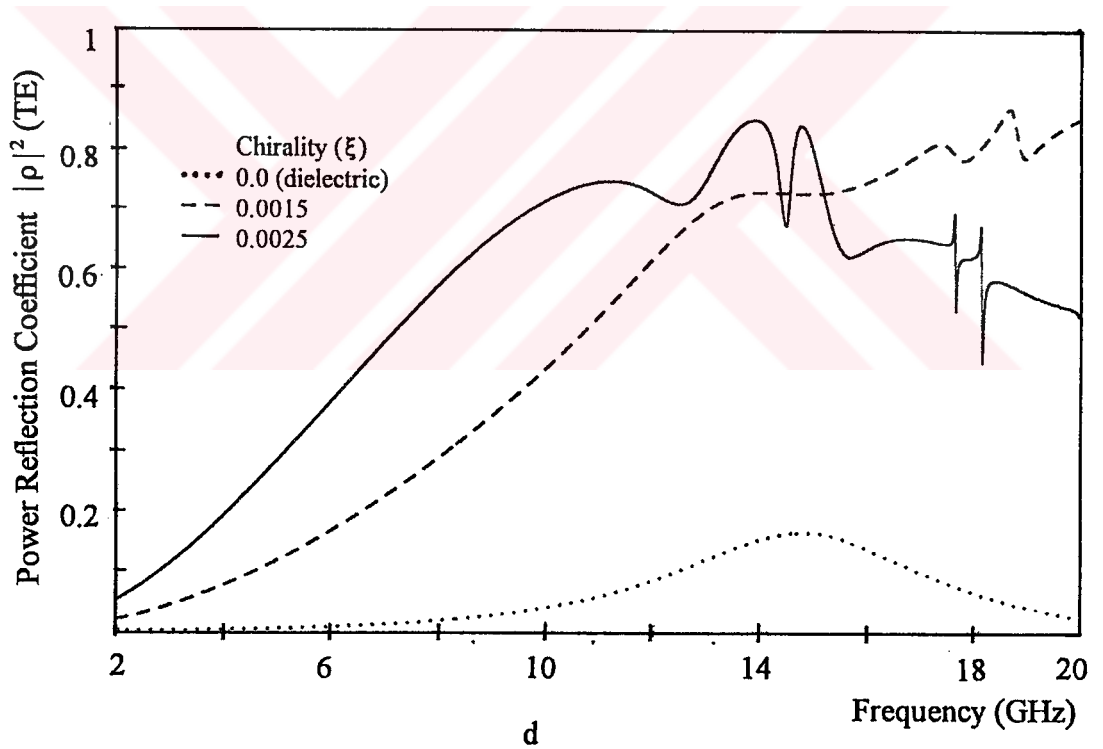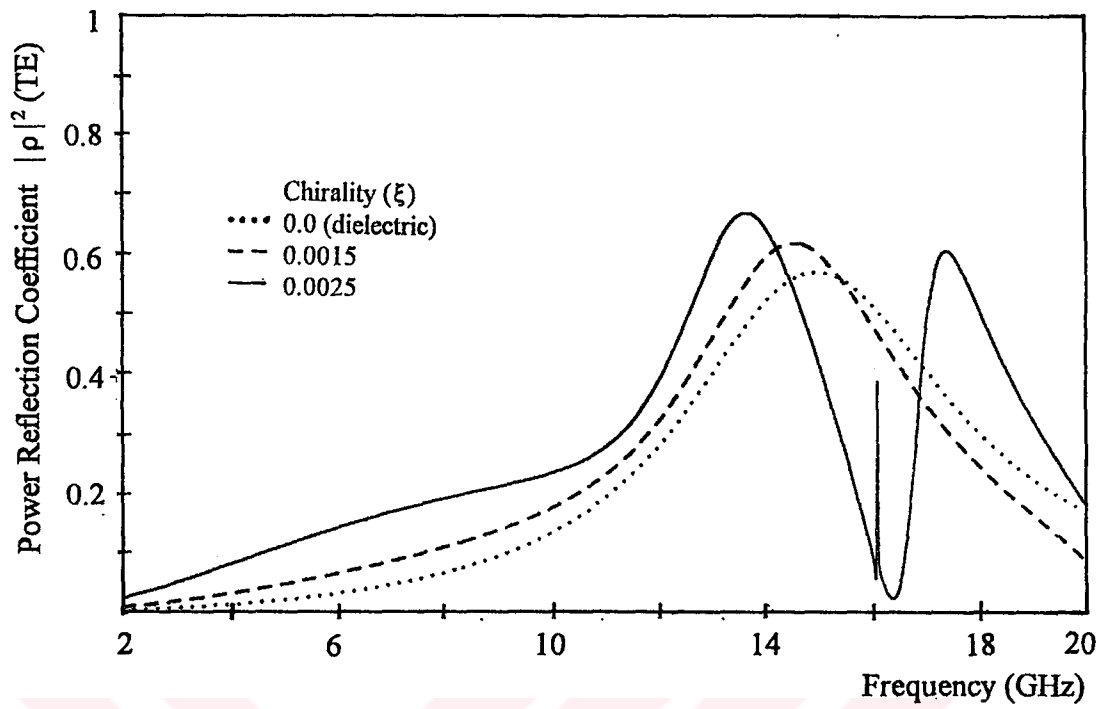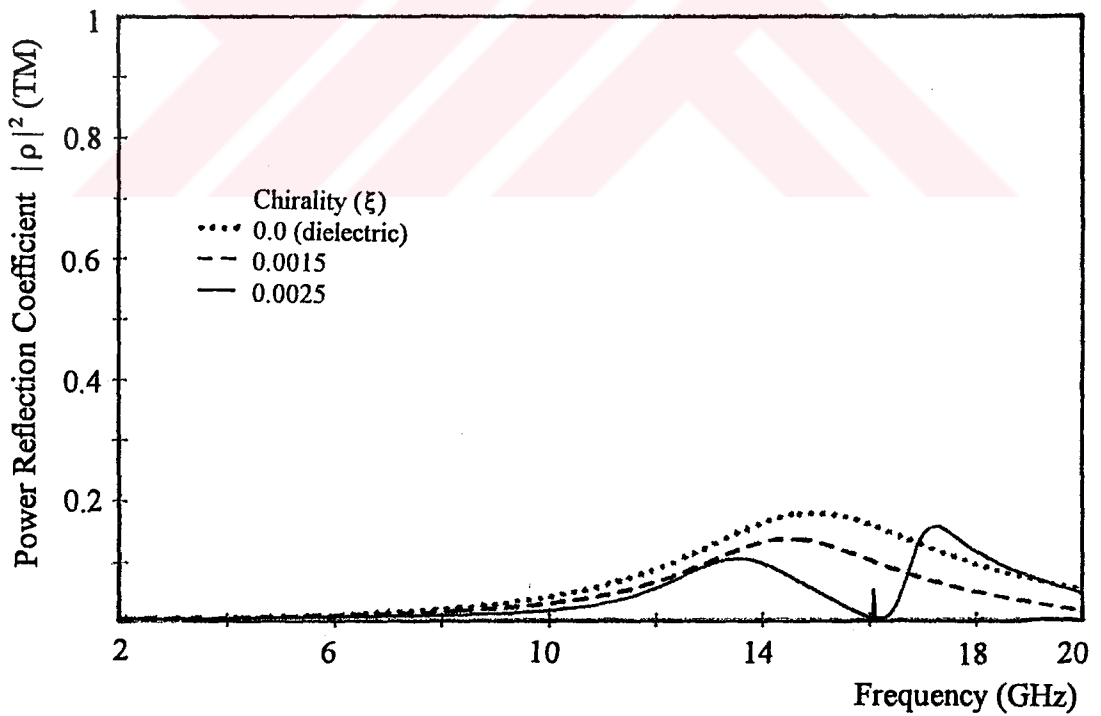transmission coefficient (TE), c) Power transmission coefficient (TM).

80

4.2. Chiro-FSS Comprised of Cross Dipoles

The unit cell geometry of a two frequency selective surface consists of cross dipoles loaded by an isotropic chiral slab is depicted in Figure 4.2.1.
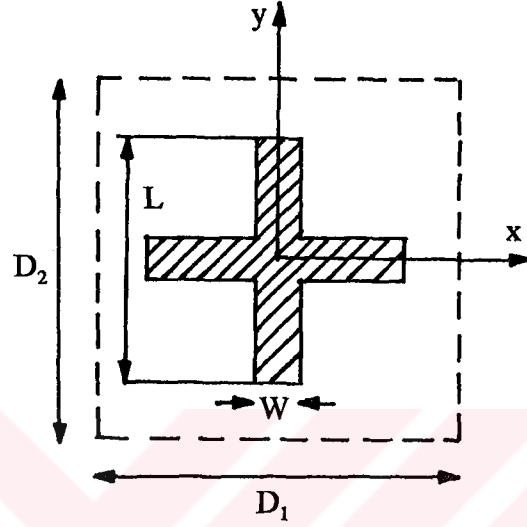
Figure 4.2.1   Unit cell geometry of Chiro-FSS with cross dipoles

The geometry suggests to treat seperately its two arms introducing two vector basis functions with two different domain. The unknown current density induced on a cross dipole can be expressed as,

$$\vec{J}(x',y') = \sum_{n=1}^{N} a_n \, \vec{I}_{nx'}(x',y') + \sum_{k=1}^{K} b_k \, \vec{I}_{ny'}(x',y') \qquad (4\text{-}19)$$

where

$$\vec{I}_{nx'} = \frac{1}{\sqrt{1 - (\frac{2y'}{W})^2}} \begin{bmatrix} \cos \\ \sin \end{bmatrix} (\frac{n\pi x'}{L}) \, \vec{a}_{x'} \qquad \begin{bmatrix} n & odd \\ n & even \end{bmatrix} \qquad (4\text{-}20)$$

and

$$\vec{I}_{ny'} = \frac{1}{\sqrt{1 - (\frac{2x'}{W})^2}} \begin{bmatrix} \cos \\ \sin \end{bmatrix} (\frac{k\pi y'}{L}) \, \vec{a}_{y'} \qquad \begin{bmatrix} k & odd \\ k & even \end{bmatrix} \qquad (4\text{-}21)$$

where a_n and b_k are the undetermined coefficients.

After changing the variables of integration, the inner products are evaluated as,

x'-directed current :

For cosine (symmetrical) terms,

$$\vec{I}_{nx'} = \frac{1}{\sqrt{1 - (\frac{2y'}{W})^2}} \cos (\frac{n\pi x'}{L}) \, \vec{a}_{x'} \qquad n = 1,3,5.. \quad (\, n \quad odd \,) \qquad (4\text{-}22)$$

the inner products,

$$<\vec{I}_{nx'}, \vec{\Psi}_{mpq}^{*}> = \frac{1}{\sqrt{A}} \left[(\cos \gamma \, \vec{a}_x - \sin \gamma \, \vec{a}_y) . \vec{u}_{mpq} \right] \frac{W}{4} \pi L J_0 (\frac{vW}{2}).$$

$$\left[\frac{\sin (\frac{uL}{2} + \frac{n\pi}{2})}{(\frac{uL}{2} + \frac{n\pi}{2})} + \frac{\sin (\frac{uL}{2} - \frac{n\pi}{2})}{(\frac{uL}{2} - \frac{n\pi}{2})} \right] \qquad (4\text{-}23)$$

and

$$<\vec{I}_{nx'}, \vec{\Psi}_{mpq}> = <\vec{I}_{nx'}, \vec{\Psi}_{mpq}^{*}> \qquad (4\text{-}24)$$

For sine (asymmetrical) terms,

$$\vec{I}_{nx'} = \frac{1}{\sqrt{1 - (\frac{2y'}{W})^2}} \sin (\frac{n\pi x'}{L}) \, \vec{a}_{x'} \qquad n = 2,4,6.. \quad (\, n \quad even \,) \qquad (4\text{-}25)$$

Corresponding inner products are,

$$<\vec{I}_{nx'}, \Psi_{mpq}^*> = \frac{1}{\sqrt{A}} \left[(\cos \gamma \, \vec{a}_x - \sin \gamma \, \vec{a}_y) \cdot \vec{u}_{mpq} \right] \frac{W}{4} \pi L J_0(\frac{vW}{2}).$$

$$\left[\frac{\sin(\frac{uL}{2} - \frac{n\pi}{2})}{(\frac{uL}{2} - \frac{n\pi}{2})} - \frac{\sin(\frac{uL}{2} + \frac{n\pi}{2})}{(\frac{uL}{2} + \frac{n\pi}{2})} \right] \tag{4-26}$$

and

$$<\vec{I}_{nx'}, \Psi_{mpq}> = -<\vec{I}_{nx'}, \Psi_{mpq}^*> \tag{4-27}$$

y'-directed current:

For cosine (symmetrical) terms,

$$\vec{I}_{ny'} = \frac{1}{\sqrt{1 - (\frac{2x'}{W})^2}} \cos(\frac{n\pi y'}{L}) \vec{a}_{y'}, \qquad n = 1,3,5.. \ (n \quad odd) \tag{4-28}$$

$$<\vec{I}_{ky'}, \Psi_{mpq}^*> = \frac{1}{\sqrt{A}} \left[(\sin \gamma \, \vec{a}_x + \cos \gamma \, \vec{a}_y) \cdot \vec{u}_{mpq} \right] \frac{W}{4} \pi L J_0(\frac{uW}{2}).$$

$$\left[\frac{\sin(\frac{vL}{2} + \frac{k\pi}{2})}{(\frac{vL}{2} + \frac{k\pi}{2})} + \frac{\sin(\frac{vL}{2} - \frac{k\pi}{2})}{(\frac{vL}{2} - \frac{k\pi}{2})} \right] \tag{4-29}$$

and

$$<\vec{I}_{ky'}, \Psi_{mpq}> = <\vec{I}_{ky'}, \Psi_{mpq}^*> \tag{4-30}$$

For sine (asymmetrical) terms,

$$\vec{I}_{ky'} = \frac{1}{\sqrt{1 - (\frac{2x'}{W})^2}} \sin(\frac{n\pi y'}{L}) \vec{a}_{y'}, \qquad n = 2,4,6.. \ (n \quad even) \tag{4-31}$$

83

Corresponding inner products are obtained as,

$$
<\vec{I}_{ky'}, \Psi^*_{mpq}> = \frac{1}{\sqrt{A}} \left[(\sin\gamma\ \vec{a}_x + \cos\gamma\ \vec{a}_y) . \vec{u}_{mpq} \right] \frac{W}{4} \pi L J_0 (\frac{uW}{2}) .
$$

$$
\left[\frac{\sin(\frac{vL}{2} - \frac{k\pi}{2})}{(\frac{vL}{2} - \frac{k\pi}{2})} - \frac{\sin(\frac{vL}{2} + \frac{k\pi}{2})}{(\frac{vL}{2} + \frac{k\pi}{2})} \right] \qquad (4\text{-}32)
$$

and

$$
<\vec{I}_{ky'}, \Psi_{mpq}> = - <\vec{I}_{ky'}, \Psi^*_{mpq}> \qquad (4\text{-}33)
$$

4.2.1. Numerical Results of the Chiro-FSS with Cross Dipoles.

The cross dipoles are commonly used as the scatterers for frequency selective surfaces. Simply a cross dipole is comprised of two narrow strips that are junctioned at their centers with an angle of 90°. The Chiro-FSS considered in this section, comprised of two dimensional infinite arrays of perfectly conducting cross dipoles loaded by an isotropic chiral slab. The numerical results of spectral characteristics of the Chiro-FSS for various type geometry are presented.

First example of the Chiro-FSS with cross dipoles is assumed to have the following design paramaters; The cross diploes have a length of 9.2 mm and a width of 1 mm, arranged in a square lattice having the dimensions of $D_1 = D_2 = 10$ mm. The chiral slab is used to support the perfectly conducting cross dipoles has a thickness of 5 mm and dielectric constant 1.06. Figure 4.2.2 is the plot of variations of reflection and transmission coefficients with frequency for the Chiro-FSS which is illuminated by a normally incident plane wave of TE ploarisation. The figure is obtained for four different

84

values of chirality admittance of the slab, $\xi = 0.0$ (dielecteric), 0.0005, 0.0015 and 0.0025 mho. Similar to the characteristics obtained for Chiro-FSS with narrow strips, for small value of chirality admittance, the spectral response of the Chiro-FSS with cross diploes is nearly same as the spectral characteristics of the conventional FSS (zero chirality). When the chirality admittance is further increased to $\xi = 0.0015$ and 0.0025 mho, two and four resonances (full reflection) are obtained in the reflection characteristics, respectively. Transmission characteristics of both co- (TE) and cross-polar (TM) components are also changed drastically as the chirality admittance is increased. As seen in Figure 4.2.2 , it is possible to obtain almost full transmission for the cross-polar (TM) component for $\xi = 0.0015$ and 0.0025 mho.

When the thickness of the chiral slab is decreased from 5 mm to 4 mm, the variations in the spectral characteristic can be seen by comparing the Figure 4.2.2 with Figure 4.2.3. Figure 4.2.3 represents the reflection and transmission characteristics of the Chiro-FSS having same design parameters as in Figure 4.2.2, except thickness.It can be seen that, in this case (t = 4 mm), less resonances with wider bandwidth compared with the previous case are obtained. The isolation of the resonances obtained are not good in the second case. A remarkable change in the magnitude of the cross-polar transmission coefficient observed only for $\xi = 0.0025$ mho as can be seen from Figure 4.2.3.

The effect of incresing the dielectric constant of the slab to $\epsilon_r = 1.32$, on the reflection and transmission curve of the Chiro-FSS designed with same parameters as is Figure 4.2.2, can be seen in Figure 4.2.4. The figure is obtained for $\xi = 0.0$, 0.0015 and 0.0025 mho. Comparison of these figures gives that the general characteristics of the spectral response of the Chiro-FSS are similar to each other, but the resonance frequencies of all resonances are shifted towards to the lower frequencies. Another cahange observed in the co-polar (TE) transmission characteristics is that exactly full transmission is obtained in the case of $\epsilon_r = 1.32$. When the thickness of the chiral slab is reduced from t = 5 mm to t = 4 mm while keeping the dielectric constant $\epsilon_r = 1.32$, the spectral characteristics obtained for this case versus frequency is shown in Figure 4.2.5. If Figure 4.2.4 is compared with Figur 4.2.5, one can see that, one more full reflection is obtained in the former case and the bandwidth of all the resonances associated and resonance frequencies

are smaller than that of the later case.

The second example of a Chiro-FSS is comprised of cross dipoles have the length of L = 8 mm and a width of W=1 mm printed on an isotropic 5 mm thick chiral slab. Dielectric constant of the slab is assumed as ϵ_r =1.05. Note that the length of the cross dipoles are smaller that the length of the cross dipoles used in the first example and in both cases the cross diploes are arranged in a square lattice geometry, D_1= D_2= 10 mm, α=90°. Figure 4.2.6 are the plot of magnitude of reflection and transmission coefficients of the Chiro-FSS versus frequency, when the screen is illuminated by a plane wave with TE polarisation of normal incidende. One can notice that, two main differences are observed, after comparison of Figure 4.2.2 correspons to L=9.2 mm with Figure 4.2.6 corresponds to L=8 mm. They are that, as the dipole length is decreased the resonances occur at higher frequencies, and the second difference, the resonance bandwidths of the smaller dipoles case are narrower than the bandwidth of the resonances obtained in the case of longer dipoles. Similar effects are also observed in the reflection and transmission characteristics when the thickness of the chiral slab is reduced from t=5 mm to t= 4 mm as shown in Figure 4.2.7.

The third Chiro-FSS configuration is choosen such that the cross dipoles having a length of L=9.2 mm and a width of W=1 mm are arranged in a triangular lattice geometry, i.e. α=60°. The periodicities along the η_1 and η_2 axes are D_1= D_2= 10 mm. The cross dipoles are supproted by a 5 mm thick isotropic chiral slab having a dielectric constant of ϵ_r =1.06. The numerical results obatined for this configuration are shown in Figure 4.2.8 for normally incident TE plane wave excitation. Note that in this configurarion (triangular lattice) the cross dipoles are closely packed compared with the square lattice geometry.

Arranging the cross dipoles in the triangular lattice geometry, modifies the reflection and transmission performance of the Chiro-FSS radically. As can be seen from Figure 4.2.8 the frequency of the resonances obtained are shifted to higher frequencies for all valeu chirality admittance, ξ=0.0, 0.0015 and 0.0025 mho.The bandwidths of the resonances are larger for triangular lattice geometry. Another interesting change observed in the spectral characteristics is that, the spikes are observed between two

86

adjacent resonances for high vale of chirality admittance. Remember that the similar spikes are also obtained in the response of the Chiro-FSS comprised of narrow strips.

Similar effects in the spectral response of the Chiro-FSS having triangular geometry are also obtained as the previous cases when the thickness of the slab is reduced from t = 5 mm to t = 4 mm as shown in Figure 4.2.9.

Up to here, the numerical results presented are obtained for normally incident plane wave of TE polarisation. Due to symmetry of the cross dipoles, the numerical results corresponding to the normally incident TM excitation are exactly same as the results of the TE case, as expected.

Figure 4.2.10 and Figure 4.2.11 shows the variations of the power reflection and transmission coefficients of the Chiro-FSS versus frequency for illumination of obliquely incident TE and TM polarised plane waves with θ =0°, ϕ =30°. The Chiro-FSS is assumed to has the same design paremeters as in the first example, i.e. L=9.2 mm, W=1 mm, D_1=D_2=10 mm, square lattice (α=90°), ϵ_r =1.06 and t= 5 mm. No cross-polar component is reflected by the Chiro-FSS for both TE and TM case. The reflection and transmission characteristics obtained for both case are very similar to each other, except in the TM case all the resonance frequencies are shifted to lower frequencies very slightly for the values of the chirality admittance of ξ= 0.0015 and 0.0025 mho.

Increasing the azimuth angle (ϕ) from 30° to 45° causes very slight changes in the spectral response of the Chiro-FSS for both TE and TM case. One should notice that, due to symmetry of the cross dipole with respect to the azimuth angle, exactly same responses are obtained for both TE and TM case. The plots of spectral response of the Chiro-FSS obtained for these conditons is given in Figure 4.2.13.

Figure 4.2.13 and Figure 4.2.14 shows the power reflection and transmission characteristics of the same Chiro-FSS illuminated by obliquely incident TE and TM plane wave (θ =30°, ϕ =0°), respectively. In both TE and TM case neither full reflection nor full transmission are obtained. Note that, the magnitude of the co-polar reflection coefficient are relatively higher than that of the TM illumination case for non-zero chirality admittance.

The last example is the reflection and transmission characteristics of the Chiro-FSS subjected to the oblique incidence (θ =30°, ϕ =45°) . The power reflection and transmission coefficients versus frequency are plotted in Figure 4.2.15 and Figure 4.2.16 for TE and TM case respectively. In both case, cross-polar reflection coeffient are very small compraing with the magnitude of the co-polar one. The resonances (full reflection) obtained in the TM case have narower bandwidth than the bandwidth of the resonances in TE case for all values of the chirality admittance, ξ= 0.0, 0.0015 and 0.0025 mho. Although there are many resonances obtained in both TE and TM case, only one resonance occurs at the same frequency for ξ=0.0025. Co-polar transmission characteristcs are very similar for ξ=0.0015 and 0.0025 mho. But its magnitue is relatively small when compared with the cross-polar component.

According to the results obtained, the spectral characteristics of the Chiro-FSS comprised of two dimensional infinite periodic array of cross dipoles printed on an isotropic chiral slab can be summarized as;

- When a FSS comprised of cross dipoles is loaded by an isotropic chiral slab, depending on the value of the chirality admittance more than one resonance can be obtained at normal incidence. Due to symmetry of the cross dipole, for normal incidece the Chiro-FSS with cross dipoles exhibits same spectral responses for TE and TM polarised plane wave.

- The number of resonances also strongly depend on the thickness and dielectric constant of the chiral slab, as well as the value of the chirality admittance.

- The bandwidth of the resonances are affected by the size of the cross dipoles and chirality admittance of the slab. Shortening the length of the dipoles decreases the bandwith of the resonances. One should notice that, any change in the size of the cross dipoles alter the all resonance frequencies whereas the change in chirality admittance does not affect the first resonance frequency.

- Use of triangular lattice geometry instead of square lattice changes the spectral response of the Chiro-FSS drastically. In the triangular lattice geometry the crosses are more coupled than the square lattice geometry and hence the periodic screen resonates at higher frequencies and bandwidth of the resonances are larger.

- The spectral response of the Chiro-FSS with cross dipoles is affected very slightly by the variation of the azimuth angle of the incident plane wave of TE and TM polarisation. For the oblique incidence case having zero polar angle (θ) cross polar components does not arises as in the normal incidence case.

- Variation of polar angle of the incident plane wave of TE and TM polarisation causes great changes in the spectral response of the Chiro-FSS. Whereas the cross-polar component of the reflected wave arise as the polar angle increaes, it is still relatively small comparing with the magnitude of the co-polar component reflected.
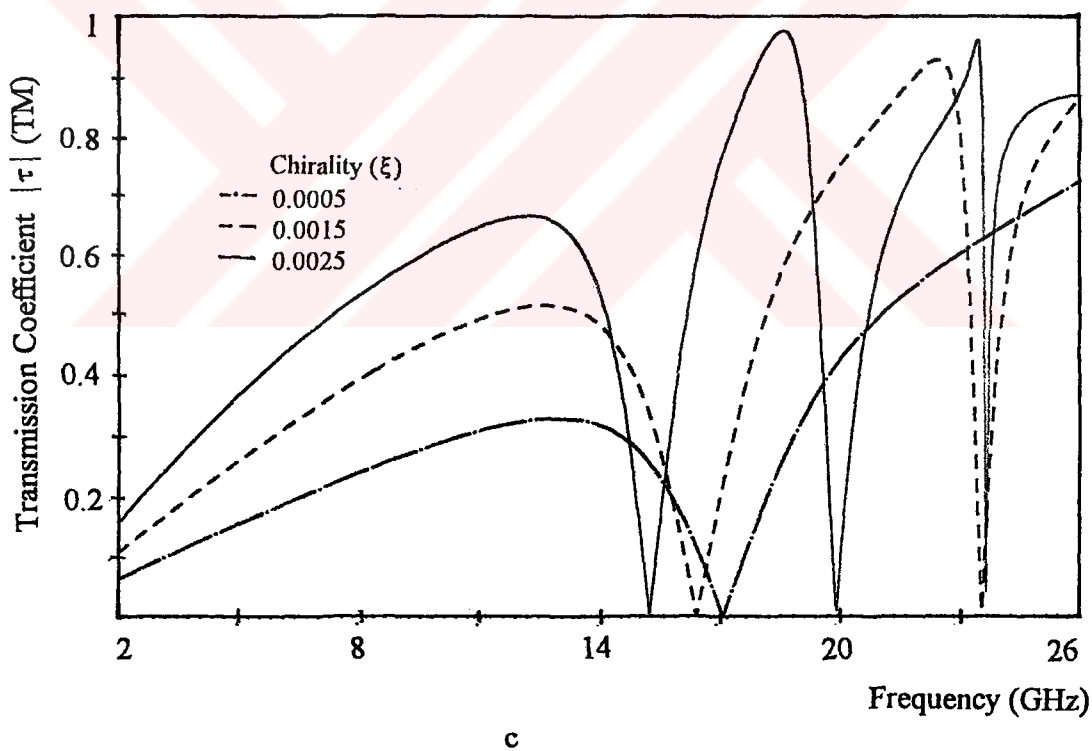
a

b

90
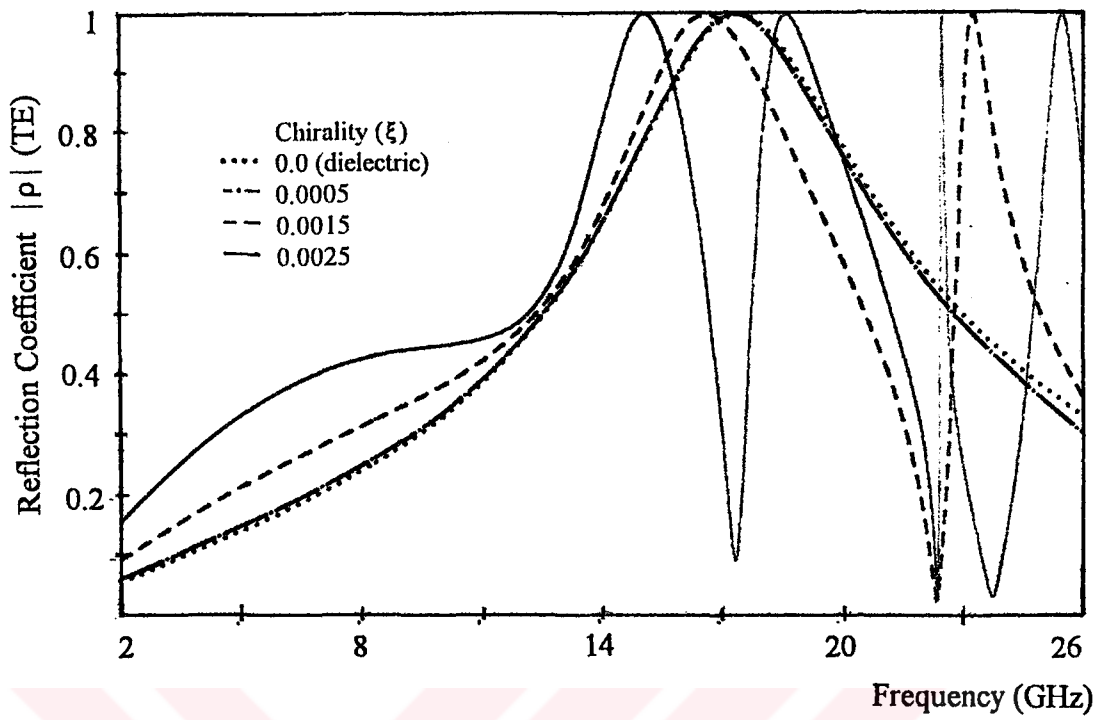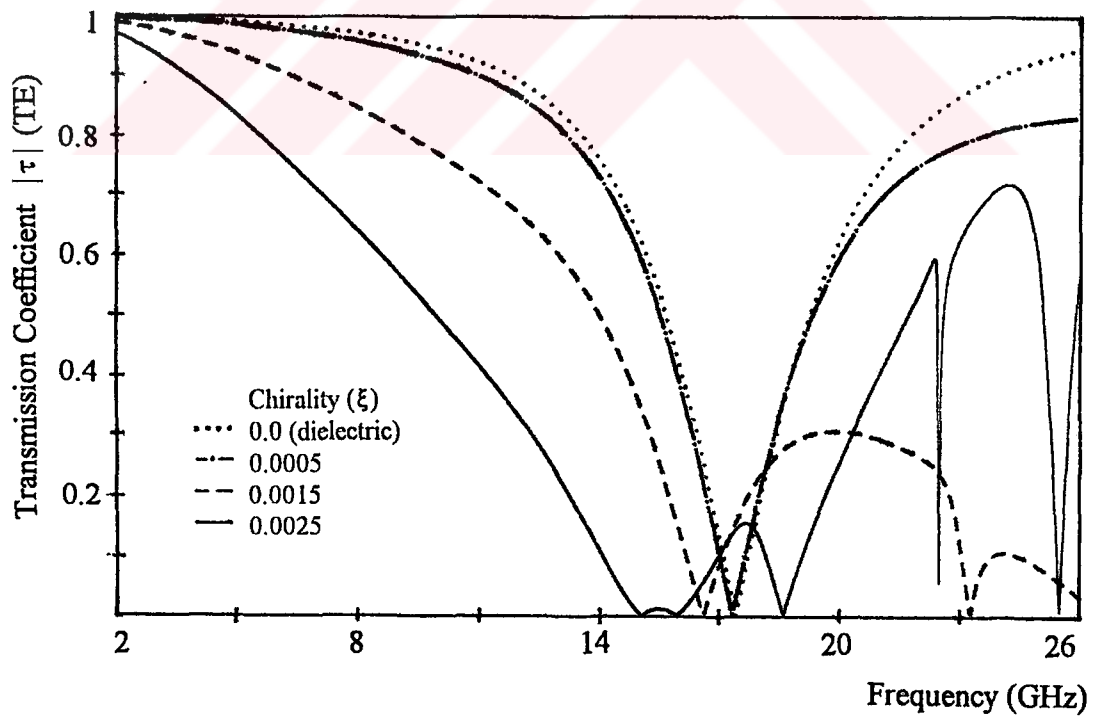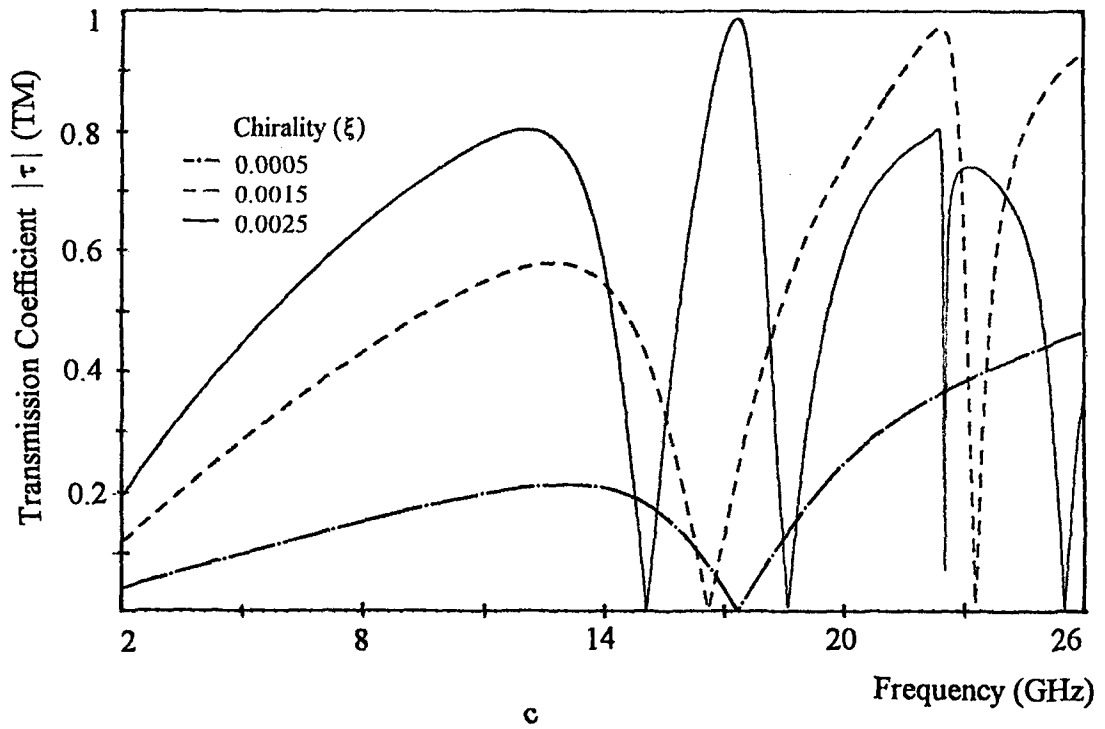
Figure 4.2.2   Spectral characteristics of Chiro-FSS with cross dipoles; TE incidence
($\phi = 0°$, $\theta = 0°$), square lattice ($\alpha = 90°$), $D_1 = D_2 = 9.2$ mm, L=8 mm, W=1
mm, $\epsilon_r = 1.06$, t =5 mm. a) Reflection coefficient (TE), b) Transmission
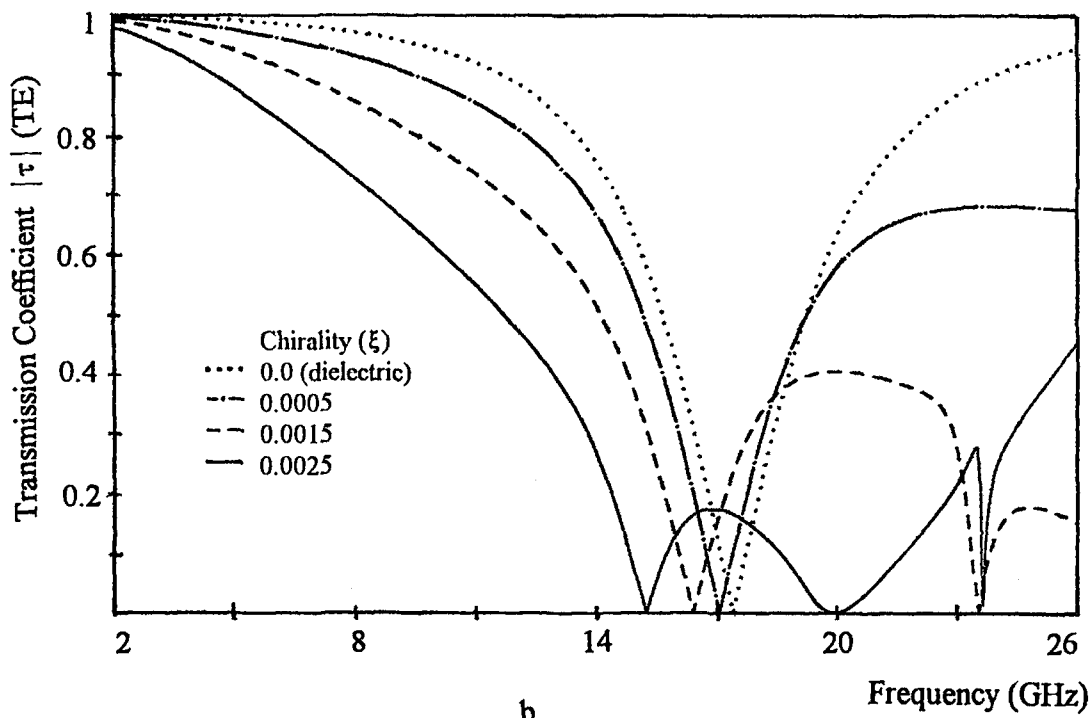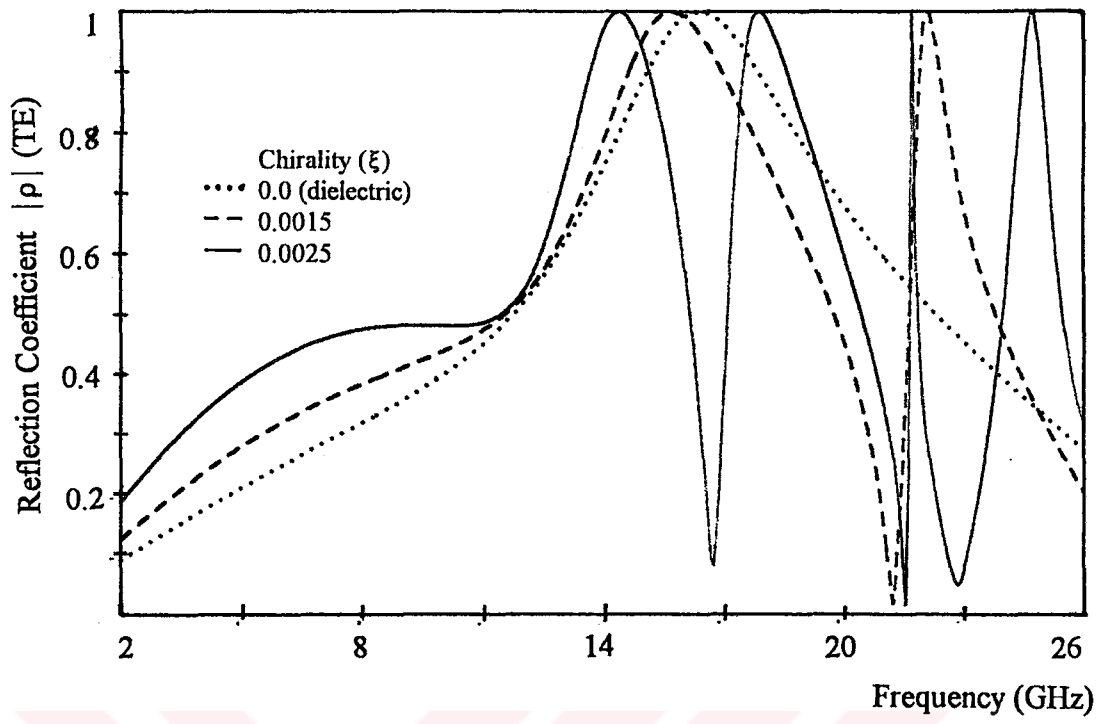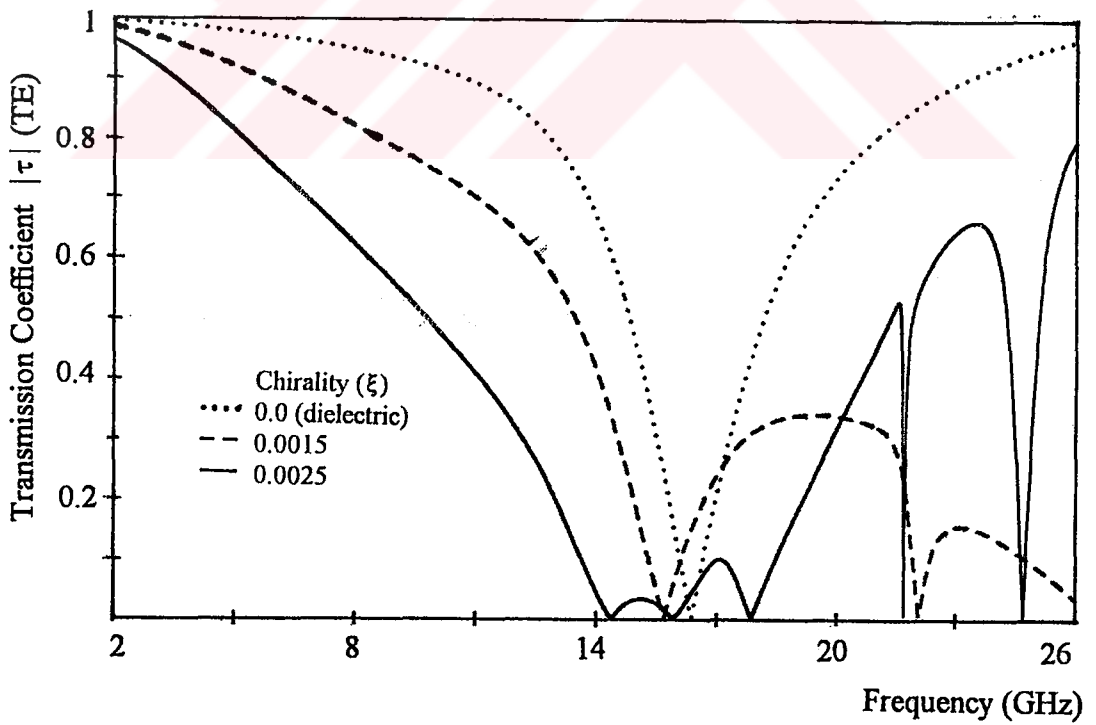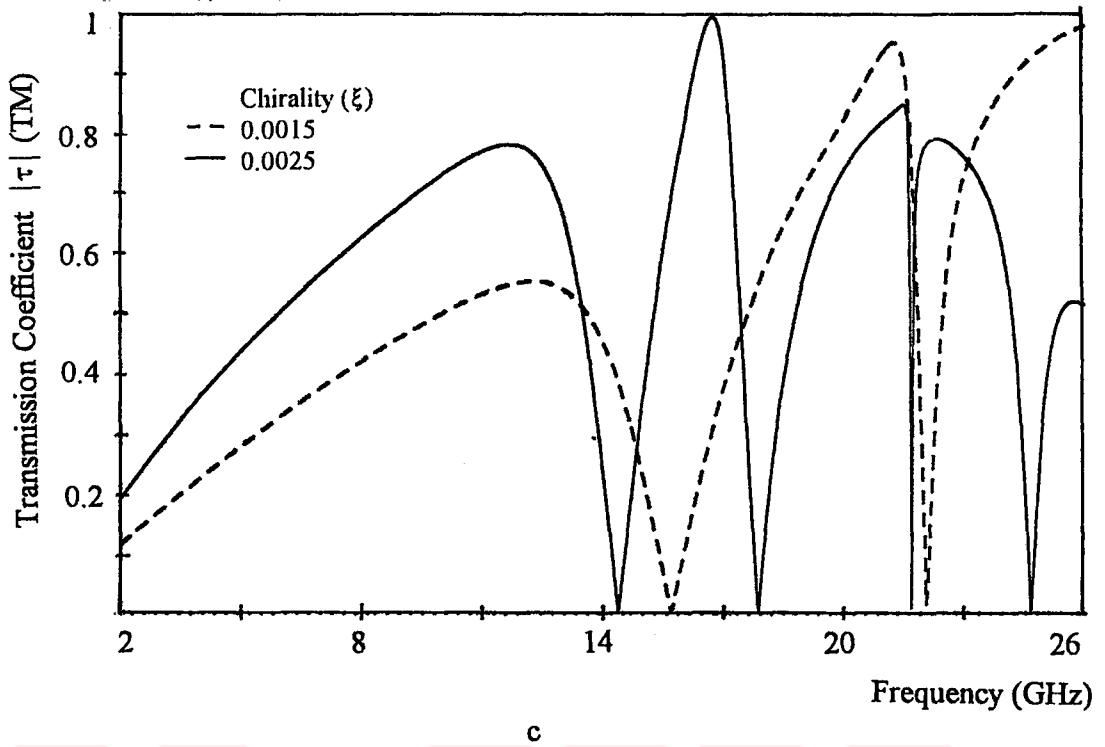coefficient (TE), c) Transmission coefficient (TM).
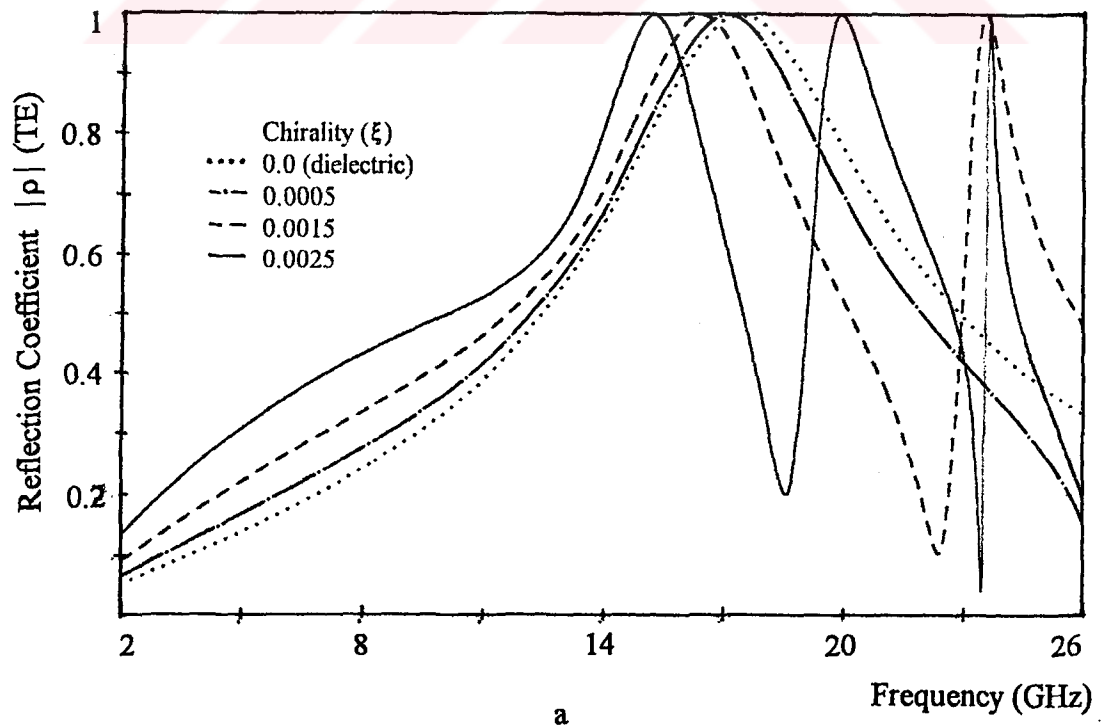
Figure 4.2.3   Spectral characteristics of Chiro-FSS with cross dipoles; TE incidence
(ϕ= 0°, θ=0°), square lattice (α= 90°), D_1=D_2=9.2 mm, L=8 mm, W=1
mm, ϵ_r=1.06, t =4 mm. a) Reflection coefficient (TE), b) Transmission
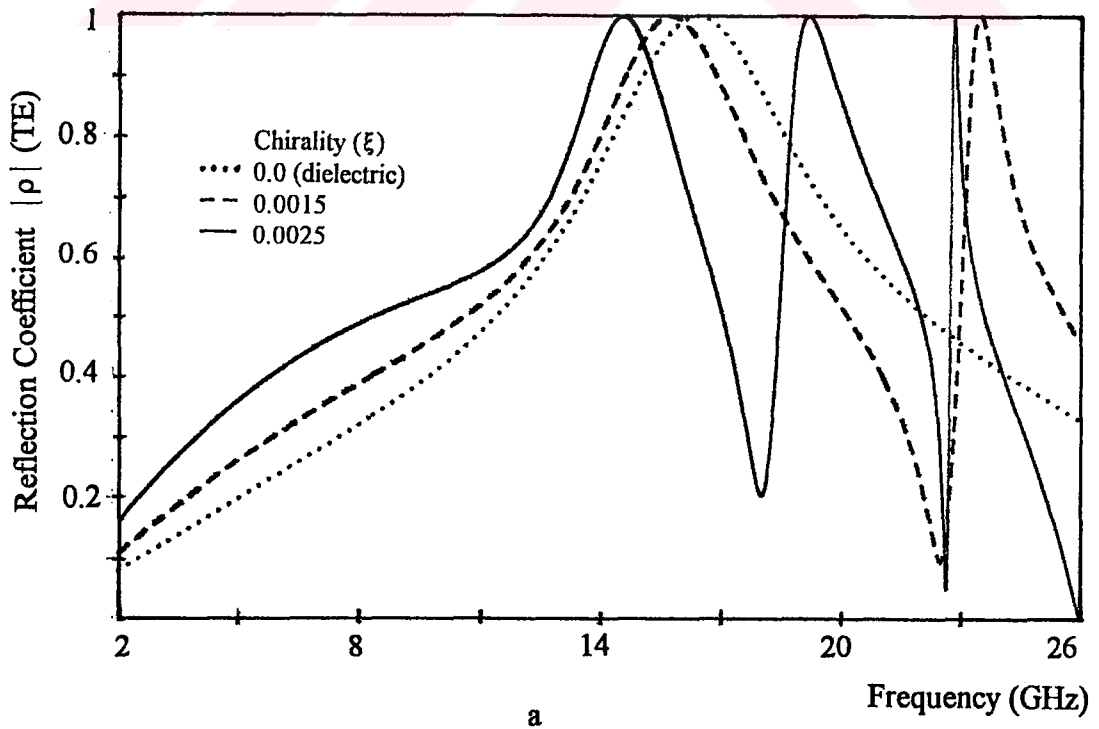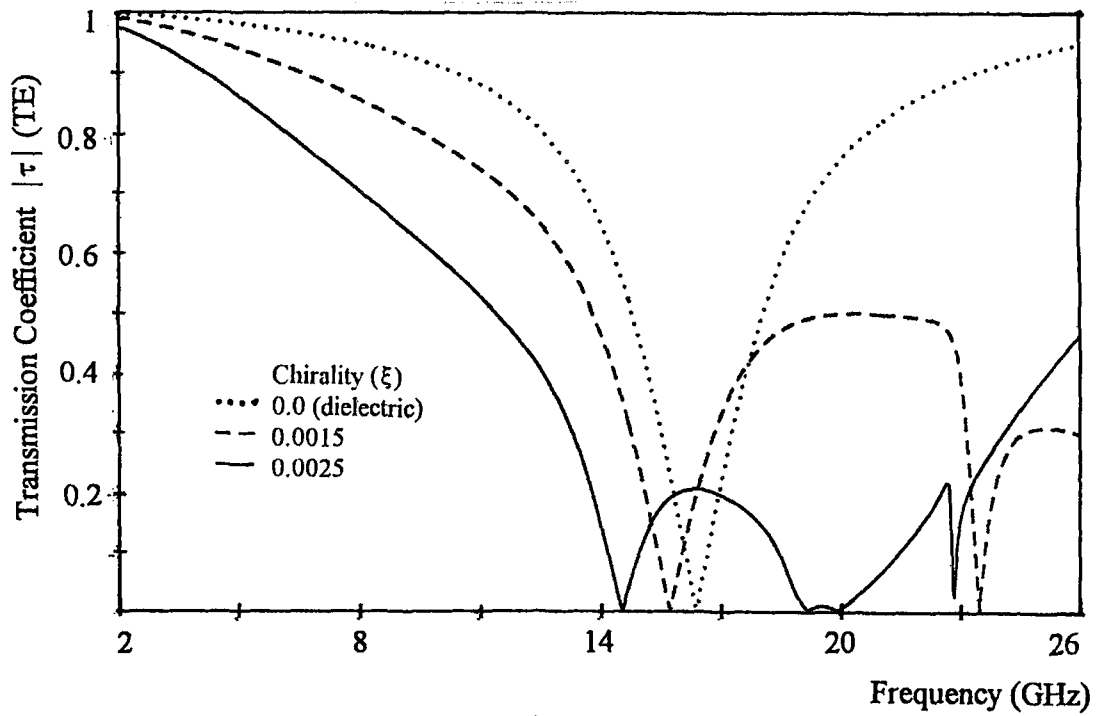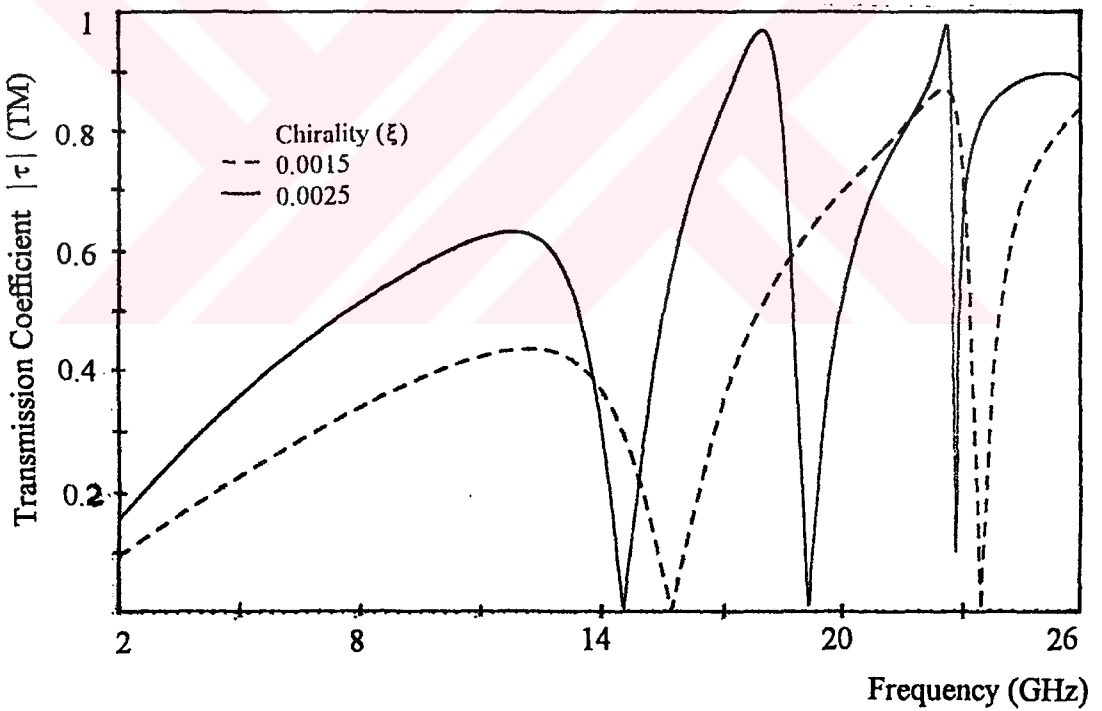coefficient (TE), c) Transmission coefficient (TM).

92

a

b

93

Figure 4.2.4　Spectral characteristics of Chiro-FSS with cross dipoles; TE incidence ($\phi = 0°$, $\theta = 0°$), square lattice ($\alpha = 90°$), $D_1 = D_2 = 9.2$ mm, L=8 mm, W=1 mm, $\epsilon_r = 1.32$, t =5 mm. a) Reflection coefficient (TE), b) Transmission coefficient (TE), c) Transmission coefficient (TM).

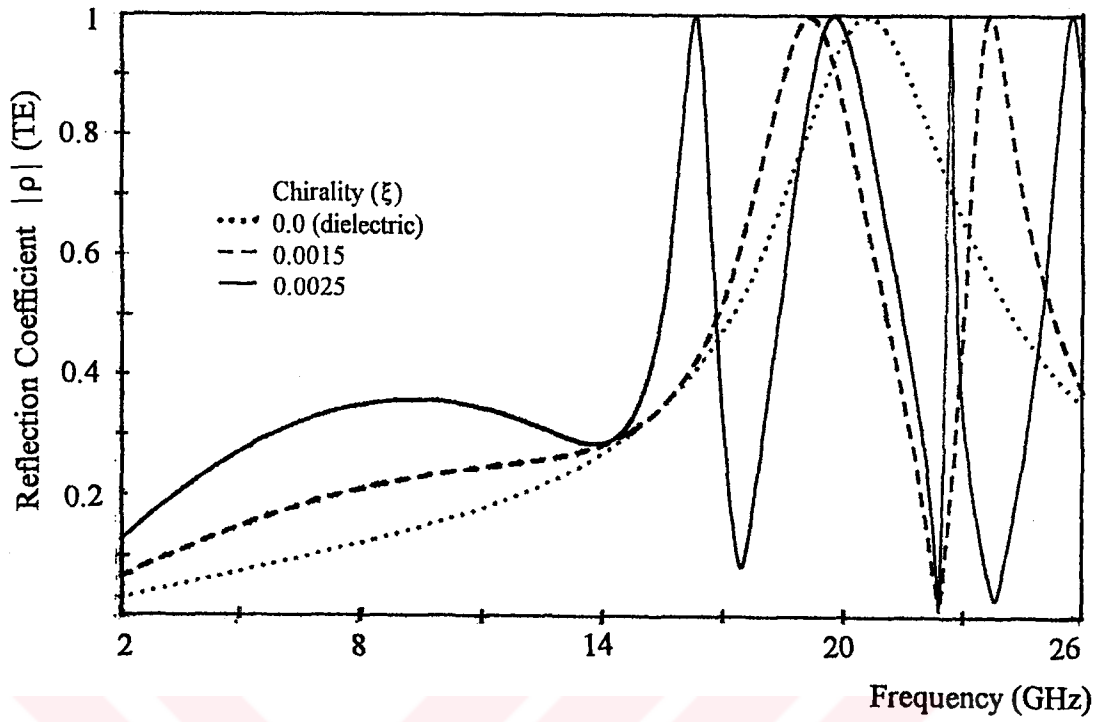94

Figure 4.2.5   Spectral characteristics of Chiro-FSS with cross dipoles; TE incidence
($\phi = 0°$, $\theta = 0°$), square lattice ($\alpha = 90°$), $D_1 = D_2 = 9.2$ mm, L=8 mm, W=1
mm, $\epsilon_r = 1.32$, t =4 mm. a) Reflection coefficient (TE), b) Transmission
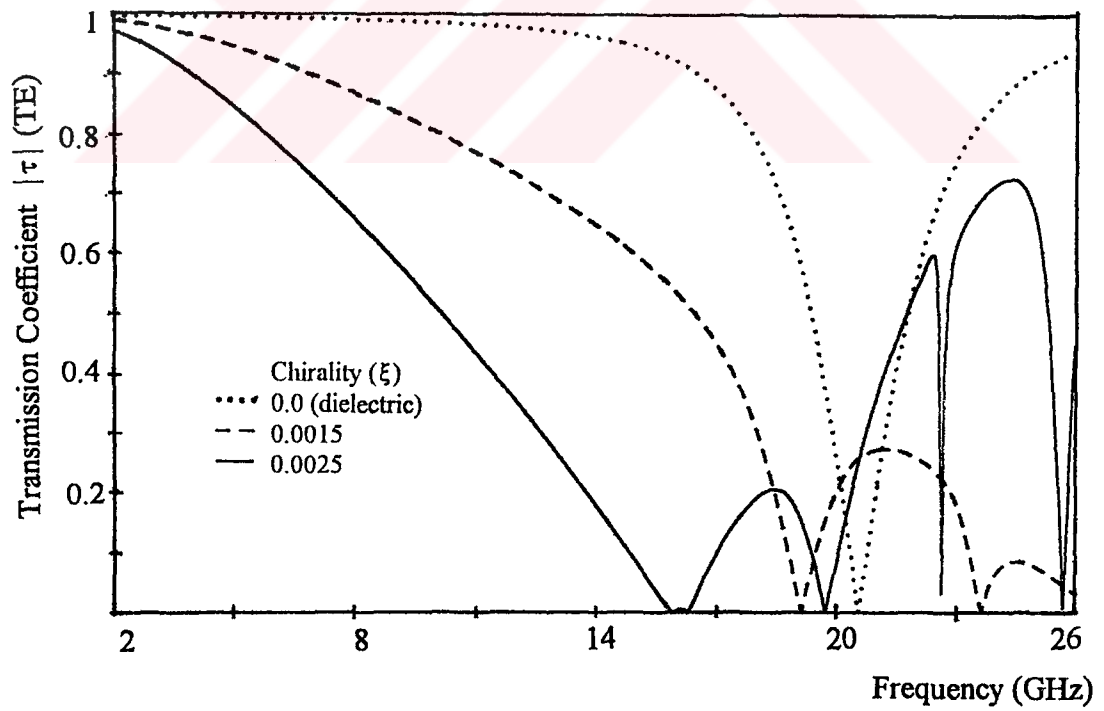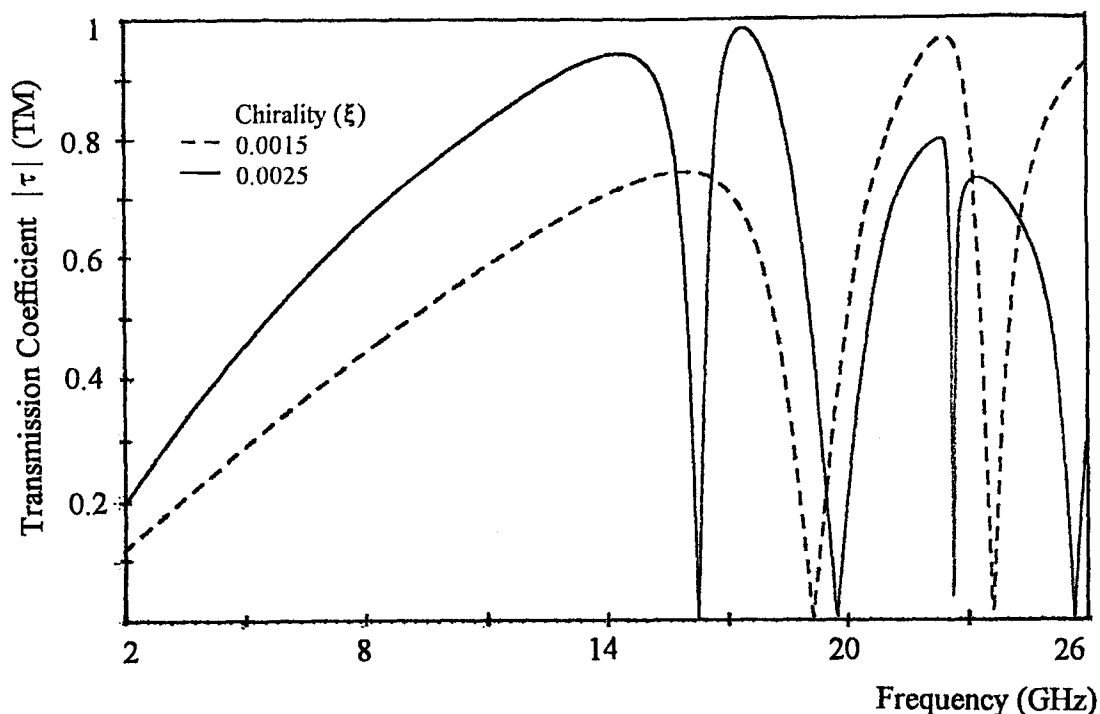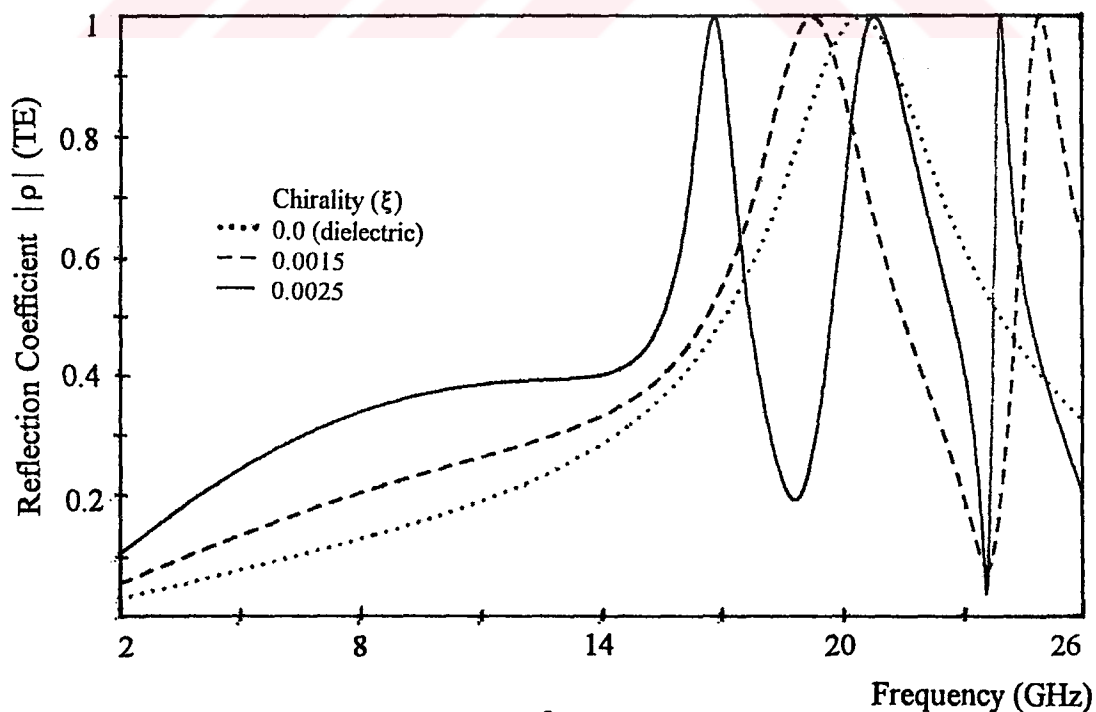coefficient (TE), c) Transmission coefficient (TM).

a

b

96

Figure 4.2.6   Spectral characteristics of Chiro-FSS with cross dipoles; TE incidence
(ϕ= 0°, θ=0°), square lattice (α= 90°), D_1=D_2= 9.2 mm, L= 6.5 mm,
W= 0.7 mm, ϵ_r= 1.06, t = 5 mm. a) Reflection coefficient (TE),
b) Transmission coefficient (TE), c) Transmission coefficient (TM).

Figure 4.2.7 Spectral characteristics of Chiro-FSS with cross dipoles; TE incidence

(ϕ= 0°, θ=0°), square lattice (α= 90°), D_1=D_2= 9.2 mm, L= 6.5 mm,

W= 0.7 mm, ϵ_r= 1.06, t = 4 mm. a) Reflection coefficient (TE),

b) Transmission coefficient (TE), c) Transmission coefficient (TM).

a

b

99

Figure 4.2.8   Spectral characteristics of Chiro-FSS with cross dipoles; TE incidence
(ϕ= 0°, θ=0°), triangular lattice (α= 60°), D_1=D_2=9.2 mm, L=8 mm,
W=1mm, ϵ_r=1.06, t =5 mm. a) Reflection coefficient (TE),
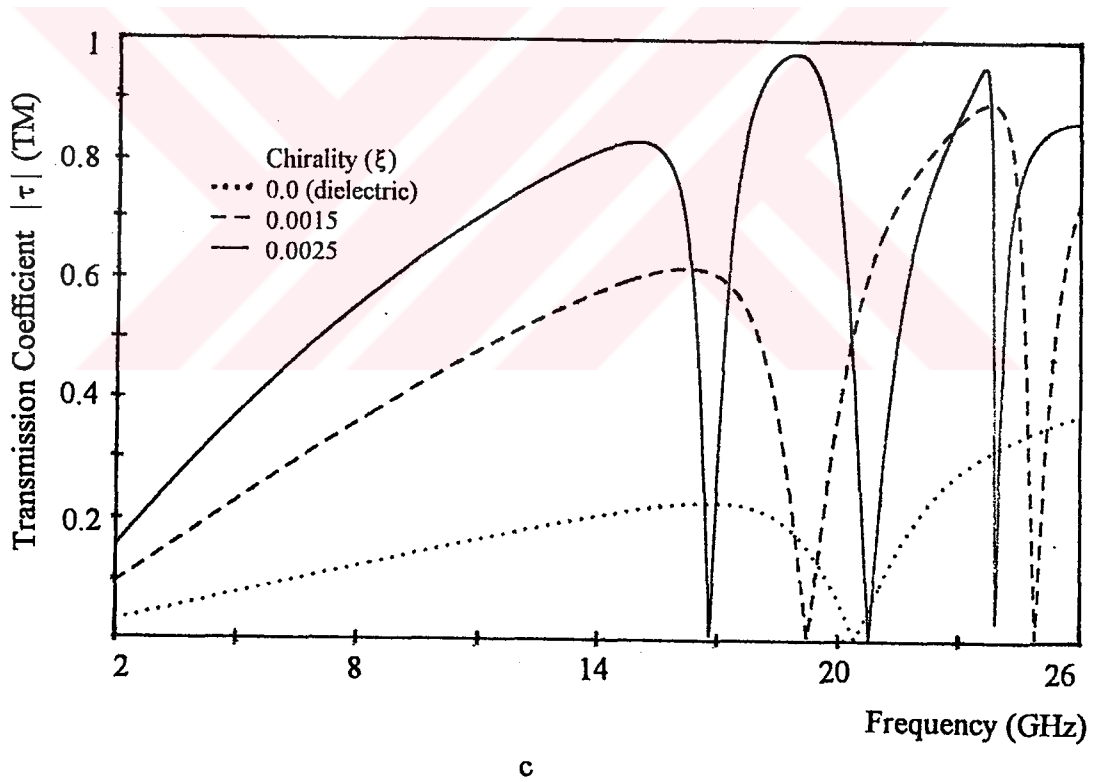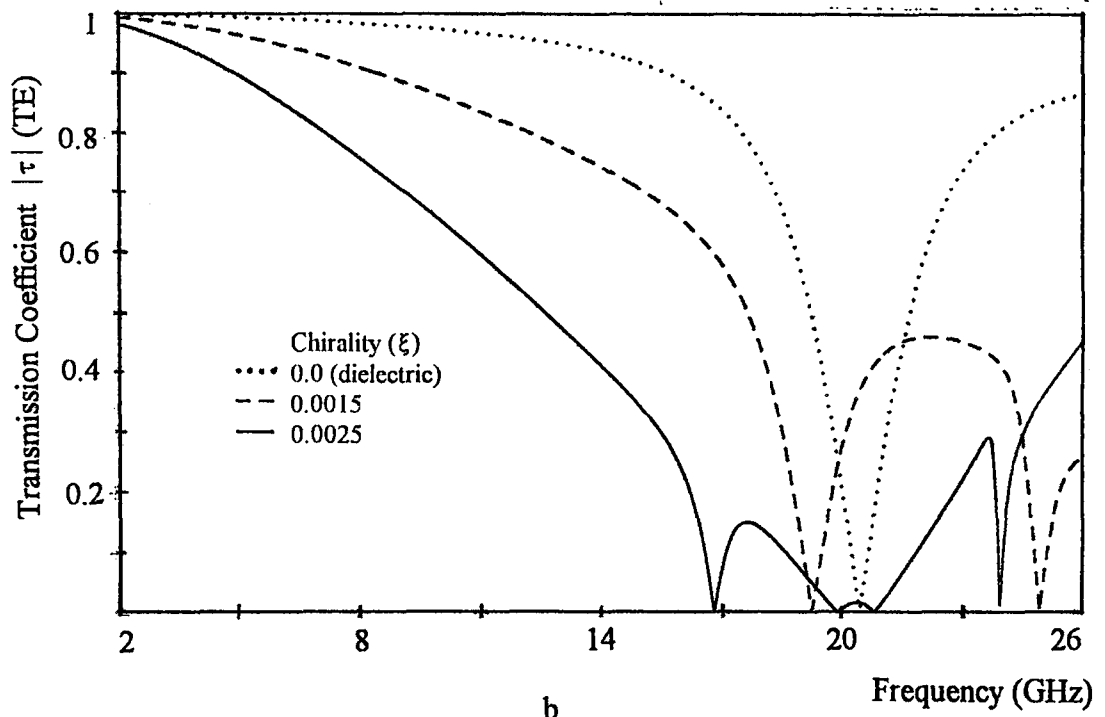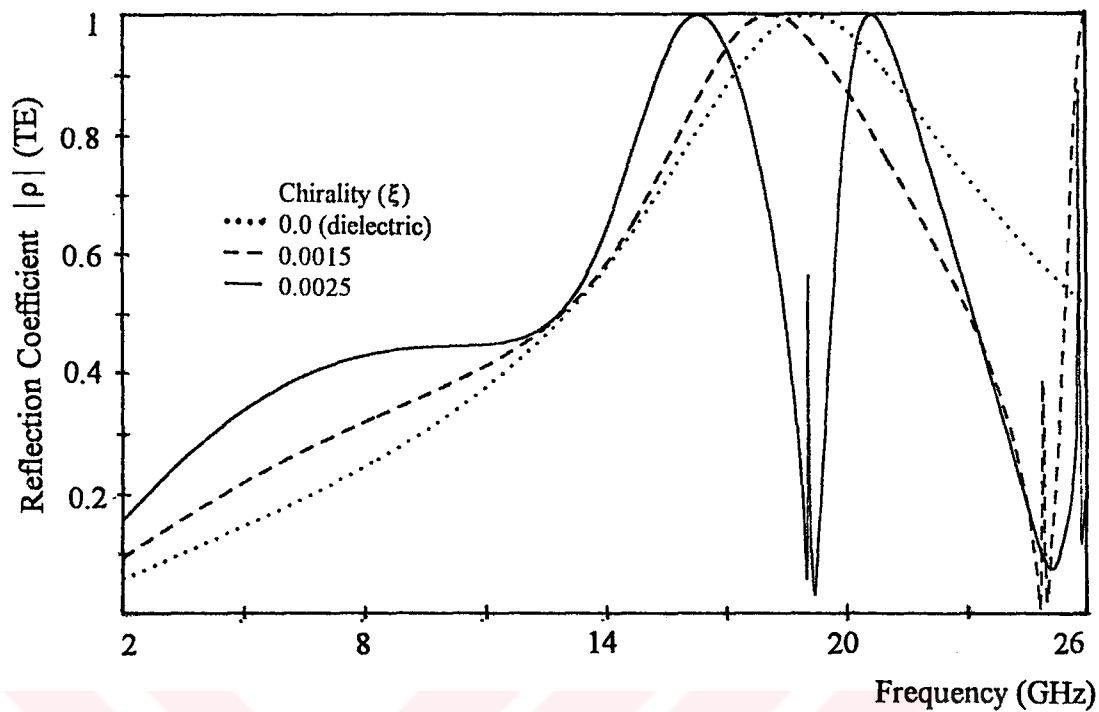b) Transmission coefficient (TE), c) Transmission coefficient (TM).

b

c

Figure 4.2.9 Spectral characteristics of Chiro-FSS with cross dipoles; TE incidence

(ϕ= 0°, θ=0°), triangular lattice (α= 60°), D_1=D_2=9.2 mm, L=8 mm,

W=1mm, ϵ_r=1.06, t =4 mm. a) Reflection coefficient (TE),

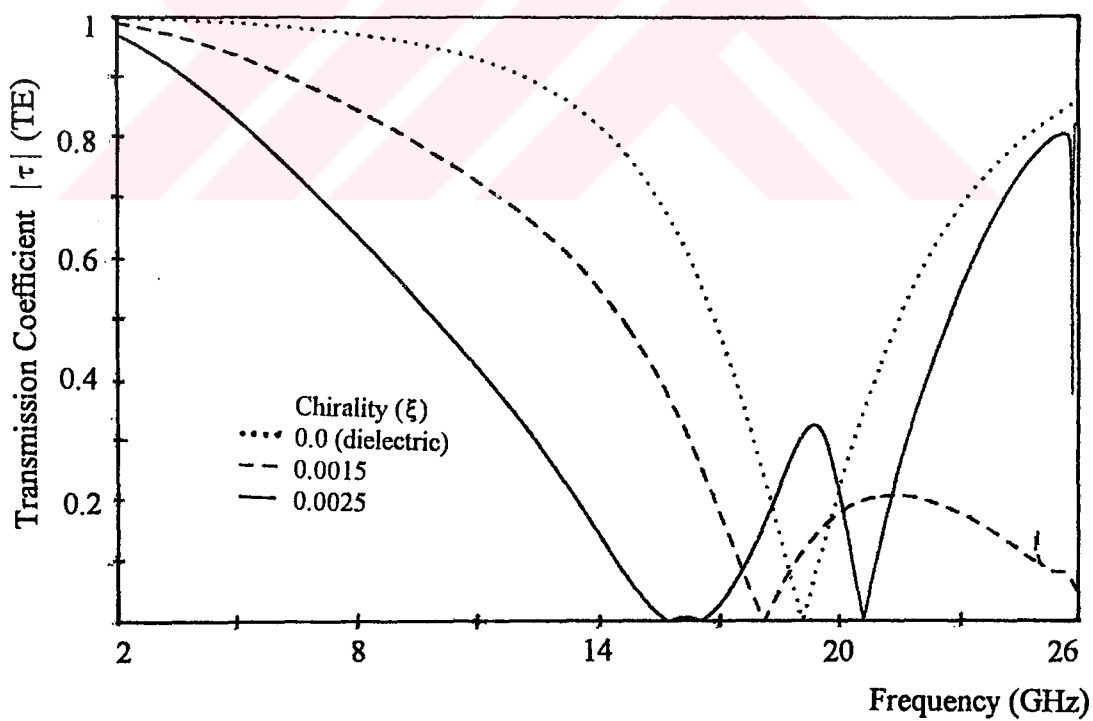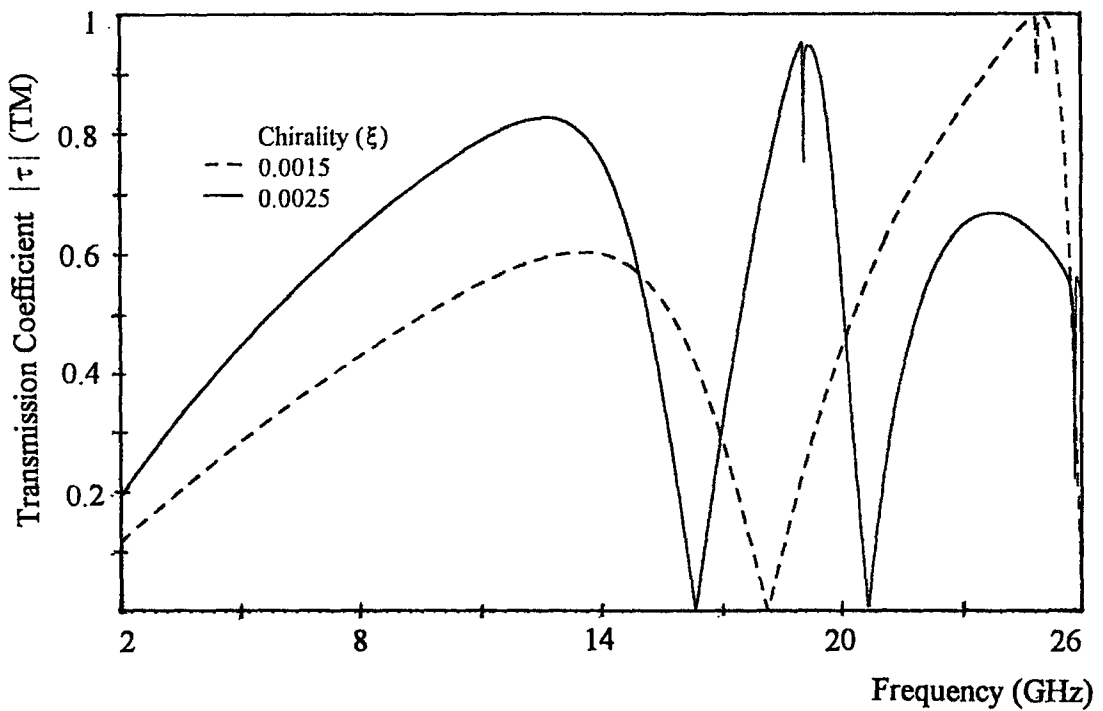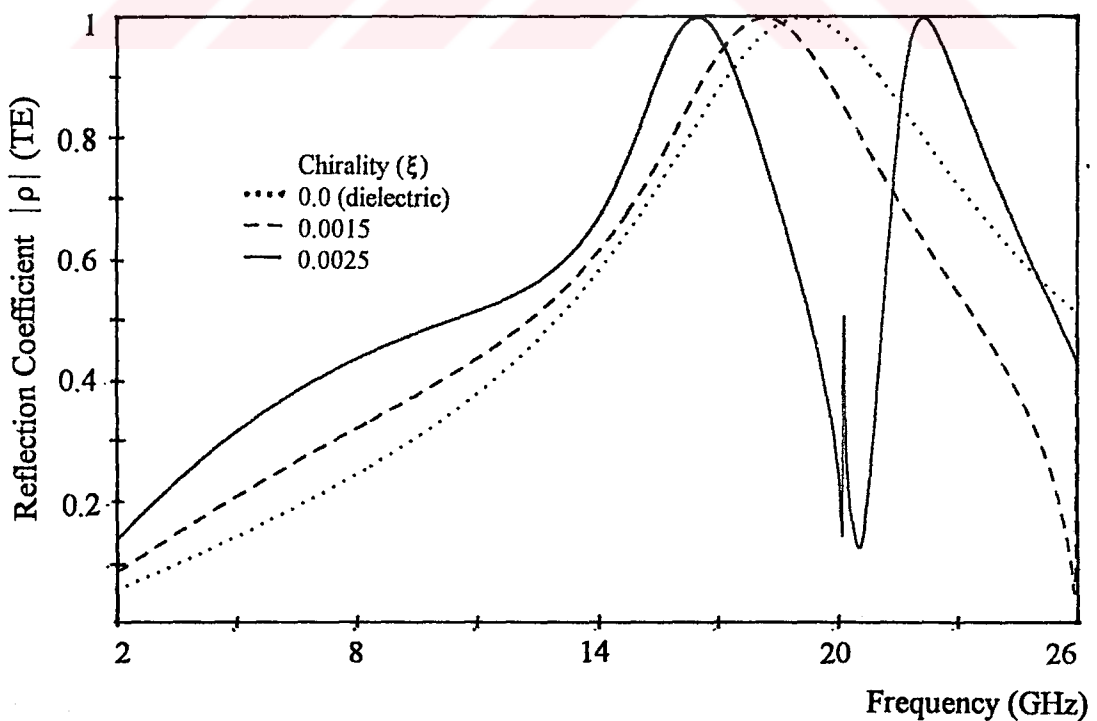b) Transmission coefficient (TE), c) Transmission coefficient (TM).

101

a

b
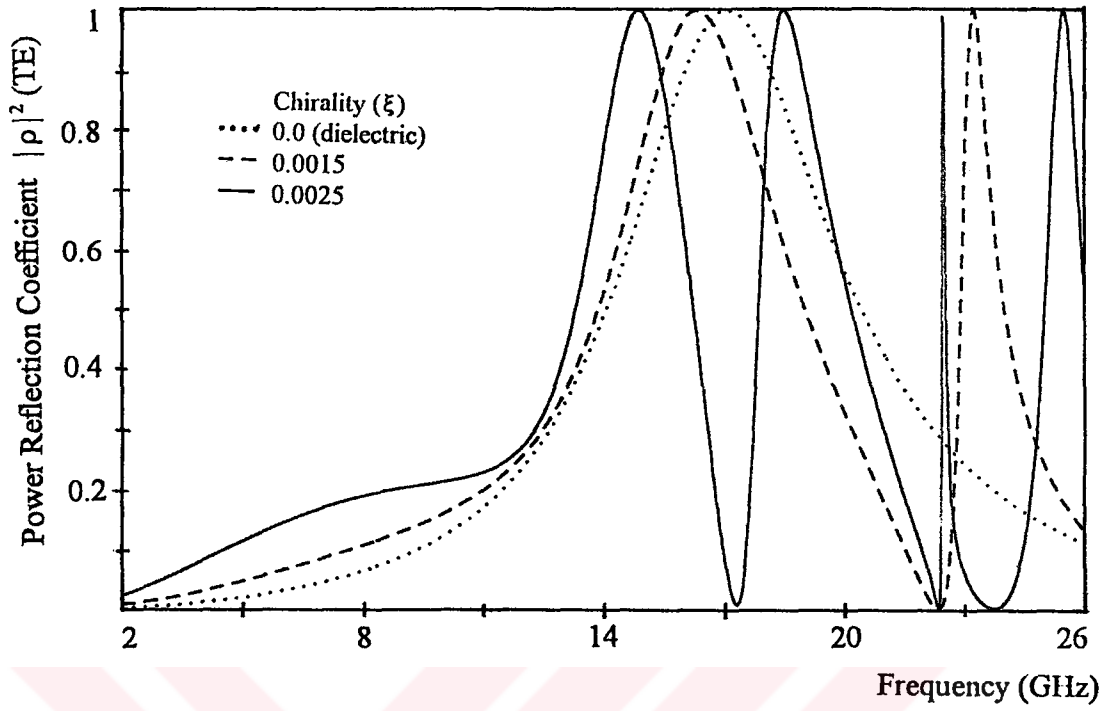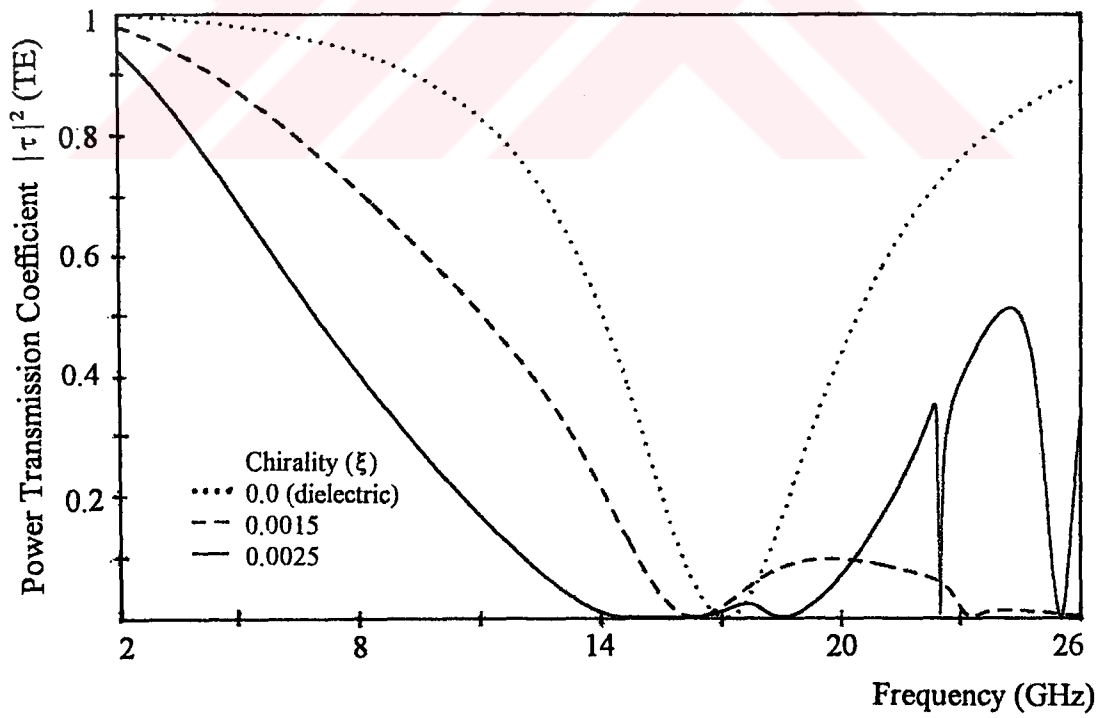
Figure 4.2.10   Spectral characteristics of Chiro-FSS with cross dipoles; TE incidence (ϕ= 30°,θ=0°), square lattice (α= 90°), D_1=D_2= 9.2, L= 8 m, W=1 mm, ϵ_r=1.06, t = 5mm. a) Power reflection coefficient (TE), b) Power transmission coefficient (TE), c) Power transmission coefficient (TM).

103
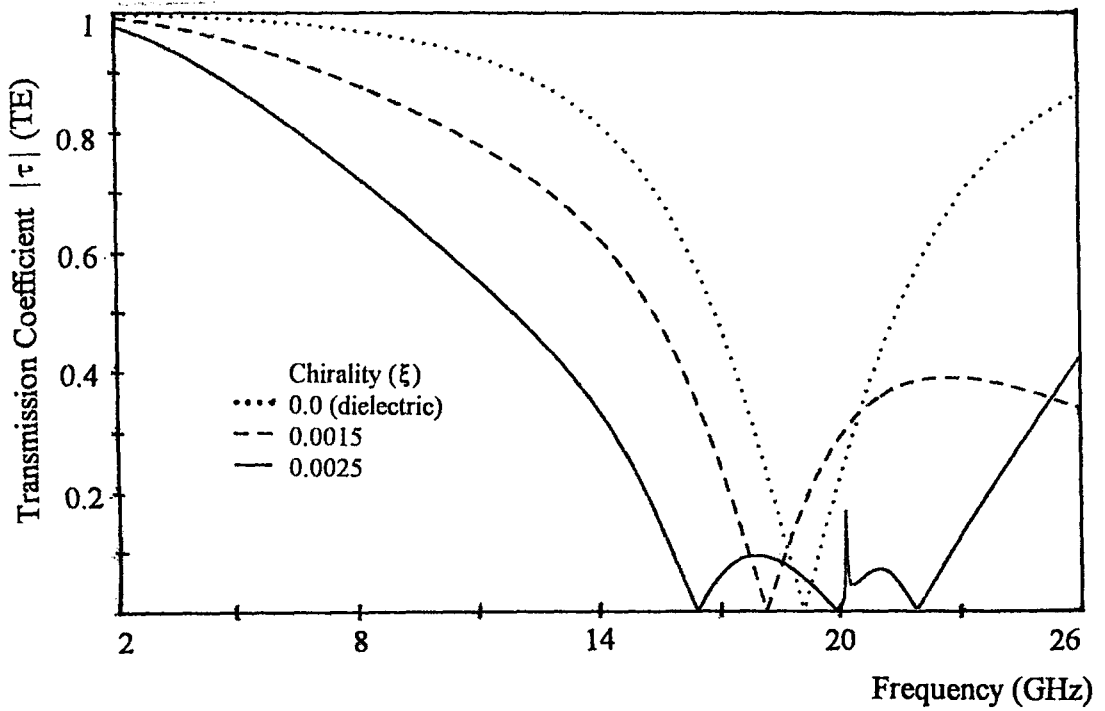
Figure 4.2.11 Spectral characteristics of Chiro-FSS with cross dipoles; TM incidence (ϕ= 30°,θ=0°), square lattice (α= 90°), D_1=D_2= 9.2, L= 8 m, W=1 mm, ϵ_r=1.06, t = 5mm. a) Power reflection coefficient (TM), b) Power transmission coefficient (TE), c) Power transmission coefficient (TM).
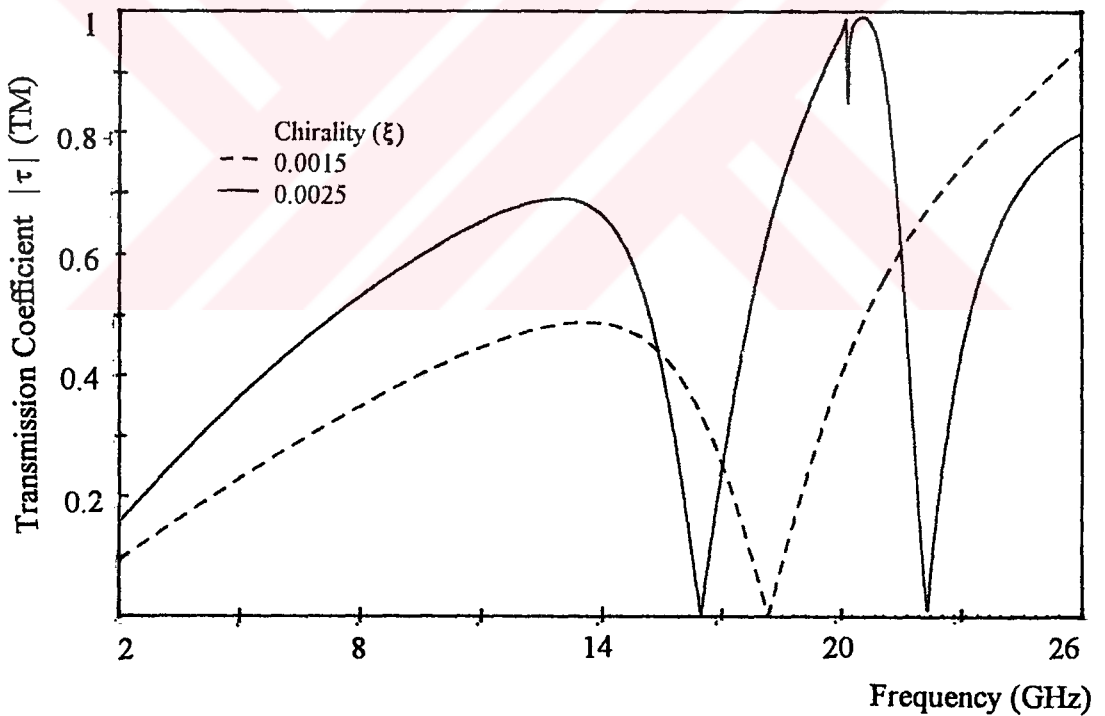
104

a

b

c

Figure 4.2.12   Spectral characteristics of Chiro-FSS with cross dipoles;TE incidence (ϕ= 45°,θ=0°), square lattice (α= 90°), D_1=D_2= 9.2, L= 8 m, W=1 mm, ϵ_r=1.06, t=5mm. a) Power reflection coefficient (TE), b) Power transmission coefficient (TE), c) Power transmission coefficient (TM).


a

Power Reflection Coefficient $|\rho|^2$ (TM) vs Frequency (GHz)

Chirality (ξ)
- - - 0.0015
——— 0.0025

b

Power Transmission Coefficient $|\tau|^2$ (TE) vs Frequency (GHz)

Chirality (ξ)
· · · · 0.0 (dielectric)
- - - 0.0015
——— 0.0025

c

107
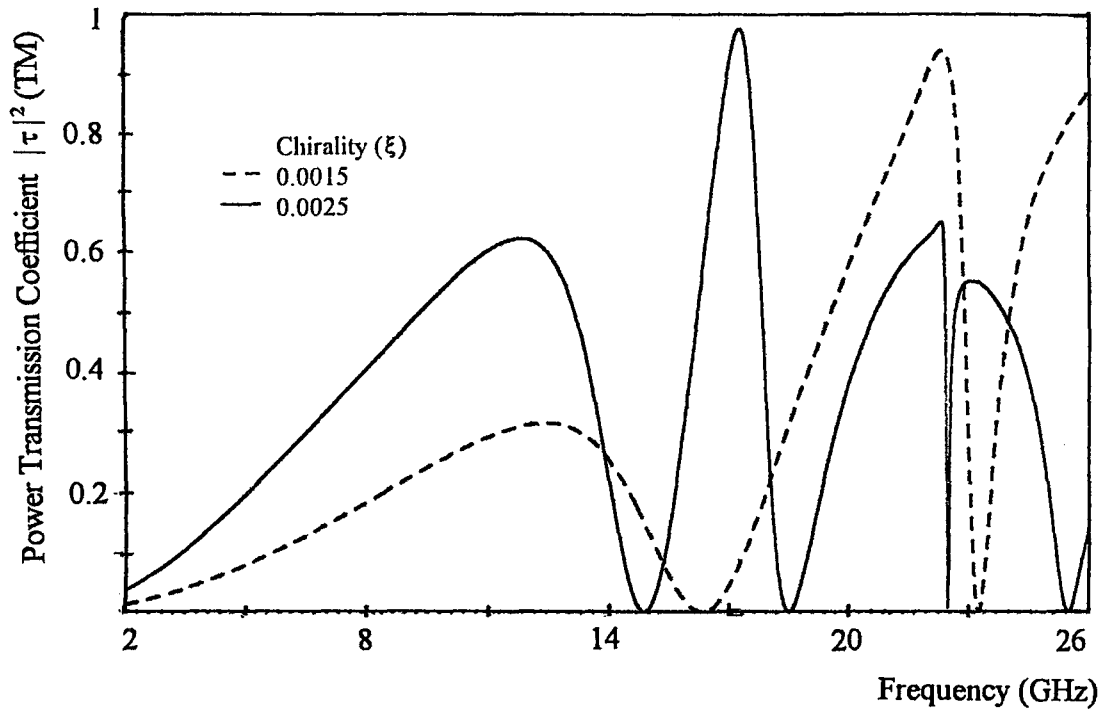
Figure 4.2.13   Spectral characteristics of Chiro-FSS with cross dipoles; TE incidence ($\phi=0°,\theta=30°$), square lattice ($\alpha=90°$), $D_1=D_2=9.2$ mm, L= 8 mm, W=1 mm, $\epsilon_r=1.06$, t = 5mm. a) Power reflection coefficient (TE), b) Power reflection coefficient (TM), c) Power transmission coefficient (TE), d) Power transmission coefficient (TM).
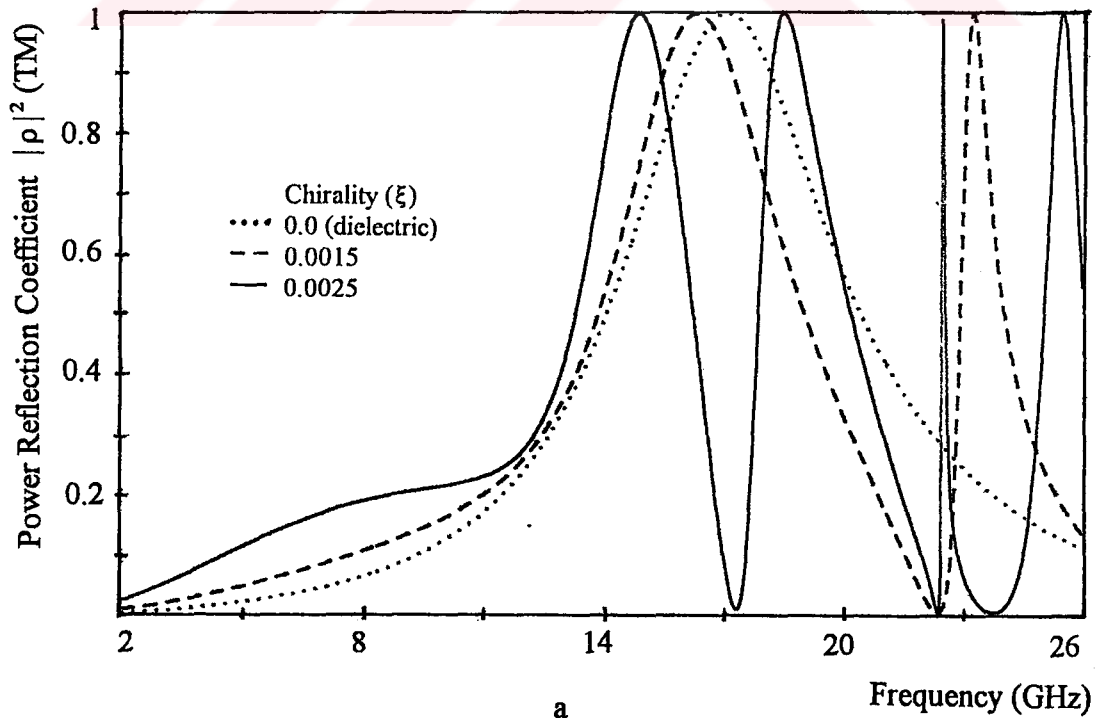
b

c

Figure 4.2.14 Spectral characteristics of Chiro-FSS with cross dipoles; TM incidence ($\phi=0°$, $\theta=30°$), square lattice ($\alpha=90°$), $D_1=D_2=9.2$ mm, L= 8 mm, W=1 mm, $\epsilon_r=1.06$, t = 5mm. a) Power reflection coefficient (TE), b) Power reflection coefficient (TM), c) Power transmission coefficient (TE), d) Power transmission coefficient (TM).
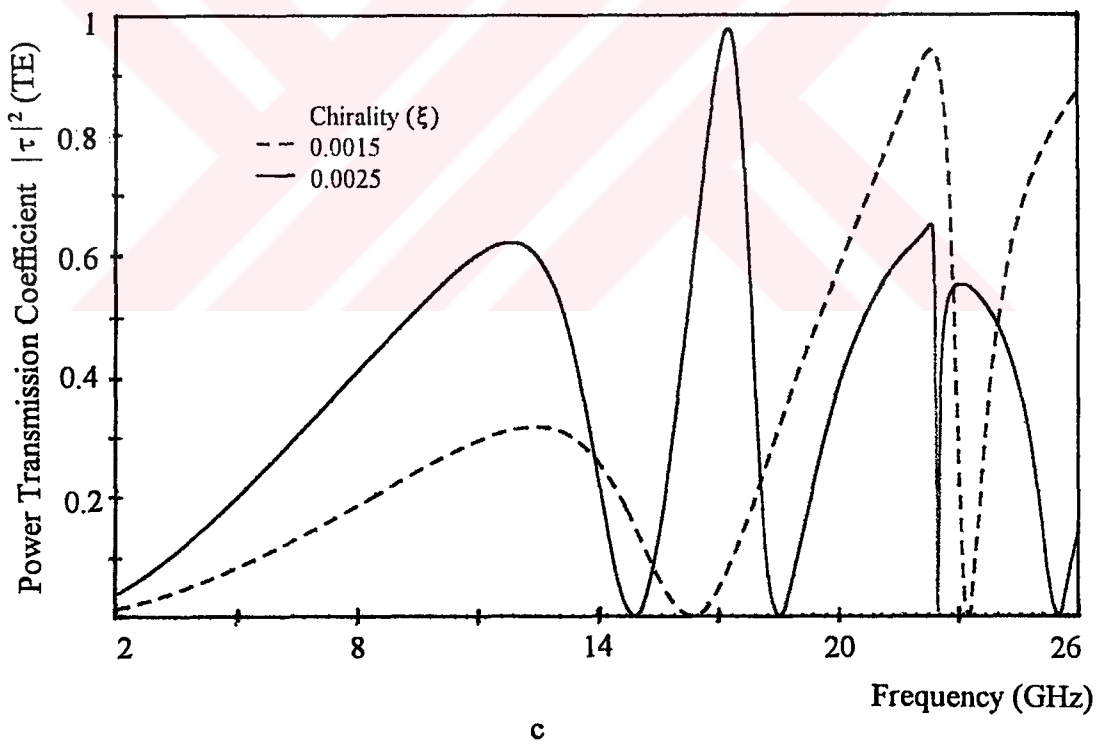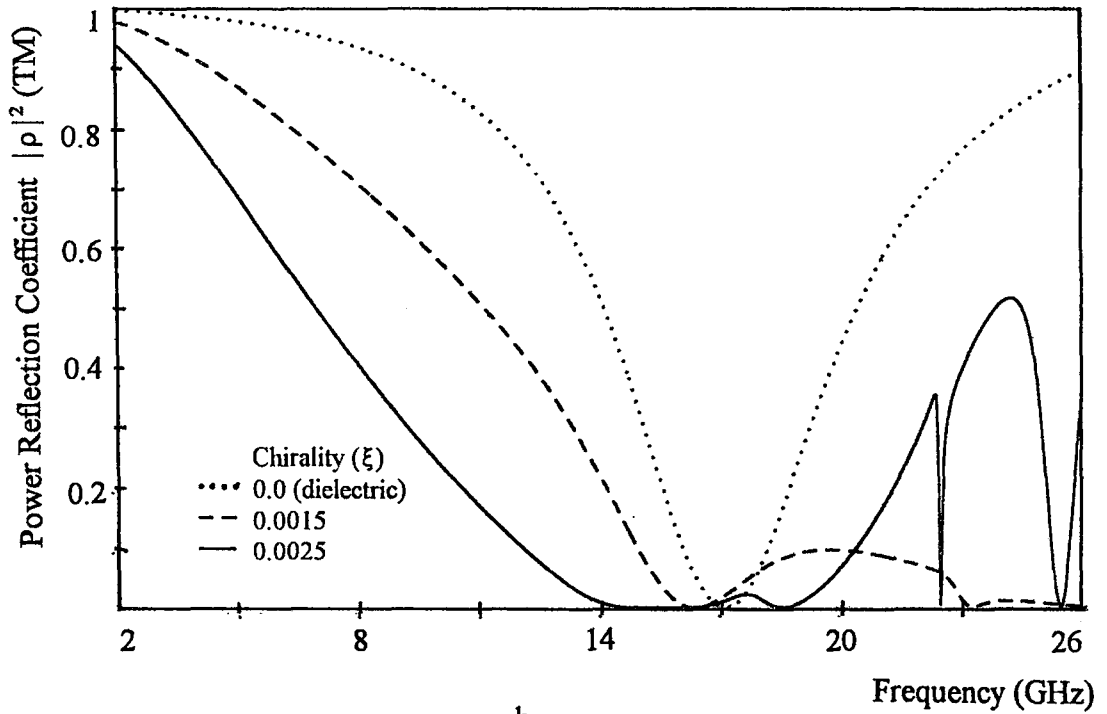

a

b

c

111
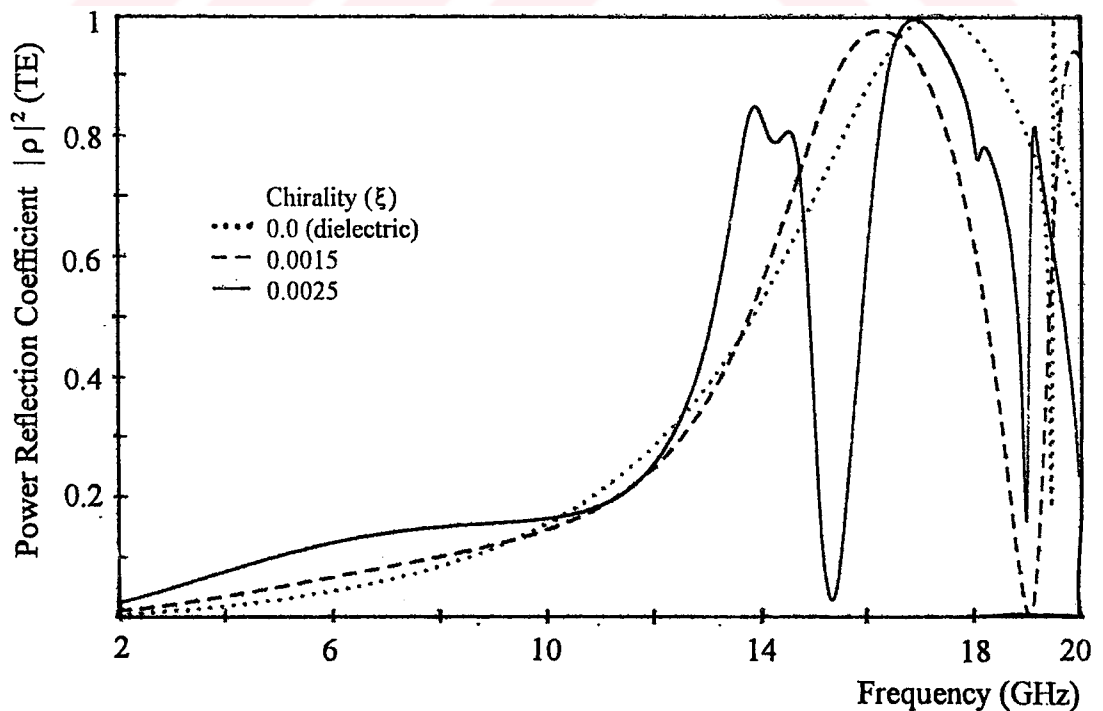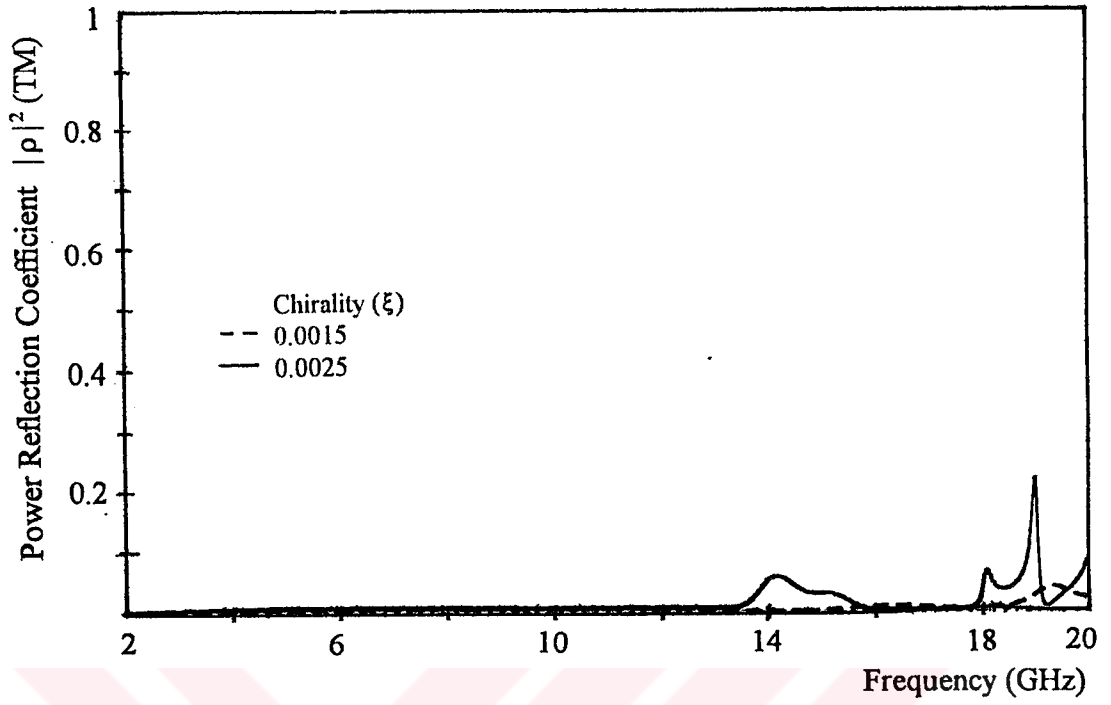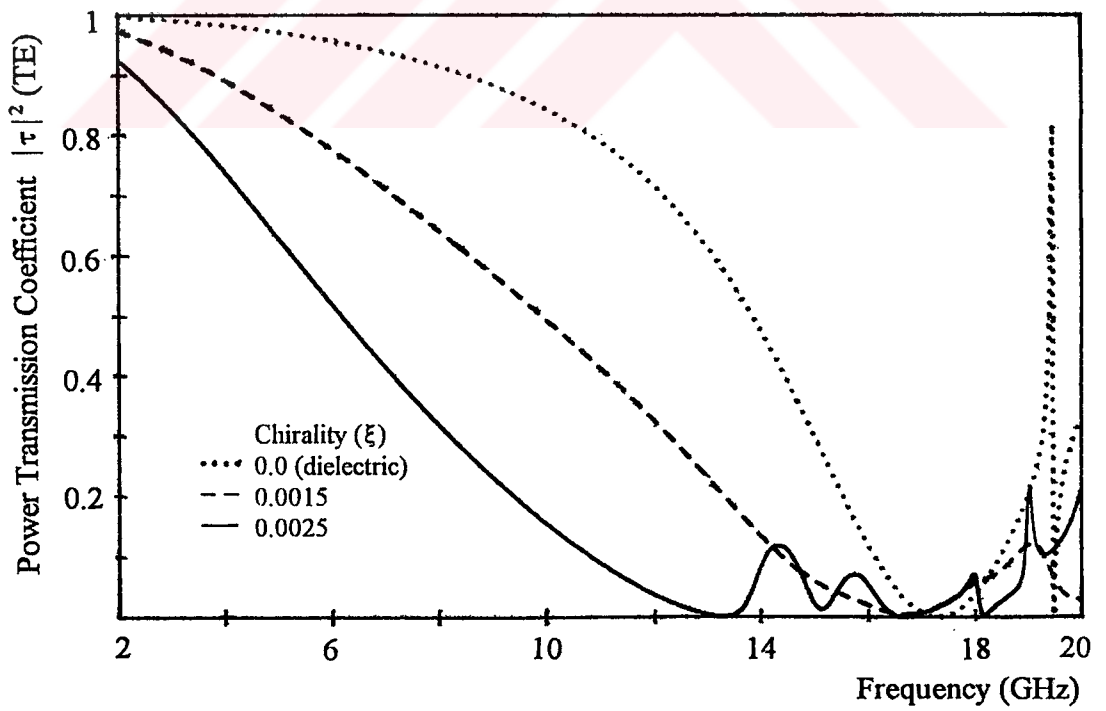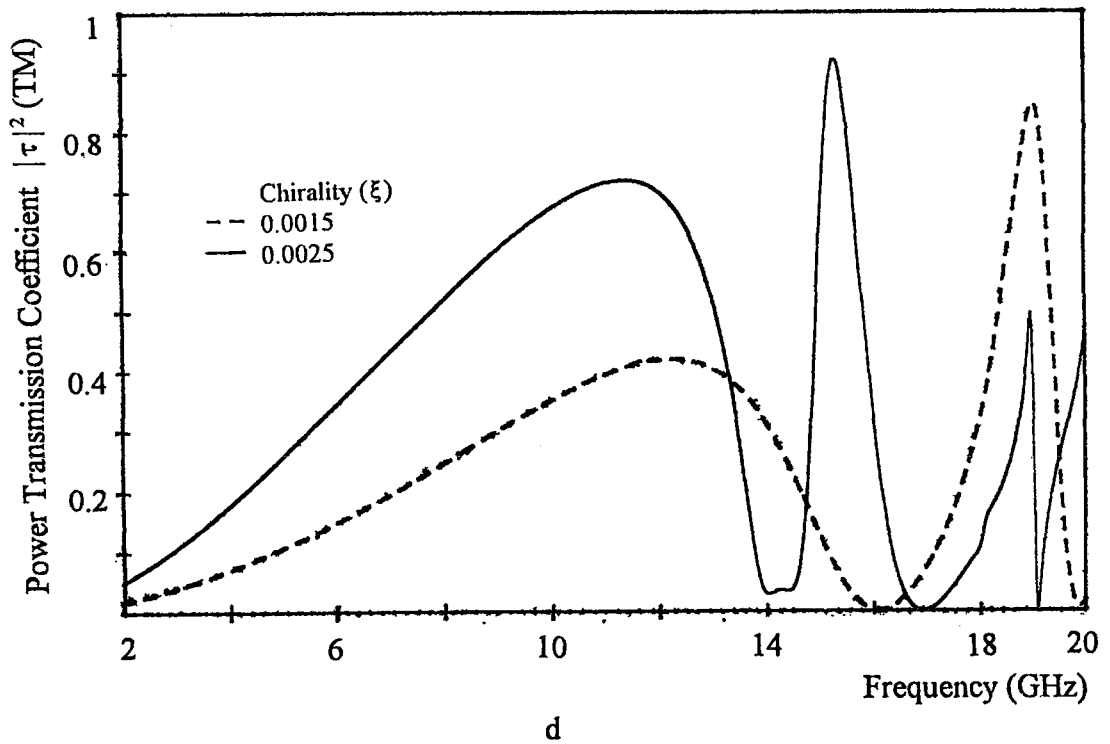
Figure 4.2.15 Spectral characteristics of Chiro-FSS with cross dipoles; TE incidence ($\phi=45°$, $\theta=30°$), square lattice ($\alpha=90°$), $D_1=D_2=9.2$ mm, L= 8 mm, W=1 mm, $\epsilon_r=1.06$, t = 5mm. a) Power reflection coefficient (TE), b) Power reflection coefficient (TM), c) Power transmission coefficient (TE), d) Power transmission coefficient (TM).
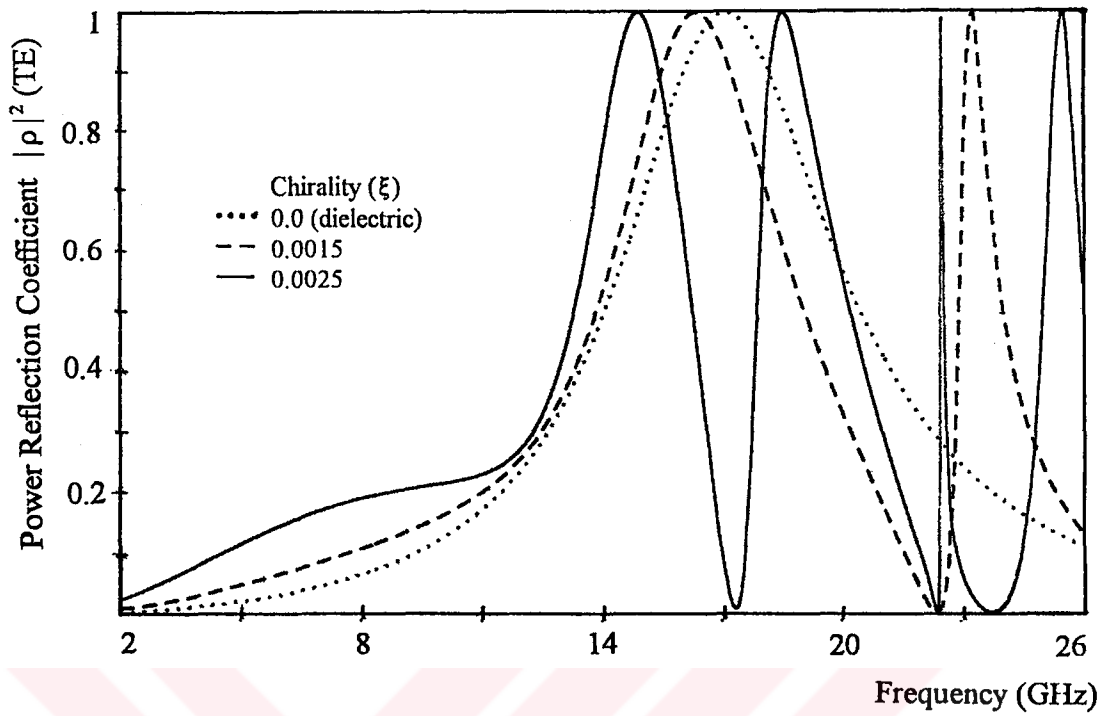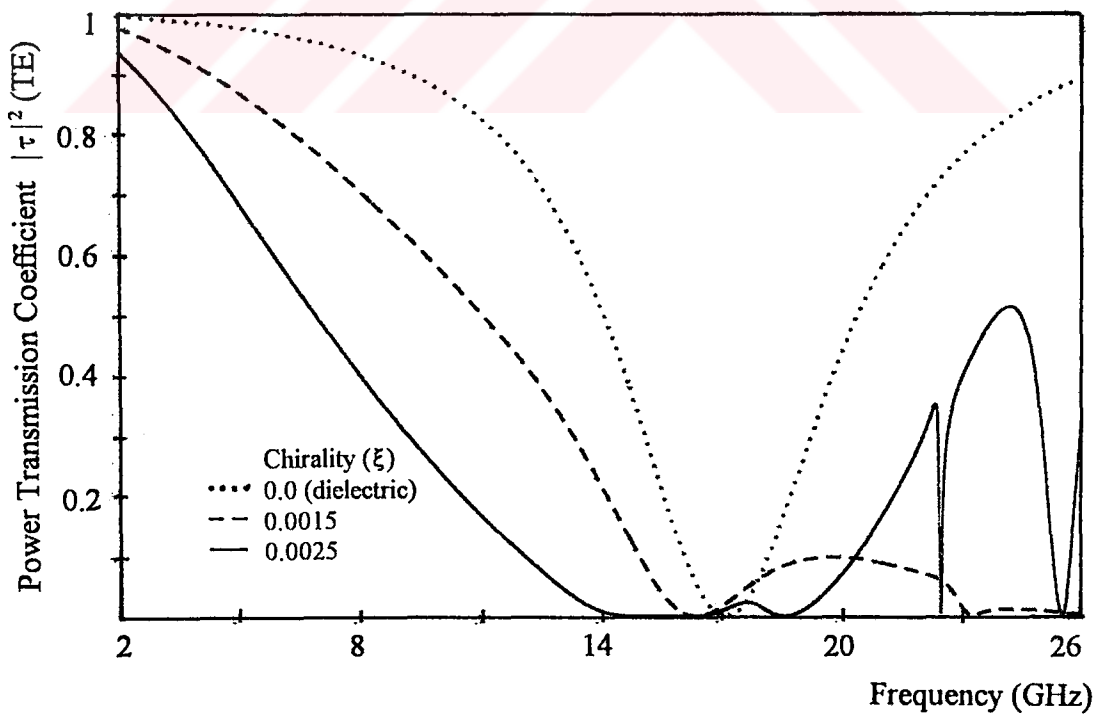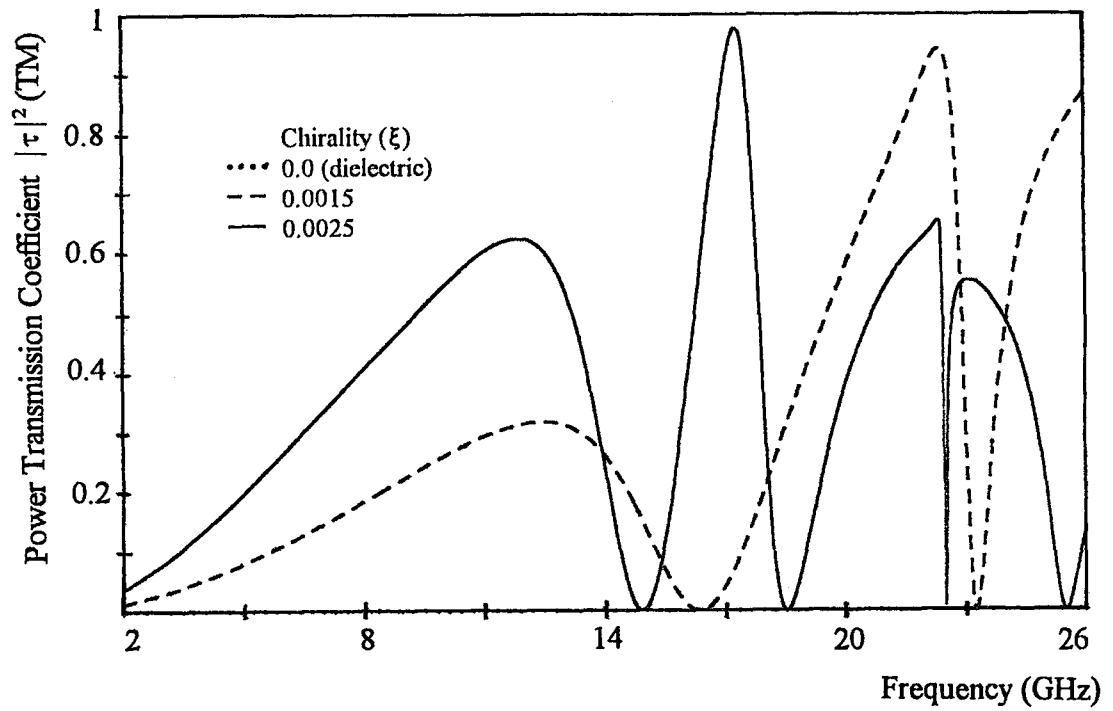
b

c

113
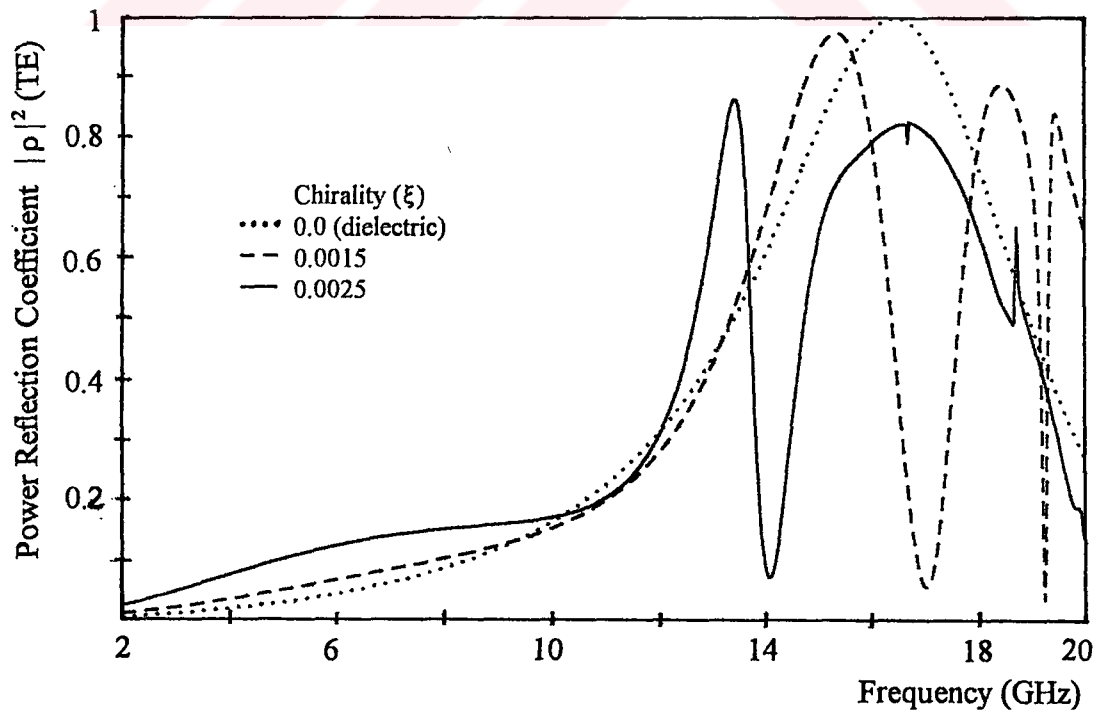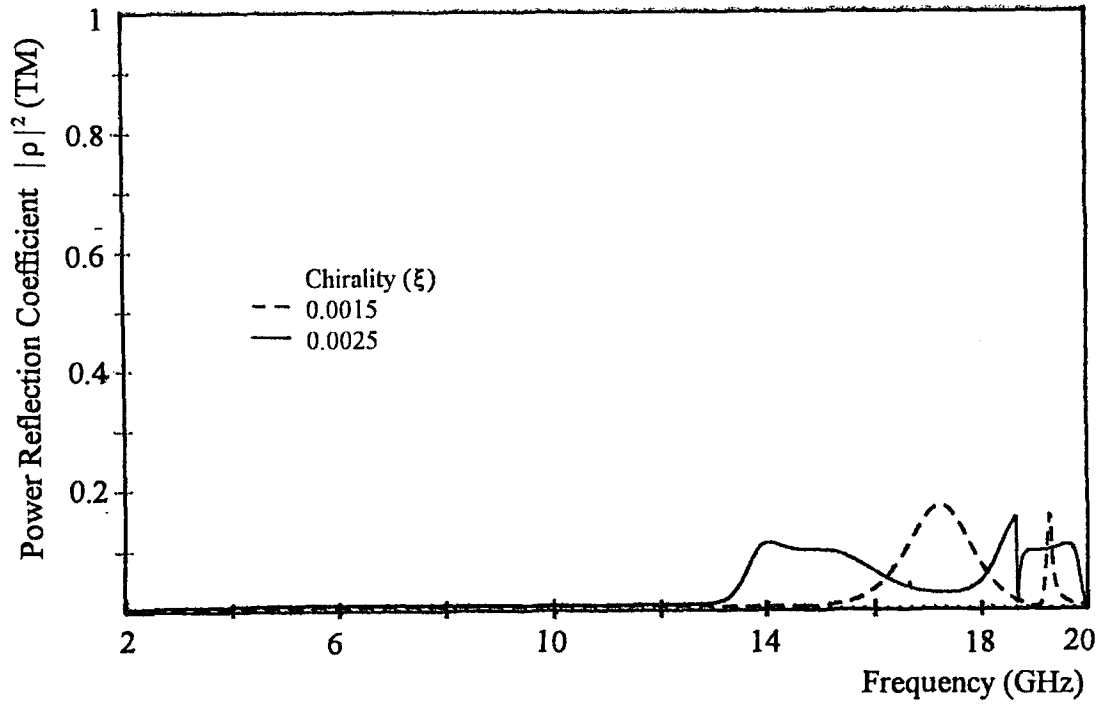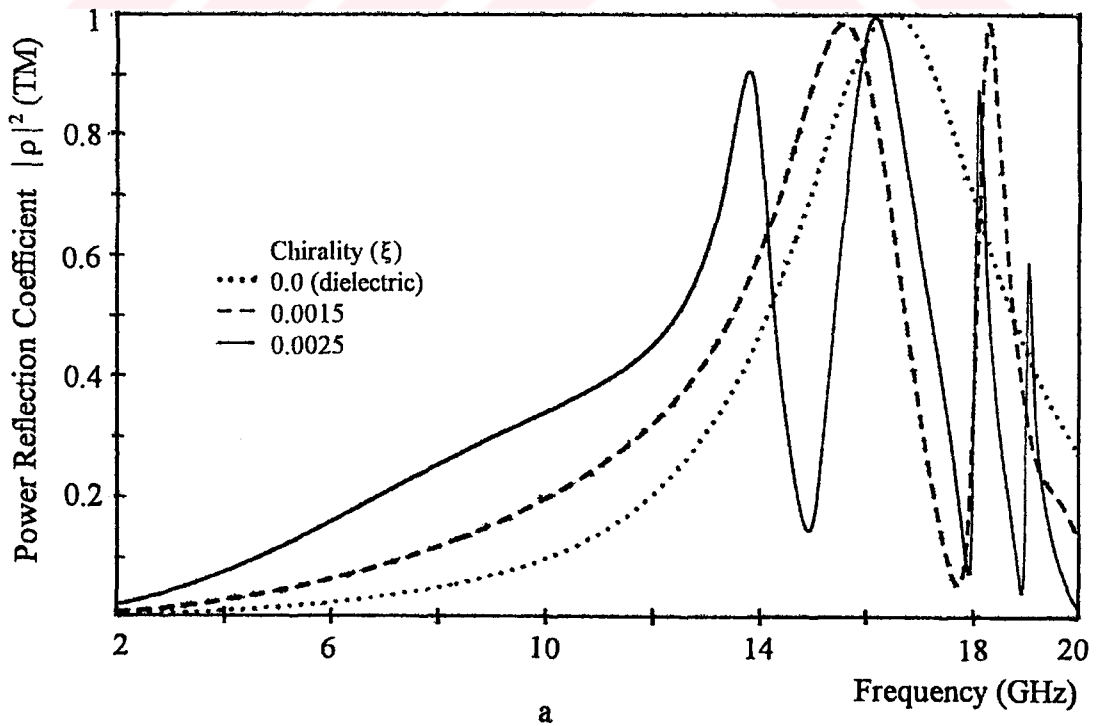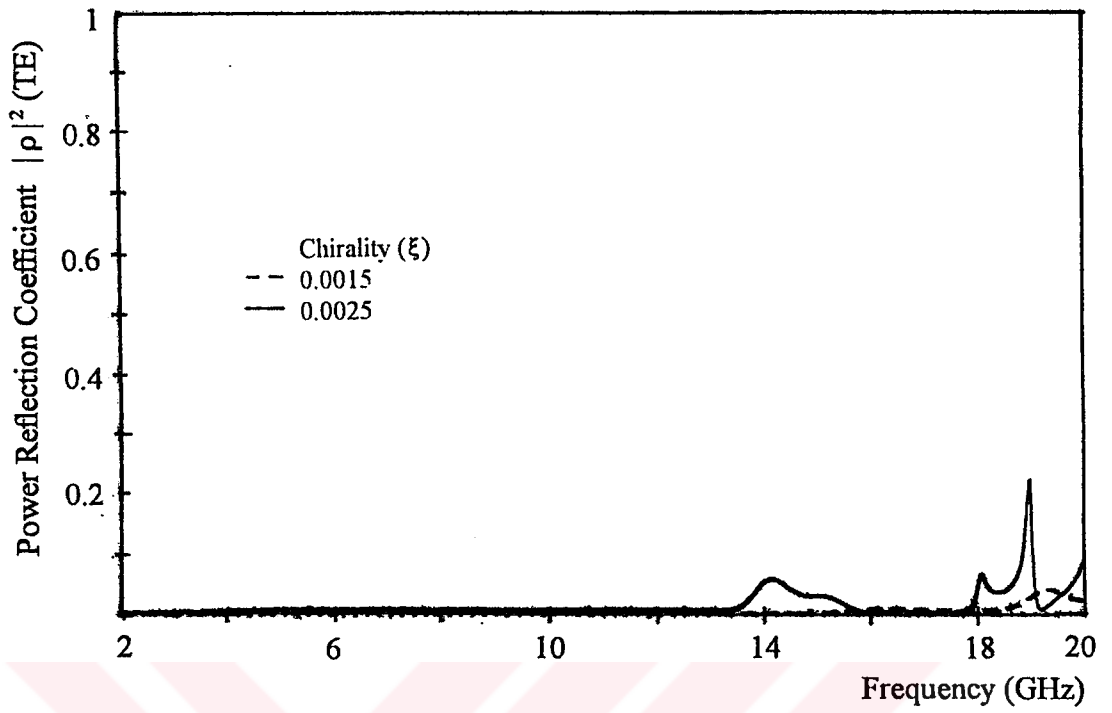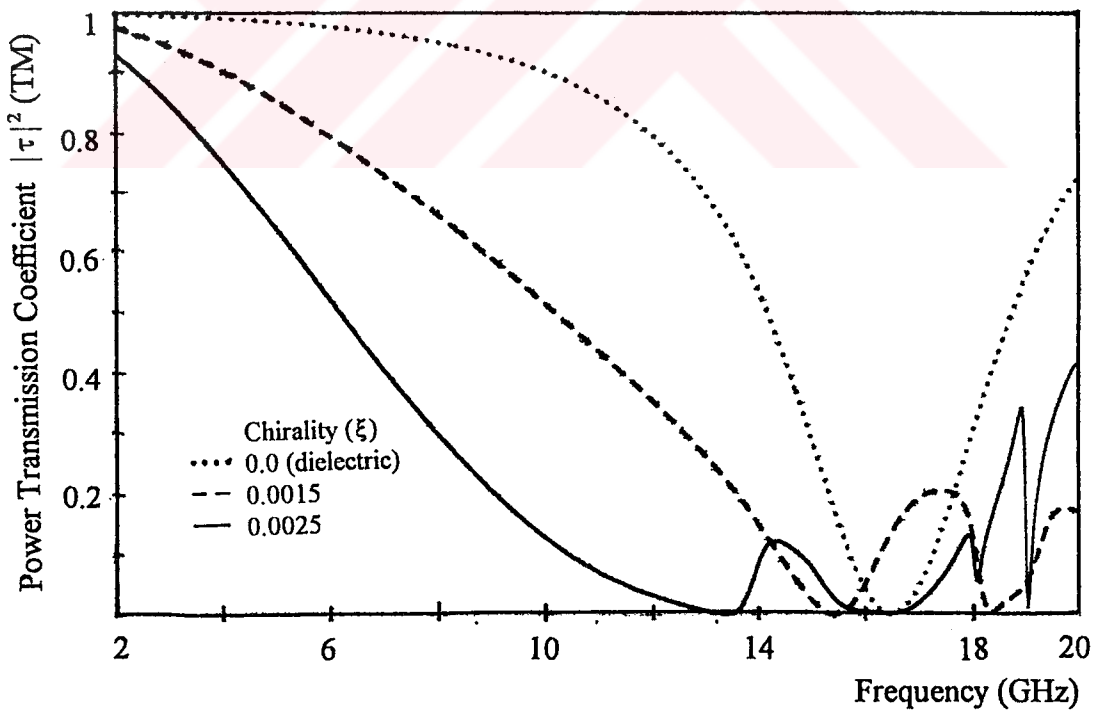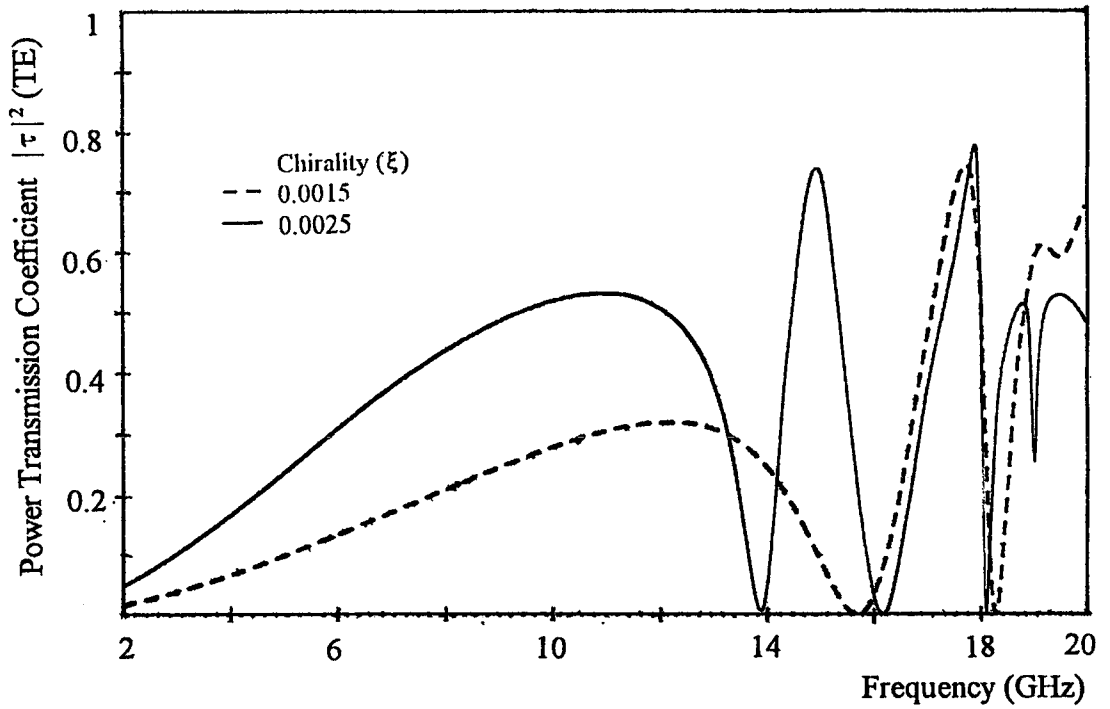
d
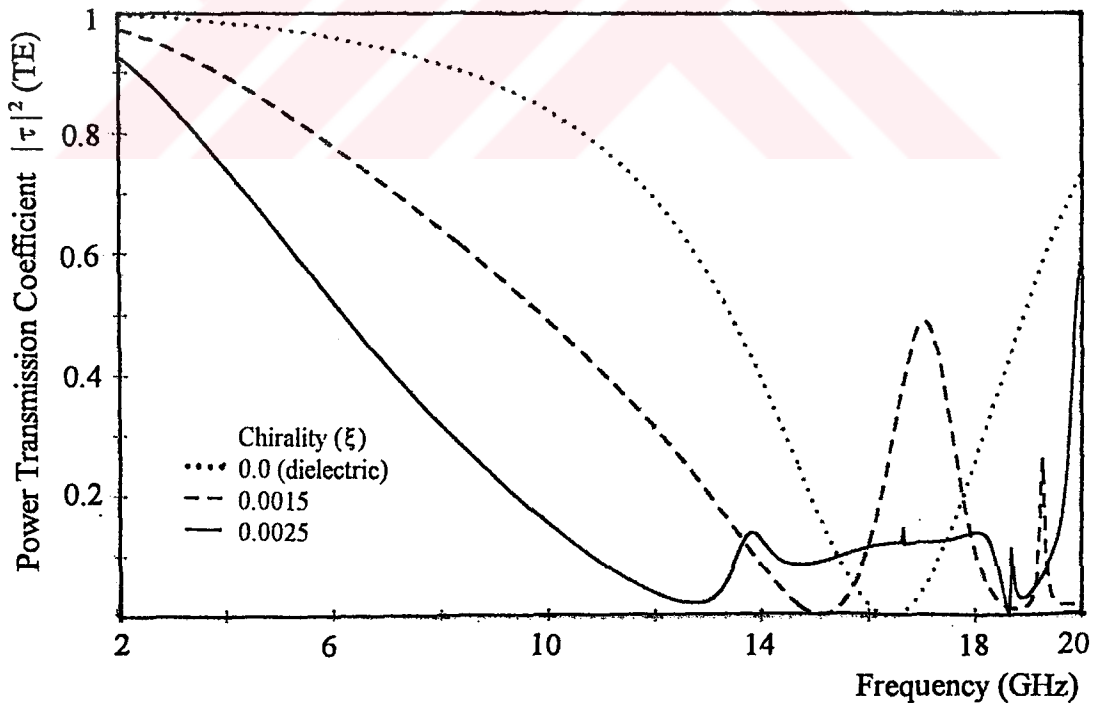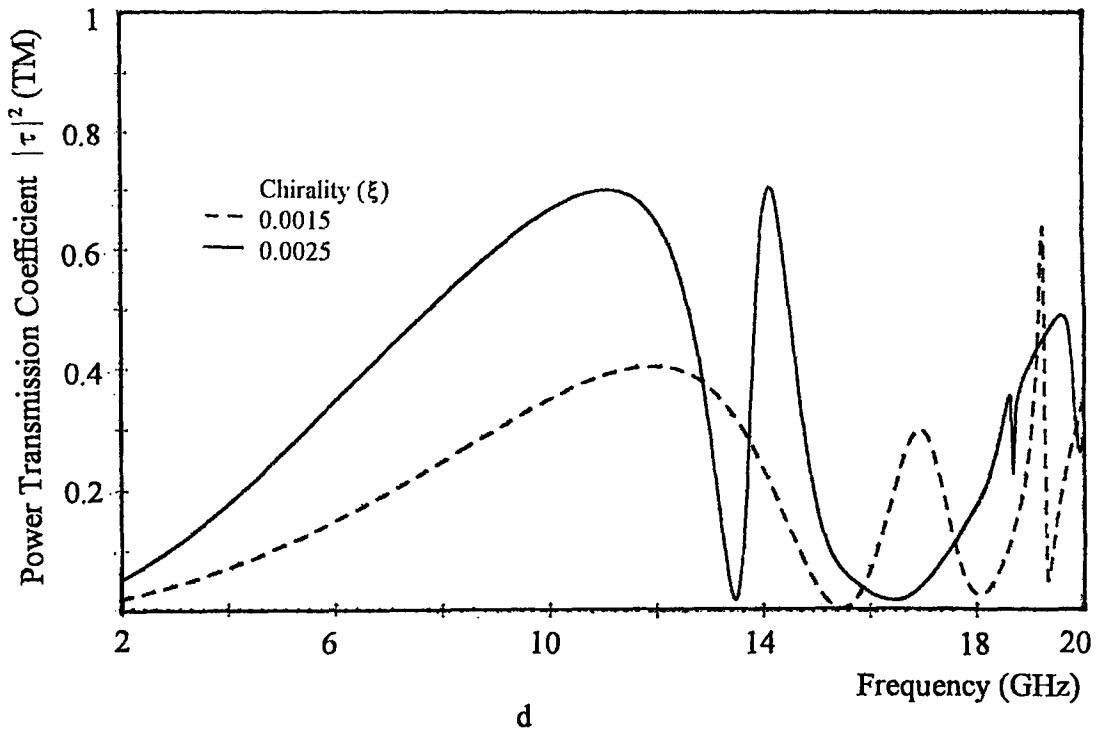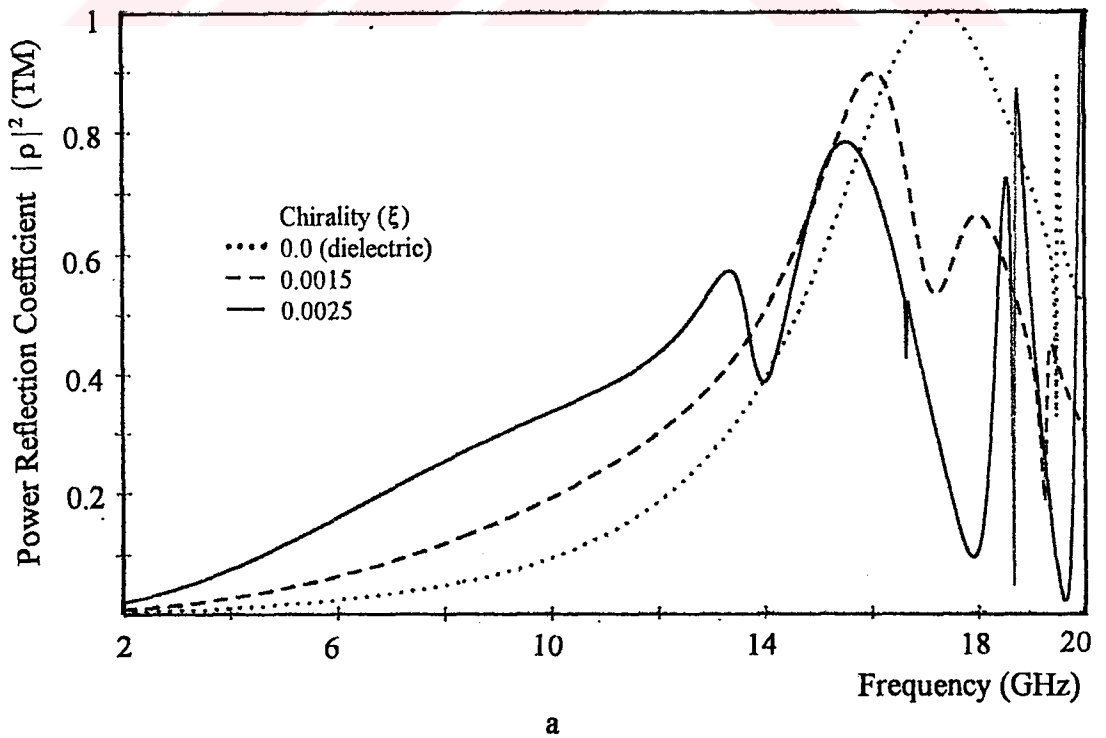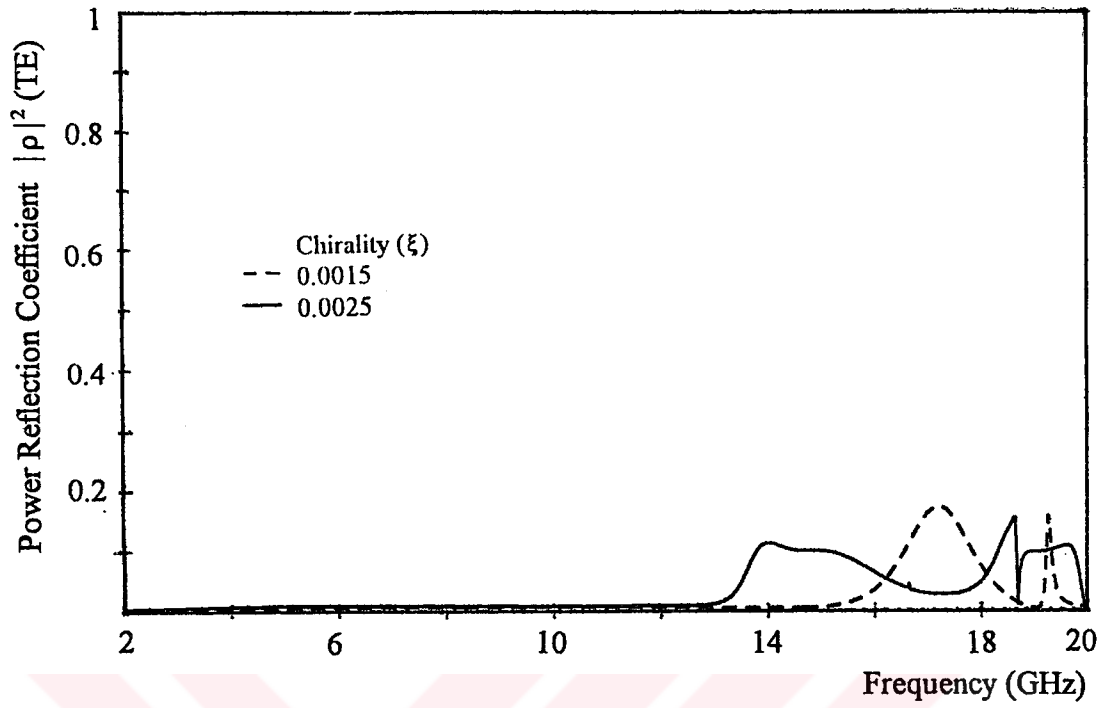
Figure 4.2.16 Spectral characteristics of Chiro-FSS with cross dipoles; TM incidence ($\phi=45°,\theta=30°$), square lattice ($\alpha=90°$), $D_1=D_2=9.2$ mm, L= 8 mm, W=1 mm, $\epsilon_r=1.06$, t = 5mm. a) Power reflection coefficient (TE), b) Power reflection coefficient (TM), c) Power transmission coefficient (TE), d) Power transmission coefficient (TM).

4.3. Chiro-FSS Comprised of Circular Rings

In this section the computed results of reflectirn and transmission characteristics of the FSS considered consisting of two dimensional infinte array of conducting rings loaded by an isotropic chiral slab are presented. A single unit cell geometry in an infinite array of these geometries forming the Chiro-FSS is shown in Figure 4.3.1.
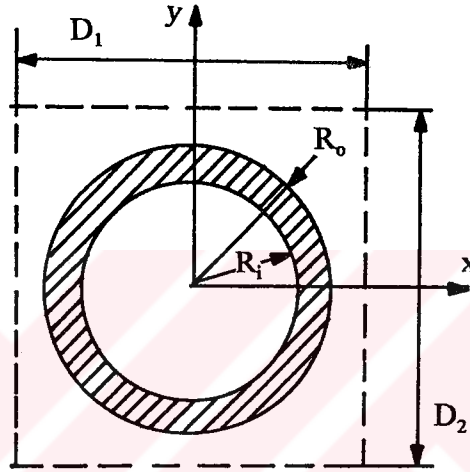
Figure 4.3.1   Unit cell geometry of Chiro-FSS with circular rings.

For this geometry, the assumption that the width of the ring is so small when compared with the wavelength of the incident field and the circumfrence of the ring has been made. Therefore the unknown current density induced on a ring is asummed to has only angular variation and no variation in the radial direction. Then the induced current density on a ring in an unit cell can be expressed as,

$$\vec{J} = \sum_{n=1}^{N} a_n \, \vec{I}_{nc} + \sum_{k=1}^{K} b_k \, \vec{I}_{ks} \tag{4-37}$$

where,

$$\vec{I}_{nc} = \cos(n\phi) \, \vec{a}_\phi \qquad\qquad \vec{I}_{ms} = \sin(m\phi) \, \vec{a}_\phi \tag{4-38}$$

115

and a_k and b_k are the unknown coefficients to be deteremined, where

$$\vec{a}_\phi = - \sin\phi\, \vec{a}_x + \cos\phi\, \vec{a}_y \tag{4-39}$$

Evaluation of the integrals corresponding to the inner products as follows,

Integrals involve cosine terms:

Introducing the polar coordinate variables ($x = \rho\cos\phi$, $y = \rho\sin\phi$) to the above equation those involves cosine terms, one can rearranged as,

$$<\vec{I}_{nc}, \vec{\Psi}^{\cdot}_{mpq}> = -\frac{1}{\sqrt{A}} \int_{R_i}^{R_o} \int_0^{2\pi} \sin(\phi_1 - \phi)\, e^{j\rho k_{Tpq} \sin(\phi + \alpha)} \cos(n\phi)\rho\, d\rho\, d\phi \tag{4-40}$$

where,

$$\phi_1 = \tan^{-1}\left(\frac{u_{mpqy}}{u_{mpqx}}\right), \qquad k_{Tpq} = \sqrt{k_{xpq}^2 + k_{ypq}^2}, \qquad \alpha = \tan^{-1}\left(\frac{k_{xpq}}{k_{ypq}}\right) \tag{4-41}$$

Now, let us consider only the integration with respect to ϕ.

$$I = \int_0^{2\pi} \sin(\phi_1 - \phi)\, e^{j\rho k_{Tpq} \sin(\phi + \alpha)} \cos(n\phi)\, d\phi \tag{4-42}$$

let, $u = \phi + \alpha$ the the above equation becomes,

$$I = \frac{1}{2} \int_\alpha^{\alpha+2\pi} e^{j\rho k_{Tpq} \sin u} \left(\sin(\gamma_1 + m\,u) + \sin(\gamma_2 - l\,u) \right) du \tag{4-43}$$

where

$$\begin{array}{ll} \gamma_1 = \phi_1 - (n-1)\alpha & m = n - 1 \\[2mm] \gamma_2 = \phi_1 + (n+1)\alpha & l = n + 1 \end{array} \tag{4-44}$$

rearranging the last integral,

$$I = \frac{1}{2} \int_{\alpha}^{\alpha + 2\pi} e^{j\rho\, k_{Tpq}\, \sin u} \left(\sin \gamma_1 \cos(m\,u) + \cos \gamma_1 \sin(m\,u) + \right.$$

$$\left. \sin \gamma_2 \cos(l\,u) - \cos \gamma_2 \sin(l\,u) \right) du \tag{4-45}$$

Above equation is of the type,

$$I = \frac{1}{2} \int_{\alpha}^{\alpha + 2\pi} e^{j\rho\lambda\,\sin\theta} \begin{bmatrix} \cos(k\theta) \\ \sin(k\theta) \end{bmatrix} d\theta = \begin{bmatrix} 2\pi J_k(\rho\lambda) & even & k \\ 0 & odd & k \end{bmatrix} \tag{4-46}$$

where J_k is the Bessel function of the first type. The inner products with out complex conjugations are can be obtained as,

$$\langle \vec{I}_{nc}, \Psi_{mpq}^* \rangle = \frac{\pi}{\sqrt{A}} \int_{R_i}^{R_o} \rho \, (\, j \cos \gamma_1 \, J_{n-1}(k_{Tpq}\rho) - $$

$$j \cos \gamma_2 \, J_{n+1}(k_{Tpq}\rho) \,) \, d\rho \qquad even \quad n \tag{4-47}$$

$$\langle \vec{I}_{nc}, \Psi_{mpq}^* \rangle = \frac{\pi}{\sqrt{A}} \int_{R_i}^{R_o} \rho \, (\, j \sin \gamma_1 \, J_{n-1}(k_{Tpq}\rho) + $$

$$j \sin \gamma_2 \, J_{n+1}(k_{Tpq}\rho) \,) \, d\rho \qquad odd \quad n \tag{4-48}$$

The inner poducts without complex conjugations are obtained simply by letting,

$$\langle \vec{I}_{nc}, \Psi_{mpq} \rangle = \frac{\pi}{\sqrt{A}} \int_{R_i}^{R_o} \rho \, (\, j \cos \gamma_1' \, J_{n-1}(k_{Tpq}\rho) - $$

$$j \cos \gamma_2' \, J_{n+1}(k_{Tpq}\rho) \,) \, d\rho \qquad even \quad n \tag{4-50}$$

and

$$\gamma_1' = \phi_1 - (n-1)\alpha + \pi$$

$$\gamma_2' = \phi_1 + (n+1)\alpha + \pi \tag{4-49}$$

117

$$<\vec{I}_{nc}, \Psi_{mpq}> = \frac{\pi}{\sqrt{A}} \int_{R_i}^{R_o} \rho \ (\ j \sin \gamma_1' \ J_{n-1}(k_{Tpq}\rho) \ +$$

$$j \sin \gamma_2' \ J_{n+1}(k_{Tpq}\rho) \ ) \ d\rho \qquad odd \quad n \qquad (4\text{-}51)$$

In a similar manner the inner products corresponding to the sine terms,

$$<\vec{I}_{ks}, \overset{*}{\Psi}_{mpq}> = \frac{\pi}{\sqrt{A}} \int_{R_i}^{R_o} \rho \ (\ j \sin \gamma_2 \ J_{n+1}(k_{Tpq}\rho) \ +$$

$$j \sin \gamma_1 \ J_{n-1}(k_{Tpq}\rho) \ ) \ d\rho \qquad even \quad n \qquad (4\text{-}52)$$

$$<\vec{I}_{ks}, \overset{*}{\Psi}_{mpq}> = \frac{\pi}{\sqrt{A}} \int_{R_i}^{R_o} \rho \ (\ j \cos \gamma_2 \ J_{n+1}(k_{Tpq}\rho) \ -$$

$$j \cos \gamma_1 \ J_{n-1}(k_{Tpq}\rho) \ ) \ d\rho \qquad odd \quad n \qquad (4\text{-}53)$$

and

$$<\vec{I}_{ks}, \Psi_{mpq}> = \frac{\pi}{\sqrt{A}} \int_{R_i}^{R_o} \rho \ (\ j \sin \gamma_2' \ J_{n+1}(k_{Tpq}\rho) \ +$$

$$j \sin \gamma_1' \ J_{n-1}(k_{Tpq}\rho) \ ) \ d\rho \qquad even \quad n \qquad (4\text{-}54)$$

$$<\vec{I}_{ks}, \Psi_{mpq}> = \frac{\pi}{\sqrt{A}} \int_{R_i}^{R_o} \rho \ (\ j \cos \gamma_2' \ J_{n+1}(k_{Tpq}\rho) \ -$$

$$j \cos \gamma_1' \ J_{n-1}(k_{Tpq}\rho) \ ) \ d\rho \qquad odd \quad n \qquad (4\text{-}55)$$

4.3.1. Numerical Results of the Chiro-FSS with Circular Rings.

The circular ring is another type of scatterer has been found many application in

forming the frequency selective surfaces. Thre resonant wavelength, in fact, is slightly less than the circumference of the ring. This criterion is of general validity when the free standing array considered.In this section numerical results of the Chiro-FSS comprised of two dimensional infinite arrays of circular rings printed on an isotropic chiral slab are presented. Effects of the design parameters of this type of Chiro-FSS on the reflection and transmission characteristics are examined.

First , let us consider a Chiro-FSS comprised of circular rings arranged in a square lattice having the periodicies of $D_1=D_2=10$ mm. The inner and outer radius of the rings is $R_i= 3.7$ mm and $R_o= 4.7$ mm, respectively. The array of rings are loaded by a 5 mm thick isotropic chiral slab having a dielectric constant of 1.06. The reflection and transmission characteristics of the Chiro-FSS versus frequency are represented in Figure 4.3.2 for the chirality admittance of $\xi= 0.0$ (dielectric), 0.0005, 0.0015 and 0.0025 mho. The screen is illuminated by normally incident plane wave of TE polarisation.

As it seen from Figure 4.3.2, for small value of chirality admittance the spectral characteristics obtained are similar to the spectral characteritics of the conventional FSS (zero chirality). As the chirality admittance is further increased to $\xi= 0.0015$ and 0.0025 mho, one and three extra resonances are observed, respectively. In the transmission characteristics, almost full transmission for the cross-polar component of the transmitted wave are obtained for $\xi= 0.0015$ and 0.0025 mho. Note that the frequency at which the screen is transparent (full transmission) is shifted to lower frequencies as the chirality admittance increased.

Figure 4.3.3. represents the spectral characteristics of the Chiro-FSS having same design parameters as in the previous example except thickness. For these results the slab thickness is choosen as 4 mm and chirality admittances of $\xi=0.0$, 0.0015 and 0.0025 mho. In the reflection characteristics, the bandwidth of the resonances are broadened as the thickness of the slab is decreased to t= 4 mm. Another change in the spectral characteristics of the reflection coefficient is that, the isolations between the resonances are not better as in the privious case (t = 5 mm). One interesting results obtained by comparing the Figure 4.3.3 and Figure 4.3.4 is that, the frequency of the first resonance is almost unchanged as the thickness is reduced to t=4 mm, whereas the higher order

frequencies are moved to the higher ferquencies.

In order to see the effects of dielectric constant on the reflection and transmission characteristics of the Chiro-FSS, the dielectric constant of the chiral slab is increased from 1.06 to 1.32 while the other paremeters are kept same as the first example. The curve corresponding to these design paremeters are depicted in Figure 4.3.5. Comparision of Figure 4.3.2 (ϵ_r=1.06) with Figure 4.3.3 (ϵ_r=1.32) reveals that in the later case the resonance frequencies are shifted to the lower frequencies and more narrower bandwidths associated are observed. The transmission characteristics are also modified such that, similar to the reflection curves the frequencies at which the full transmission is achieved for cross-polar components are also shifted.

The spectral characteristics of the Chiro-FSS having 4 mm thick slab (ϵ_r=1.32) are presented in Figure 4.3.6. In this case loading effect of the slab observed is similar to the previous case (ϵ_r=1.06).

Figure 4.3.7 shows the spectral characteritics of the Chiro-FSS with circular rings having a inner (R_i) and outer (R_o) radius of 3 and 4 mm, respectively. The arrays of rings are arranged in a square lattice geometry (D_1=D_2= 10 mm), loaded by a 5 mm thick chiral slab. Dielectric constant of the slab is assumed to be ϵ_r= 1.06. The figure are obtained for three different values of chirality admittances, ξ=0.0 (dielectric), 0.0015 and 0.0025 mho, and the screen illuminated by a TE plane wave of normal incidence. Comparision of Figure 4.3.7 with Figure 4.3.2 yields that the decreasing the radius of the circular rings shifts the resonances frequencies towards to the higher frequencies for all values of the chirality admittance. Although the bandwidths of the higher resonances are changed very slightly, there is a considerable reduction in the bandwidth of the first resonance is observed. Similar effects are also obtained in the transmission characteristics of the cross-polar component. It obvious that the increase in the resonance frequencies is due to the reduction of the mean circumference of the circular ring scatterers.

Reducing the thickness of the slab to t=4 mm for the previous configuration changes the spectral response of the Chiro-FSS as shown Figure 4.3.7. In this case as it seen from the figure isolation between the first two resonances is no good as in the case of t=5 mm (previous example) and bandwidth of the higher resonances obtained are more narrower.

Dielectric constant of the 5 mm thick slab is increased to from 1.06 to 1.32 while the other design parameters are same in the first example, consirerable changes are observed in the reflection and transmission characteristics as depicted in Figure 4.3.8. For this configuration, very narrow bandwidths associated to the resonances are obtained in the reflection characteritics. It seen that the isolations between the resonances are very good.

The effects of the array geometry of the pefrectly conducting circular rings on the spectral response of the Chiro-FSS can be seen by comparing the results given in Figure 4.3.2 and Figure 4.3.9. The later stiuation corresponding to the arranging the circular rings in a triangular alttice (α= 60°) and the former one correponding to the square lattice while the other deging parameters are kept same as in first example. In the triangular lattice configuration the circular rings are more coupled, so that the resonanse frequencies are shifted towards to the higher bands and bandwiths are also broadened. These results are expected and similar effects are also obtained in the other type Chiro-FSS comprised of narrow strips, cross dipoles etc.. The results are obtained in both case for the follwing desing parameters; $D_1=D_2$=10 mm, ϵ_r=1.06, t= 5 mm and three different values of chirality admittance ξ= 0.0 (dielectric), 0.0015 and 0.0025 mho.

When only dielectric constant is changed (ϵ_r=1.32) for the trinagular lattice configuration some noticable differences are obtained and corresponig results of spectral characteritics are given in Figure 4.3.10. Comparision of Figure 4.3.10 with Figure 4.3.4 gives that when the dielectric constant of the slab increased t0 ϵ_r=1.32, the resonance bandwidths of all the resonances obtained for triangular lattice geometry are more larger than the resonance bandwidths in the reflection curve corresponding to the square lattice geometry. Another interesting results observed is that in contrast to the case of ϵ_r=1.06, in the case of ϵ_r=1.32 more resonances are obtained for the square lattice than that of triangular lattice geometry. To conclude these results, the increase in bandwidth of the resonances is not due to only arranging the arrays more coupled but also owing to the relatively higher dielectric constant of the chiral slab.

The all results presented in the previous cases are obtained for the normally incident TE polarised plane wave. Due to symmetry of the geometry, excatly same results are also obtained for TM polarised plane wave illumination, as expected. In other words, the

121

reflection and transmission characteritics of the both conventional FSS and Chiro-FSS comprised of circular rings are the same for both TE and TM polarised plane wave excitation.

It ỷs obtained that the spectral respones of the cChiro-FSS with circular rings remain unchanged when the screen is illuminated by a incident TE and TM plane waves having only zero polar angle, $\theta = 0°$. This is expected due to preserving the symmetry of the problem with respect to the azimuth angle, ϕ, of the circular ring scatteres. As an illustrative example of the case of existing only non-zero azimuth angle, ϕ, the variation of the power reflection and transmission coefficient of the Chiro-FSS comprised of circular rings are shown in Figure 4.3.11. The Chiro-FSS is illuminated by a TE plane wave having $\theta = 0°$ and $\phi = 45°$. The design parameters of the Chiro-FSS are assumed to be same as the first eaxmple, i.e., $D_1 = D_2 = 10$ mm, t = 5 mm, $\epsilon_r = 1.06$, square array lattice, $R_i = 3.7$ mm and $R_o = 4.7$ mm for three values of chirality admittance $\xi = 0.0$ (dielectric), 0.0015 and 0.0025 mho. The results presented in Figure 4.3.11 are absolutely same as the results shown in Figure 4.3.2.

Figure 4.3.12 and Figure4.3.13 are the plots of the power reflection and transmission coeffcents of the Chiro-FSS haqving the same design parameters s the previous example, for theobliquely TE and TM plane wave illuminations with $\theta = 30°$ and $\phi = 30°$, respectively. It is seen that from Figure 4.3.12, for $\xi = 0.015$ mho the spectral characteritics of the Chiro-FSS with circular ringr are very similar to that of a dielectrically backed FSS ($\xi = 0.0$). As the chirality admittance of the slab is increased to $\xi = 0.0025$ mho, some variations are obtained after first resonance frequency. Magnitude of the reflected cross-polar (TM) component are relatively too small compared with the magnitue of the co-polar (TE) component. In the transmission characteristics, for both co- and cross-polar coefficients does not reach to unity, i.e., neither full transmission is obtained for both components.

The reflection characteristics of the Chiro-FSS for TM illimunation case are quite different than the response of the TE incidence case. Although the cross-polar (TE) reflection is somewhat similar to the case of TE illumination, the spectral characteristics of the other components are very sensitive to the frequency of the excitation field for the

chirality admittance of ξ= 0.0015 and 0.0025 mho. Note that resonance frequency of the Chiro-FSS for TM illuminatin are almost the same as the resonance frequency of the TE case.

When the polar angle θ, is steered from 30° to 45° of the incident plane wave, the spectral characteritics of the Chiro-FSS are plotted in Figure 4.3.14 and Figure 4.3.15 for TE and TM polarised plane wave excitation respectively. Generally, the reflection and transmission characteristics obtained for both polarisations show many similarities with the previous example (θ =30°, ϕ= 0°). But some differences are also observed such as, increasing the polar angle θ to 45° shifts the resonance frequencies to the higher band and bandwidths associated are more larger for both TE and TM polarisation case. Another feature observed for TM incidence case is that, almost full transmission is obtained for high value of chirality admittance, ξ= 0.0025 mho.

The last example presented is the variation of power reflection and transmission characteristics of the Chiro-FSS having the same structure as in the previous example as a function of frequency as illustrated in Figure 4.3.16 and Figure 4.3.17 when the screen is illuminated by TE and TM polarised plane wave with θ =30°, ϕ= 30°, respectively. The results indicate that for this case the spectral characteritics of the Chiro-FSS are very sensitive to the frequency. It can be seen that from the figures, for both polarisation the cross-polar components are rather small comparing with the cross-polar components. Full transmission (null in reflection) is not observed for both polarisation. A distinguishable feature obtained between the TE and TM polarisation is that, for high value of chirality admittance ξ= 0.0025 mho, a second resonance is obtained for TE polarisation case whereas for TM polarisation no higher resonances are obtained in the reflection characteristics of the Chiro-FSS.

According to the results, the general spectral characteristics of the Chiro-FSS comprised of circular rings can be summarized as;

- Similar ro the other type of Chiro-FSS comprised of cross dipoles, narrow strips. etc.. the spectral characteristics of the Chiro-FSS comprised of chiral slab having a small value of chirality admittance resembles to the spectral characteristics of the conventional FSS (zero chirality).

- Although the first resonance frequency obtained for all case is nearly same as the resonance frequency of the conventional FSS, frequencies and badwidths associated for higher resonances strongly depend upon the value of the chirality admittance of the slab.

- Decresing the radius of the circular rings causes some variations in the spectral responce of the Chiro-FSS, such that resonance frequencies are shifted to the higher frequecy band and more narrow bandwidths are obtained.

- Another interesting feature of the Chiro-FSS with circular rings is observed in the triangular array configuration. For small values of dielectric constant of the slab the bandwidth of the resonances are enlarged slightly, but when the dielectric constant is further increased the broadening of the resonance bandwidths is considerable.

- The spectral response of the Chiro-FSS with circular ring are not changed when the screen is illuminated having zero polar angle is due to the symmetry of the geometry with respect to the azimuth direction.

- Altough for the all case of normal incidence the multiple resonance are obtained in the spectral response of the Chiro-FSS with circular ring, in the case of obliquely incidence the multiple resonances can be obtainable for some cases.

- Comparision of the spectral characteritics of the Chiro-FSS reveals that, this type of Chiro-FSSs are less sensitive to the variation of the polar and azimuth angle of the obliquely inciden plane wave.
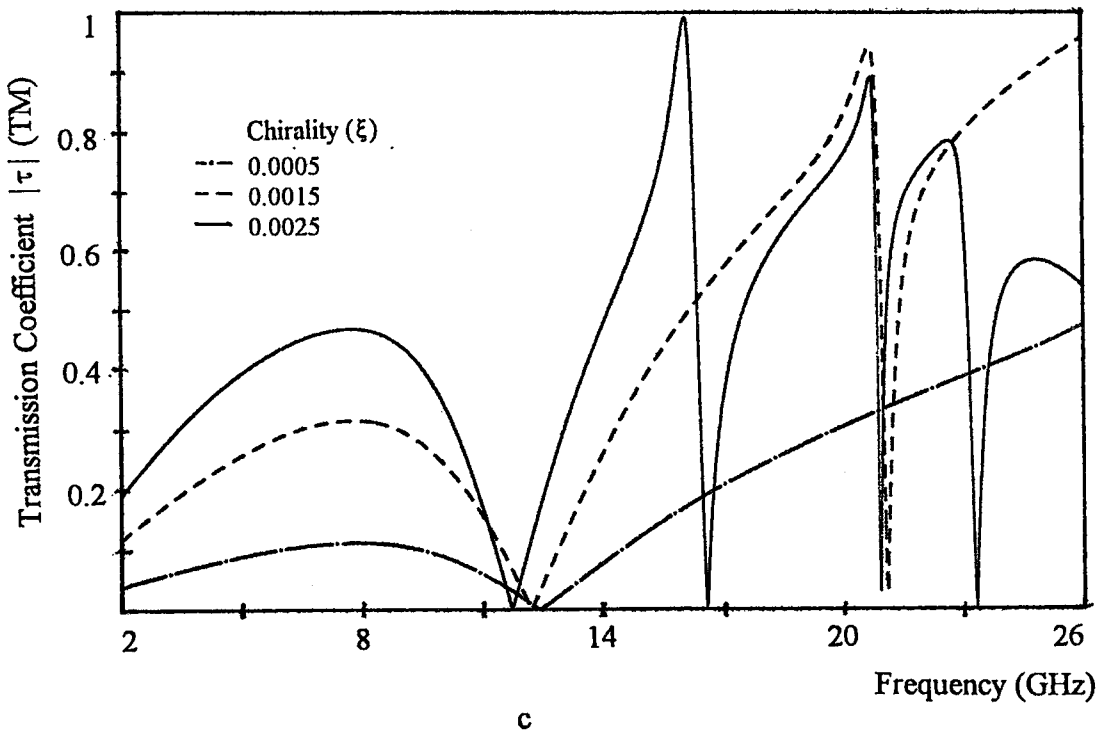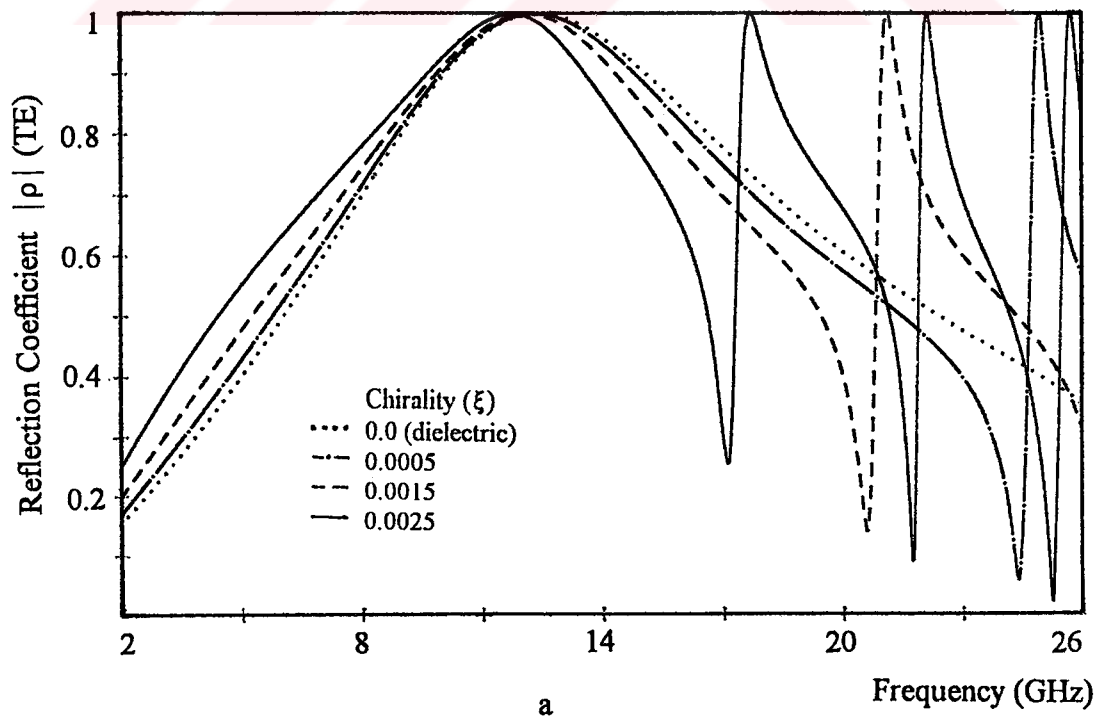
a

b

125

c
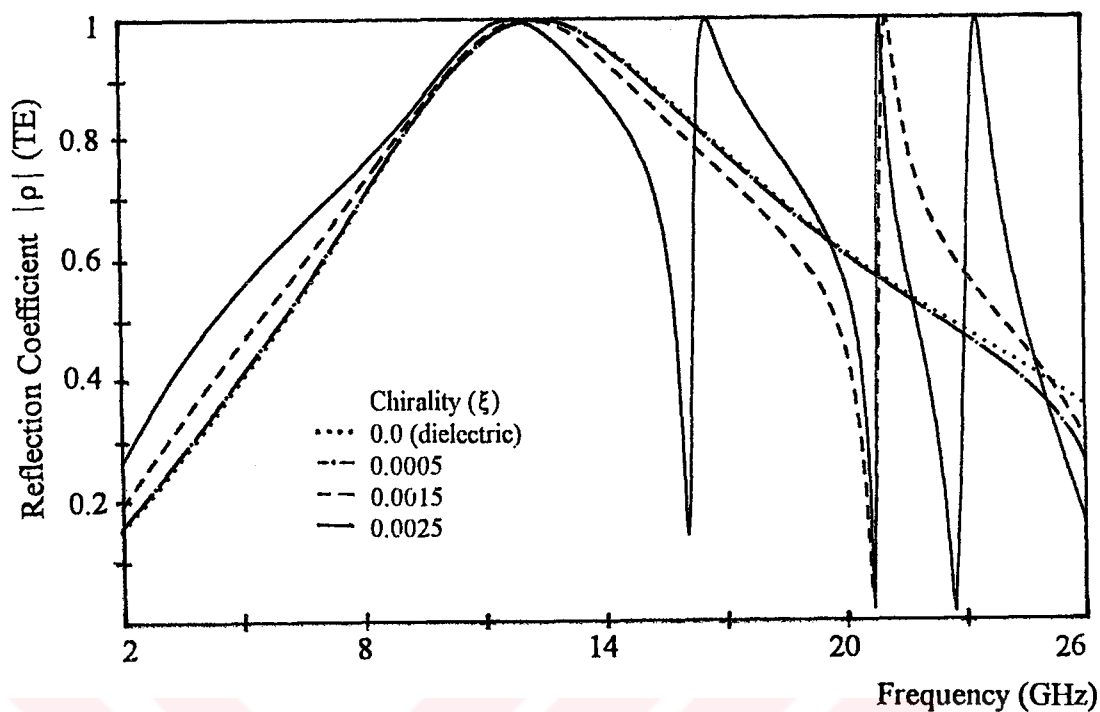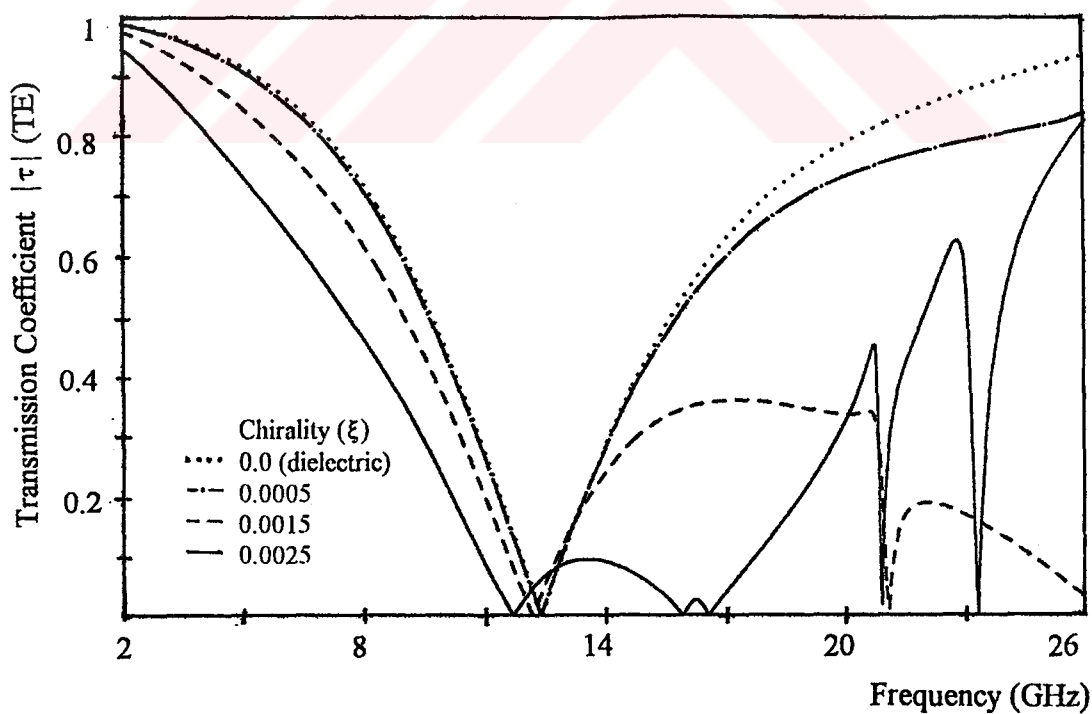
Figure 4.3.2　Spectral characteristics of Chiro-FSS with circular rings; TE incidence
(ϕ= 0°, θ=0°), square lattice (α= 90°), D_1=D_2=10 mm, R_i =3.7 mm,
R_o= 4.7 mm, ϵ_r=1.06, t = 5 mm. a) Reflection coefficient (TE),
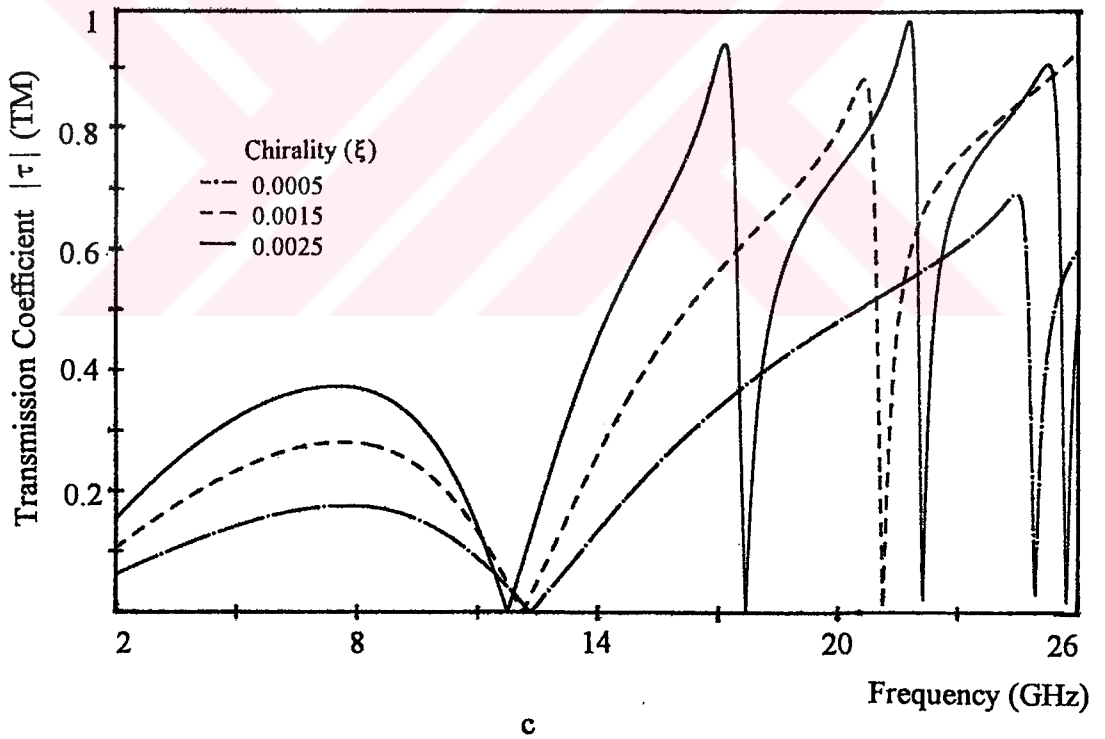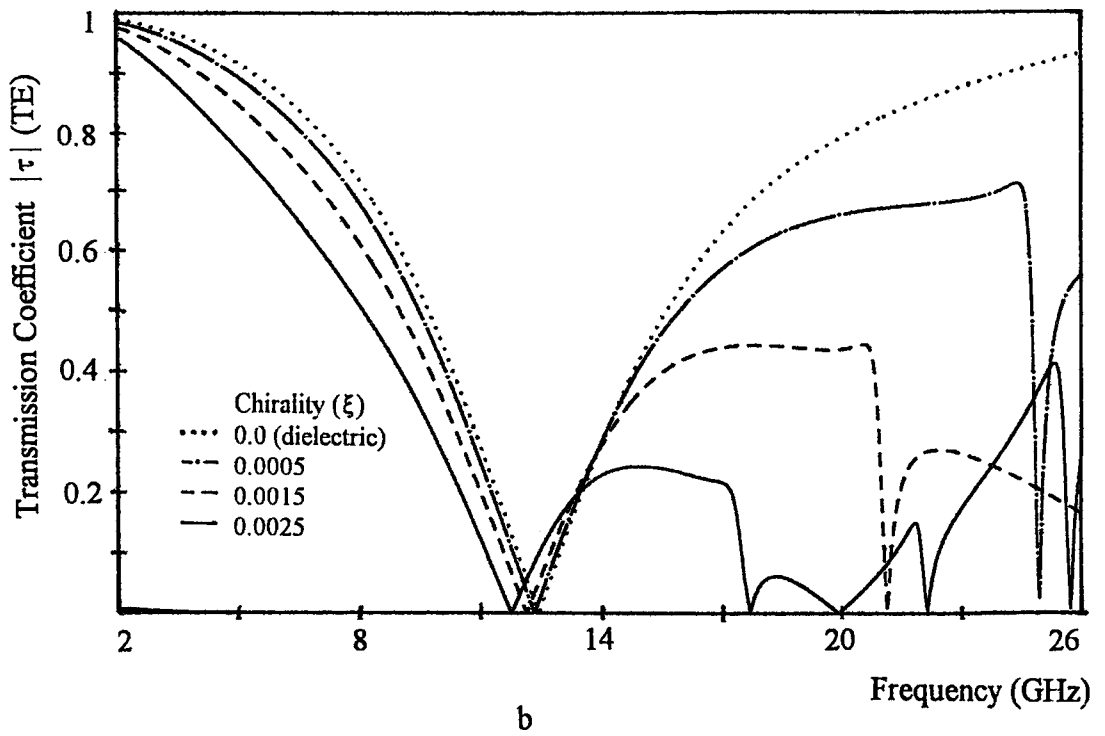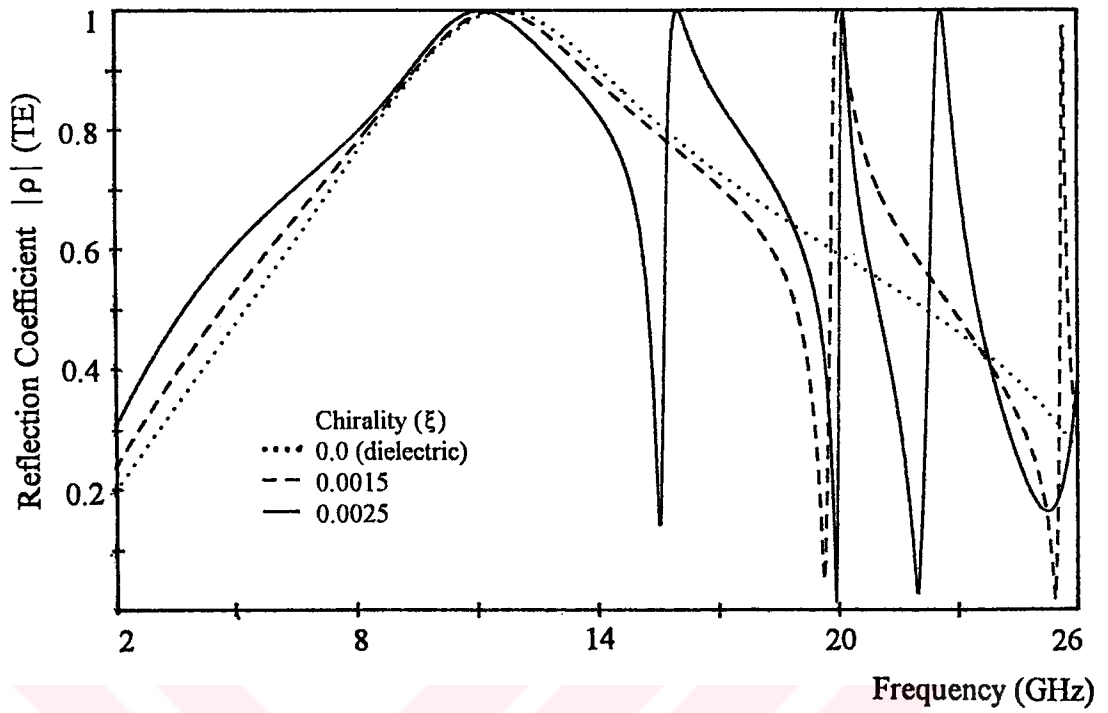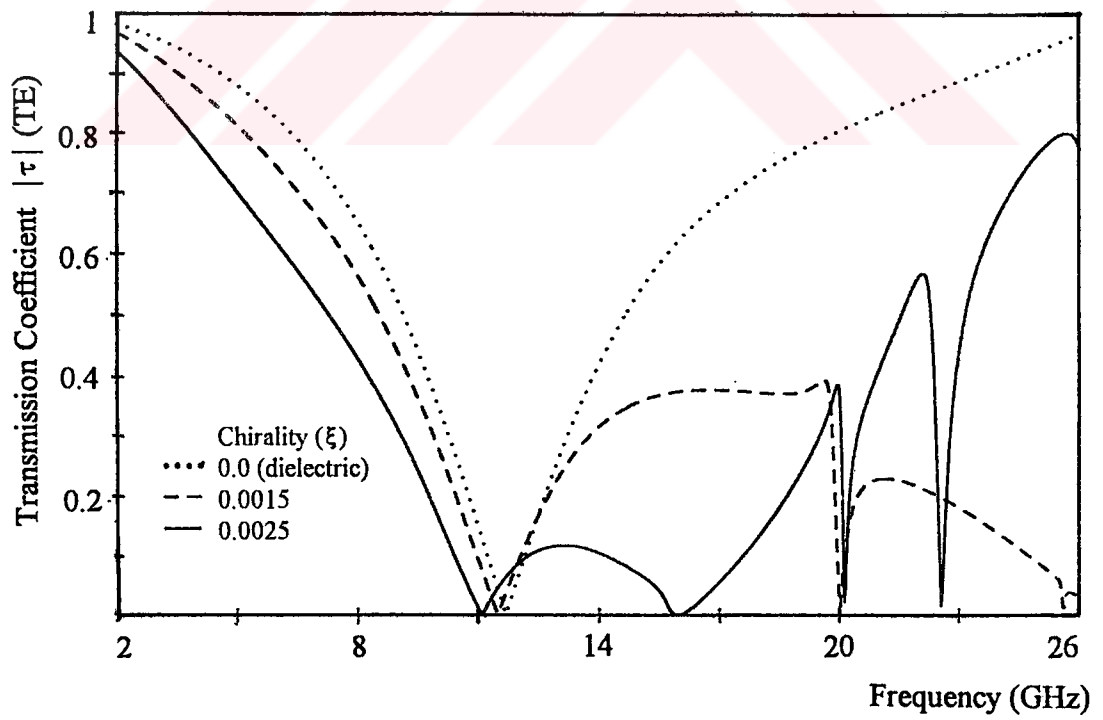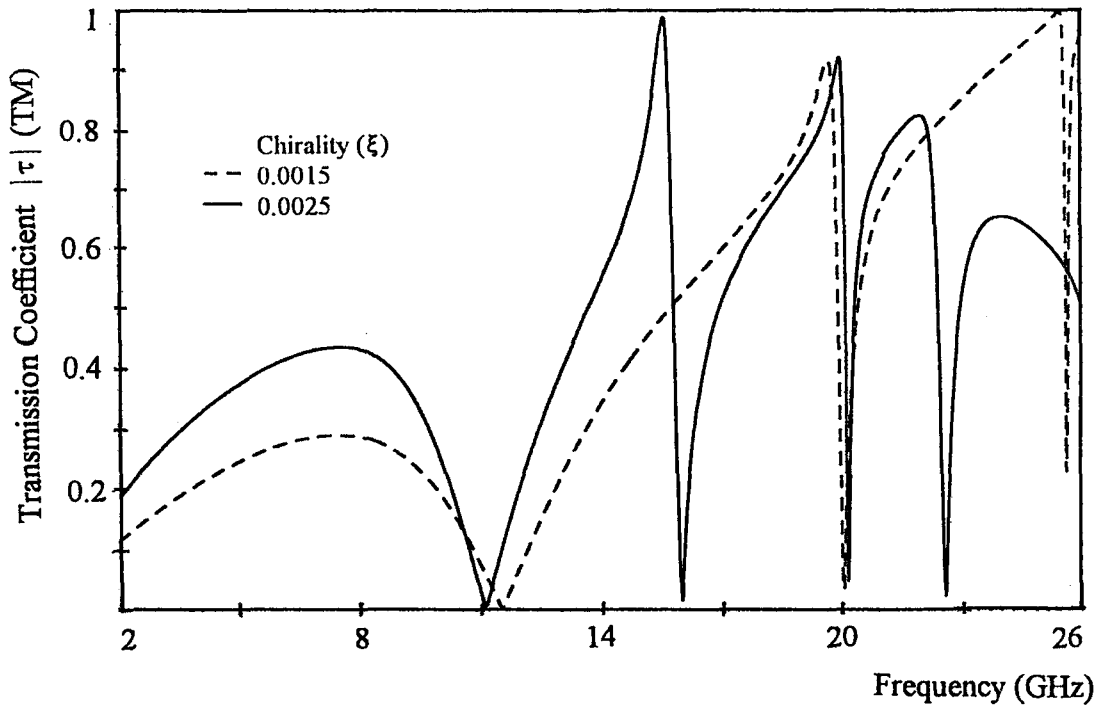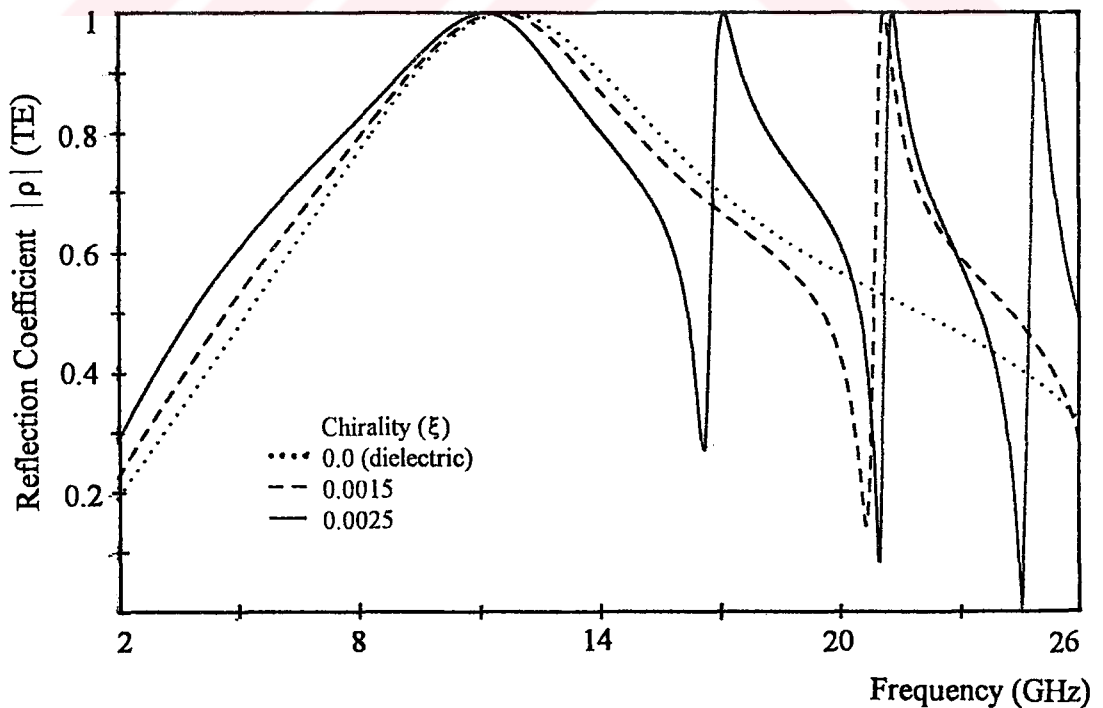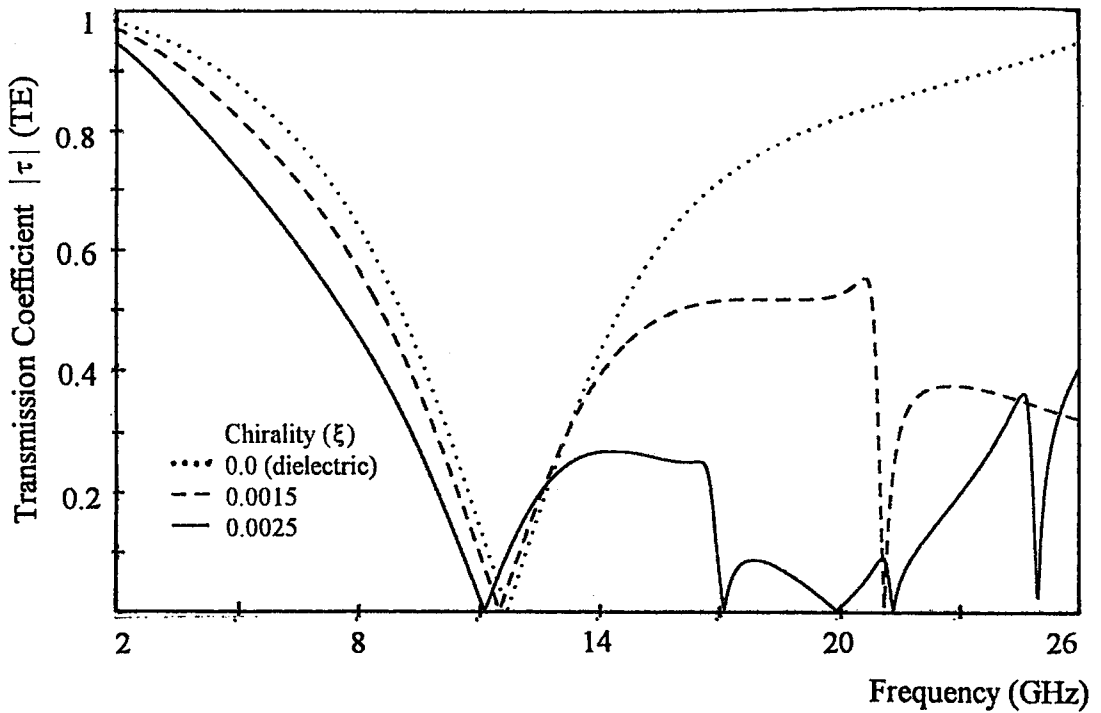b) Transmission coefficient (TE), c) Transmission coefficient (TM).

a

Figure 4.3.3   Spectral characteristics of Chiro-FSS with circular rings; TE incidence
(ϕ= 0°, θ=0°), square lattice (α= 90°), D_1=D_2=10 mm, R_i =3.7 mm,
R_o= 4.7 mm, ϵ_r=1.06, t = 4 mm. a) Reflection coefficient (TE),
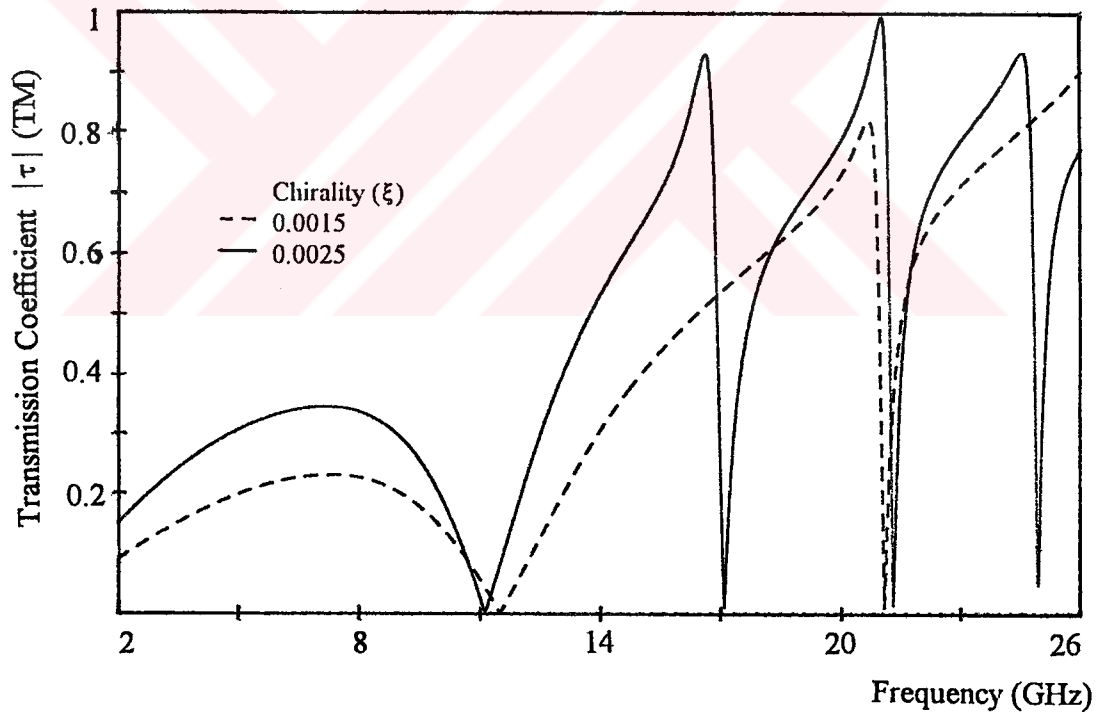b) Transmission coefficient (TE), c) Transmission coefficient (TM).

127

a

b

128

c

Figure 4.3.4   Spectral characteristics of Chiro-FSS with circular rings; TE incidence
($\phi = 0°$, $\theta = 0°$), square lattice ($\alpha = 90°$), $D_1 = D_2 = 10$ mm, $R_i = 3.7$ mm,
$R_o = 4.7$ mm, $\epsilon_r = 1.32$, t = 5 mm. a) Reflection coefficient (TE),
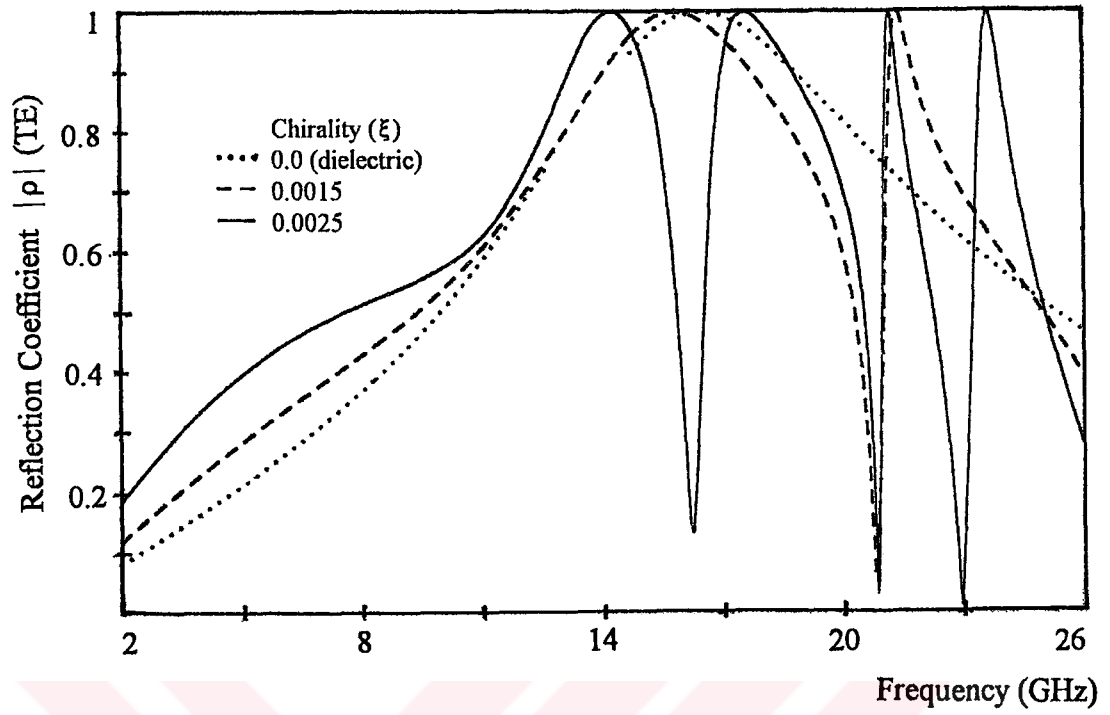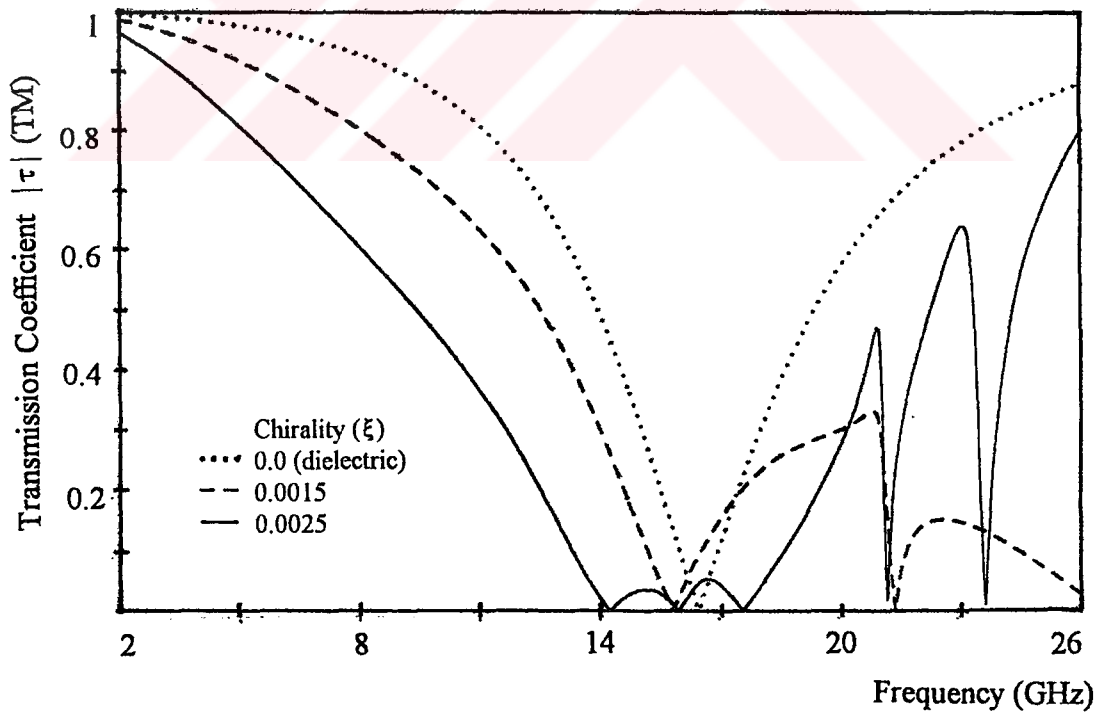b) Transmission coefficient (TE), c) Transmission coefficient (TM).

a

129

Figure 4.3.5   Spectral characteristics of Chiro-FSS with circular rings; TE incidence

(ϕ= 0°, θ=0°), square lattice (α= 90°), D_1=D_2=10 mm, R_i =3.7 mm,

R_o= 4.7 mm, ϵ_r=1.32, t = 4 mm. a) Reflection coefficient (TE),

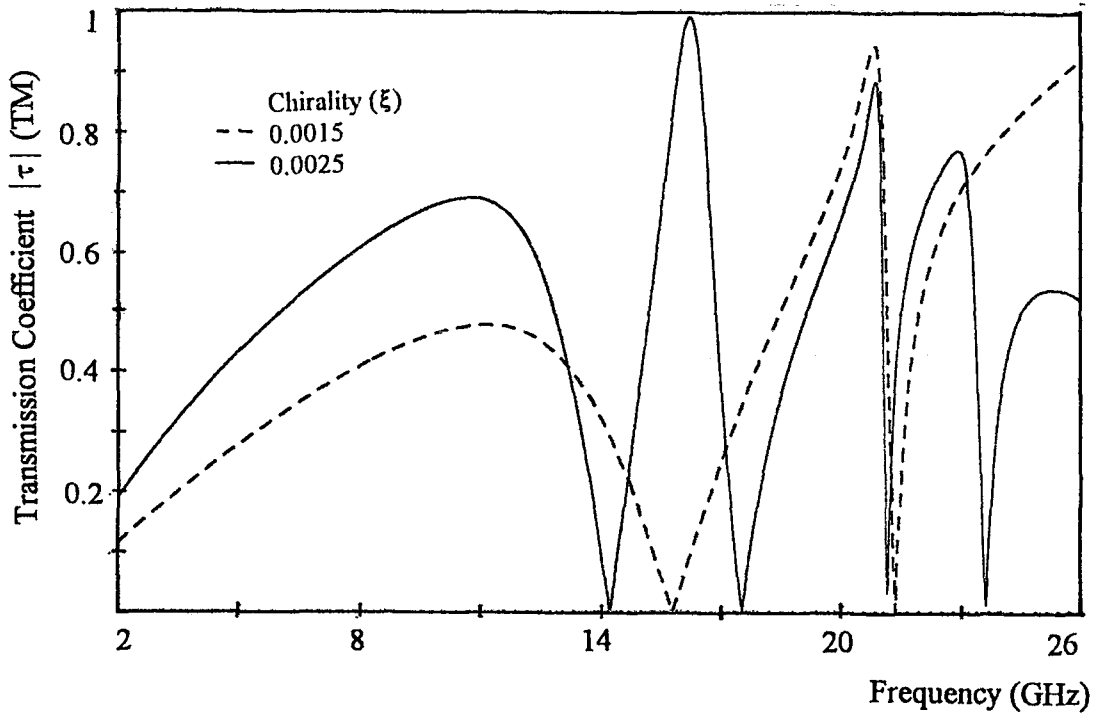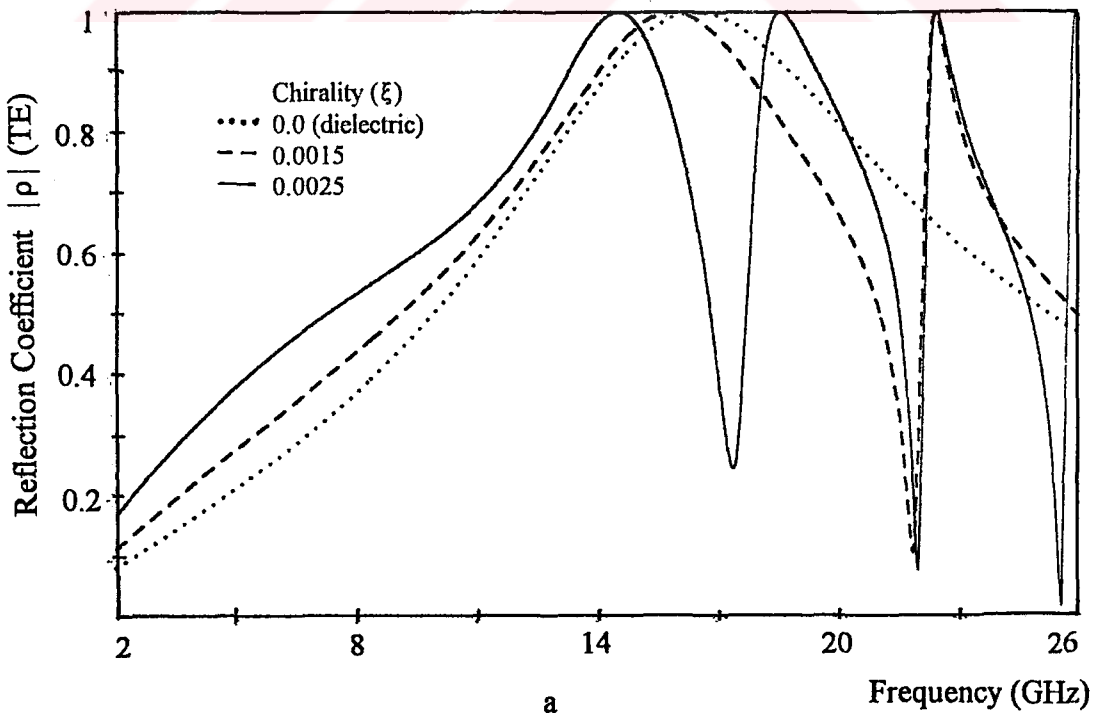b) Transmission coefficient (TE), c) Transmission coefficient (TM).

a

b

c

Figure 4.3.6   Spectral characteristics of Chiro-FSS with circular rings; TE incidence
(ϕ= 0°, θ=0°), square lattice (α= 90°), D_1=D_2=10 mm, R_i = 3 mm,
R_o= 4 mm, ϵ_r=1.06, t = 5 mm. a) Reflection coefficient (TE),
b) Transmission coefficient (TE), c) Transmission coefficient (TM).

a

132

Figure 4.3.7 Spectral characteristics of Chiro-FSS with circular rings; TE incidence
($\phi= 0°$, $\theta=0°$), square lattice ($\alpha= 90°$), $D_1=D_2=10$ mm, $R_i = 3$ mm,
$R_o= 4$ mm, $\epsilon_r=1.06$, t = 4 mm. a) Reflection coefficient (TE),
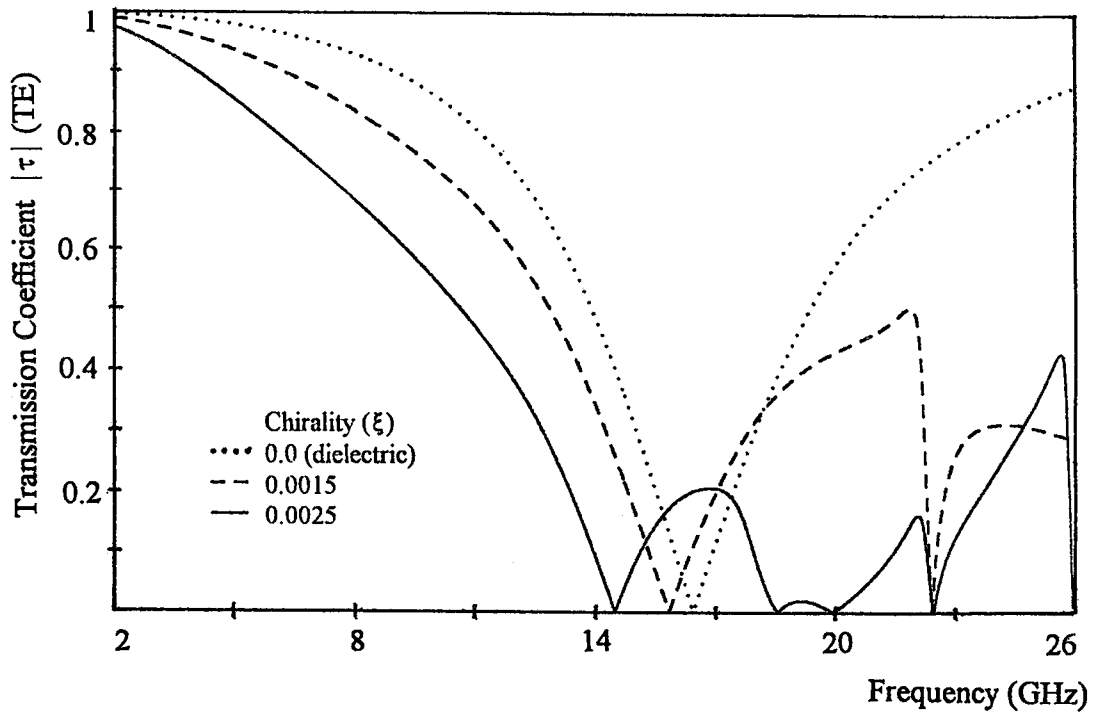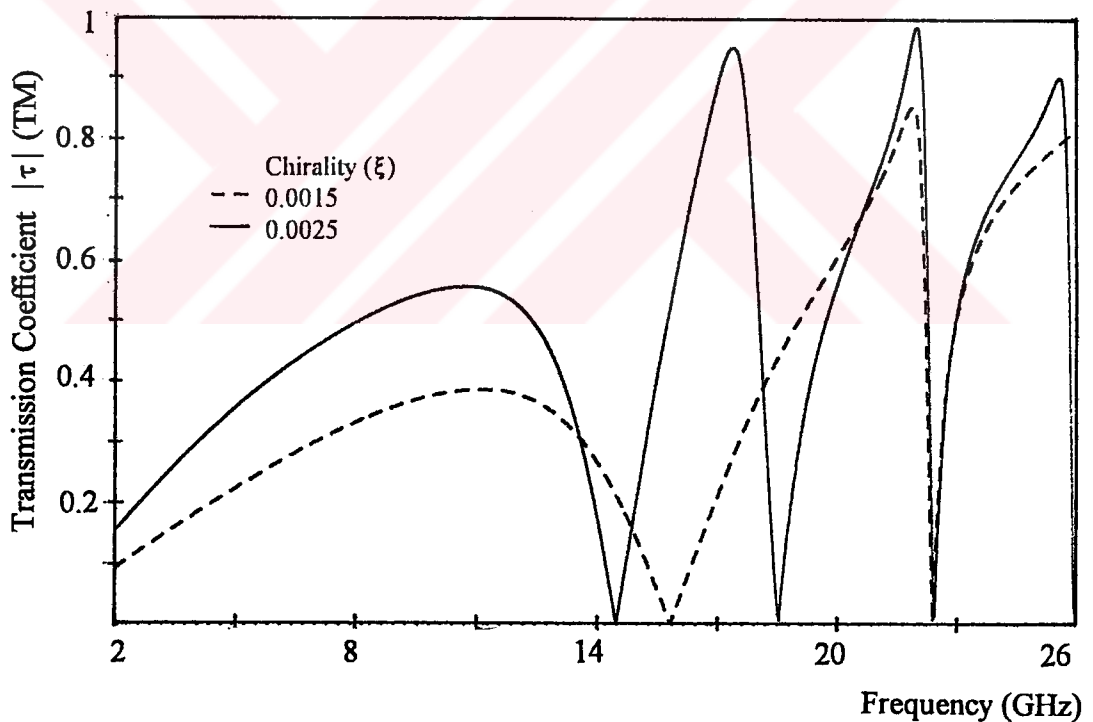b) Transmission coefficient (TE), c) Transmission coefficient (TM).

133

a

b

134

Figure 4.3.8   Spectral characteristics of Chiro-FSS with circular rings; TE incidence
(ϕ= 0°, θ=0°), square lattice (α= 90°), D_1=D_2=10 mm, R_i = 3 mm,
R_o= 4 mm, ϵ_r=1.32, t = 5 mm. a) Reflection coefficient (TE),
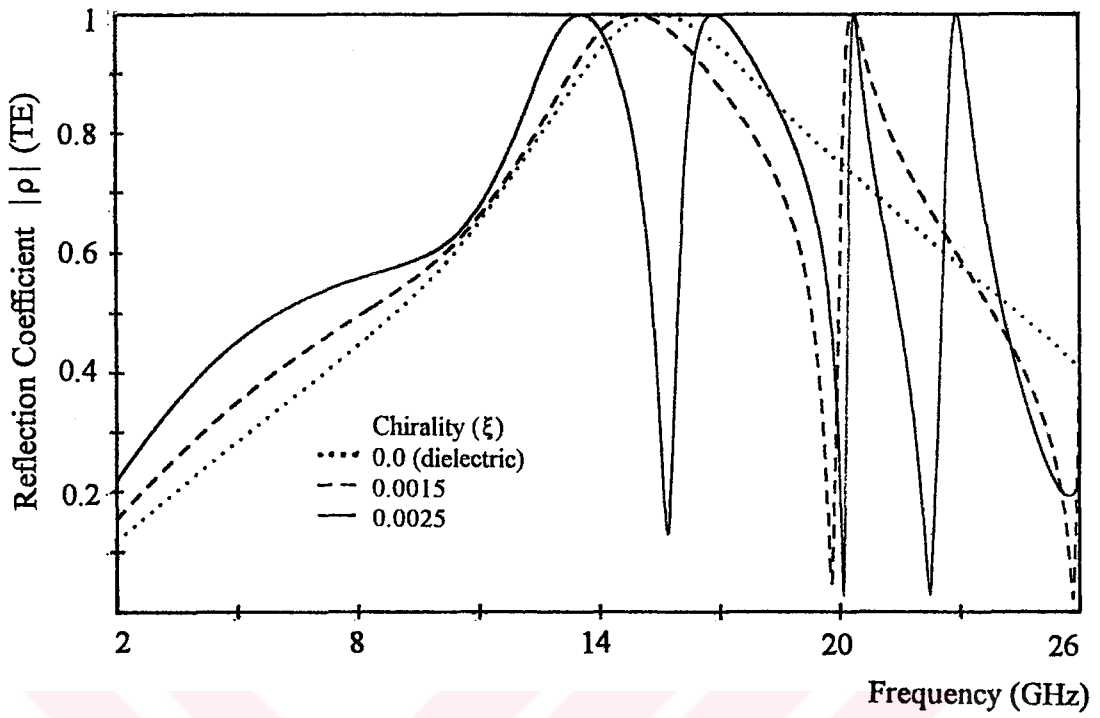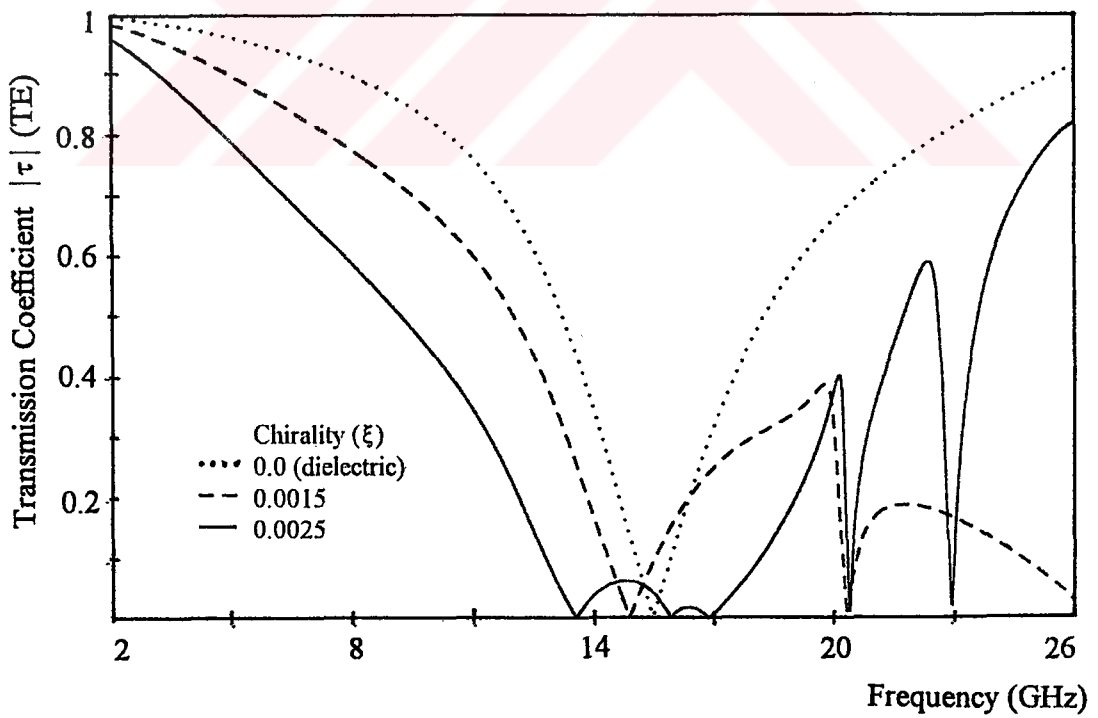b) Transmission coefficient (TE), c) Transmission coefficient (TM).

135

Figure 4.3.9   Spectral characteristics of Chiro-FSS with circular rings; TE incidence
($\phi= 0°$, $\theta=0°$), triangular lattice ($\alpha= 60°$), $D_1=D_2=10$ mm, $R_i = 3.7$ mm,
$R_o= 4.7$ mm, $\epsilon_r=1.06$, t = 5 mm. a) Reflection coefficient (TE),
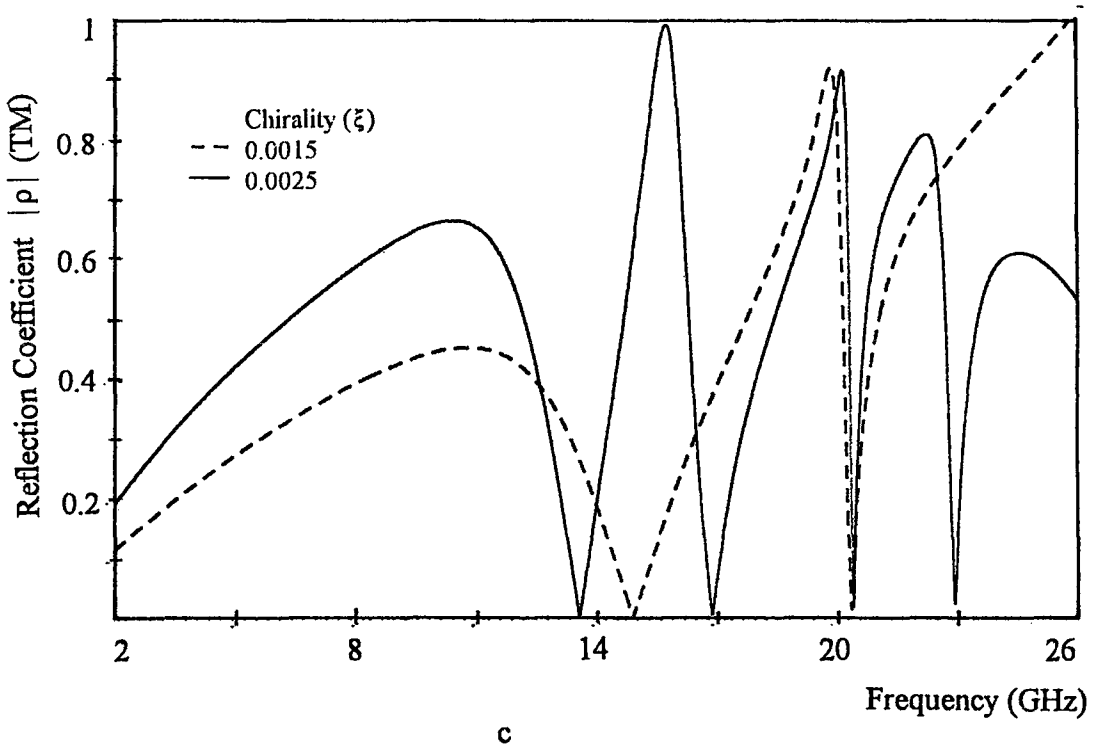b) Transmission coefficient (TE), c) Transmission coefficient (TM).

136

a

b

137

Figure 4.3.10   Spectral characteristics of Chiro-FSS with circular rings; TE incidence

(ϕ= 0°, θ=0°), triangular lattice (α= 60°), D_1=D_2=10 mm, R_i = 3.7 mm,

R_o= 4.7 mm, ϵ_r=1.32, t = 5 mm. a) Reflection coefficient (TE),

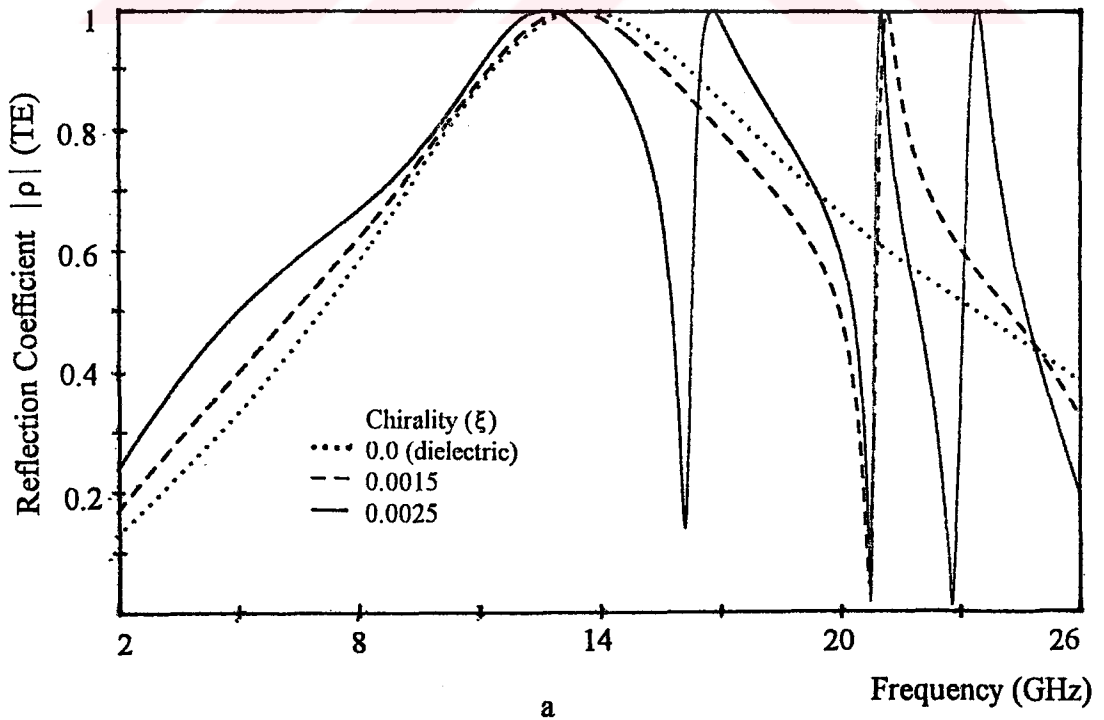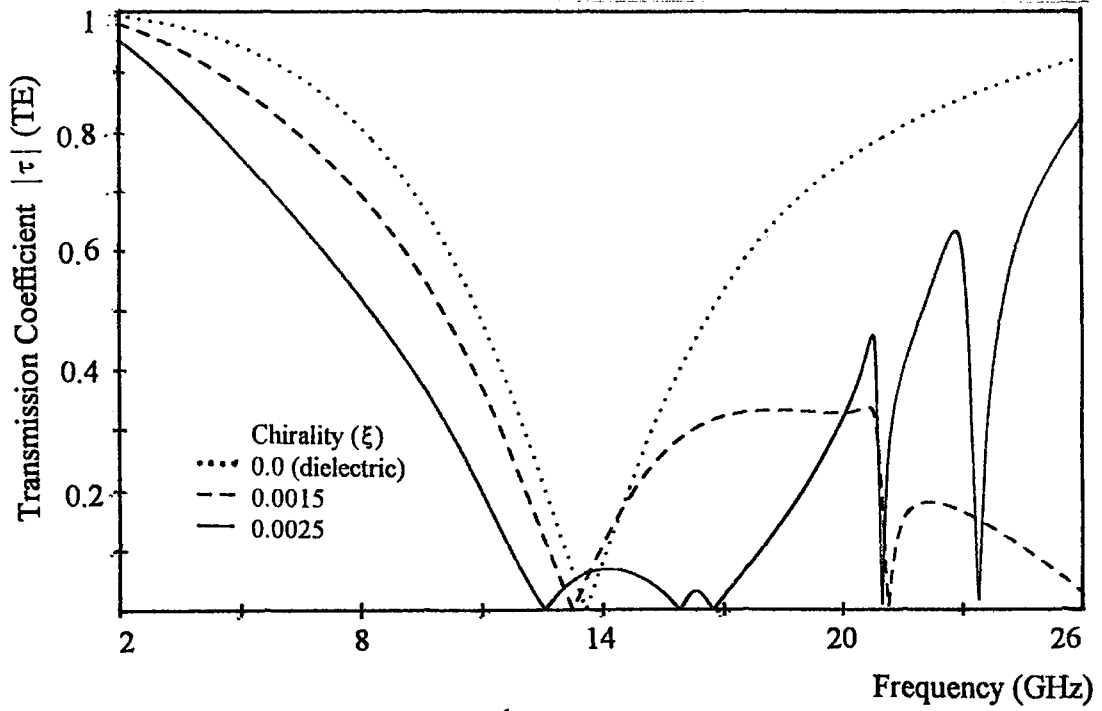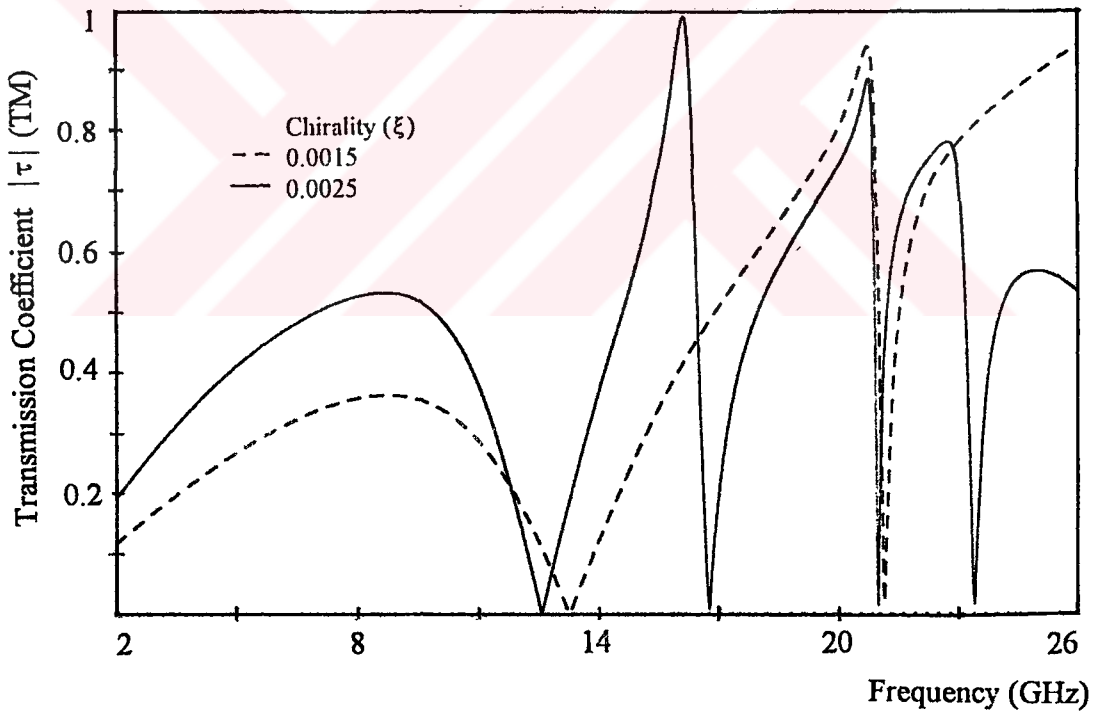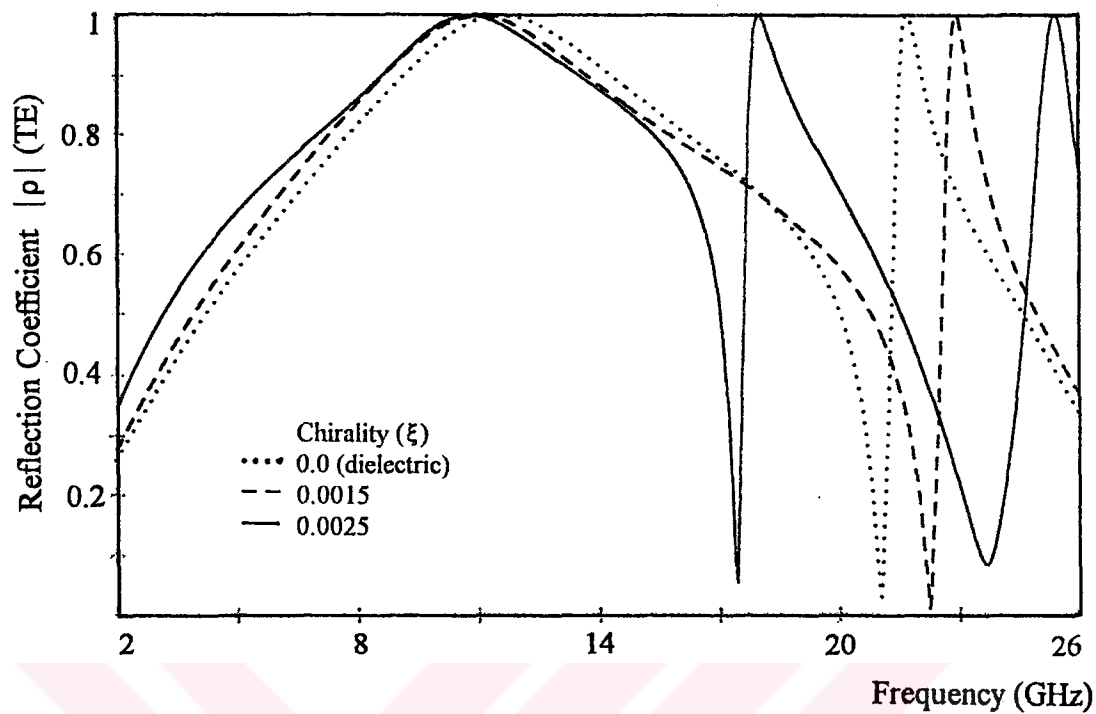b) Transmission coefficient (TE), c) Transmission coefficient (TM).

138

b

c

Figure 4.3.11   Spectral characteristics of Chiro-FSS with circular rings; TE incidence

(ϕ= 45°, θ=0°), square lattice (α= 90°), D_1=D_2=10 mm, R_i = 3.7 mm,

R_o= 4.7 mm, ϵ_r=1.06, t = 5 mm. a) Power reflection coefficient (TE),

b) Power transmission coefficient (TE), c) Power transmission coefficient

(TM).

139

Chirality (ξ)
..... 0.0 (dielectric)
- - - 0.0015
—— 0.0025

Power Reflection Coefficient |ρ|² (TE)

1
0.8
0.6
0.4
0.2

2   6   10   14   18   20
Frequency (GHz)

a

Chirality (ξ)
- - - 0.0015
—— 0.0025

Power Reflection Coefficient |ρ|² (TM)

1
0.8
0.6
0.4
0.2

2   6   10   14   18   20
Frequency (GHz)

b

140
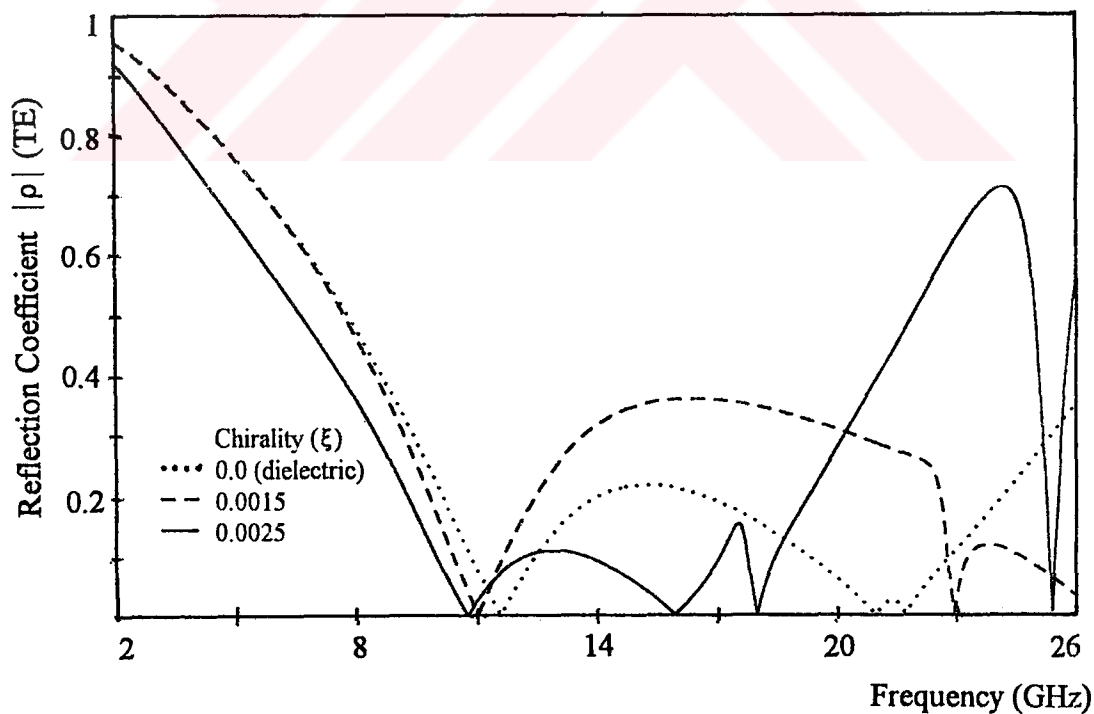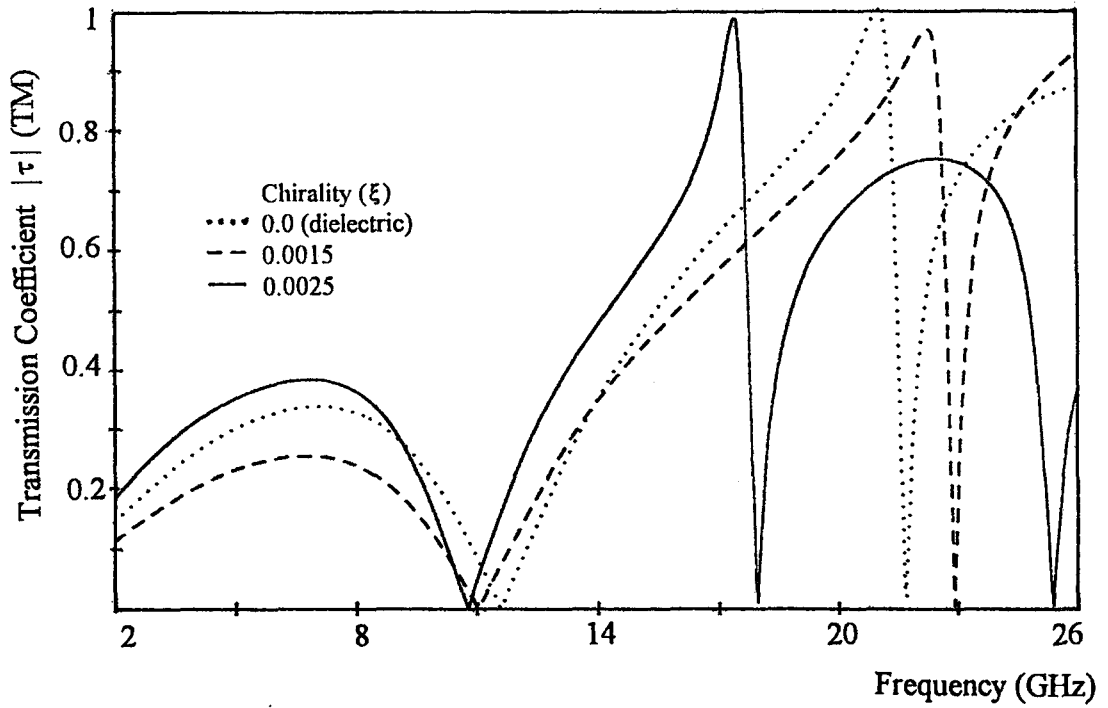
Figure 4.3.12 Spectral characteristics of Chiro-FSS with circular rings; TE incidence
(ϕ= 0°, θ=30°), square lattice (α= 90°), D_1=D_2=10 mm, R_i = 3.7 mm,
R_o= 4.7 mm, ϵ_r=1.06, t = 5 mm. a) Power reflection coefficient (TE),
b) Power reflection coefficient (TM), c) Power transmission coefficient
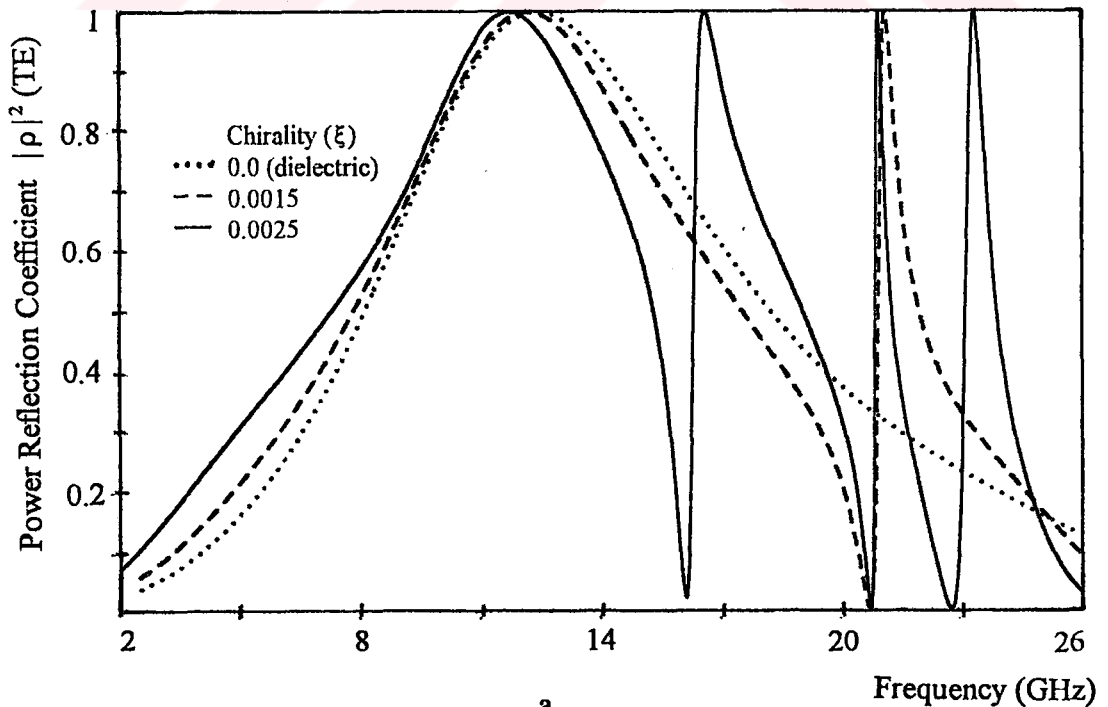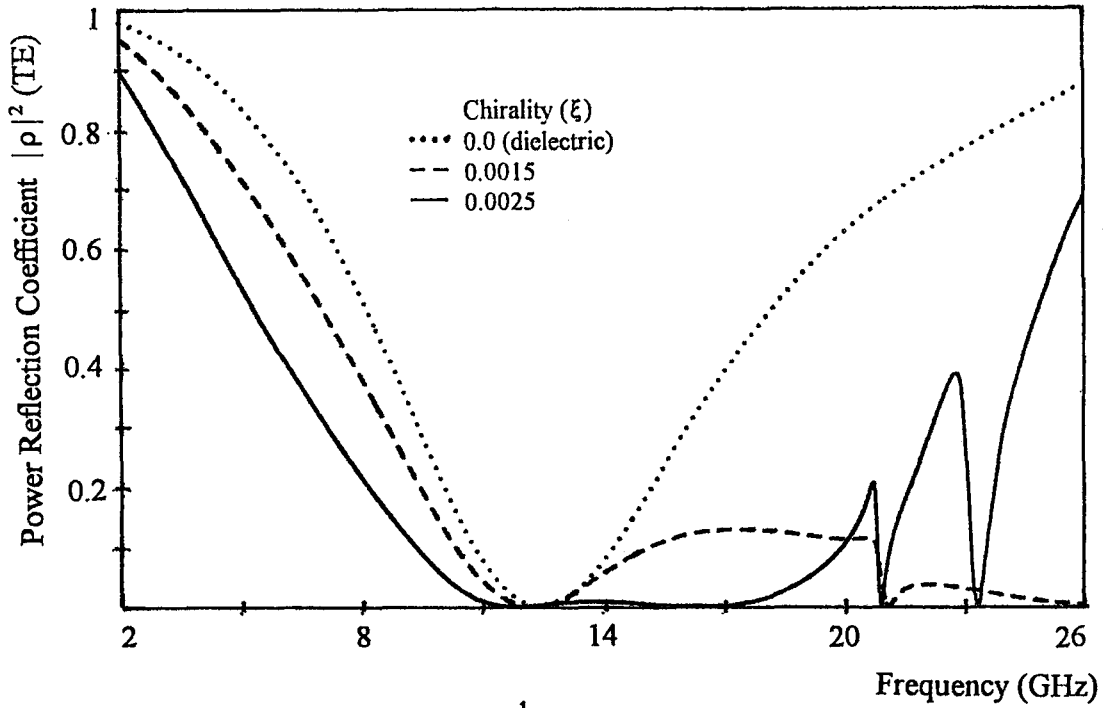(TE), d) Power transmission coefficient (TM).

a

b

142

Figure 4.3.13 Spectral characteristics of Chiro-FSS with circular rings; TM incidence
($\phi= 0°$, $\theta=30°$), square lattice ($\alpha= 90°$), $D_1=D_2=10$ mm, $R_i = 3.7$ mm,
$R_o= 4.7$ mm, $\epsilon_r=1.06$, t = 5 mm. a) Power reflection coefficient (TE),
b) Power reflection coefficient (TM), c) Power transmission coefficient
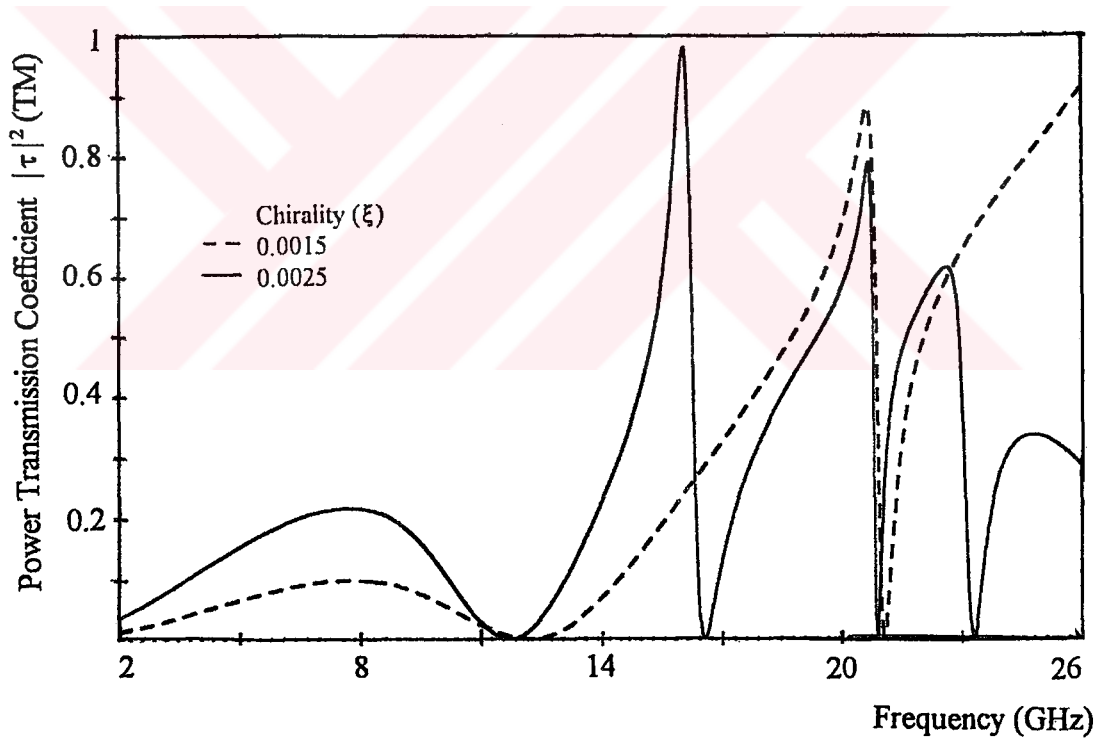(TE), d) Power transmission coefficient (TM).

143

a

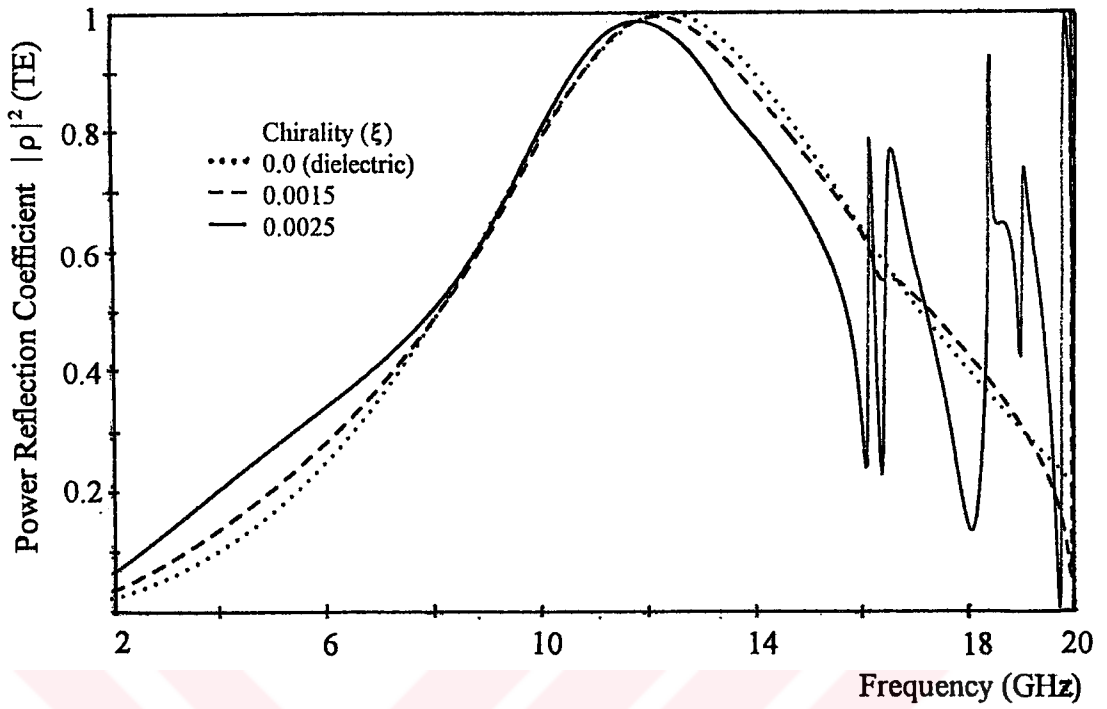
b

144

Figure 4.3.14   Spectral characteristics of Chiro-FSS with circular rings; TE incidence

($\phi = 0°$, $\theta = 45°$), square lattice ($\alpha = 90°$), $D_1 = D_2 = 10$ mm, $R_i = 3.7$ mm,

$R_o = 4.7$ mm, $\epsilon_r = 1.06$, t = 5 mm. a) Power reflection coefficient (TE),

b) Power reflection coefficient (TM), c) Power transmission coefficient

(TE), d) Power transmission coefficient (TM).

145

a

b

146
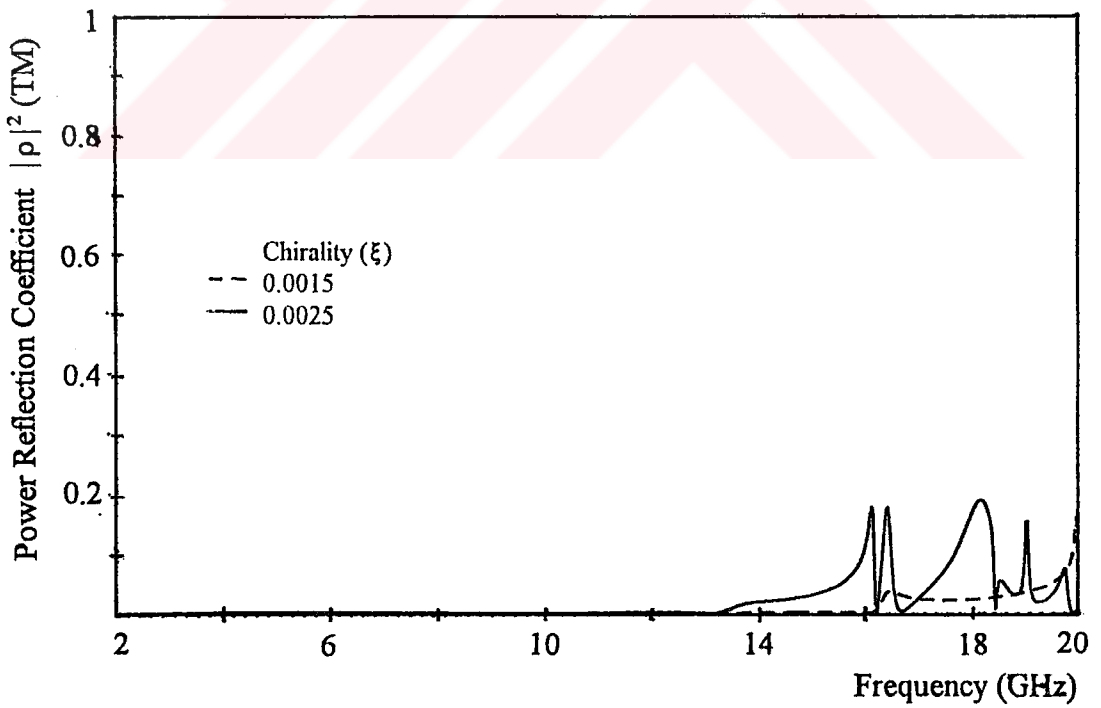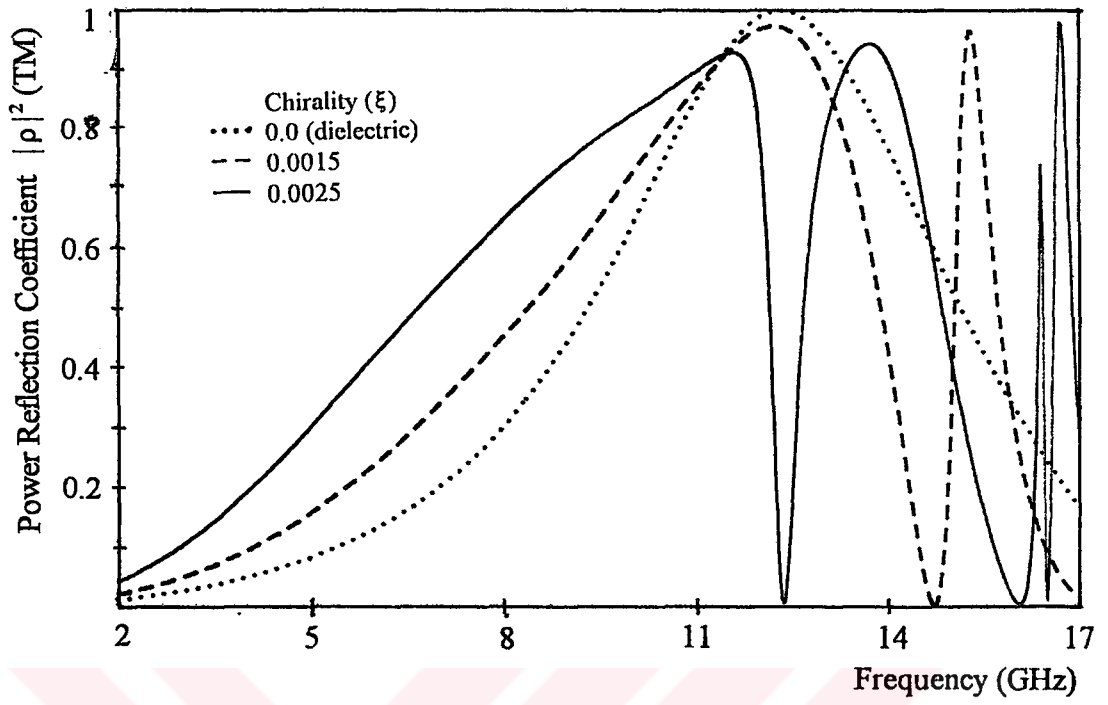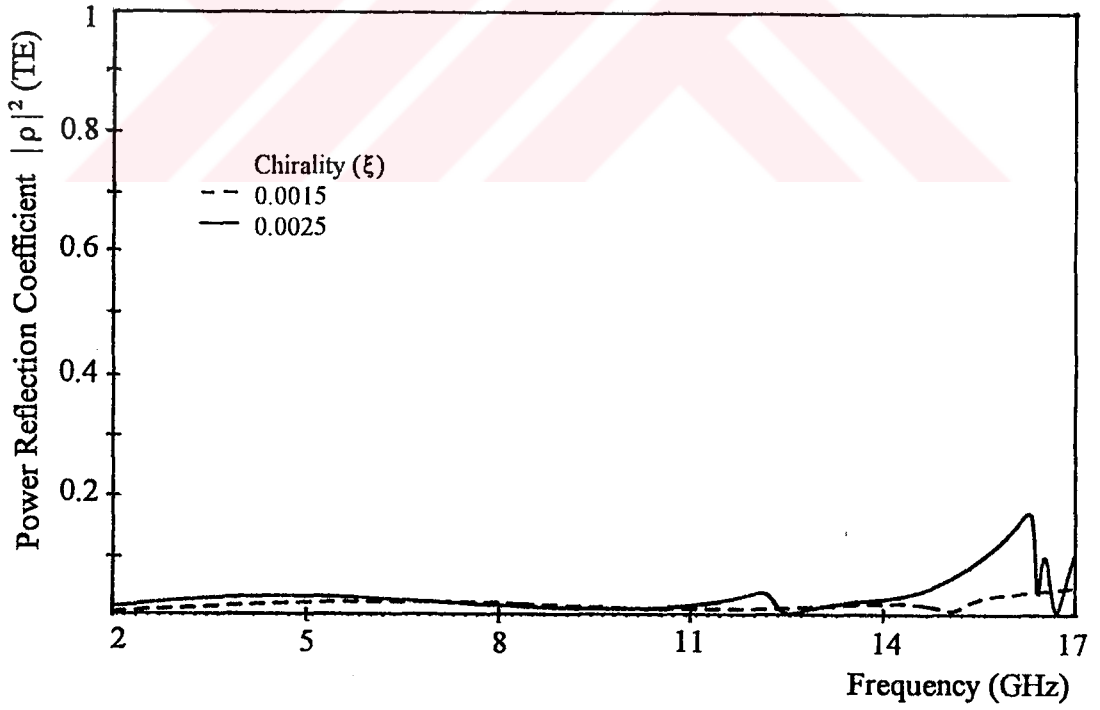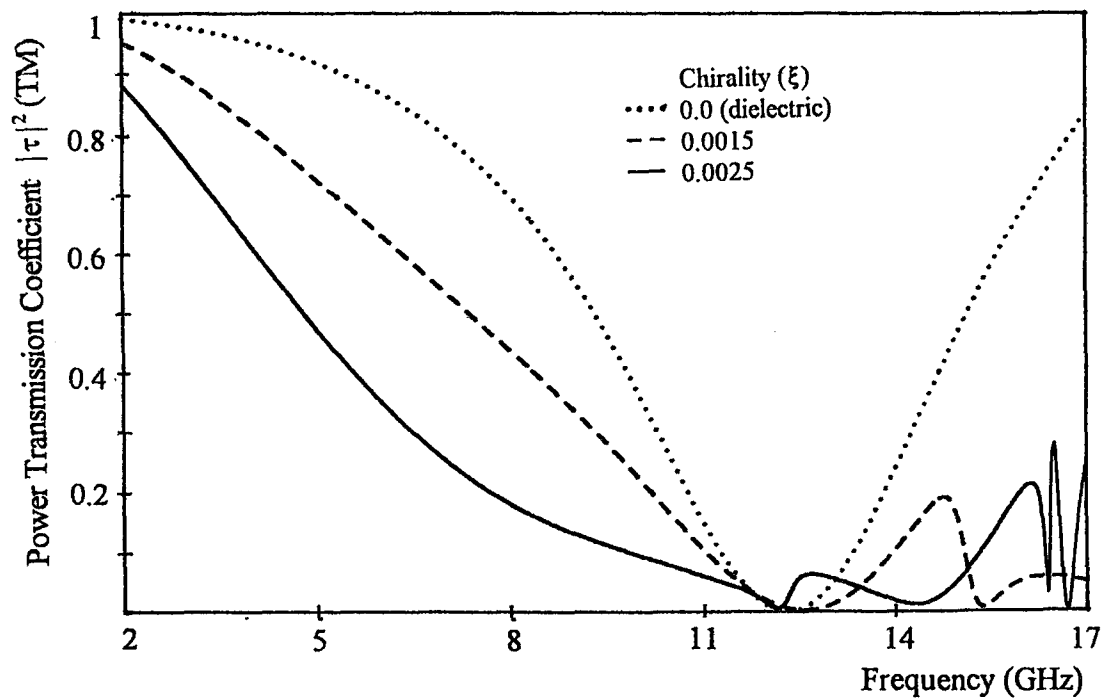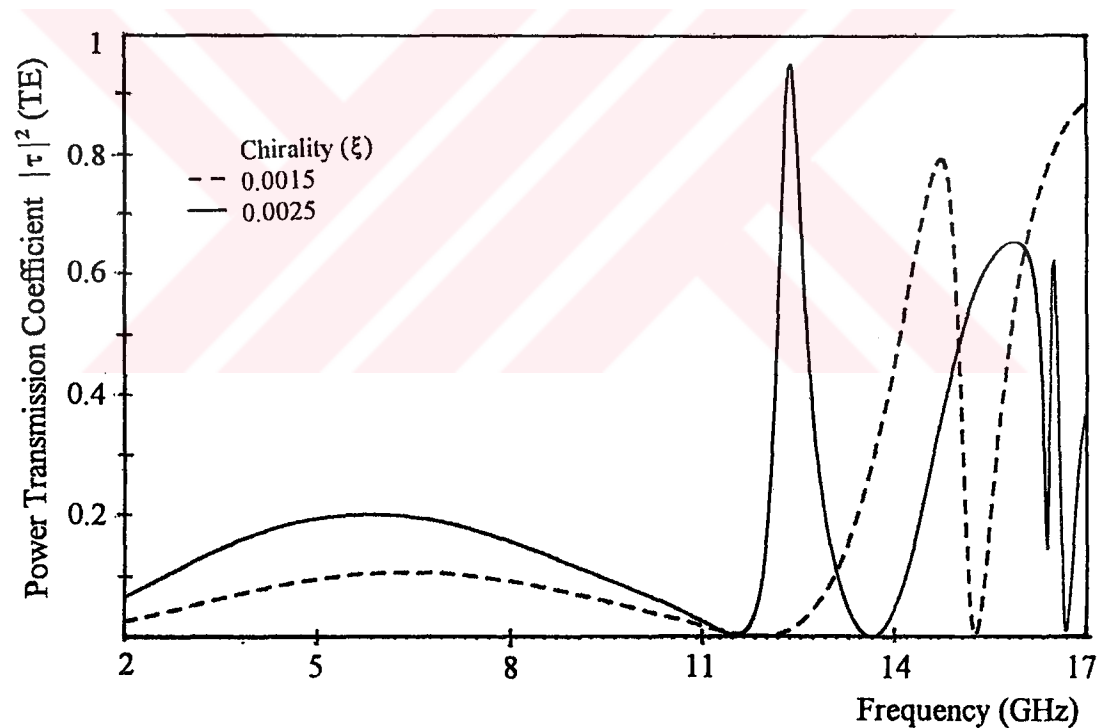
Figure 4.3.15   Spectral characteristics of Chiro-FSS with circular rings; TM incidence
(ϕ= 0°, θ=45°), square lattice (α= 90°), D_1=D_2=10 mm, R_i = 3.7 mm,
R_o= 4.7 mm, ϵ_r=1.06, t = 5 mm. a) Power reflection coefficient (TE),
b) Power reflection coefficient (TM), c) Power transmission coefficient
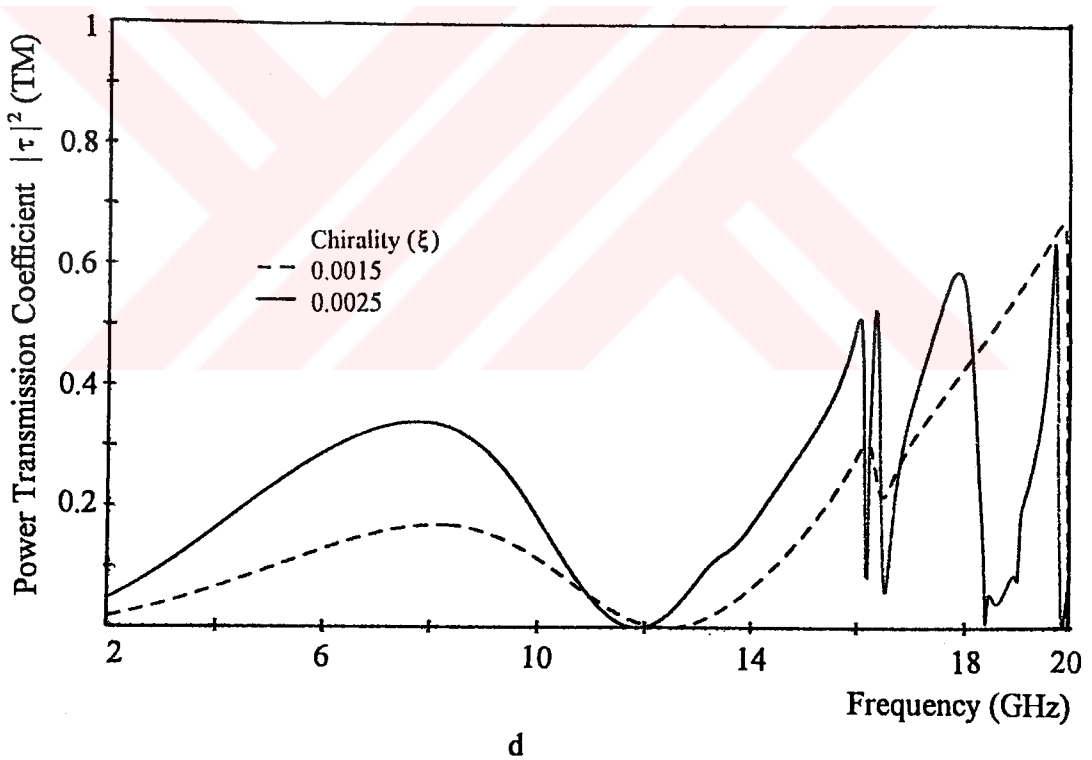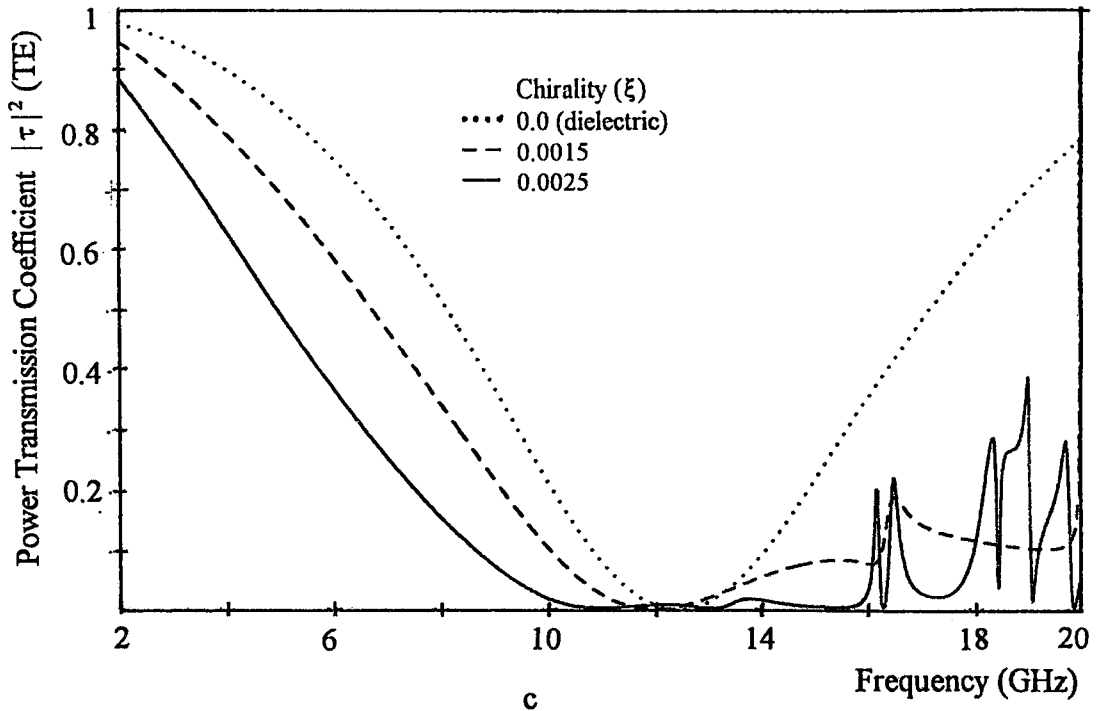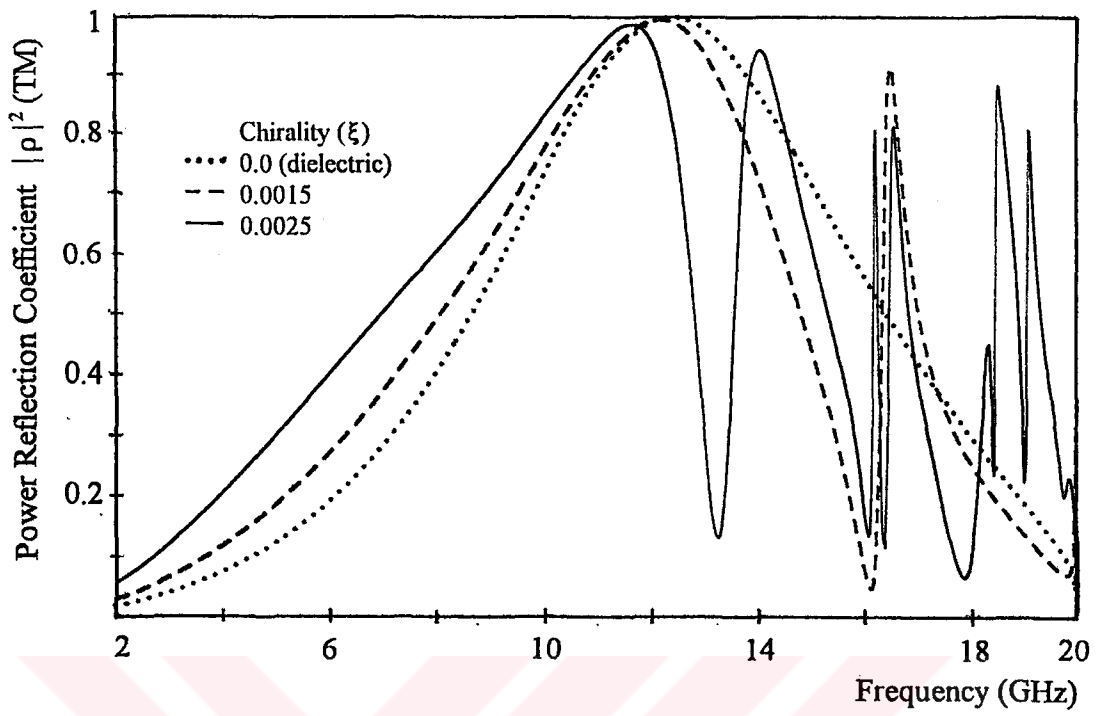(TE), d) Power transmission coefficient (TM).

147

a

b

148
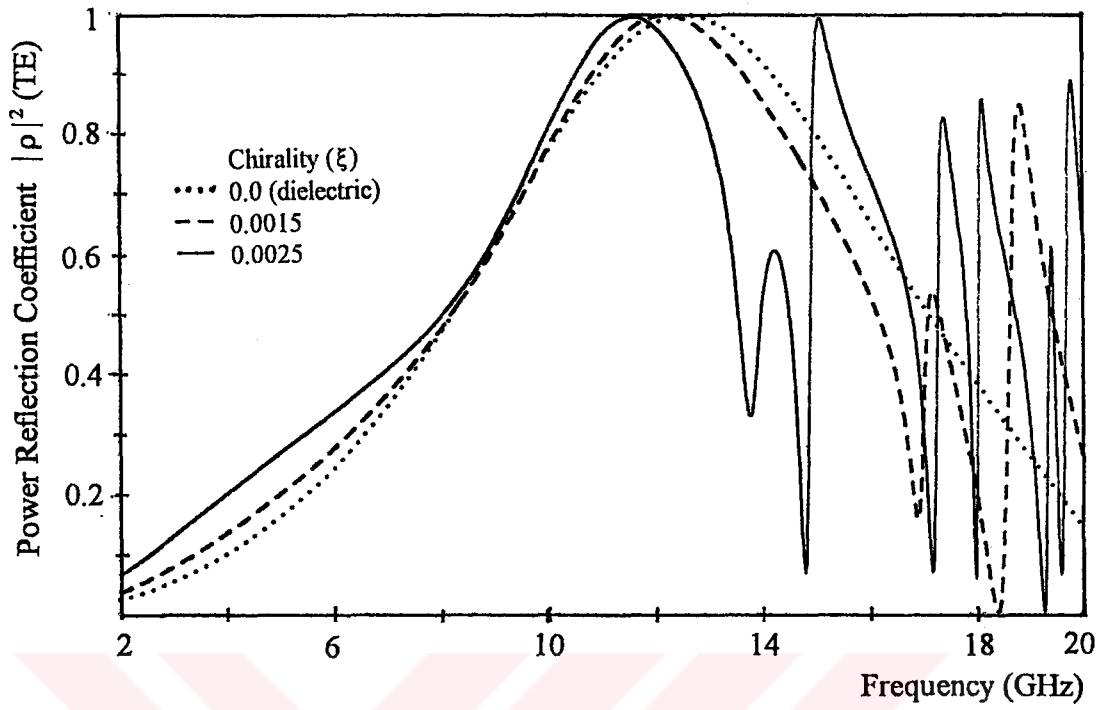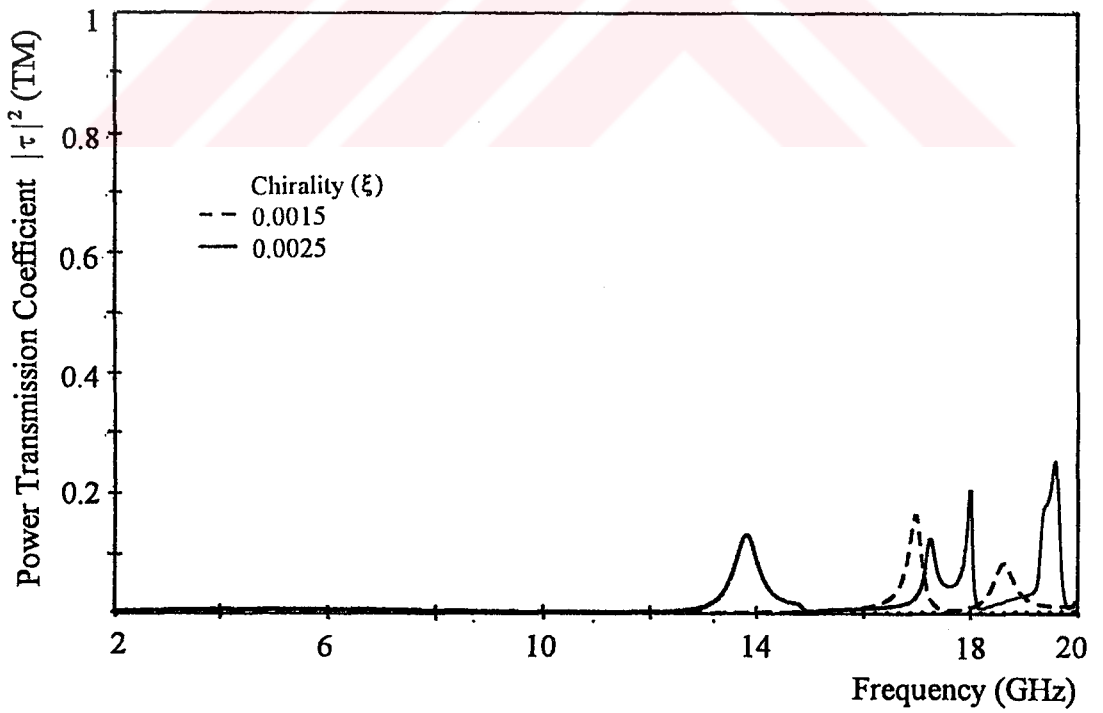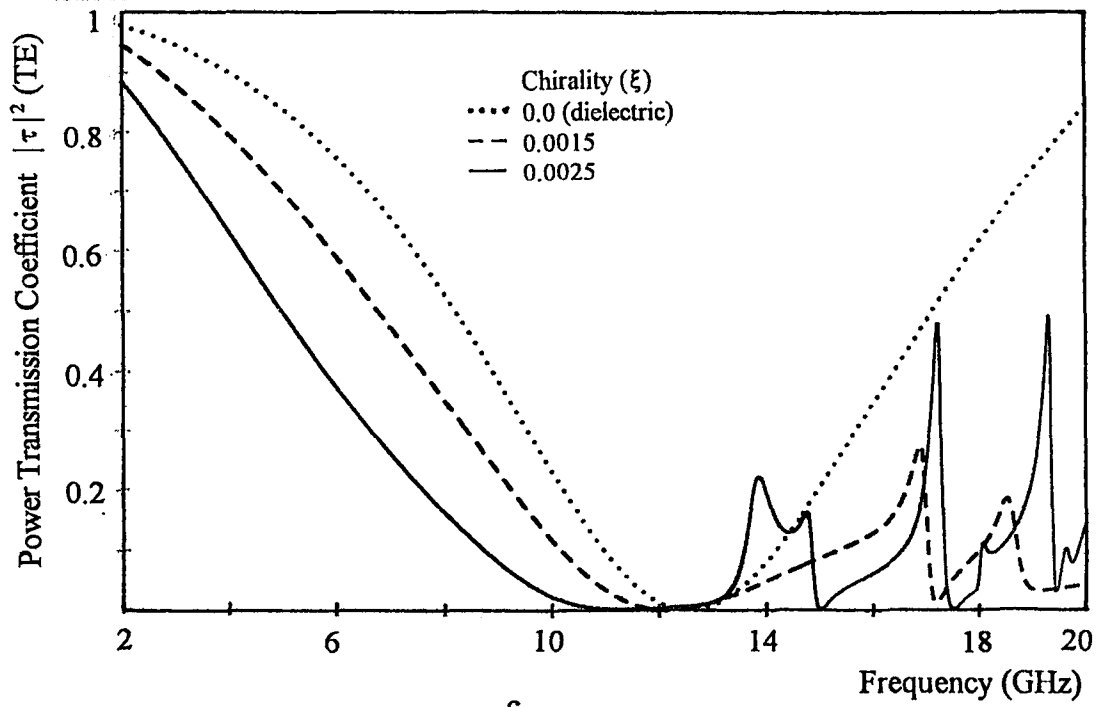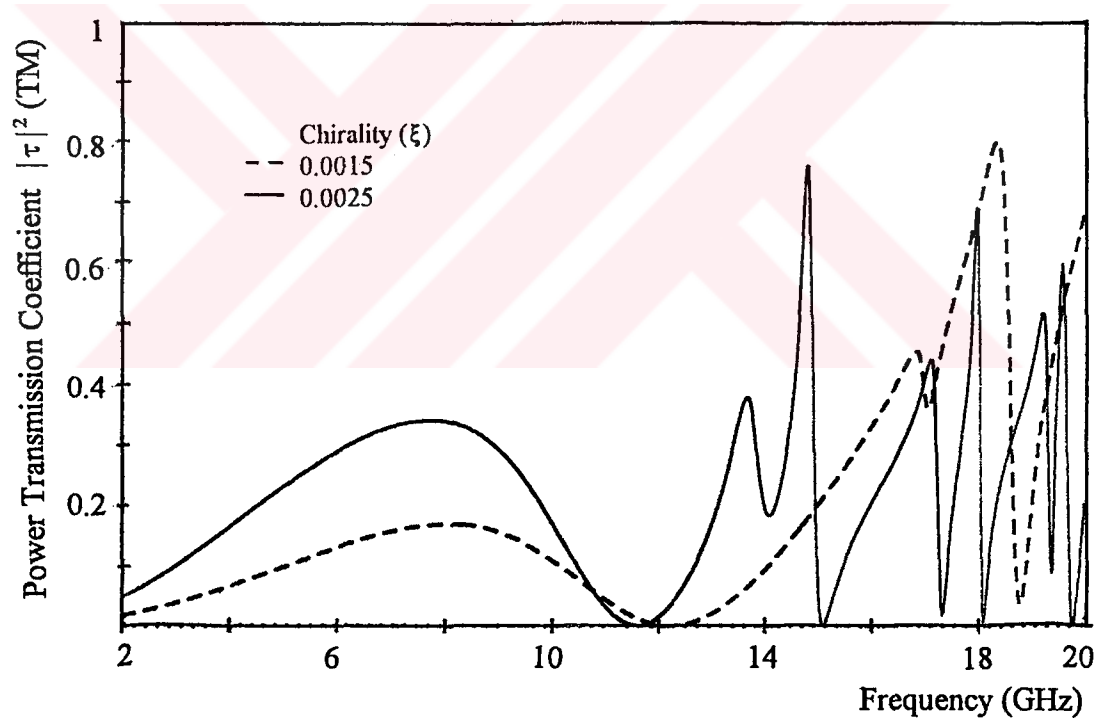
Figure 4.3.16   Spectral characteristics of Chiro-FSS with circular rings; TE incidence

(ϕ= 30°, θ=30°), square lattice (α= 90°), D_1=D_2=10 mm, R_i = 3.7 mm,

R_o= 4.7 mm, ϵ_r=1.06, t = 5 mm. a) Power reflection coefficient (TE),

b) Power reflection coefficient (TM), c) Power transmission coefficient
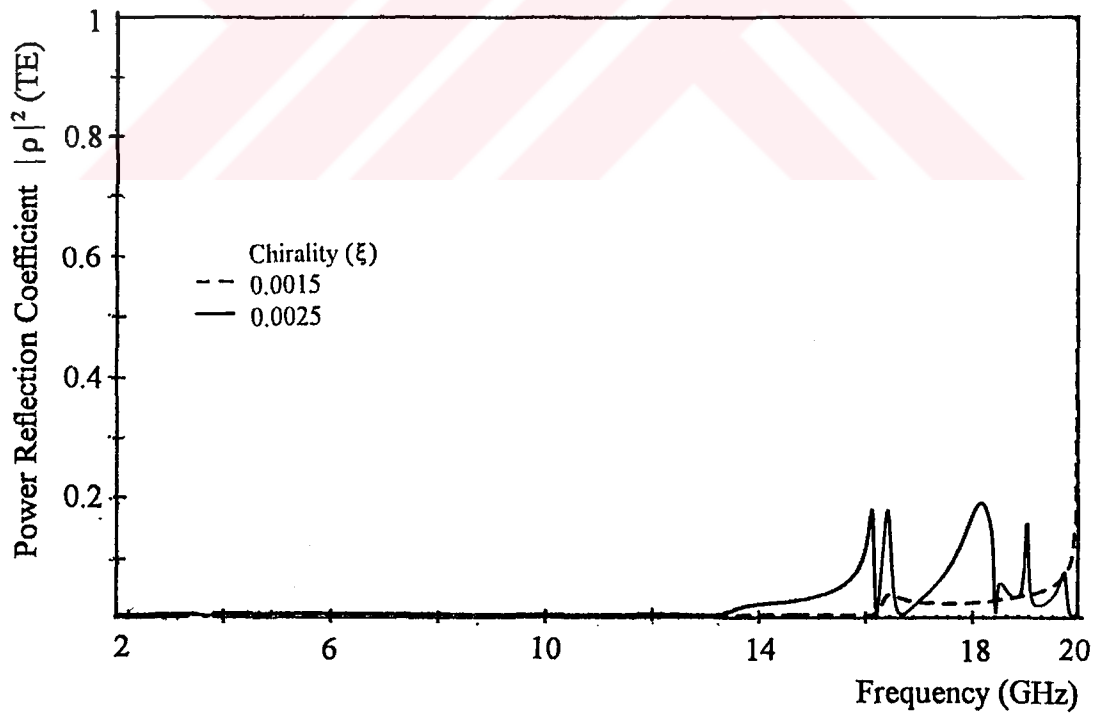
(TE), d) Power transmission coefficient (TM).

149

a

b

150
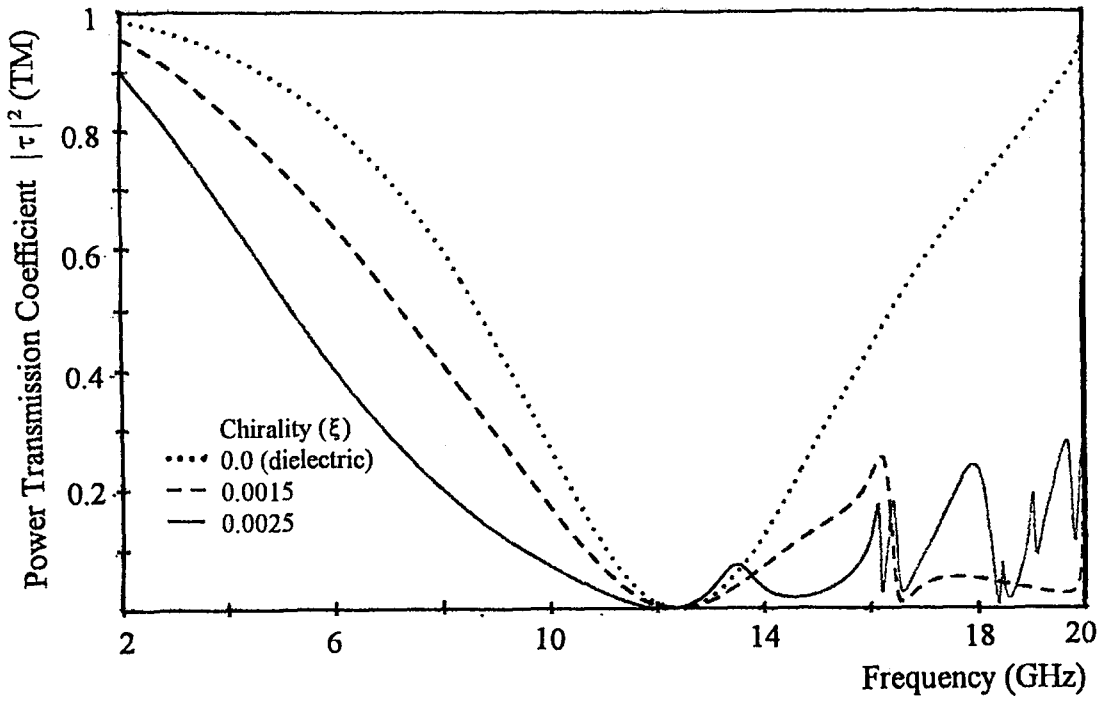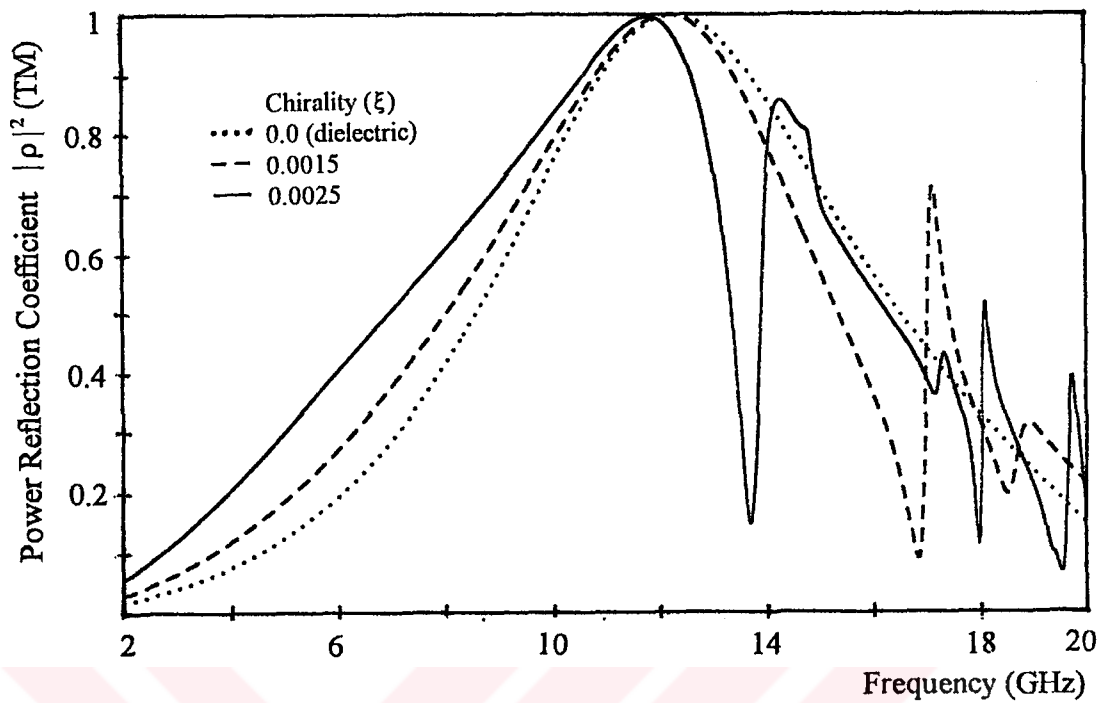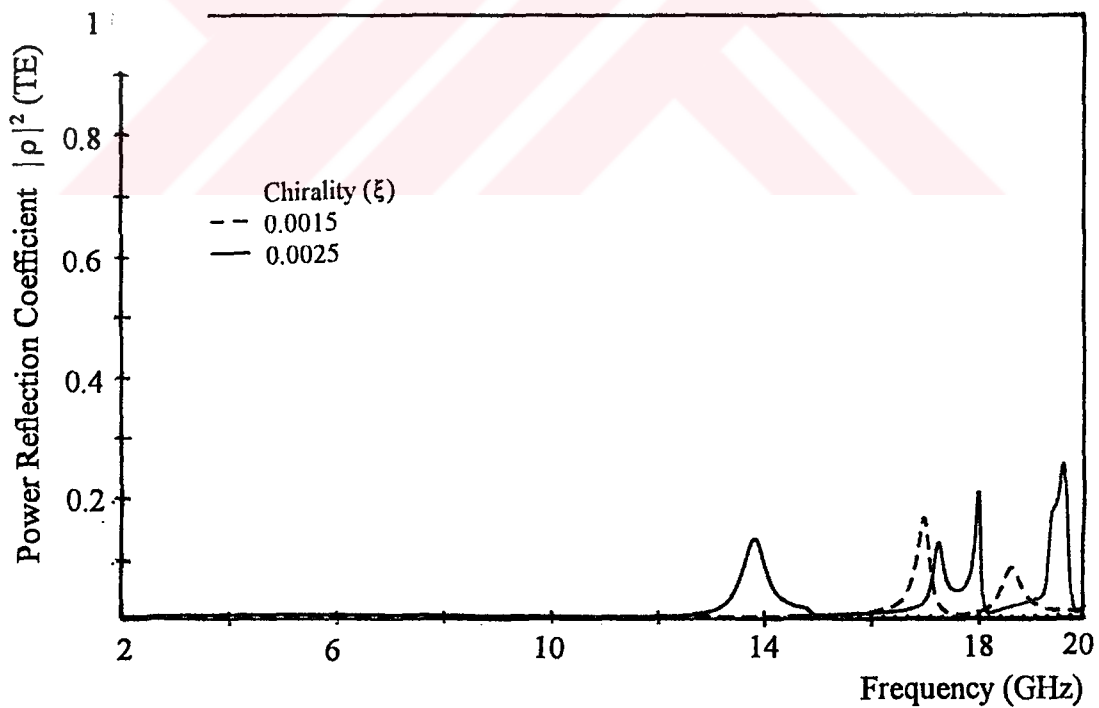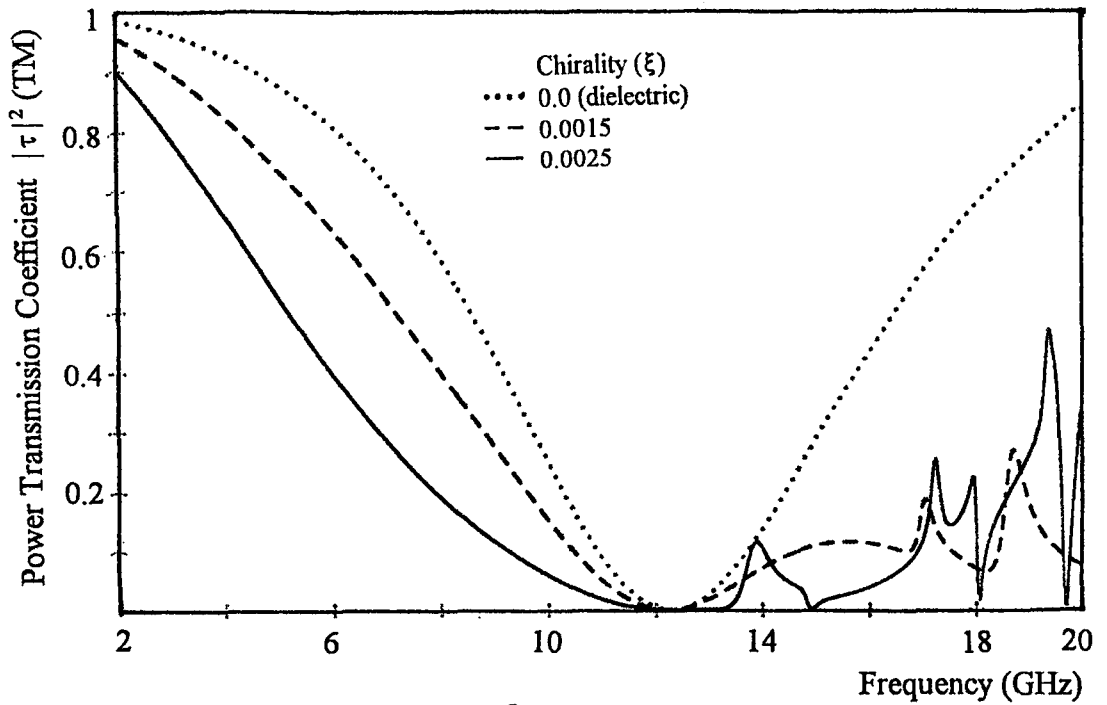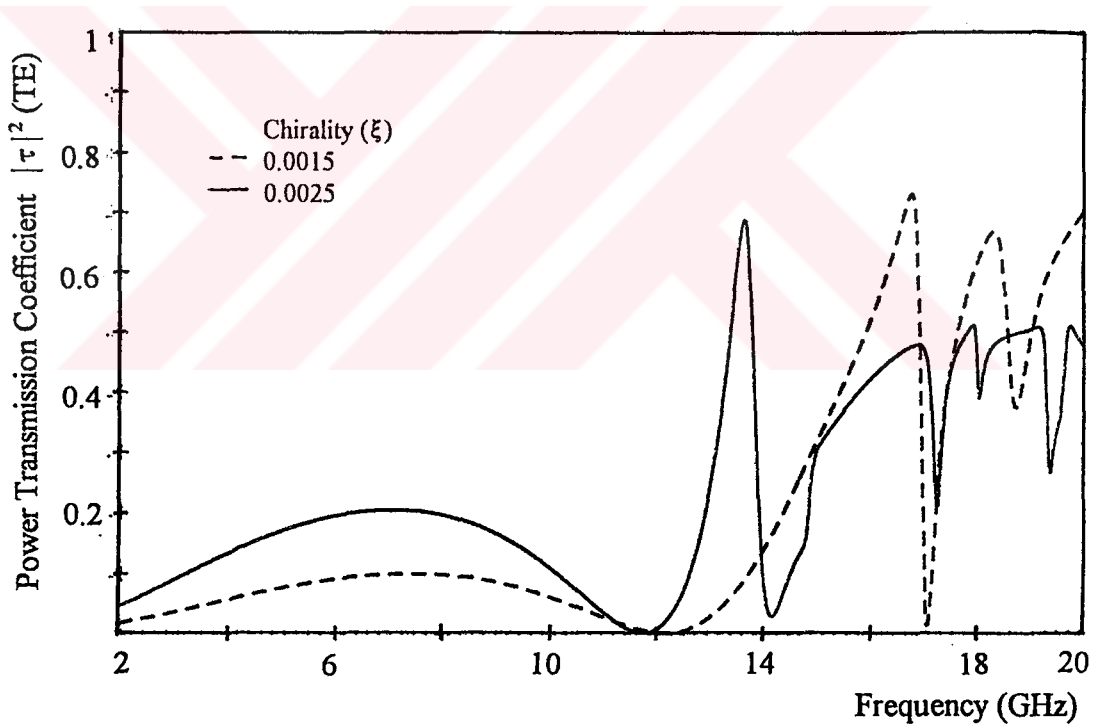
Figure 4.3.17   Spectral characteristics of Chiro-FSS with circular rings; TM incidence

(ϕ= 30°, θ=30°), square lattice (α= 90°), D_1=D_2=10 mm, R_i = 3.7 mm,

R_o= 4.7 mm, ϵ_r=1.06, t = 5 mm. a) Power reflection coefficient (TE),

b) Power reflection coefficient (TM), c) Power transmission coefficient

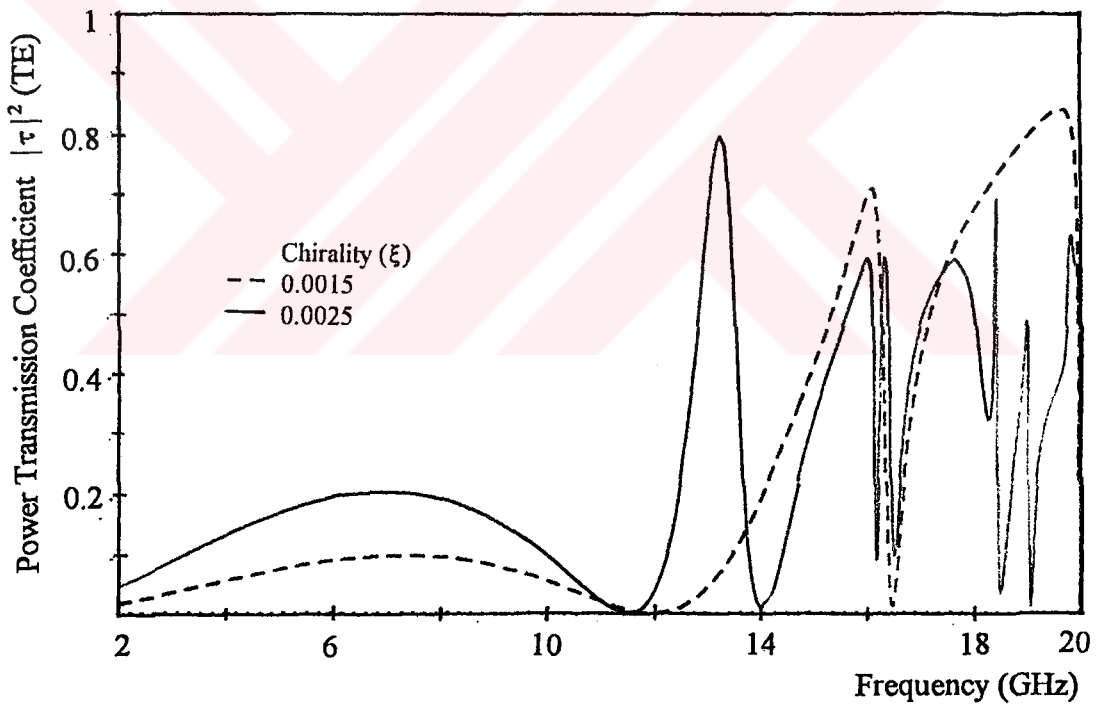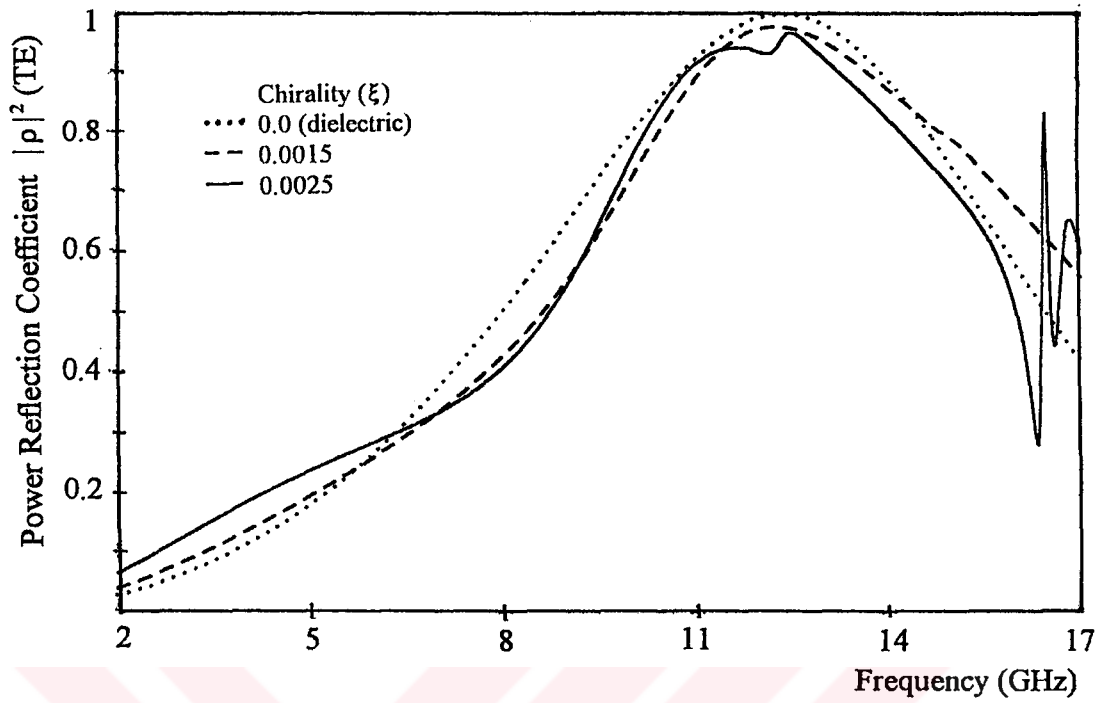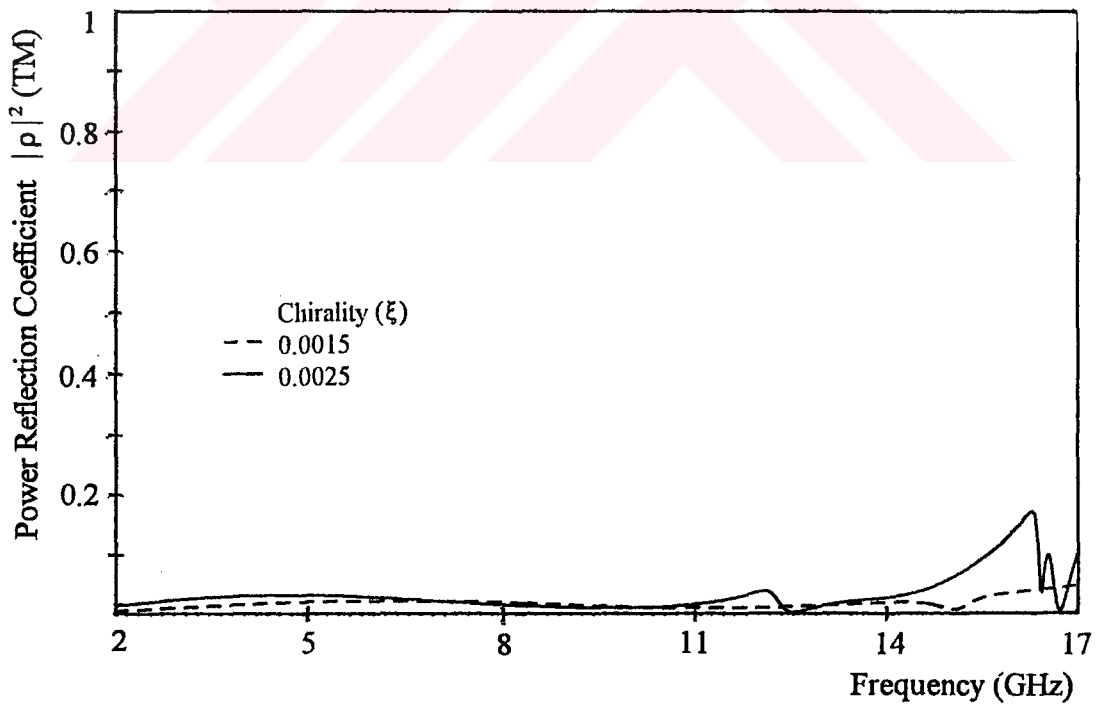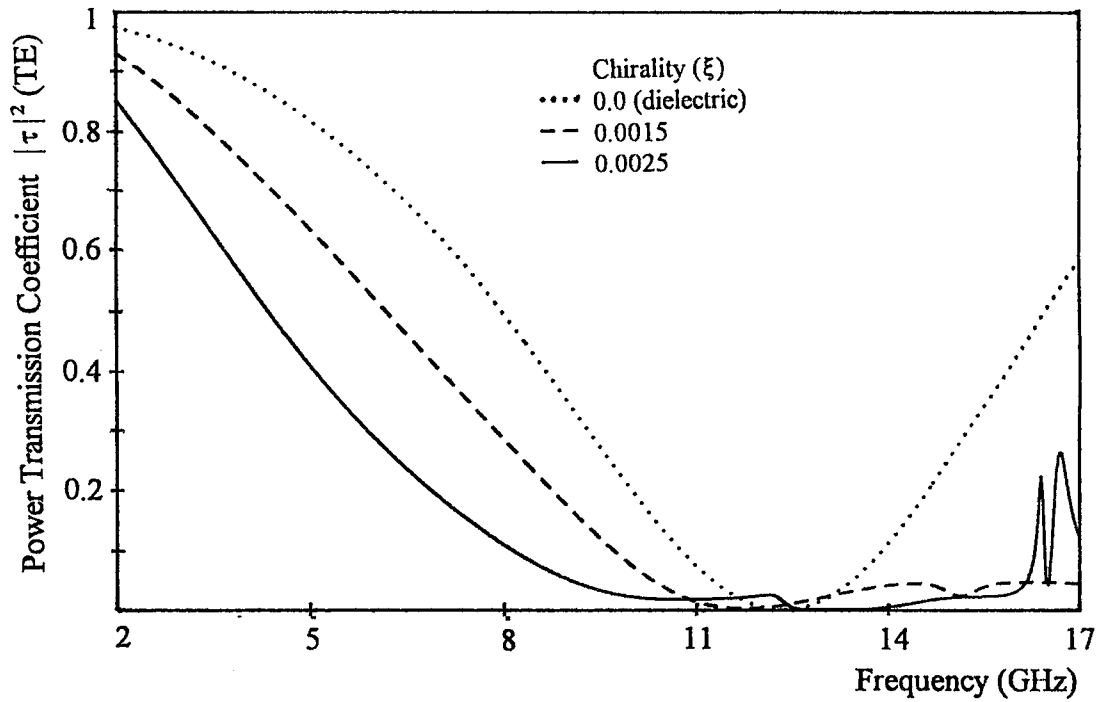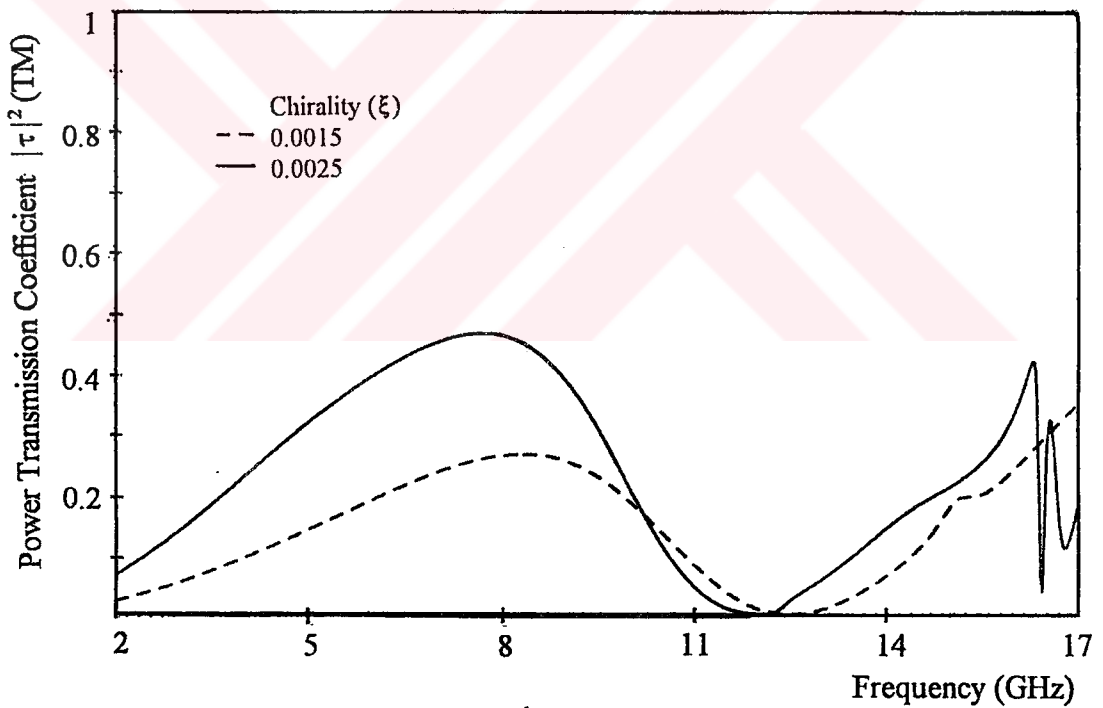(TE), d) Power transmission coefficient (TM).

151

4.4. Chiro-FSS Comprised of Rectangular Loops

Another Chiro-FSS analysed comprised of two dimensional array of rectangular loops shaped perfectly conducting elements printed on an isotropic chiral slab. The unit cell geometry is shown in Figure 4.4.1. For this geometry the width of the rectangular loop is assumed to be smaller than the wavelength of the excitation field.
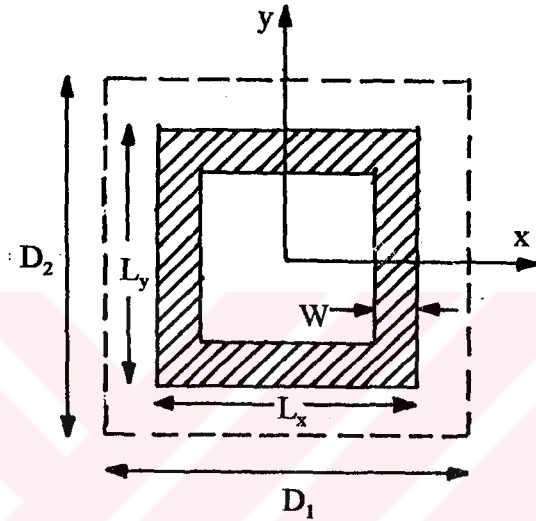
Figure 4.4.1   Unit cell geometry of Chiro-FSS with square loops.

Induced current density is expressed for each arm of the loop as a sum of sine and cosine functions having unknown coefficients that are to be determined as follows,

$$\vec{J} = \sum_{i=1}^{4} \vec{J}_i \qquad (4\text{-}56)$$

where i denotes the no. of branches.

For first and third branches ($i=1,3$):

$$\vec{J}_i(x',y') = \sum_{n=0}^{N_i} a_{inc}\, \vec{I}_{inc}(x',y') + \sum_{k=1}^{K_i} b_{iks}\, \vec{I}_{iks}(x',y') \qquad (4\text{-}57)$$

where,

$$\vec{I}_{inc} - \frac{1}{\sqrt{1 - (\frac{2x'}{W})^2}} \cos(\frac{n\pi y'}{L_y}) \vec{a}_{y'} \quad \pm \frac{L_x}{2} \mp \frac{W}{2} \leq \pm x' \leq \pm \frac{L_x}{2} \pm \frac{W}{2}$$

(4-58)

$$\vec{I}_{iks} - \frac{1}{\sqrt{1 - (\frac{2x'}{W})^2}} \sin(\frac{n\pi y'}{L_y}) \vec{a}_{y'} \quad \frac{L_y}{2} \leq y' \leq \frac{L_y}{2}$$

and a_i and b_i are the unknown coefficients.

The inner products are obtained as,

$$<\vec{I}_{inc}, \Psi_{mpq}^{*}> - \frac{1}{\sqrt{A}} [(\sin\gamma \, \vec{a}_x + \cos\gamma \, \vec{a}_y) . \vec{u}_{mpq}] \frac{W}{4} \pi L_y J_0(\frac{uW}{2}).$$

$$e^{\mp j\frac{L_x}{2}u} \left[\frac{\sin(\frac{vL_y}{2} + \frac{n\pi}{2})}{(\frac{vL_y}{2} + \frac{n\pi}{2})} + \frac{\sin(\frac{vL_y}{2} - \frac{n\pi}{2})}{(\frac{vL_y}{2} - \frac{n\pi}{2})} \right]$$

(4-59)

$$<\vec{I}_{inc}, \Psi_{mpq}> - <\vec{I}_{i,3nc}, \Psi_{mpq}^{*}>$$

(4-60)

and

$$<\vec{I}_{iks}, \Psi_{mpq}^{*}> - \frac{j}{\sqrt{A}} [(\sin\gamma \, \vec{a}_x + \cos\gamma \, \vec{a}_y).\vec{u}_{mpq}] \frac{W}{4} \pi L_y J_0(\frac{uW}{2}).$$

$$e^{\mp j\frac{L_x}{2}u} \left[\frac{\sin(\frac{vL_y}{2} - \frac{k\pi}{2})}{(\frac{vL_y}{2} - \frac{k\pi}{2})} - \frac{\sin(\frac{vL_y}{2} + \frac{k\pi}{2})}{(\frac{vL_y}{2} + \frac{k\pi}{2})} \right]$$

(4-61)

$$<\vec{I}_{inc}, \Psi_{mpq}> - - <\vec{I}_{inc}, \Psi_{mpq}^{*}>$$

(4-62)

For second and fouth branches (i=2, 4)

153

$$\vec{I}_{inc} - \frac{1}{\sqrt{1 - (\frac{2y'}{W})^2}} \cos(\frac{n\pi x'}{L_x}) \vec{a}_{x'} \qquad \pm \frac{L_y}{2} \mp \frac{W}{2} \leq \pm x' \leq \pm \frac{L_y}{2} \pm \frac{W}{2}$$

<div align="right">(4-63)</div>

$$\vec{I}_{iks} - \frac{1}{\sqrt{1 - (\frac{2y'}{W})^2}} \sin(\frac{n\pi x'}{L_x}) \vec{a}_{x'} \qquad \frac{L_x}{2} \leq x' \leq \frac{L_x}{2}$$

The inner products are expressed as,

$$<\vec{I}_{inc}, \Psi_{mpq}^{*}> - \frac{1}{\sqrt{A}} \left[(\cos\gamma\, \vec{a}_x - \sin\gamma\, \vec{a}_y) \cdot \vec{u}_{mpq} \right] \frac{W}{4} \pi L_x J_0(\frac{vW}{2}) \cdot$$

$$e^{\mp j \frac{L_y}{2} v} \left[\frac{\sin(\frac{uL_x}{2} + \frac{n\pi}{2})}{(\frac{uL_x}{2} + \frac{n\pi}{2})} + \frac{\sin(\frac{uL_x}{2} - \frac{n\pi}{2})}{(\frac{uL_x}{2} - \frac{n\pi}{2})} \right]$$

<div align="right">(4-64)</div>

$$<\vec{I}_{inc}, \Psi_{mpq}> - <\vec{I}_{inc}, \Psi_{mpq}^{*}>$$

<div align="right">(4-65)</div>

$$<\vec{I}_{iks}, \Psi_{mpq}^{*}> - \frac{j}{\sqrt{A}} \left[(\cos\gamma\, \vec{a}_x - \sin\gamma\, \vec{a}_y) \cdot \vec{u}_{mpq} \right] \frac{W}{4} \pi L_x J_0(\frac{vW}{2}) \cdot$$

$$e^{\mp j \frac{L_y}{2} v} \left[\frac{\sin(\frac{uL_x}{2} - \frac{k\pi}{2})}{(\frac{uL_x}{2} - \frac{k\pi}{2})} - \frac{\sin(\frac{uL_x}{2} + \frac{k\pi}{2})}{(\frac{uL_x}{2} + \frac{k\pi}{2})} \right]$$

<div align="right">(4-66)</div>

$$<\vec{I}_{iks}, \Psi_{mpq}> - - <\vec{I}_{iks}, \Psi_{mpq}^{*}>$$

<div align="right">(4-67)</div>

<div align="center">154</div>

4.4.1. Numerical Results of the Chiro-FSS with Square Loops

Next, the spectral response of the reflection and transmission characterisitcs of the Chiro-FSS comprised of square loops are analysed. The numerical results corresponding to the various type of configuretion are presnted. The dependence of the spectral response of the Chiro-FSS with square loops on the design parameters, i.e., chirality admittance, thickness and dielectric constant of the slab, geometry of the perfectly conducting square loops and incidence angle and polarisation of the incident plane wave are investigated.

The numerical results of the Chiro-FSS with square loops for the case of normal incidence, are the same for both TE and TM polarisation, due to symmerty of the geometry with respect to the two orthogonal axes x and y.

Consider a Chiro-FSS comprised of perfectlty conducting square loops having the arms length of $L_x=L_y=9.4$ mm printed on an isotropic chiral slab. The thickness and dielectric constant of the slab is assumed as t= 5 mm and 1.06, respectively. In this example square loops are arranged in a square lattice with $D_1= D_2 = 10$ mm. The computed reflection and transmission coefficients of the Chiro-FSS having design parameters mentioned above, are shown in Figure 4.4.2 when the screen is illuminated by a normally incident plane wave of TE polarisation. The reflection and transmission curves are obtained for $\xi= 0.0$ (dielectric),0.0005, 0.0015 and 0.0025 mho. Similar to the other type Chiro-FSS, small value of the chirality admittance of the slab ($\xi= 0.0005$ mho) does not alter the reponse of the Chiro-FSS, whereas when the chirality admittance is further increased multiple resonances are obtained. In the transmission characteristic of the cross-polar component, fully transmission is observed for high value of chirality admittance ($\xi= 0.0015$ and 0.0025 mho). The bandwidth of the higher resonances obtained are more narrow than the first resonance bandwidth.

Figure 4.4.3 illustrates the reflection and transmission characteristics of the same Chiro-FSS except thickness, (t = 4 mm). As it can be seen from the figures, decreasing the thickness of the slab from 5 mm to 4 mm causes the some changes. Altough the first resonance frequency remains at almost same value as in the previous case (t=5 mm),

frequencies of the resonances other than the first one are shifted to the higher frequency band. Note that, the bandwidth of the resonances are broadened. The isolation between the full reflections are reduced slightly. Similar effects are also observed in the reflection and transmission curves.

Next, we increase the dielectric constant of the slab from $\epsilon_r = 1.06$ to $\epsilon_r = 1.32$, while the other parameters are kept same as in the first example (t=5 mm). The reflection and tranmission characteristics of the Chiro-FSS for this configuration are obtained for ξ= 0.0, 0.0015 and 0.0025 mho, depicted in Figure 4.4.4. As shown figures there are three and four full reflection condition are obtained for ξ= 0.0015 and ξ= 0.0025 mho, respectively.In the reflection curve, the bandwidths of the resonances obtained for ξ= 0.0025 mho are extremely narrow comparing with the other cases, ξ= 0.0 and 0.0015 mho.

In order to illustrate the effects of the dimension of square loops on the spectral characteristics, the smaller sized square loops are considered in forming the Chiro-FSS such that $L_x = L_y$= 8 mm. In this configuration thickness and dielectric constant of the chiral slab are assumed as, 5 mm and 1.06, respectively. The numerical results of reflection and transmission coefficients versus frequency are shown in Figure 4.4.5 for ξ= 0.0 (dielectric), 0.0015 and 0.0025 mho. As the size of the square loops are reduced, the resonances frequencies are moved towards to higher frequencies. One should note that the amount of the shift of the first resonance frequency is much greater than the shifts of other resonances. In other words, the frequencies of the resonances other than the first one, are shifted slightly to the higher frequency bands.

The numerical results corresponding to the spectral characteristics of the Chiro-FSS with square loops printed on an 4 mm thick isotropic chiral slab are shown in Figure 4.4.6. In this configuration other design parameters are assumed to be the same as in the previous example, i.e., $L_x = L_y$= 8 mm, ϵ_r=1.06, $D_1 = D_2$= 10 mm. As it can be seen from the figures, reduction of thickness of the chiral slab make great variation in the spectral characteritics. All the resonance frequencies are shifted to the higher frequencies, and the bandwidth of the resonances in the reflection curve are broadened. The isolations betwwen the resonances are no good as in the previous case.

156

In the following parts of this section, the spectral characteristics of the Chiro-FSS comprised of square loops, having arm length of $L_x = L_y = 9.4$ mm, are arranged in an square lattice $D_1 = D_2 = 10$ mm are presented when the screen is illuminated by obliquely incident plane wave of TE and TM polarisations. Thicknes and dielectric constant of the chiral slab is assumed as 5 mm and 1.06, respectively. Similar to the figures given in previous section, in order to show the effects of chirality admittance on the spectral charecteristics of the Chiro-FSS, three different values of chirality admittance are chooes, $\xi = 0.0$(dielectric), 0.0015 and 0.0025 mho.

In the first case, the incident plane wave of TE and TM polarisation are assumed to have a azimuth angle of $\varphi = 30°$ and zero polar angle $\theta = 0°$. Figure 4.4.7 and 4.4.8 are the power reflection and transmission coefficients of the Chiro-FSS for the case of TE and TM illumination, respectively ($\varphi = 30°$, $\theta = 0°$). Comparision of the figures corresponding to the two case gives that the spectarl characteritics of the Chiro-FSS are almost same for TE and TM illumination. Cross-polar components does not arise in both polarisation. Figure 4.4.9 is the plots of the variation of power reflection and transmission coefficients of the Chiro-FSS when the screen is excited by a TE polarised plane wave with ($\varphi = 45°$, $\theta = 0°$). Absolutely same characteristics are obtained for TM polarised plane wave illumination case, is due to the symmetry of the geometry. In the later case ($\varphi = 45°$, $\theta = 0°$) all the resonances frequencies are shifted very slightly to the lower ferquencies when compared with the previous example ($\varphi = 30°$, $\theta = 0°$). One should be note that, as expected, the variation of the spectral response of the Chiro-FSS with square loops with the azimuth angle, φ, is not noticable, almost same characteristics are obtained for different values of the azimuth angle, φ.

In the second case, the incidence angle of the obliquely incoming plane wave of TE and TM polarisation are choosen as $\varphi = 0°$, $\theta = 30°$, to show the effects of only polar angle on the spectral characteristics. The plots corresponding to this condition are depicted in Figure 4.4.10 and 4.4.11, for TE and TM illumination, respectively. As it can be seen from the figures, the reflection and transmission characteristics of the Chiro-FSS are sensitive to the polar angle, θ, of the incident plane wave. For the zero chirality case ($\xi = 0.0$, dielectric), two resonances are obtained for TE polarisations, whereas only one

157

resonance is obserced for TM case. This is due to coupling of the current from one arm to another with phase discontiniuty as in the case of cross diploes. When the chirality admittance is of the slab is increased multiple resonances with very narrow bandwidths are obtained for both TE and TM polarsation. Altough the cross-polar components exist and increase as the chirality increases, for all case its magnitue is still rather small than the magnitude of the co-polar components for TE and TM ploarisations. Another intersting result is that, for non-zero value of the chirality admittance, the full transmission is not obtained for neither TE nor TM polariations.

In the last example, the numerical results of power reflection and transmission coefficients of the Chiro-FSS versus frequency when the screen is illuminated by a TE and TM ploarised plane wave with (ϕ =30°, θ = 30°) are shown in Figure 4.4.12 and Figure 4.4.13, respectively. Comparision of Figure 4.4.11 corresponding to the case of ϕ =0°, θ = 30° with Figure 4.4.12 reveals that, the number of resonances obatined is increased as the azimuth angle, ϕ, of the incident plane wave is increased to 30° for TE excitation.The first resonance frequency is almost the same for all values of chirality admittance. It is also seen that for the case of (ϕ =30°, θ = 30°), the spectral characteristics are very sensitive to frequency of the incident TE plane wave. Another noticable result is that, altough only one resonance is obtained for zero chirality case, but still multiple resonances are observed for ξ=0.0015 and 0.0025 mho.

In contrast to the TE illumination case, only one resonance is obtained in the reflection curve for TM plane wave excitation with the same incidence angles, (ϕ =30°, θ = 30°). The peak value of the higher resonances are reduced as the azimuth angle is increased.

According to the computed results of the analysis for the Chiro-FSS comprised of conducting square loops loaded by an isotropic chiral slab, we can express the behaviour of this structure as follows;

- The Chiro-FSS comprised of square loops exhibits very similar spectral characteritics to that of the Chiro-FSS with circular rings, for the normally incident plane wave illumination. These similarities are due to similarity between the circular ring and square loop.As in the other type of Chiro-FSS multiple resonances with narrow

158

bandwidths are obtained when the chirality admittance introduced.

- The Chiro-FSS with square loops are not sensitive to the azimuth angle variaton of the incident plane wave. But, variation of polar angle makes considerable changes in the spectral characteritics of the Chiro-FSS comprised of square loops.

- Altough the polar angle of the incident plane wave alters the spectral characteristics drastically, still multiple resonances can be obtainable for both TE and TM polariasions.

a

b

160
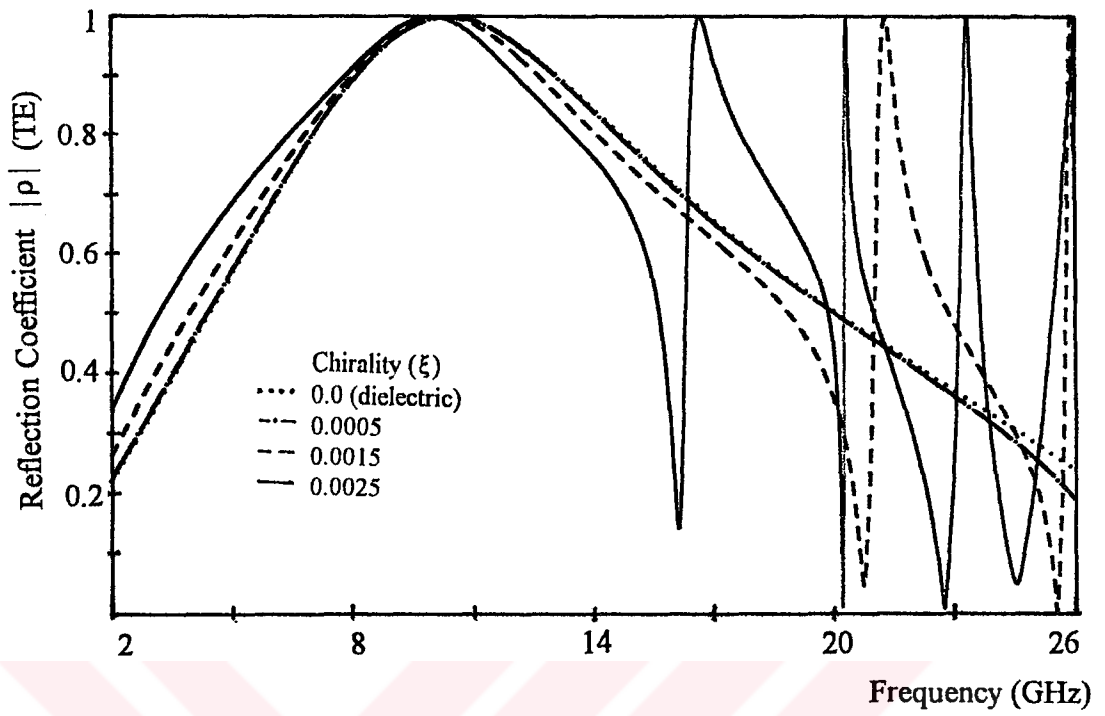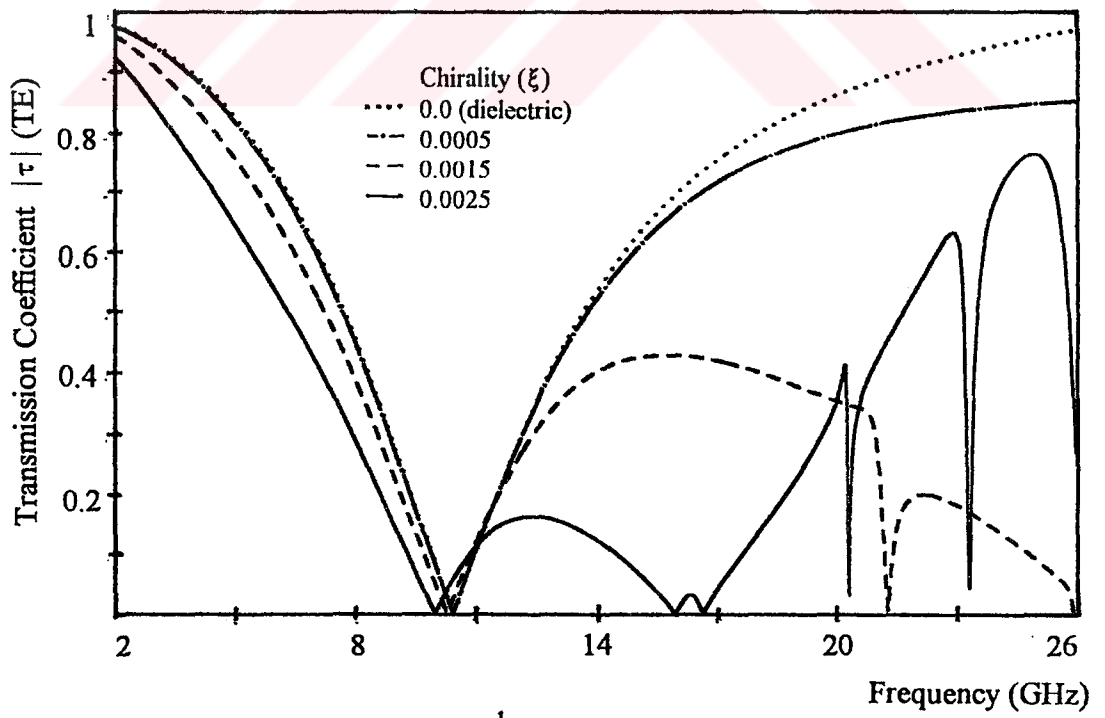
Figure 4.4.2　Spectral characteristics of Chiro-FSS with square loops; TE incidence
($\phi= 0°$, $\theta=0°$), square lattice ($\alpha= 90°$), $D_1=D_2=10$ mm, $L_x= L_y =9.4$ mm,
$W=1$ mm, $\epsilon_r=1.06$, $t = 5$ mm. a) Reflection coefficient (TE),
b) Transmission coefficient (TE), c) Transmission coefficient (TM).

Figure 4.4.3   Spectral characteristics of Chiro-FSS with square loops; TE incidence

($\phi= 0°$, $\theta=0°$), square lattice ($\alpha= 90°$), $D_1=D_2=10$ mm, $L_x= L_y =9.4$ mm,

$W=1$ mm, $\epsilon_r=1.06$, $t = 5$ mm. a) Reflection coefficient (TE),

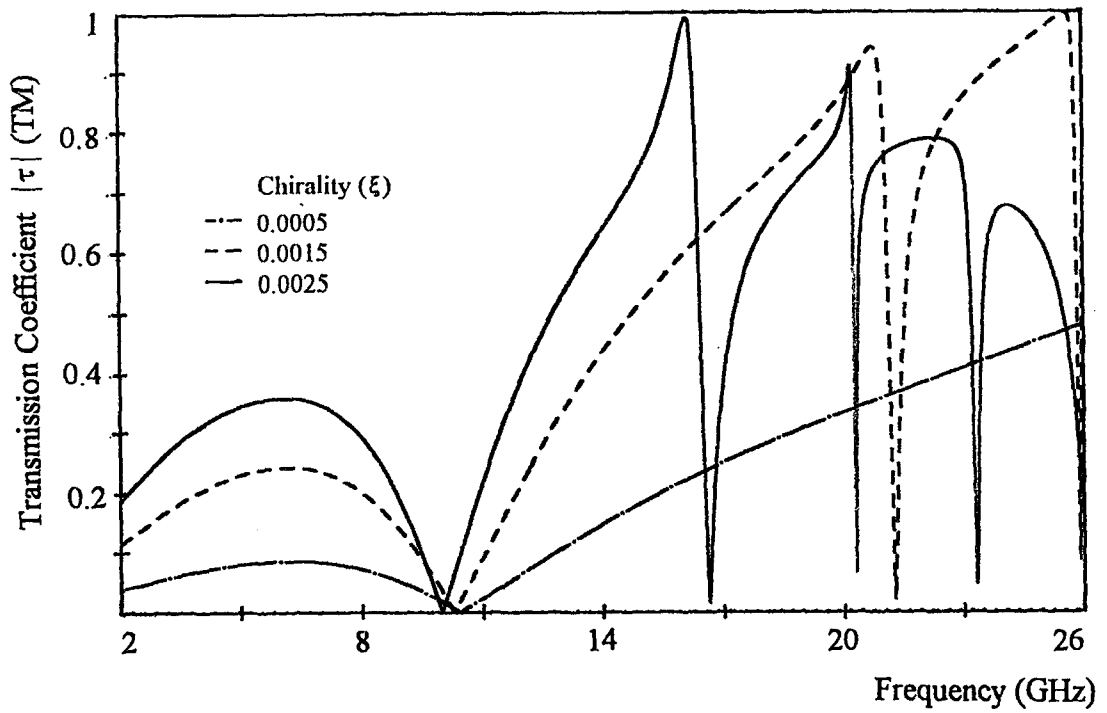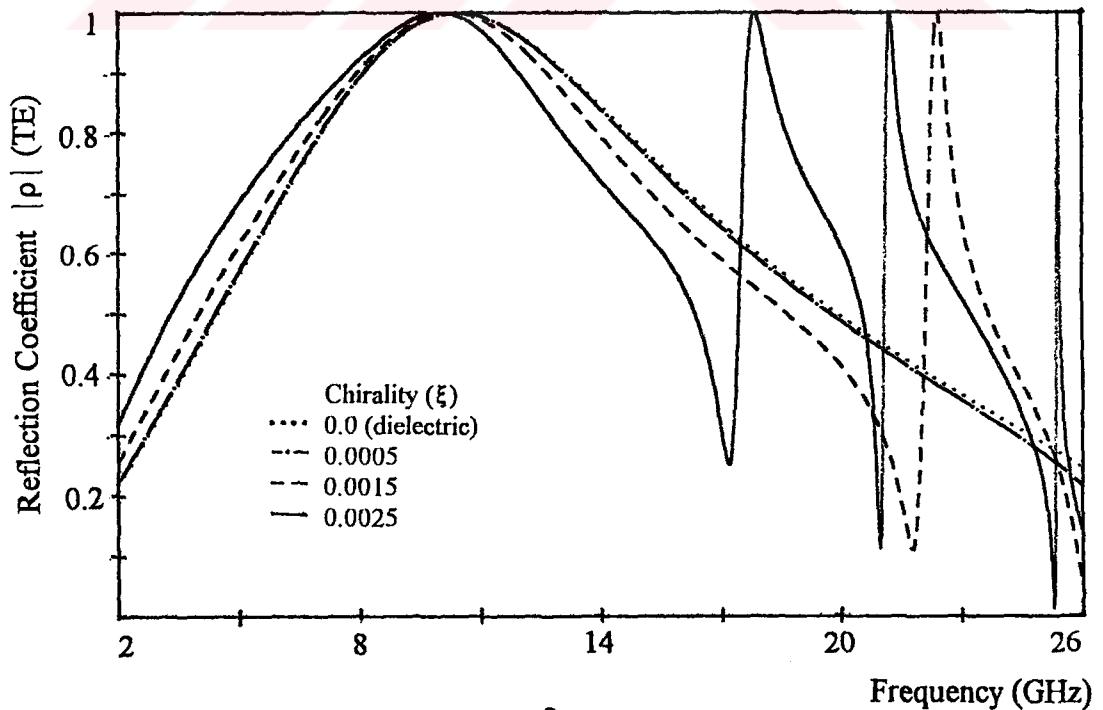b) Transmission coefficient (TE), c) Transmission coefficient (TM).

162

a

b

163

Figure 4.4.4   Spectral characteristics of Chiro-FSS with square loops; TE incidence
($\phi = 0°$, $\theta = 0°$), square lattice ($\alpha = 90°$), $D_1 = D_2 = 10$ mm, $L_x = L_y = 9.4$ mm,
W=1 mm, $\epsilon_r = 1.32$, t = 5 mm. a) Reflection coefficient (TE),
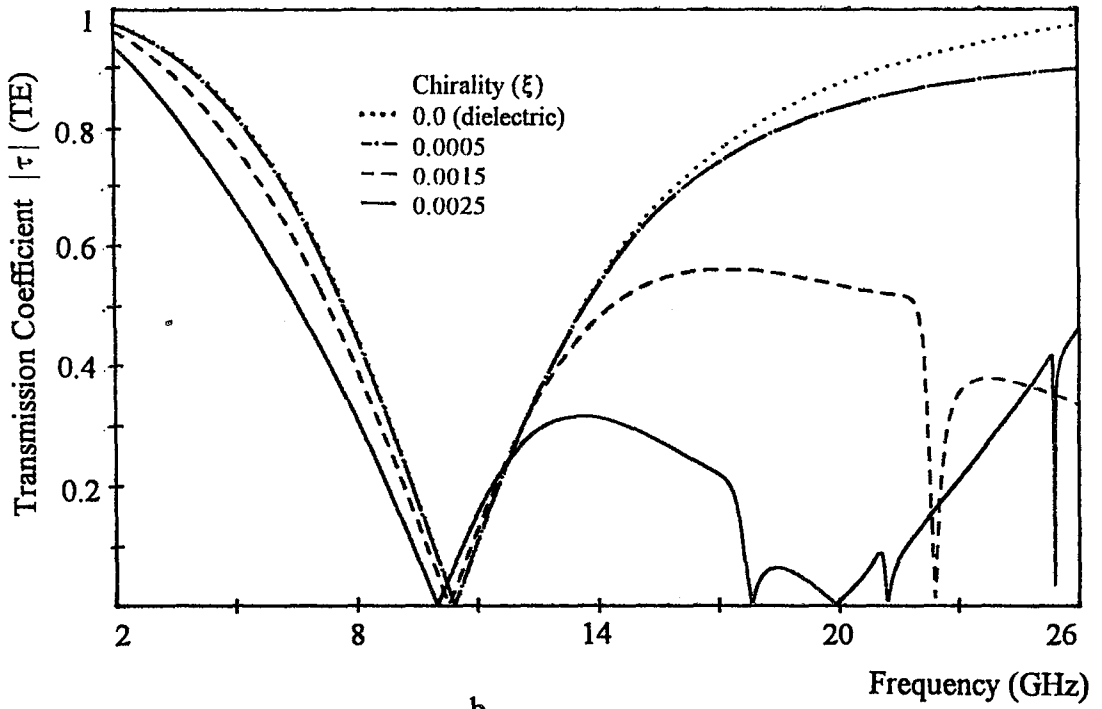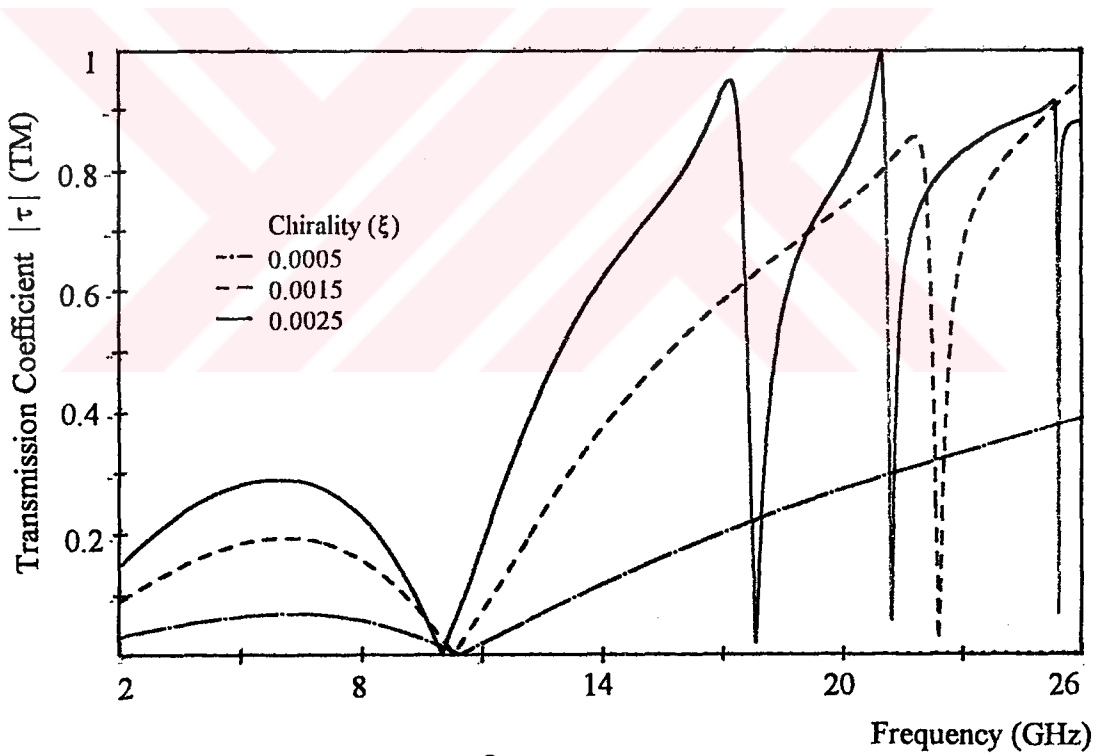b) Transmission coefficient (TE), c) Transmission coefficient (TM).

164
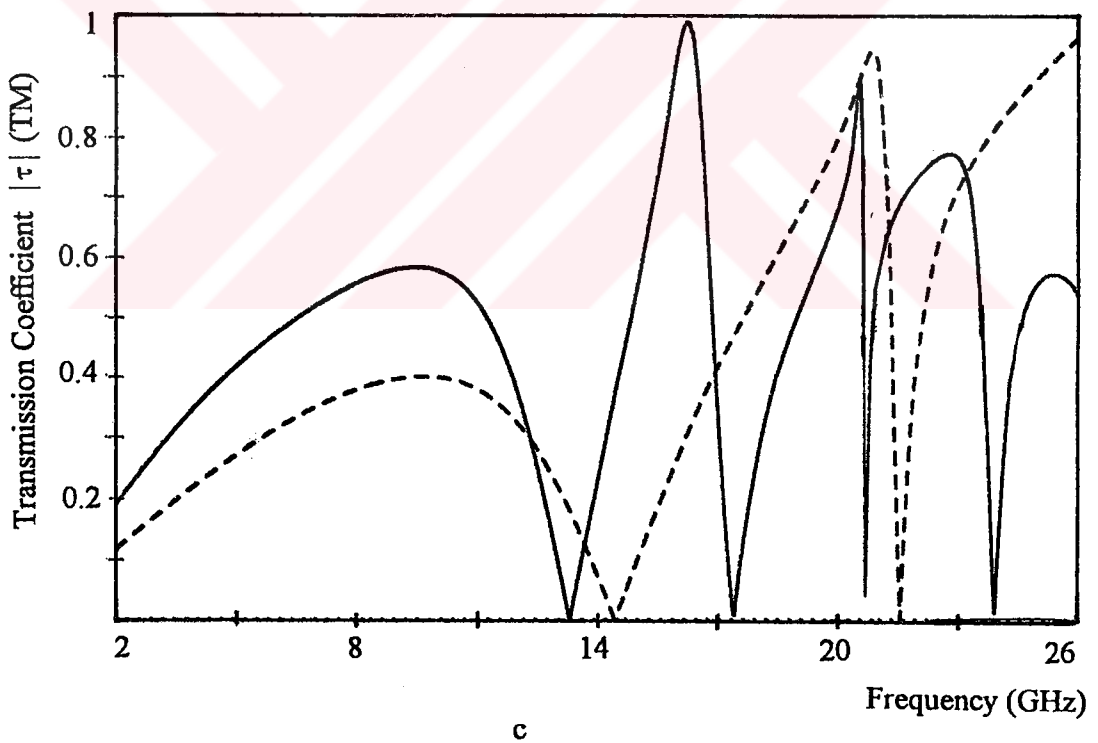
Figure 4.4.5   Spectral characteristics of Chiro-FSS with square loops; TE incidence
(ϕ= 0°, θ=0°), square lattice (α= 90°), D_1=D_2=10 mm, L_x= L_y = 8 mm,
W=1 mm, ϵ_r=1.06, t = 5 mm. a) Reflection coefficient (TE),
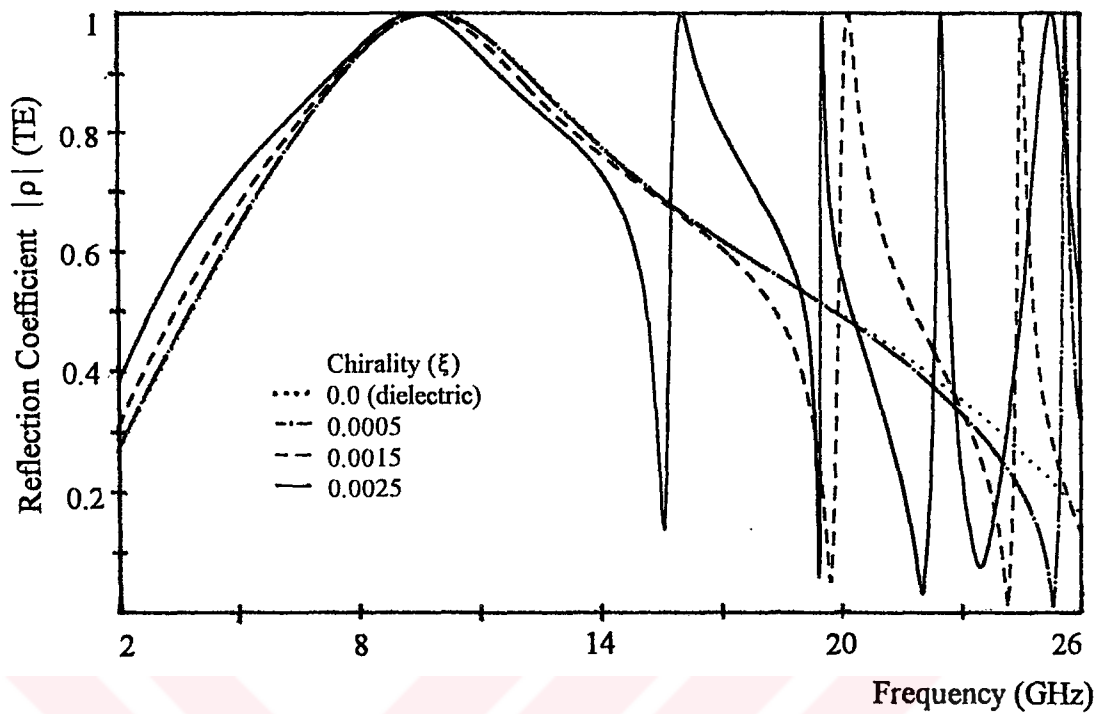b) Transmission coefficient (TE), c) Transmission coefficient (TM).

165

a

b

Figure 4.4.6   Spectral characteristics of Chiro-FSS with square loops; TE incidence
($\phi = 0°$, $\theta = 0°$), square lattice ($\alpha = 90°$), $D_1 = D_2 = 10$ mm, $L_x = L_y = 8$ mm,
W=1 mm, $\epsilon_r = 1.06$, t = 4 mm. a) Reflection coefficient (TE),
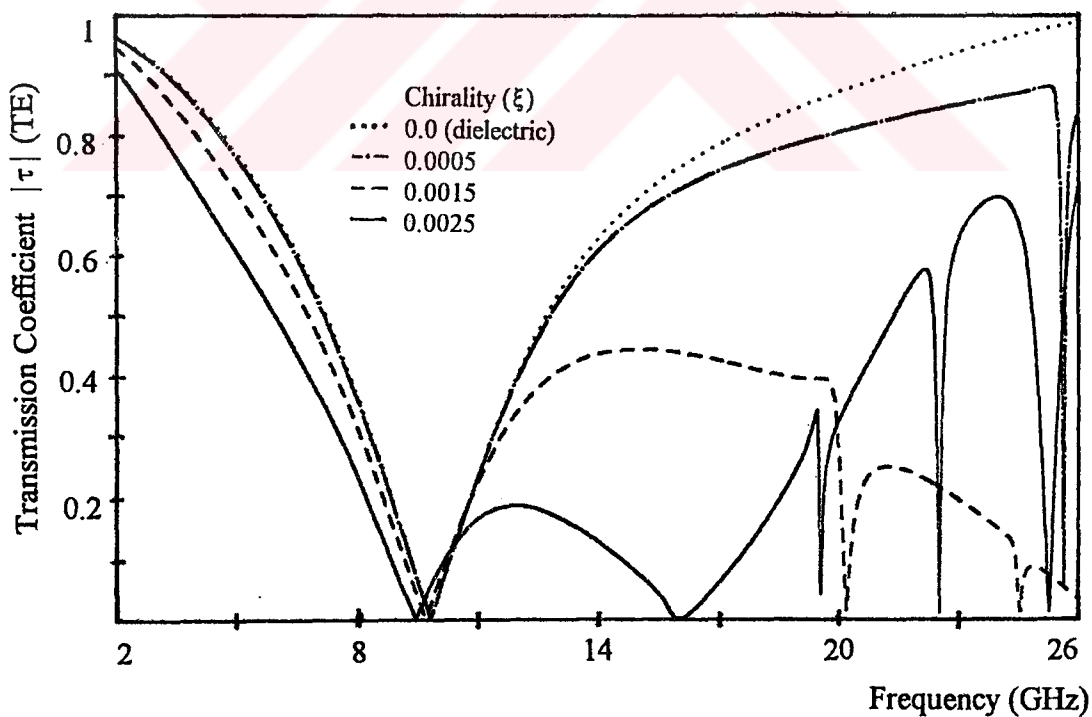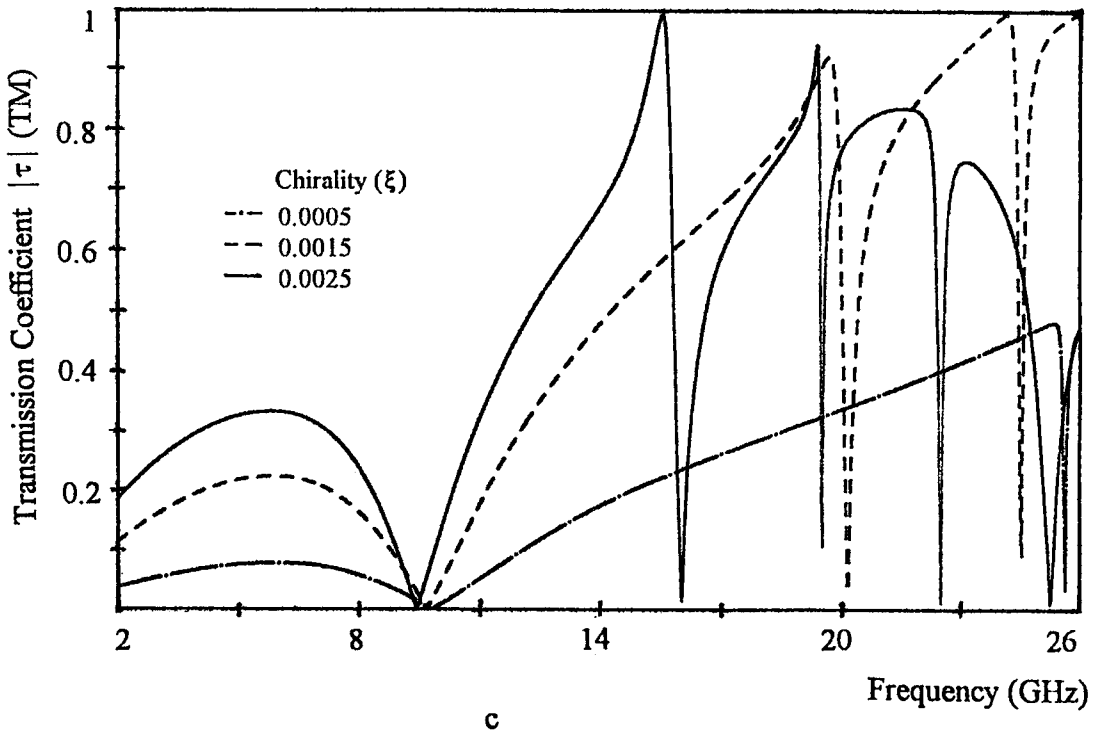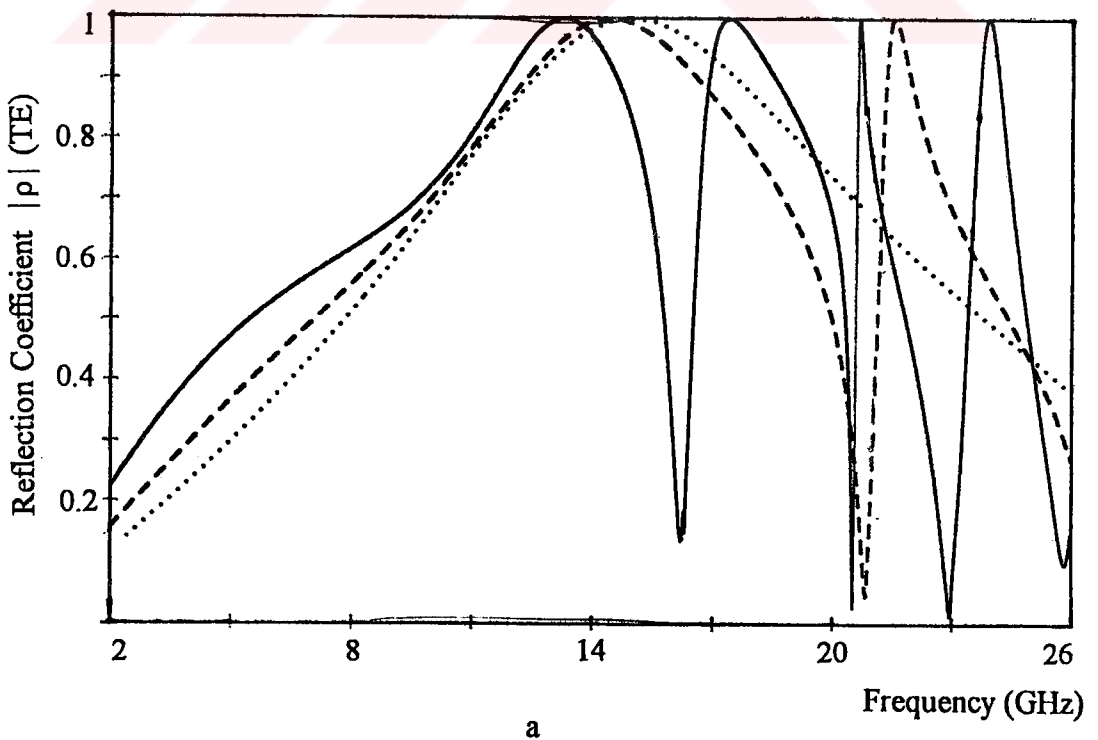b) Transmission coefficient (TE), c) Transmission coefficient (TM).

Figure 4.4.7   Spectral characteristics of Chiro-FSS with square loops; TE incidence
($\phi= 30°$, $\theta=0°$), square lattice ($\alpha= 90°$), $D_1=D_2=10$ mm, $L_x=L_y=9.4$ mm,
W=1 mm, $\epsilon_r=1.06$, t = 5 mm. a) Power reflection coefficient (TE),
b) Power transmission coefficient (TE), c) Power transmission coefficient
(TM).

a

b

169

Figure 4.4.8 Spectral characteristics of Chiro-FSS with square loops; TM incidence
($\phi = 30°$, $\theta = 0°$), square lattice ($\alpha = 90°$), $D_1 = D_2 = 10$ mm, $L_x = L_y = 9.4$ mm,
W=1 mm, $\epsilon_r = 1.06$, t = 5 mm. a) Power reflection coefficient (TM),
b) Power transmission coefficient (TE), c) Power transmission coefficient
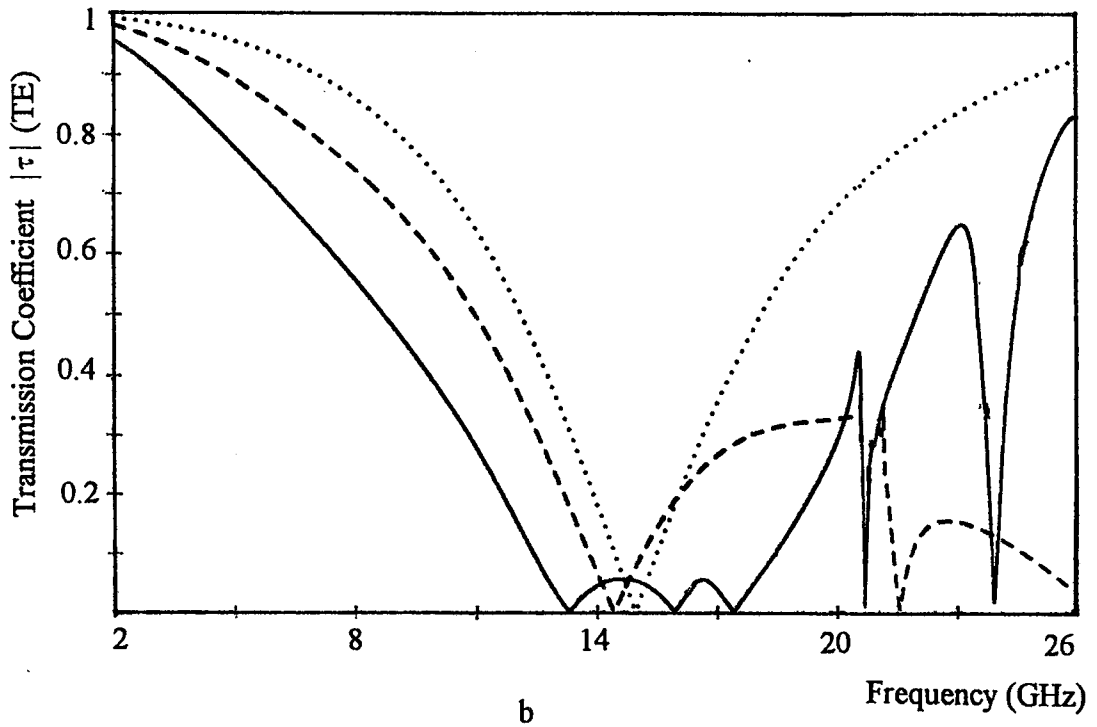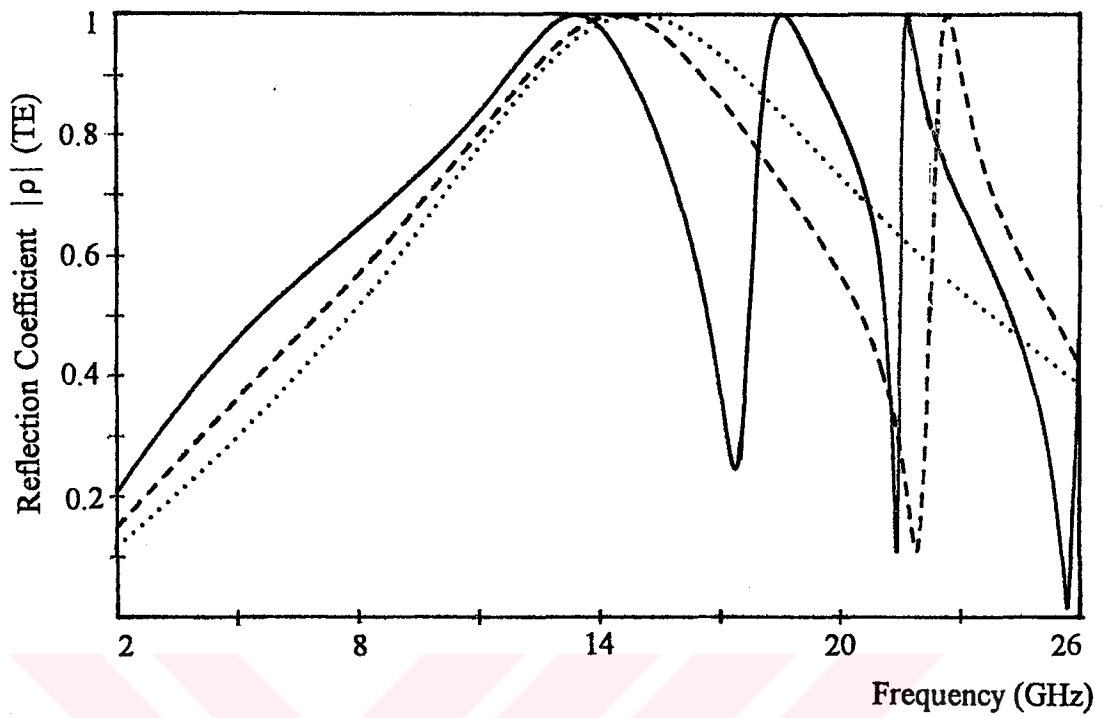(TM).

170

Figure 4.4.9   Spectral characteristics of Chiro-FSS with square loops; TE incidence
(ϕ= 45°, θ=0°), square lattice (α= 90°), D_1=D_2=10 mm, L_x=L_y=9.4 mm,
W=1 mm, ϵ_r=1.06, t = 5 mm. a) Power reflection coefficient (TE),
b) Power transmission coefficient (TE), c) Power transmission coefficient
(TM).

171

Power Reflection Coefficient $|\rho|^2$ (TE)

Chirality (ξ)
· · · · 0.0 (dielectric)
- - - 0.0015
——— 0.0025

Frequency (GHz)

a

Power Reflection Coefficient $|\rho|^2$ (TM)

Chirality (ξ)
- - - 0.0015
——— 0.0025

Frequency (GHz)

b
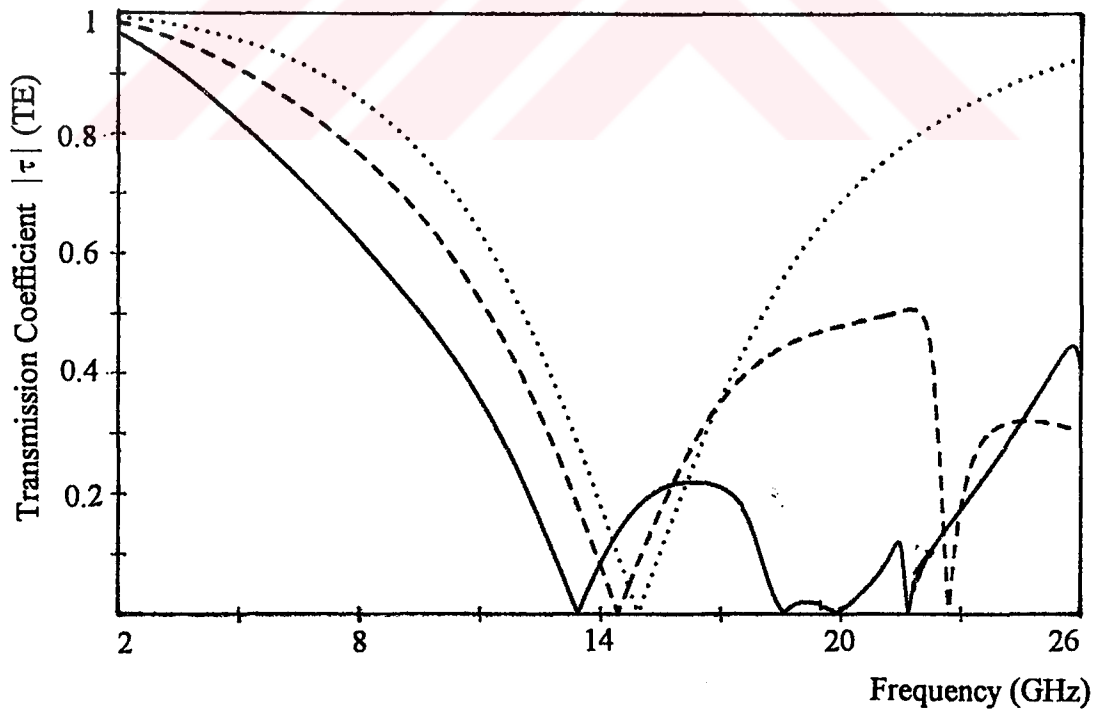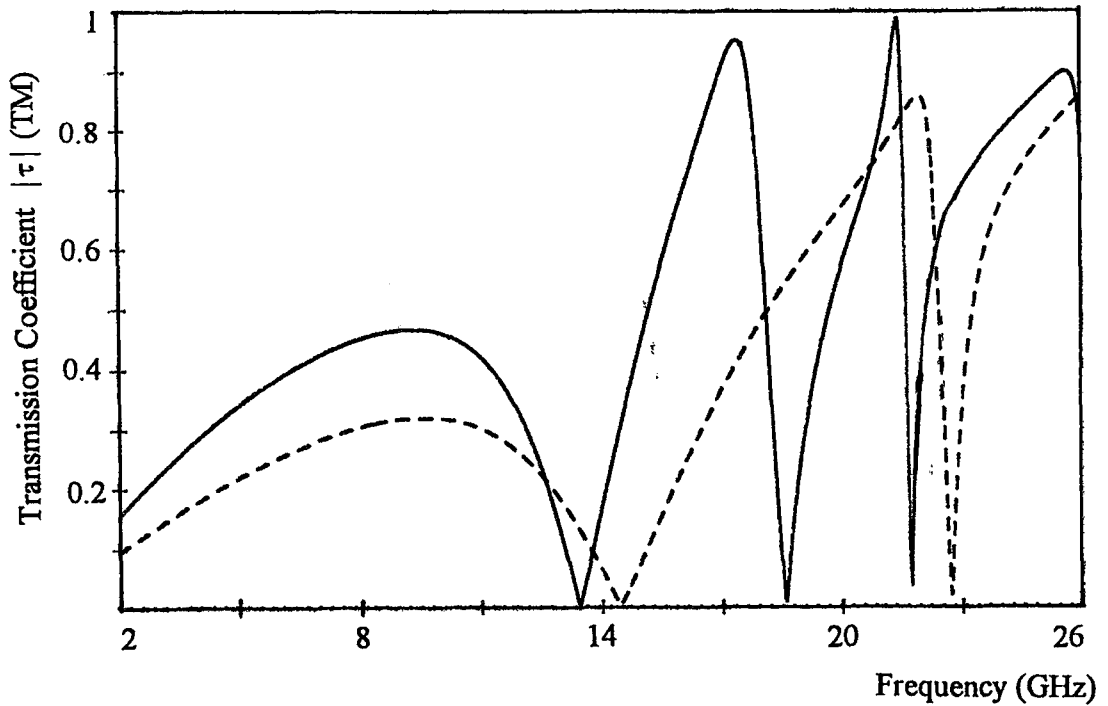
Figure 4.4.10 Spectral characteristics of Chiro-FSS with square loops; TE incidence

($\phi= 0°$, $\theta=30°$), square lattice ($\alpha= 90°$), $D_1=D_2=10$ mm, $L_x=L_y=9.4$ mm,

W=1 mm, $\epsilon_r=1.06$, t = 5 mm. a) Power reflection coefficient (TE),

b) Power reflection coefficient (TM), c) Power transmission coefficient
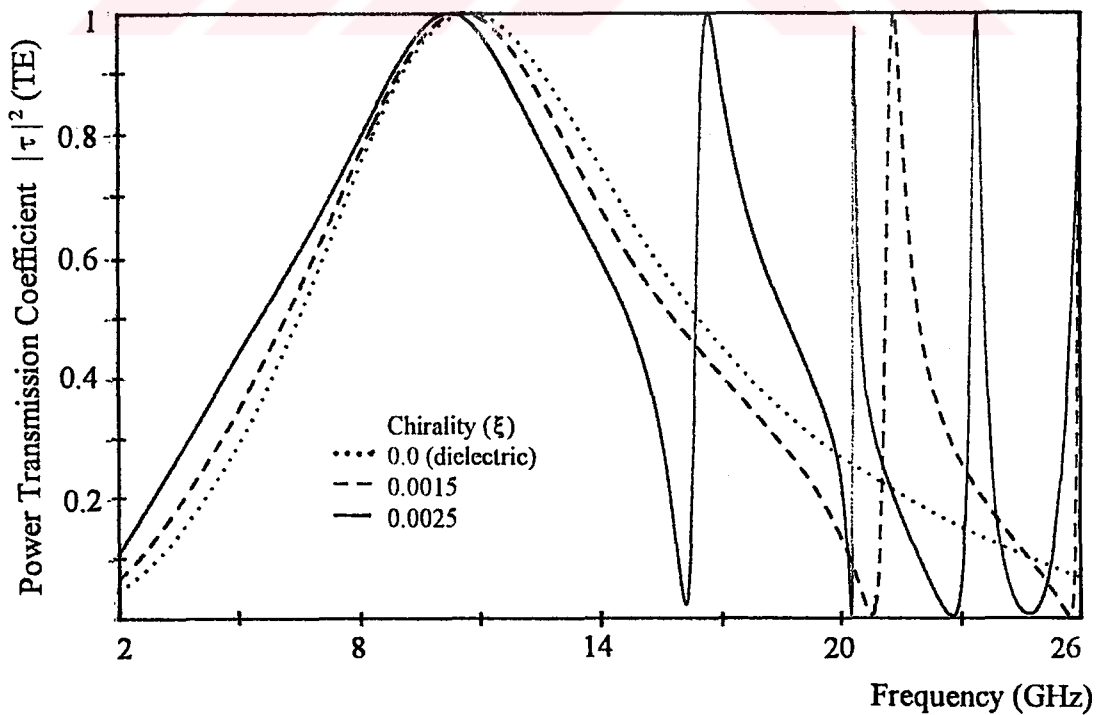
(TE), d) Power transmission coefficient (TM).

173

a

b
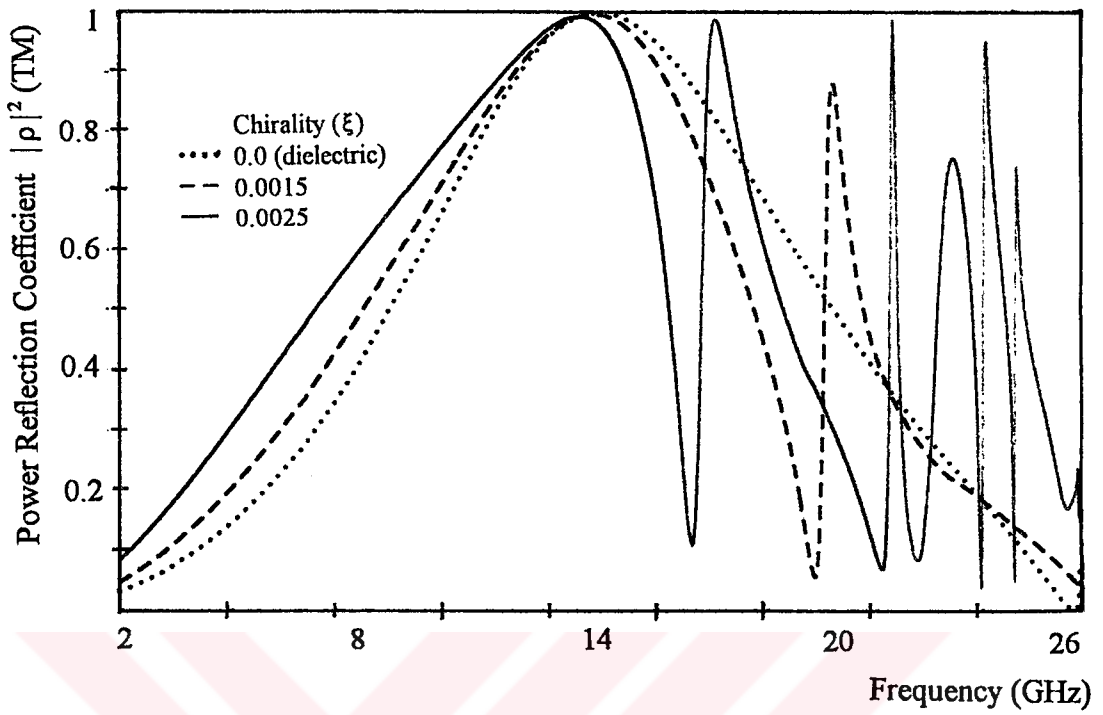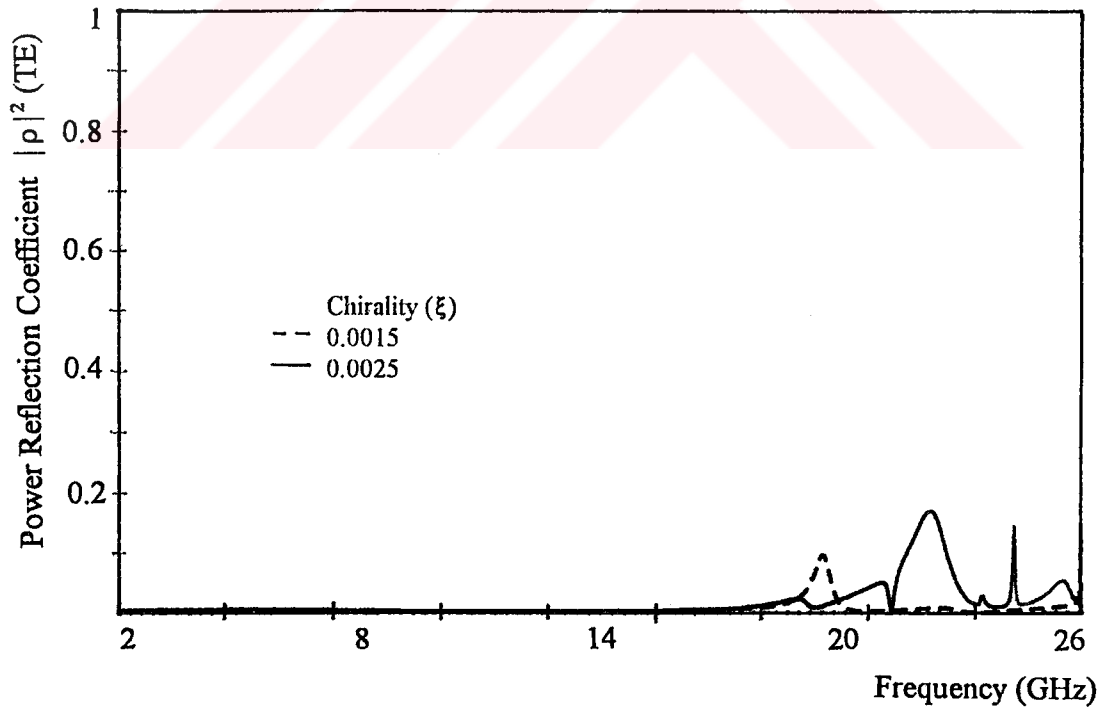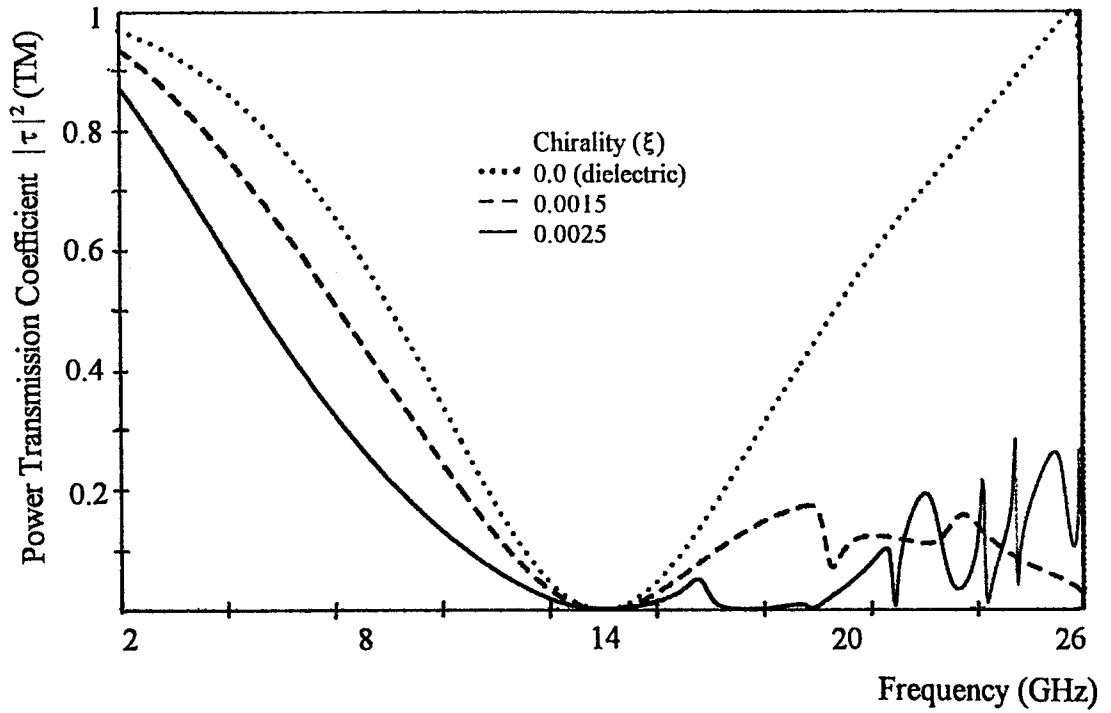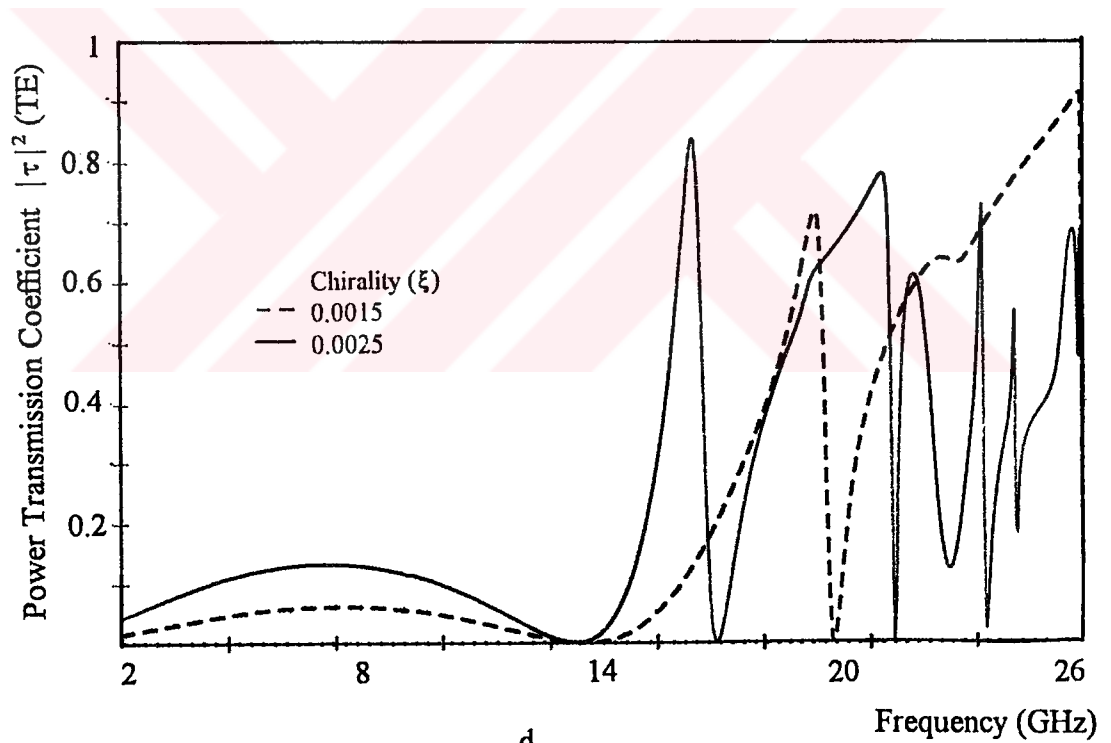
Figure 4.4.11   Spectral characteristics of Chiro-FSS with square loops; TM incidence
($\phi = 0°$, $\theta = 30°$), square lattice ($\alpha = 90°$), $D_1 = D_2 = 10$ mm, $L_x = L_y = 9.4$ mm,
W=1 mm, $\epsilon_r = 1.06$, t = 5 mm. a) Power reflection coefficient (TE),
b) Power reflection coefficient (TM), c) Power transmission coefficient
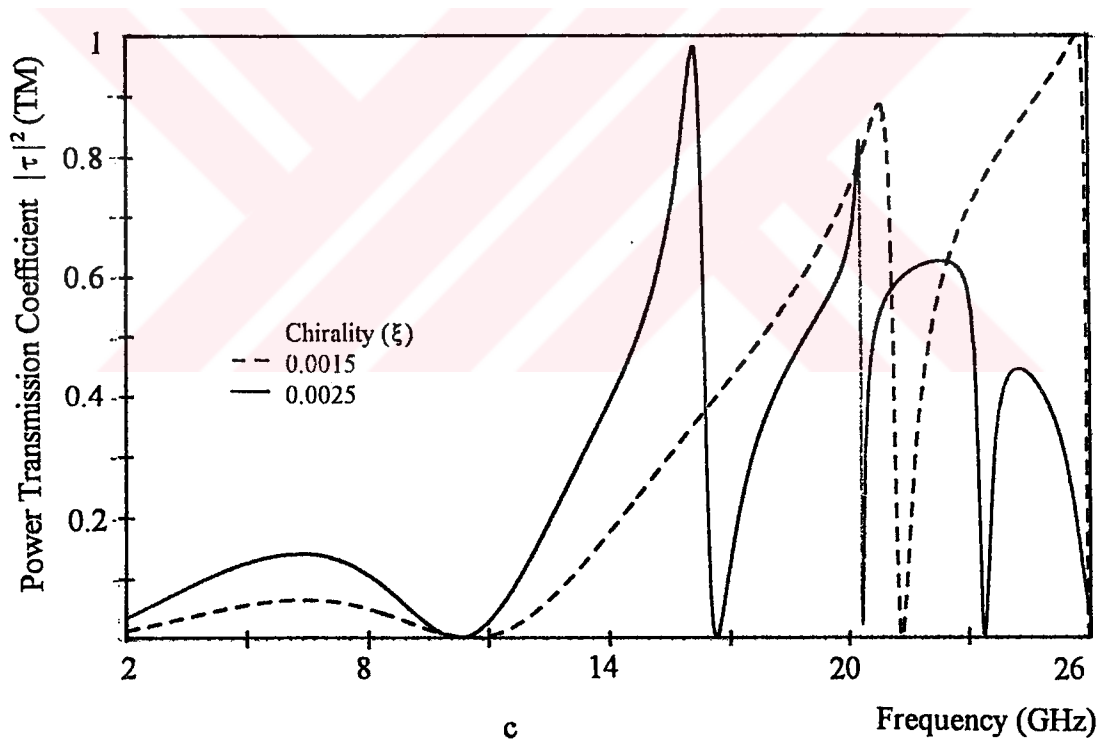(TE), d) Power transmission coefficient (TM).

175

a

b

176
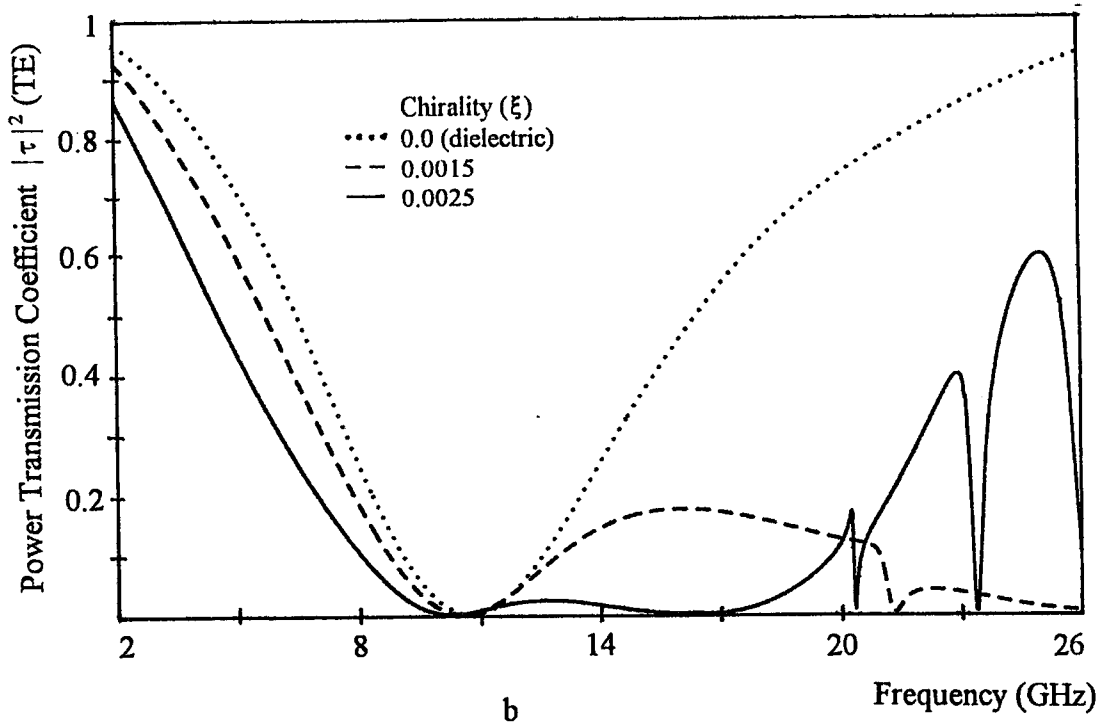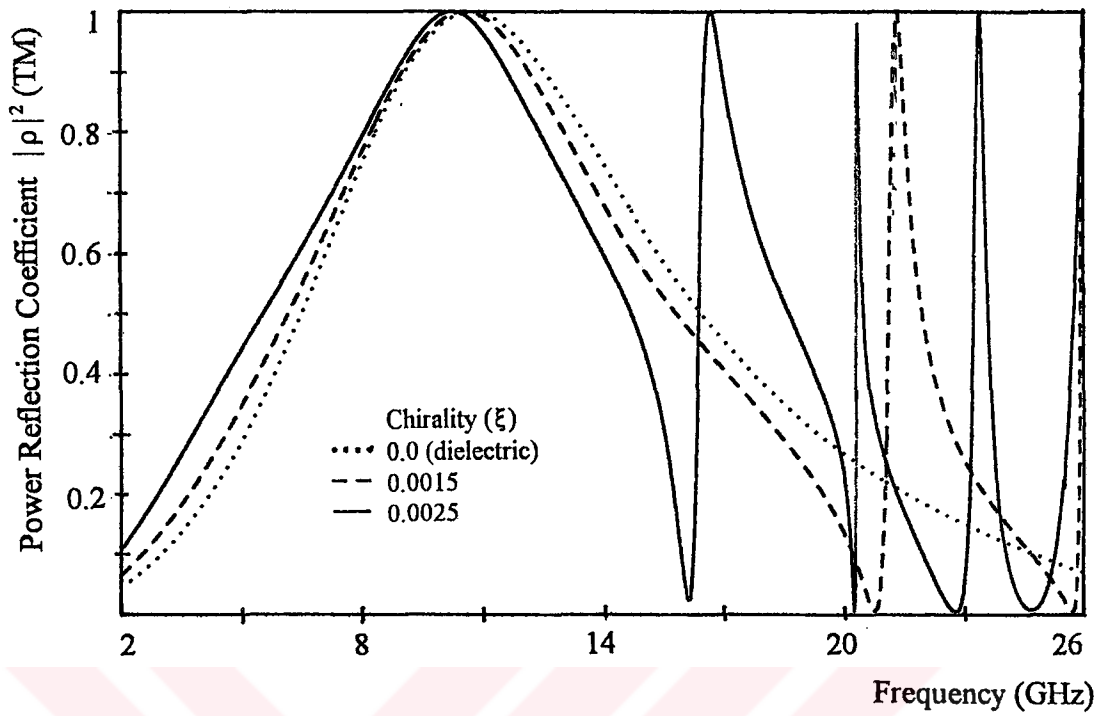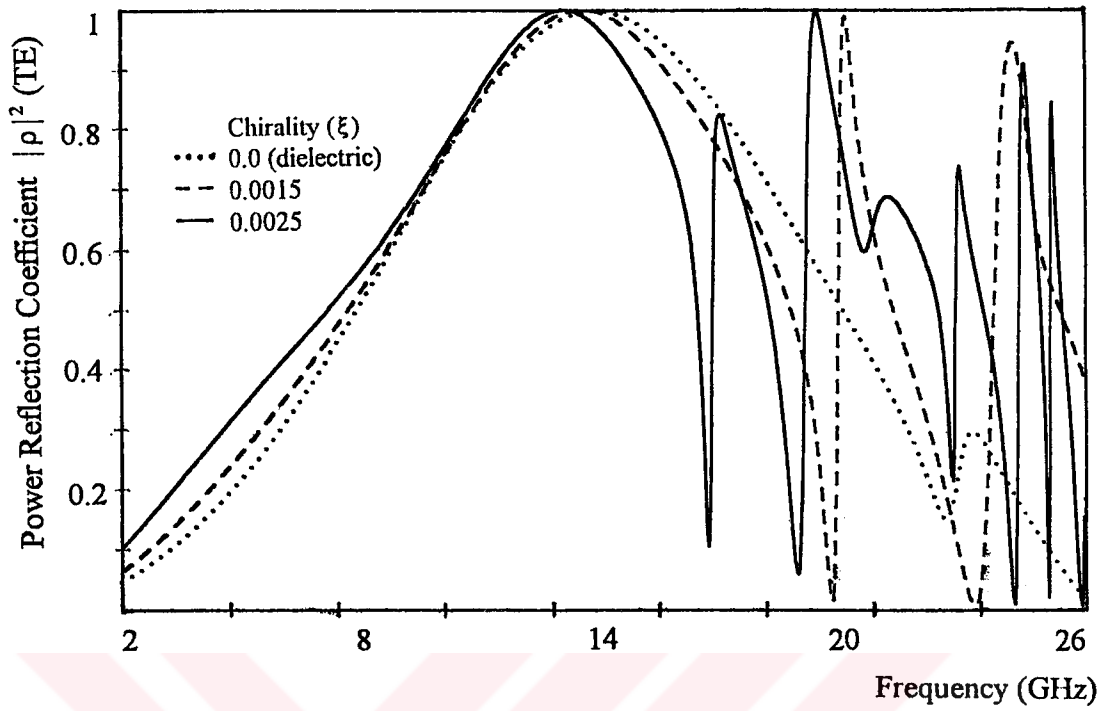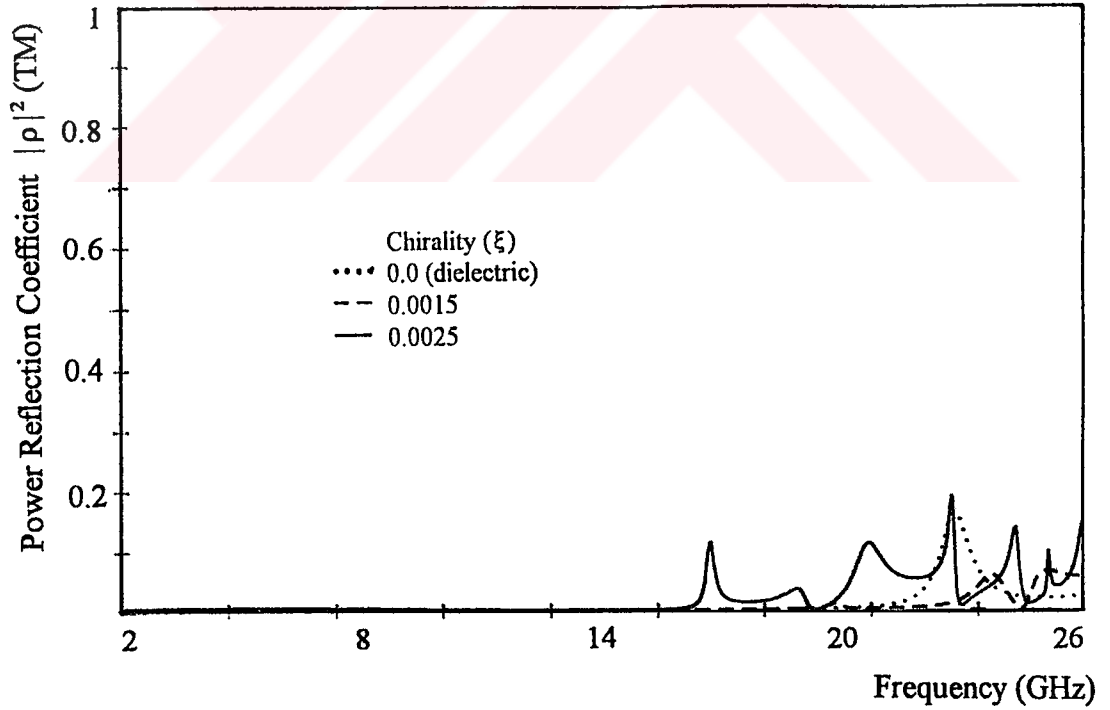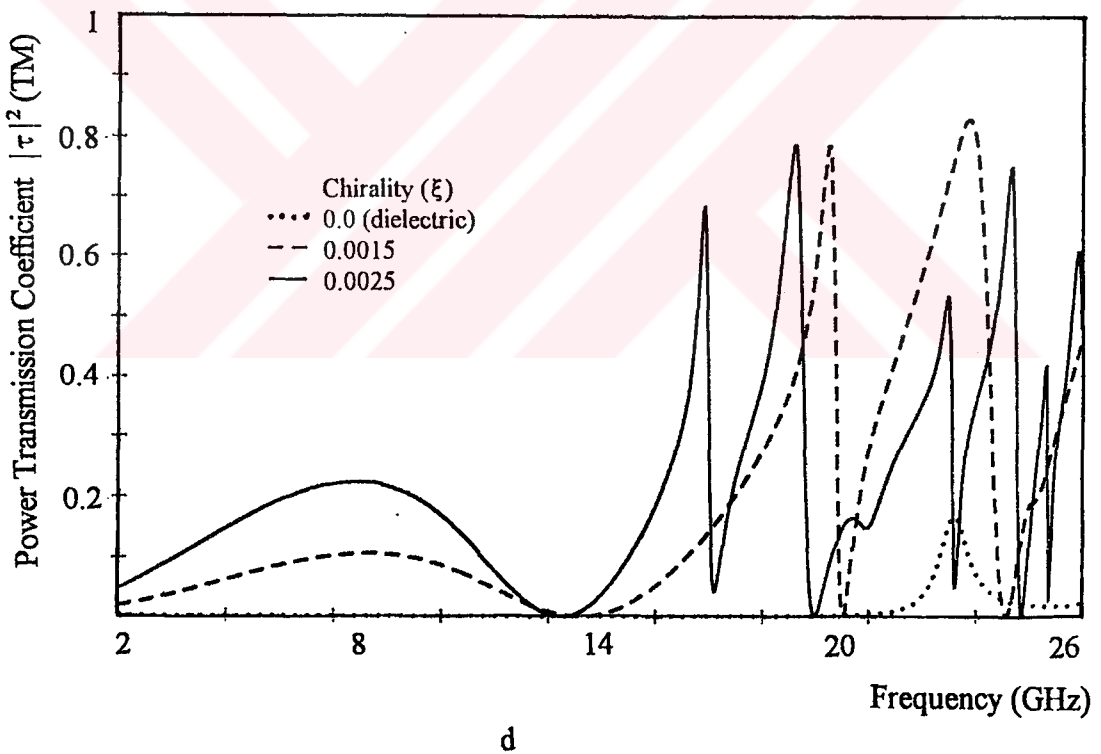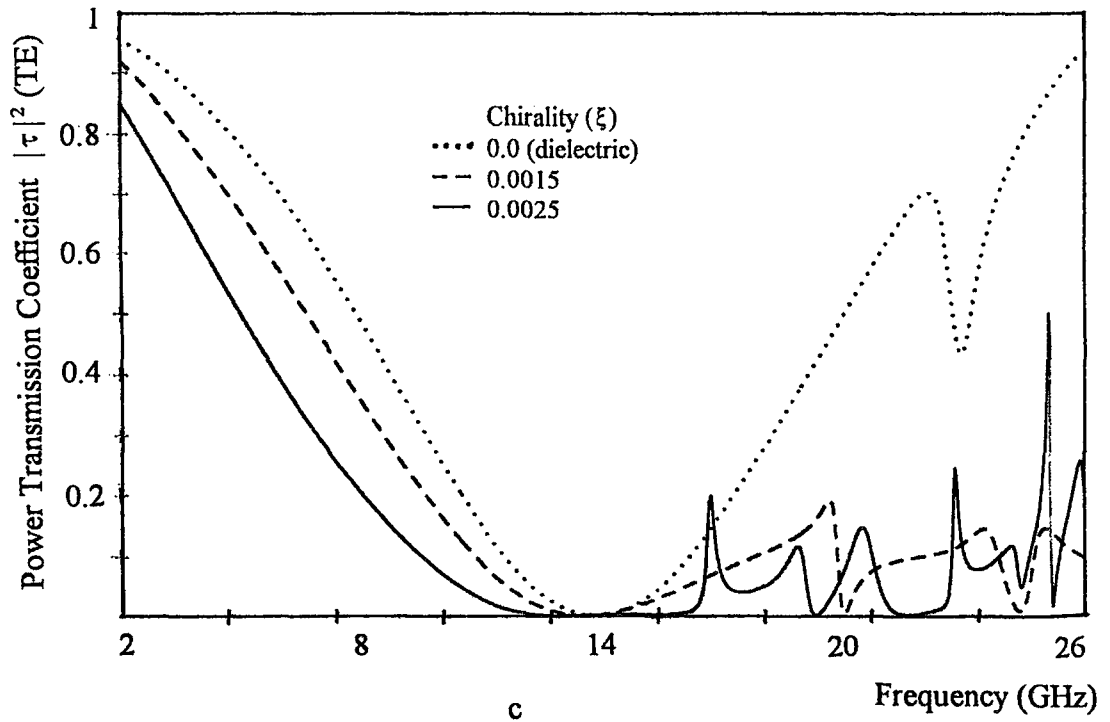
Figure 4.4.12   Spectral characteristics of Chiro-FSS with square loops; TE incidence

(ϕ= 30°,θ=30°), square lattice (α=90°), D_1=D_2=10 mm, L_x=L_y=9.4 mm,

W=1 mm, ϵ_r=1.06, t = 5 mm. a) Power reflection coefficient (TE),

b) Power reflection coefficient (TM), c) Power transmission coefficient
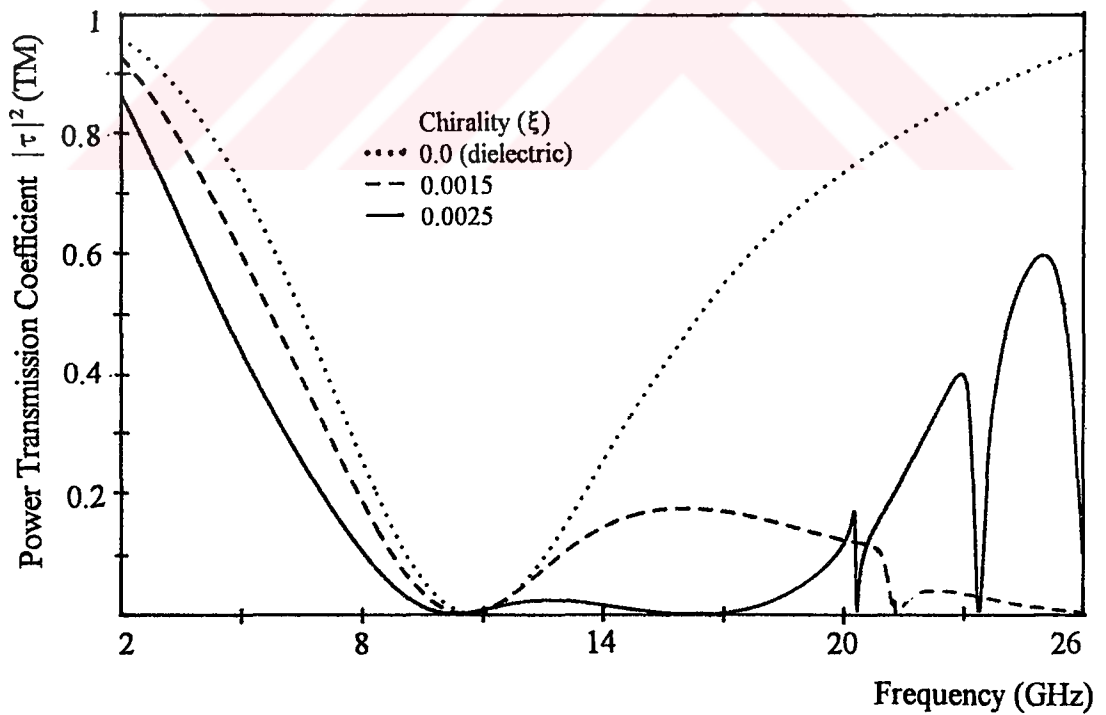
(TE), d) Power transmission coefficient (TM).

177

a

b

178
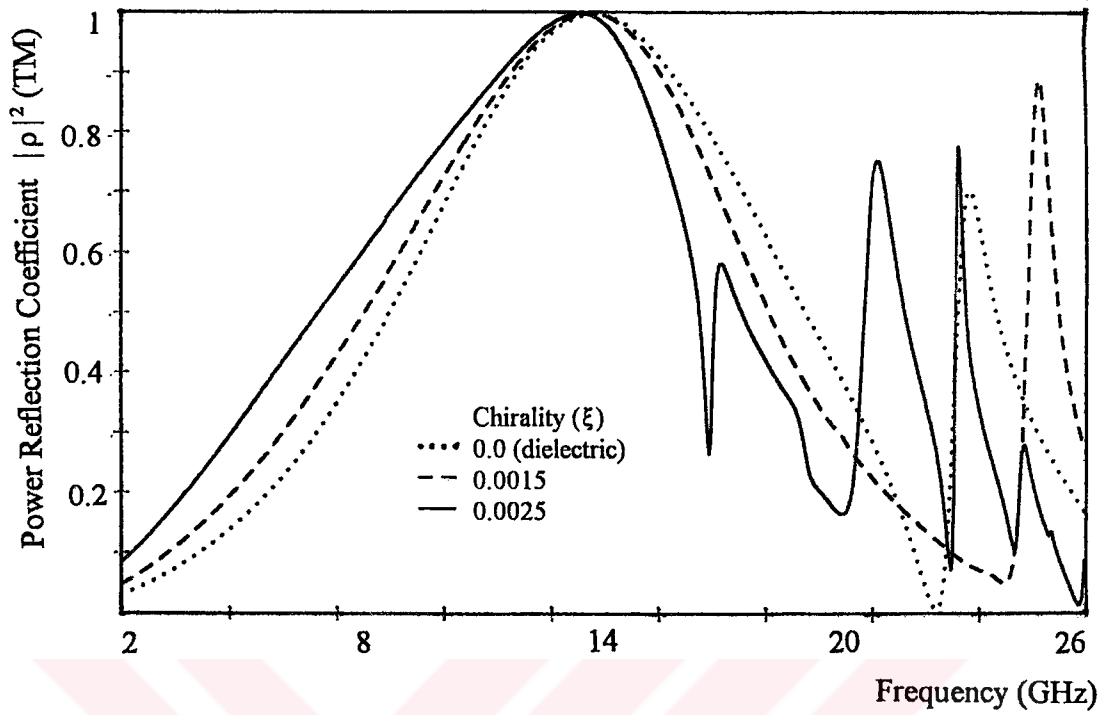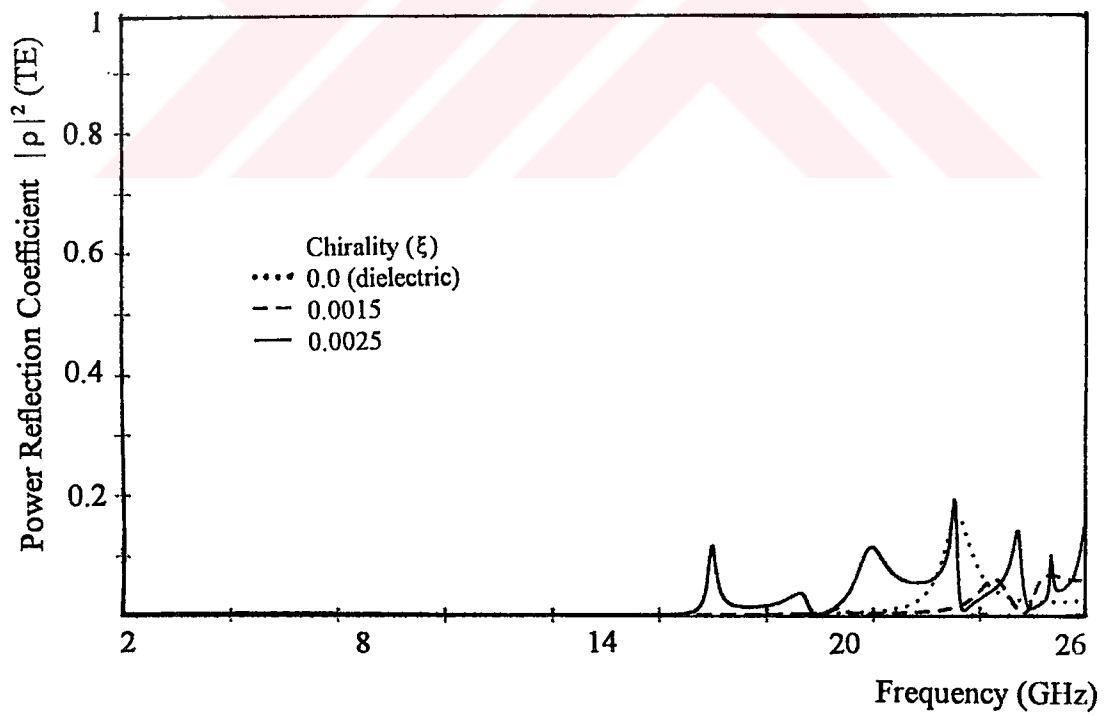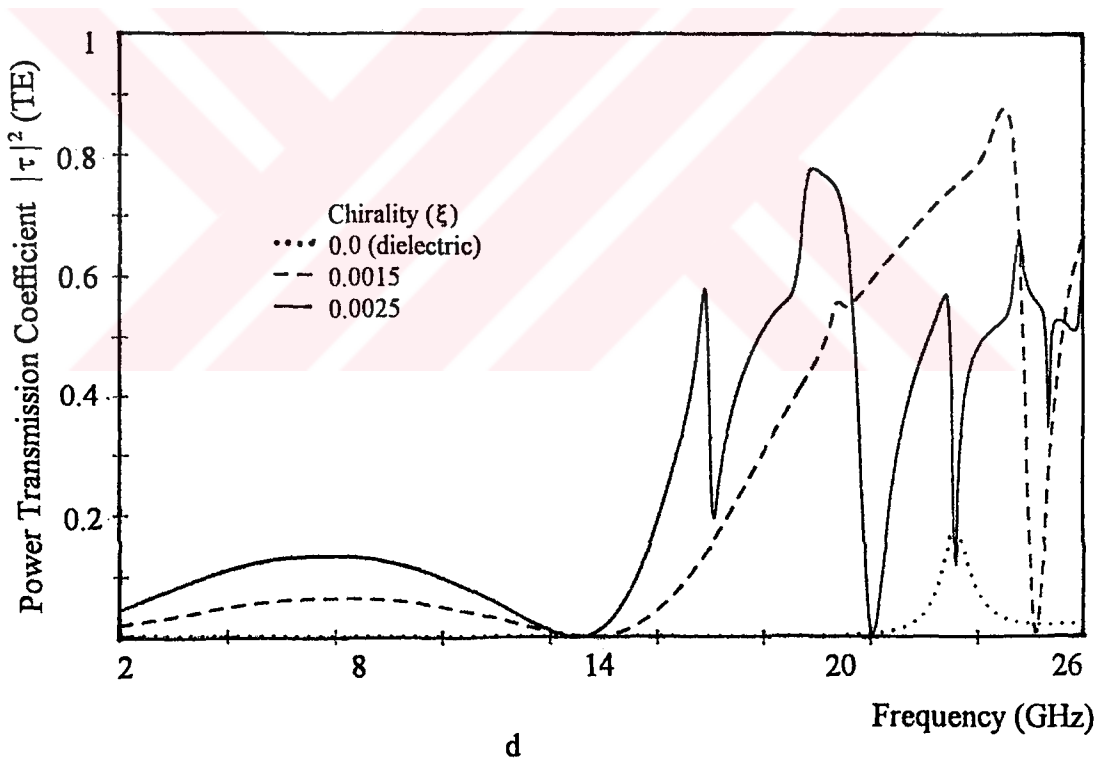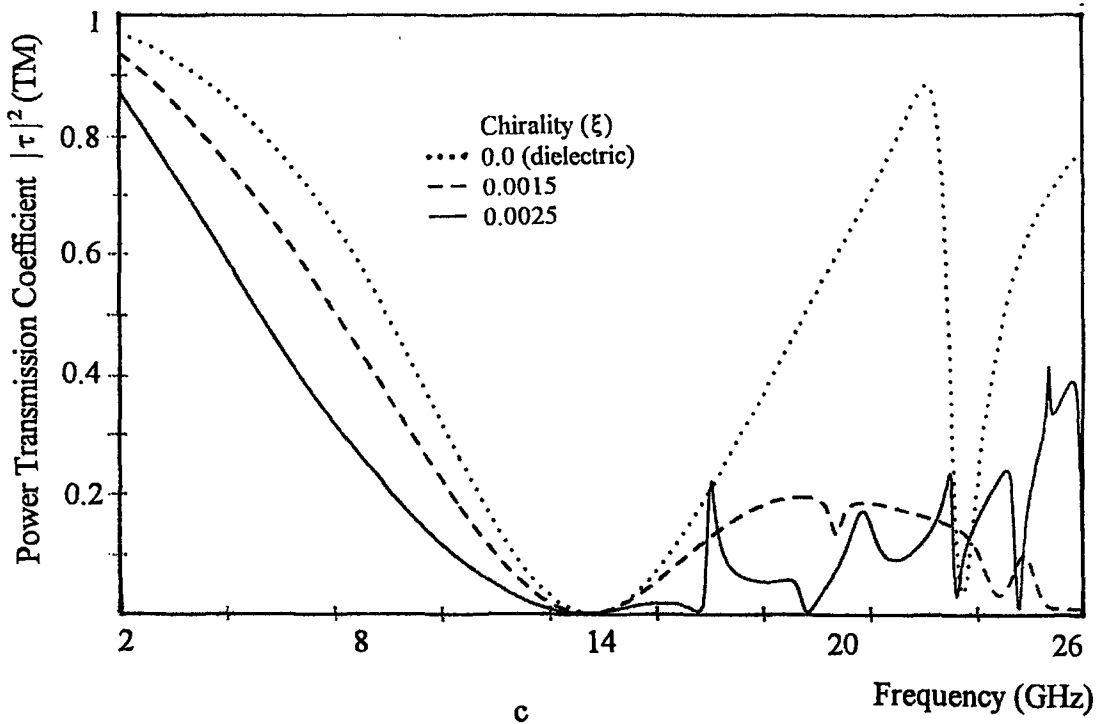
Figure 4.4.13   Spectral characteristics of Chiro-FSS with square loops; TM incidence
(ϕ= 30°,θ=30°), square lattice (α=90°), D_1=D_2=10 mm, L_x=L_y=9.4 mm,
W=1 mm, ϵ_r=1.06, t = 5 mm. a) Power reflection coefficient (TE),
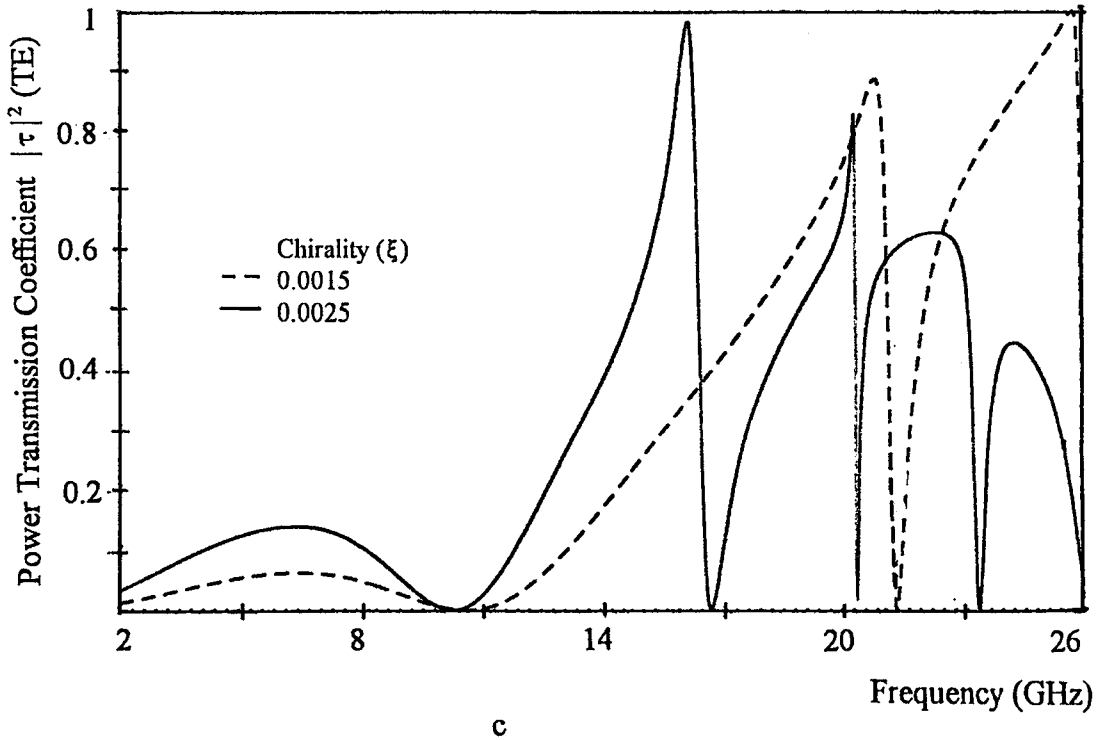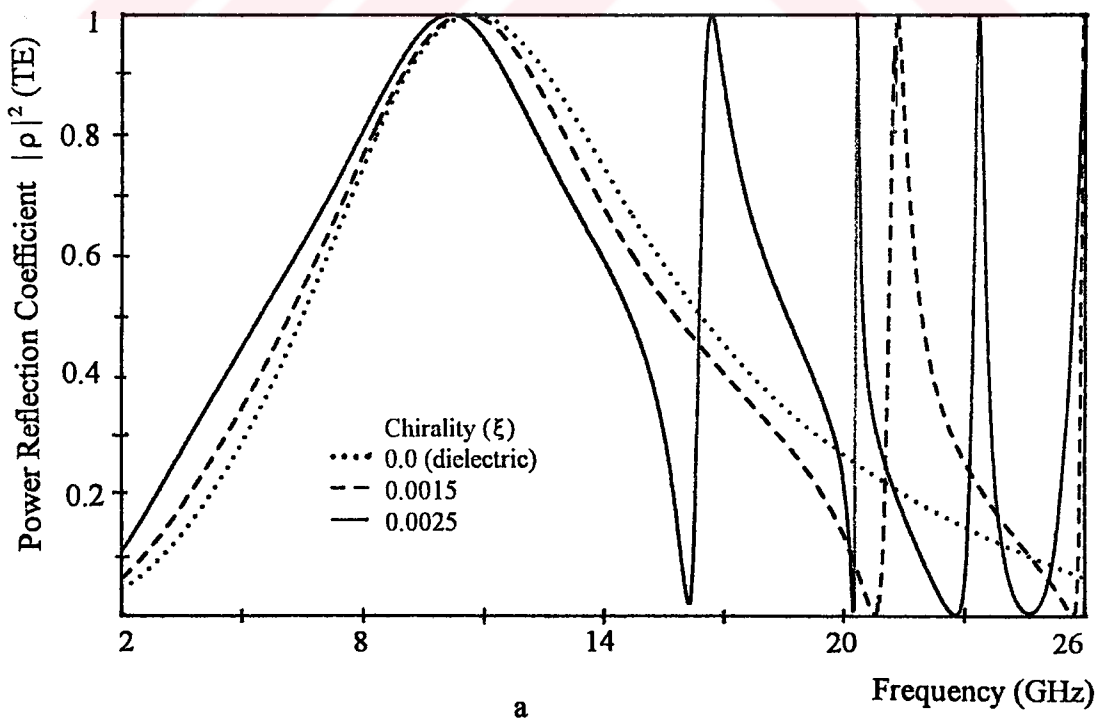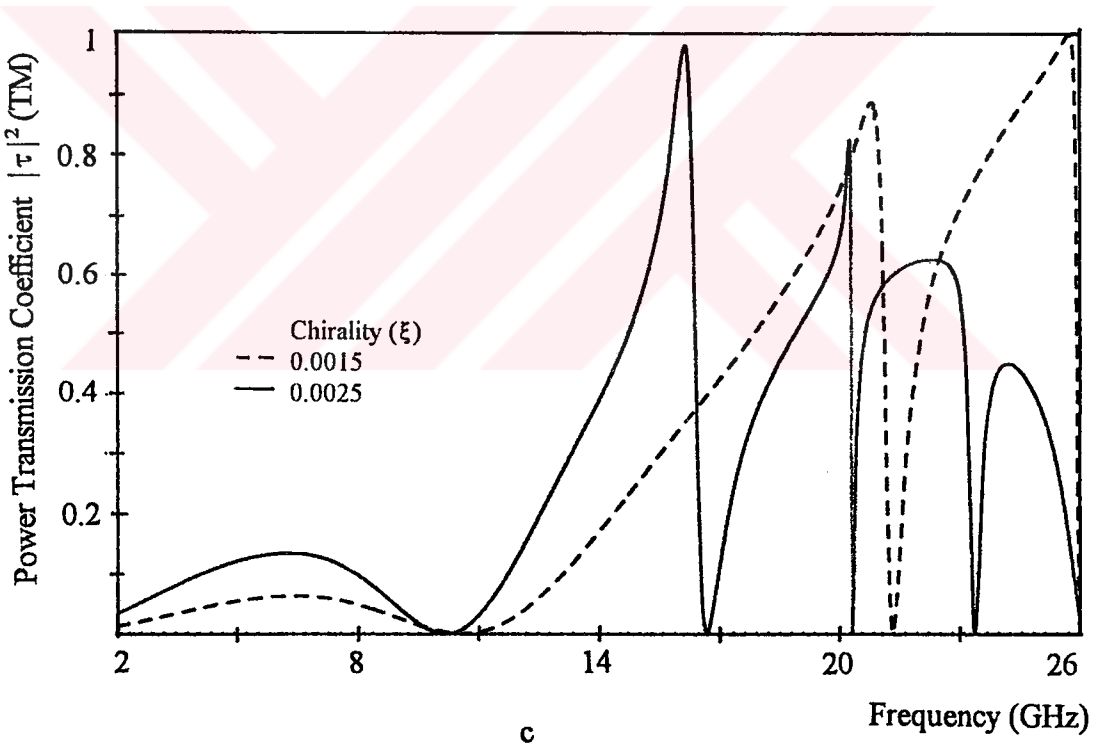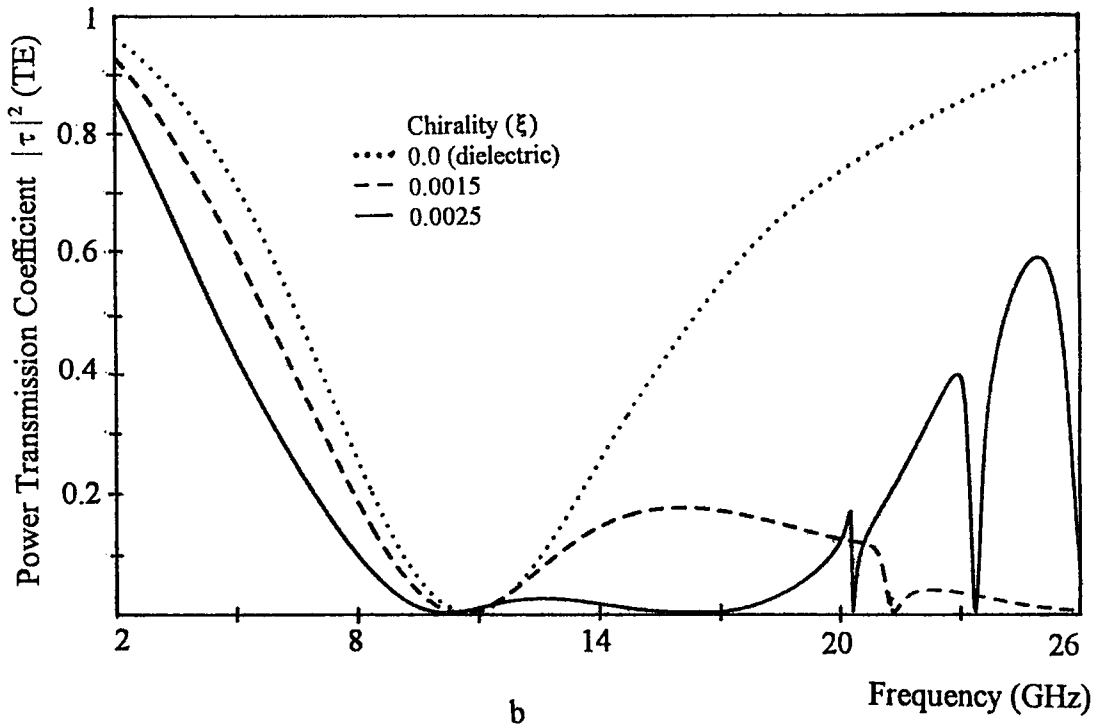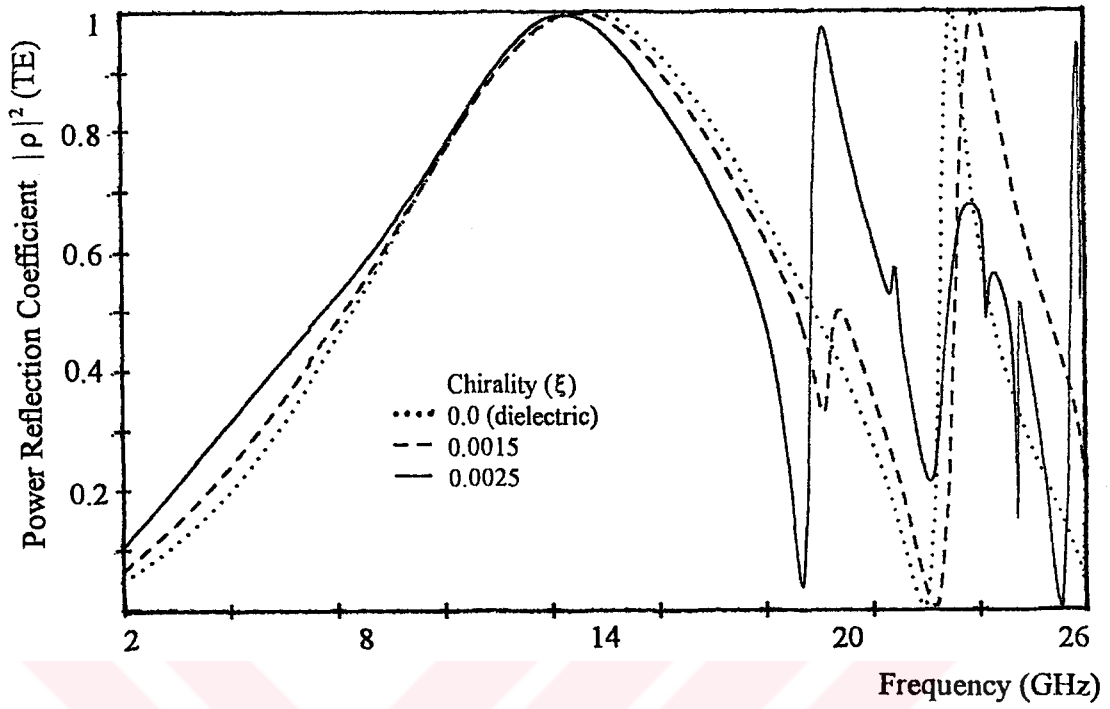b) Power reflection coefficient (TM), c) Power transmission coefficient
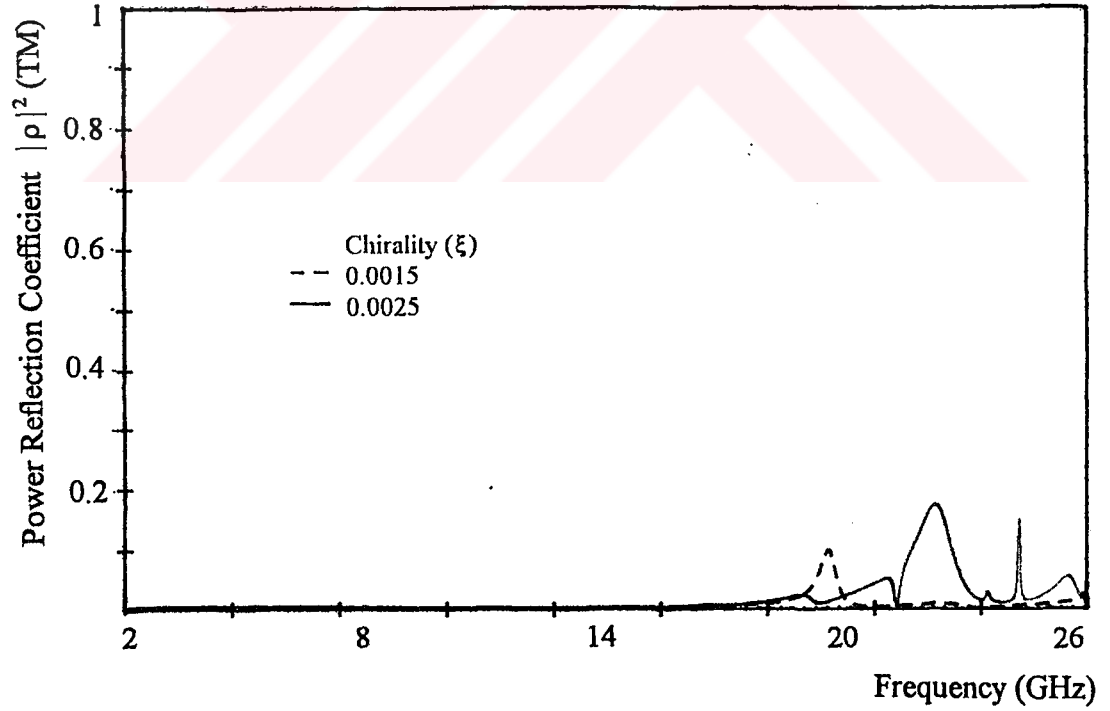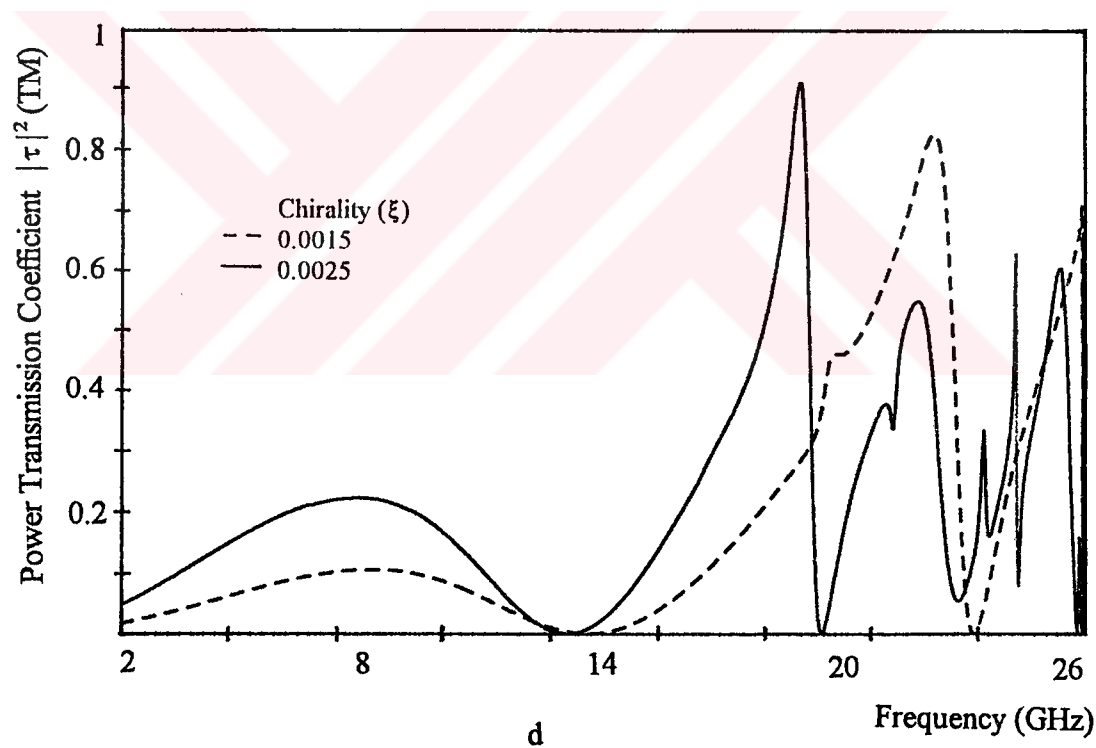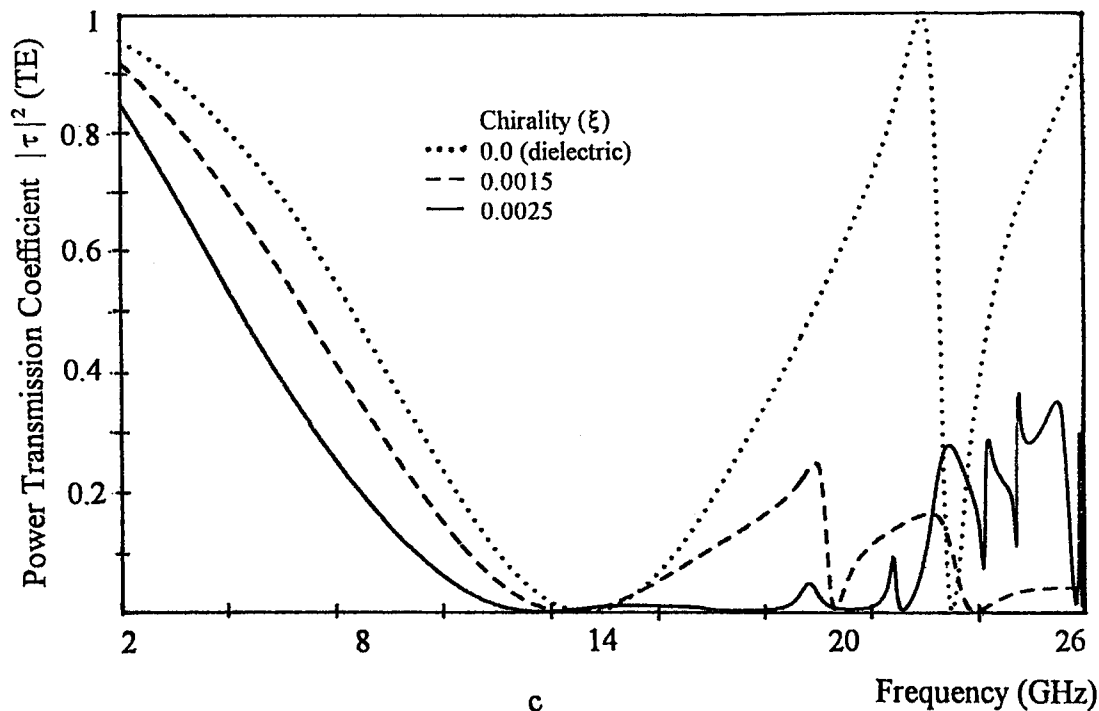(TE), d) Power transmission coefficient (TM).

179

4.5 Chiro-FSS Comprised of Rectangular Patches

Finally, the reflection and transmission characteristics of the Chiro-FSS consisting of perfectly conducting rectangular patches loaded by an isotropic chiral slab are analysed. The unit cell geometry of the structure is given in Figure 4.5.1.
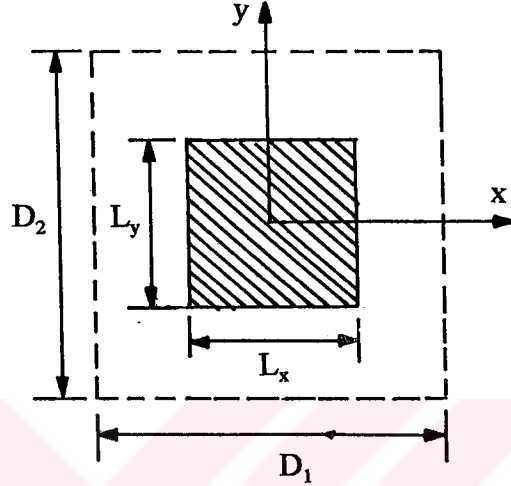
Figure 4.5.1   Unit cell geometry of Chiro-FSS with square patches.

The induced current density can be expressed as a sum of two orthogonal directed current components, $J_{x'}$ and $J_{y'}$. According to the geometry of the conducting patches, the current density must be zero in the direction of propagation at the edges and is nonzero in the direction of flow parallel to the edges allowing for the representation of the edge singularity. Therefore the unknown current density induced on a patch in an unit cell is expressed as,

$$\vec{J}(x',y') = \sum_{n=1}^{N} \sum_{r=0}^{R} a_{nr} \, \vec{I}_{x'nr}(x',y') + \sum_{k=1}^{K} \sum_{s=0}^{S} b_{ks} \, \vec{I}_{y'ks}(x',y') \qquad (4\text{-}68)$$

where,

$$\vec{I}_{nrx'} = \frac{1}{\sqrt{1 - \left(\dfrac{2\,y'}{W}\right)^{2}}} \; T_r\!\left(\frac{2\,y'}{L_y}\right) \begin{bmatrix} \cos \\ \sin \end{bmatrix} \left(\frac{n\,\pi\,x'}{L_x}\right) \vec{a}_{x'} \qquad \begin{bmatrix} n & odd \\ n & even \end{bmatrix} \qquad (4\text{-}69)$$

180

and

$$\vec{I}_{ksy'} = \frac{1}{\sqrt{1 - (\frac{2\,x'}{W})^2}} \; T_s(\frac{2\,x'}{L_x}) \begin{bmatrix} \cos \\ \sin \end{bmatrix} (\frac{k\pi y'}{L_y}) \; \vec{a}_{y'} \qquad \begin{bmatrix} n & odd \\ n & even \end{bmatrix} \qquad (4\text{-}70)$$

Now, consider the inner products for both symmetrical and asymmetrical terms can be expressed as,

For symmetrical terms, (n = 1, 3, 5, ..odd)

$$<\vec{I}_{nrx'}, \vec{\psi}^*_{mpq}> = \frac{1}{\sqrt{A}} \left[(\cos \gamma \; \vec{a}_x - \sin \gamma \; \vec{a}_y) \cdot \vec{u}_{mpq} \right] \frac{L_x L_y}{4} \pi \; (j)^r J_r(\frac{v L_y}{2}) \cdot$$

$$\begin{bmatrix} \dfrac{\sin(\dfrac{u L_x}{2} + \dfrac{n\pi}{2})}{(\dfrac{u L_x}{2} + \dfrac{n\pi}{2})} + \dfrac{\sin(\dfrac{u L_x}{2} - \dfrac{n\pi}{2})}{(\dfrac{u L_x}{2} - \dfrac{n\pi}{2})} \end{bmatrix} \qquad (4\text{-}71)$$

and

$$<\vec{I}_{nrx'}, \vec{\psi}_{mpq}> = \frac{1}{\sqrt{A}} \left[(\cos \gamma \; \vec{a}_x - \sin \gamma \; \vec{a}_y) \cdot \vec{u}_{mpq} \right] \frac{L_x L_y}{4} \pi \; (j)^r J_r(\frac{- v L_y}{2}) \cdot$$

$$\begin{bmatrix} \dfrac{\sin(\dfrac{u L_x}{2} + \dfrac{n\pi}{2})}{(\dfrac{u L_x}{2} + \dfrac{n\pi}{2})} + \dfrac{\sin(\dfrac{u L_x}{2} - \dfrac{n\pi}{2})}{(\dfrac{u L_x}{2} - \dfrac{n\pi}{2})} \end{bmatrix} \qquad (4\text{-}72)$$

For asymmetrical terms, (n = 2, 4, 6, .. even) corresponding inner products are obtaines as,

$$<\vec{I}_{nrx'}, \vec{\psi}^*_{mpq}> = \frac{1}{\sqrt{A}} \left[(\cos \gamma \; \vec{a}_x - \sin \gamma \; \vec{a}_y) \cdot \vec{u}_{mpq} \right] \frac{L_x L_y}{4} \pi \; (j)^{r+1} J_r(\frac{v L_y}{2}) \cdot$$

$$\begin{bmatrix} \dfrac{\sin(\dfrac{u L_x}{2} - \dfrac{n\pi}{2})}{(\dfrac{u L_x}{2} - \dfrac{n\pi}{2})} - \dfrac{\sin(\dfrac{u L_x}{2} + \dfrac{n\pi}{2})}{(\dfrac{u L_x}{2} + \dfrac{n\pi}{2})} \end{bmatrix} \qquad (4\text{-}73)$$

181

and

$$<\vec{I}_{nrx'}, \Psi_{mpq}> = \frac{1}{\sqrt{A}} \left[(\cos\gamma\, \vec{a}_x - \sin\gamma\, \vec{a}_y) \cdot \vec{u}_{mpq} \right] \frac{L_x L_y}{4} \pi\, (j)^{r+1} J_r\left(\frac{-vL_y}{2}\right).$$

$$\left[\frac{\sin\left(\frac{uL_x}{2} + \frac{n\pi}{2}\right)}{\left(\frac{uL_x}{2} \pm \frac{n\pi}{2}\right)} - \frac{\sin\left(\frac{uL_x}{2} - \frac{n\pi}{2}\right)}{\left(\frac{uL_x}{2} - \frac{n\pi}{2}\right)} \right] \qquad (4\text{-}74)$$

For y' directed currents, the inner products can be written as,

For symmetrical terms, (n = 1, 3, 5, ..odd)

$$<\vec{I}_{ksy'}, \Psi_{mpq}^*> = \frac{1}{\sqrt{A}} \left[(\sin\gamma\, \vec{a}_x + \cos\gamma\, \vec{a}_y) \cdot \vec{u}_{mpq} \right] \frac{L_x L_y}{4} \pi\, (j)^s J_s\left(\frac{uL_x}{2}\right).$$

$$\left[\frac{\sin\left(\frac{vL_y}{2} + \frac{k\pi}{2}\right)}{\left(\frac{vL_y}{2} + \frac{k\pi}{2}\right)} + \frac{\sin\left(\frac{vL_y}{2} - \frac{k\pi}{2}\right)}{\left(\frac{vL_y}{2} - \frac{k\pi}{2}\right)} \right] \qquad (4\text{-}75)$$

and

$$<\vec{I}_{ksy'}, \Psi_{mpq}> = \frac{1}{\sqrt{A}} \left[(\sin\gamma\, \vec{a}_x + \cos\gamma\, \vec{a}_y) \cdot \vec{u}_{mpq} \right] \frac{L_x L_y}{4} \pi\, (j)^s J_s\left(\frac{-uL_x}{2}\right).$$

$$\left[\frac{\sin\left(\frac{vL_y}{2} + \frac{k\pi}{2}\right)}{\left(\frac{vL_y}{2} + \frac{k\pi}{2}\right)} + \frac{\sin\left(\frac{vL_y}{2} - \frac{k\pi}{2}\right)}{\left(\frac{vL_y}{2} - \frac{k\pi}{2}\right)} \right] \qquad (4\text{-}76)$$

For asymmetrical current, (n = 2, 4, 6, ...even)

$$<\vec{I}_{ksy'}, \Psi_{mpq}^*> = \frac{1}{\sqrt{A}} \left[(\sin\gamma\, \vec{a}_x + \cos\gamma\, \vec{a}_y) \cdot \vec{u}_{mpq} \right] \frac{L_x L_y}{4} \pi\, (j)^{s+1} J_r\left(\frac{uL_x}{2}\right).$$

$$\left[\frac{\sin\left(\frac{vL_y}{2} - \frac{k\pi}{2}\right)}{\left(\frac{vL_y}{2} - \frac{k\pi}{2}\right)} - \frac{\sin\left(\frac{vL_y}{2} + \frac{k\pi}{2}\right)}{\left(\frac{vL_y}{2} + \frac{k\pi}{2}\right)} \right] \qquad (4\text{-}77)$$

and

$$<\vec{I}_{ksy'}, \Psi_{mpq}> = \frac{1}{\sqrt{A}} \left[(\sin\gamma\, \vec{a}_x + \cos\gamma\, \vec{a}_y) \cdot \vec{u}_{mpq} \right] \frac{L_x L_y}{4} \pi\, (j)^{s+1} J_r(\frac{-uL_x}{2}) \cdot$$

$$\left[\frac{\sin(\frac{vL_y}{2} + \frac{k\pi}{2})}{(\frac{vL_y}{2} + \frac{k\pi}{2})} - \frac{\sin(\frac{vL_y}{2} - \frac{k\pi}{2})}{(\frac{vL_y}{2} - \frac{k\pi}{2})} \right] \qquad (4\text{-}78)$$

where,

$$u = k_{xpq}\, \cos\gamma - k_{ypq}\, \sin\gamma$$

$$v = k_{xpq}\, \sin\gamma + k_{ypq}\, \cos\gamma$$

and

$$\vec{a}_{x'} = \cos\gamma\, \vec{a}_x - \sin\gamma\, \vec{a}_y$$

$$\vec{a}_{y'} = \sin\gamma\, \vec{a}_x + \cos\gamma\, \vec{a}_y$$

4.5.1. Numerical Results of the Chiro-FSS with Square Patches.

Finally, the last section is devoted to the computed results of the analyses for Chiro-FSS comprised of perfectly conducting square patches printed on isotropic chiral slab. The reflection and transmission characteristics fo the Chiro-FSS are examined for various type of configuration. Effects of design parameters, i.e., shape of the square patch, constitutive parameters of the slab and polarisation and the angle of the incident plane wave on the spectral characteristics of the Chiro-FSS are investigated.

The first Chiro-FSS considered, is the two dimensional infinte arrays of square patches having lenths of $L_x = L_y = 4$ mm, are arranged in a square lattice. The dimensions of the unit cell are $D_1 = D_2 = 10$ mm. The thickness and dielectric constant of the chiral slab is assumed to be 5 mm and 1.06, respectively.

Figure 4.5.2 is the plot of reflection and transmission characterisitcs of the Chiro-FSS

for the normally incident TE plane wave excitation. In order to illustrate how much the presence of chirality admittance of the slab modifies the spectral reponse, four different values of chirality admittance are assumed, ξ=0.0 (dielectric), 0.0007, 0.0014 and 0.0021 mho. It can be observed that from Figure 4.5.2 the multiple resonances with narrow bandwidths associated are olso obtained for this type of Chiro-FSS. As the chirality admittance is increased, there is a noticable bandwidth decrease associated with the frtequency shift to the lower frequencies. The isolation between the resonances are very good. The magnitude of the co-polar (TM) transmitted wave through the Chiro-FSS decreases as the chirality increases. One should be note that full transmission are observed in the transmission curve of the cross-polar component (TM) for ξ=0.0014 and 0.0021 mho.

When the thickness of the chiral slab is reduced to 4 mm, the reflection and transmission characteristics of the Chiro-FSS having the same parameters as in the previous example some variations are observed, as illustrated in Figure 4.5.3. The resonances frequencies are shifted to the figher frequencies. Almost full transmission with wide bandwidth are observed for the cross-polar (TM) components for high values of chirality admittance ξ=0.0021 mho.

Next example, dielectric consatnt of the 5 mm thick chiral slab is increased to 1.32. The other design parameters of the Chiro-FSS are assumed to be the same as in the first example. Numerical results of the reflection and transmission coefficients are shown in Figure 4.5.4, for ξ=0.0 (dielectric), 0.0014 and 0.0021 mho.

Comparision of Figure 4.5.2 with Figure 4.5.4 gives that shifthing of resonance frequencies to lower frequencies to lower frequency band are observed. Note that the bandwidth of the resonances are not changed in contrast to the previous types of Chiro-FSS comprised of cross dipole, circular rings, etc.. Full transmission are also possible for the case of ξ=0.0014 and 0.0021 mho. The results corresponding to the Chiro-FSS having chiral slab thickness of 4 mm, while the other parameters are unchanged are illustrated in Figure 4.5.5 for the normally incident plane wave excitation of TE polarisation.

Another design parameter is the size of the conducting patches. In the next

184

configuration we assume that the Chiro-FSS comprised of square patches having the larger size compared with the previous example. In this case, the dimensions of the square patches are taken as $L_x=L_y=6$ mm, and the square patches are arranged in a square lattice with $D_1=D_2=10$ mm. The conducting patches are supported by an isotropic chiral slab having a thickness of 5 mm and dielectric constant of 1.06. The computed results of reflection and transmission characteritics are illustrated in Figure 4.5.6 for the normal incidence plane wave illumination of TE polarisation. The plot are obtained for $\xi= 0.0$ (dielectric), 0.0014 and 0.0021 mho. As it can be seen from the figures, the spectral characteritics of the conventional FSS (zero chirality) are subjected to the great modifications when the chirality property is introduced to the slab. Similar to the other tytpes of Chiro-FSS, multiple resonanecs are also observed in the reflection curve. The bandwidth of the resonances are extremelly small compared with the reonance bandwidth of the conventional FSS. In other words, when the chirality property is introduced to the conventional FSS structure, frequency sensitivity of the FSS is further improved. In the transmission curve of cross-polar component (TM), the full transmission condition is still possible for the case of $\xi=0.0014$ and 0.0021 mho.

Note that increasing the size of the square patches from 4 mm to 6 mm, the bandwidth of the resonances are broadened for all value of chirality admittance, $\xi=0.0$, 0.0014 and 0.0021 mho. This is due to increasing the reflectivity nature of the screen by increasing the size of the conductor scatteres. Another difference of this case is the shifting the resonance frequencies to the lower frequency band. Similar effect is also obtained in the spectral respones of theother type of Chiro-FSS.

Figure 4.5.7 shows the variation of the reflection and transmission characteristics of the Chiro-FSS having the same parameters as in the previoue example except thickness, $t = 4$ mm for a TE polarised plane wave excitation. Note that, the bandwidth of the resonances obtained in this case are wider than the previou one and the isolation of the resonances are not changed considerably.

The results presented in the previour part of this section are obtained for normally incident plane wave of TE polarisation. Exactly same results are also obtained for the case of TM illumination of the screen, is due to symmetry of the conducting elements.

185

The fore the polarisation of the normally incident plane wave doe not alter the spectral characteristics of the Chiro-FSS with square patches.

In this part we present the some numerical results of the spectral response of the Chiro-FSS comprised of square patches illuminated by the non-zero azimuth and/or polar angles. First consider the Chiro-FSS has the following design parameters; $L_x = L_y = 6$ mm, $D_1 = D_2 = 10$ mm, $\epsilon_r = 1.06$, $t = 5$ mm, square lattice geometry. The results of power reflection and transmission coefficients for TE and TM plane wave illuminations with $\theta = 0°$ and $\phi = 30°$ are illutrated in Figure 4.5.8 and Figure 4.5.9, respectively. Comparision of these two results shows that the spectral response of the Chiro-FSS are almost same. For both TE and TM illumination case the magnitude of the cross-polar reflected wave is zero. The magnitude of the cross-polar transmitted waves are nearly unity at same frequencies for both case.

When the azimuth angle is increased to 45°, ($\theta = 0°$, $\phi = 45°$) the exactly same responses are observed for both polarisation as can be seen from Figure 4.510. It is seen that the spectral response is not sensitive to the azimuth angle of the incident plane wave of both TE and TM polaristion with zero polar angle, by comparing the Figure 4.5.10 with the Figure 4.5.9 and Figure 4.5.10.

Second, the computed power reflection and transmission of the Chiro-FSS illuminated by the TE and TM polarised plane waves with $\theta = 30°$, $\phi = 0°$, are shown in Figure 4.5.11 and Figure 4.5.1 respectively. In the case of TE illimunation, exactly a full reflection is obtained for zero chirality admittance, but when the chirality is increased the magnitude of the reflection coeficients of co-polar (TE) component are slightly diminished from the unity. Whereas in the TM illumination response no full reflections is observed for all values of chirality admittance. In both case of illumination magnitude of the cross-polar reflection coefficients are rafther small compared with the co-polar one.

Finally, we consider the obliquely incidence excitation of the Chiro-FSS by a TE and TM plane wave with $\theta = 30°$, $\phi = 30°$. The computed power reflection and transmission coefficients as a function of frequency for TE and TM illuminations, are depicted in Figure 4.5.13 and Figure 4.5.14, respectively. Note that in this case the azimuth angle

of the incident wave is increaesd for 0° to 30°. This increase in azimuth angle alters the spectral characteristics of the Chiro-FSS radically for both TE and TM polarisations. As can be seen from the figures, full transmission is not obtained for niether TE nor TM case. But for different values of chirality admittance, full reflection for co-poar components is possible for both polarisations. Also note that the magnitude of the cross-polar reflected wave is still too smal compared with the magnitude of theco-polar componet for both polarisations.

To conclude, due to results presented, general characteristics of the Chiro-FSS comprised of squre patches loaded by an isotropic chiral slab can be express as;

- When the chirality property is introduced to the FSSs with squre patches, its spectral characterisitcs are quite improved.

- Multiple resonances with very narrow bandwidths are obtained when the screen is illuminated by anormal incidence TE and TM plane wave.

- Similar variations are observed in the spectral characteristics of the Chiro-FSS comprised of square patches as in the spectral characteristics of the other type sof Chiro-FSS with cross dipoles, circular rings, etc. when the degin parameters of the structure i.e., thickness, dielectric constant and chirality admittnace of the slab, geometry of conducting elements and array geometry are altered.

- Very narrow bandwidths associated to the resonances are obtained when the size of the square patches are reduced. As expected, the resonances ferquencies are shifted toward to highre frequency band in the spectral characterisitcs of the Chiro-FSS.
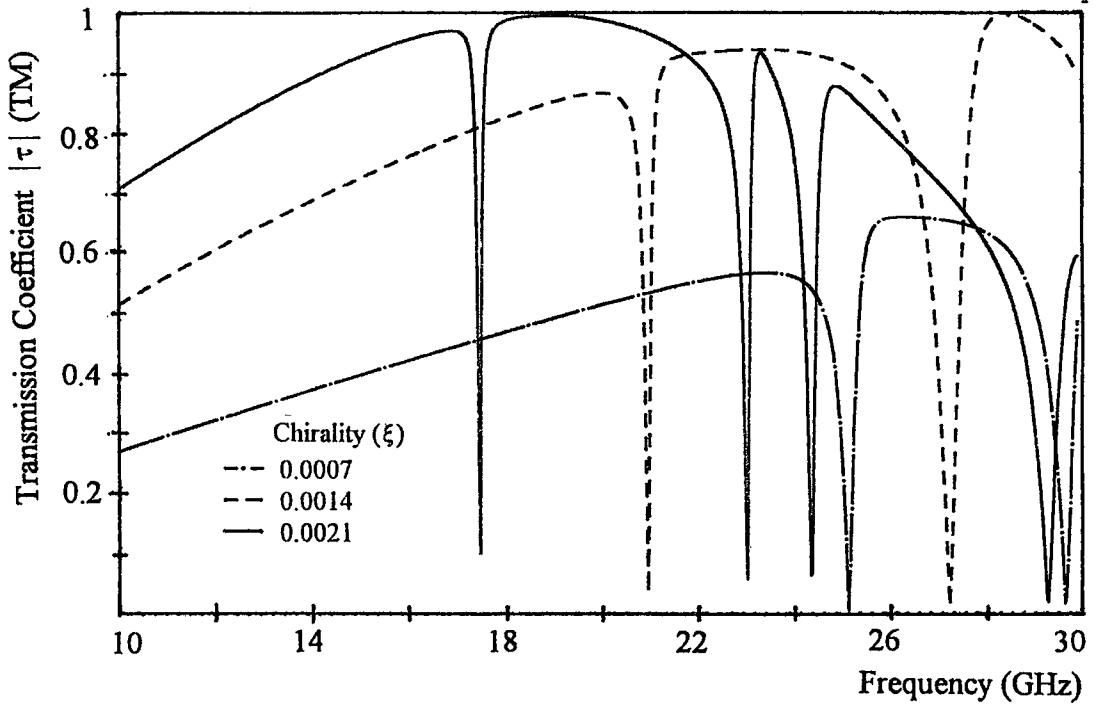
- In the case of non-zero azimuth angle, it is seen that the reflection and transimssion characteritics is not sensitive to azimuth angle. When the polar angle of the incident plane wave increased, the response of the screen is changed drastically. But in some cases one or more than one resonances are still possible when the chirality is introduced.
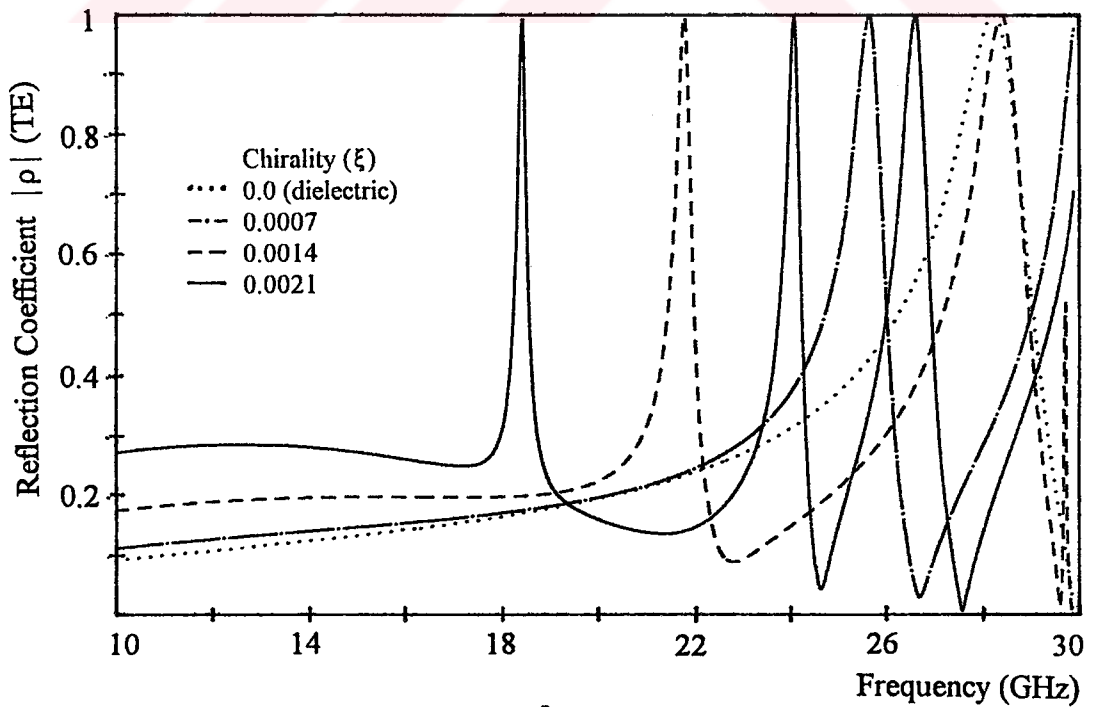
a

b

188
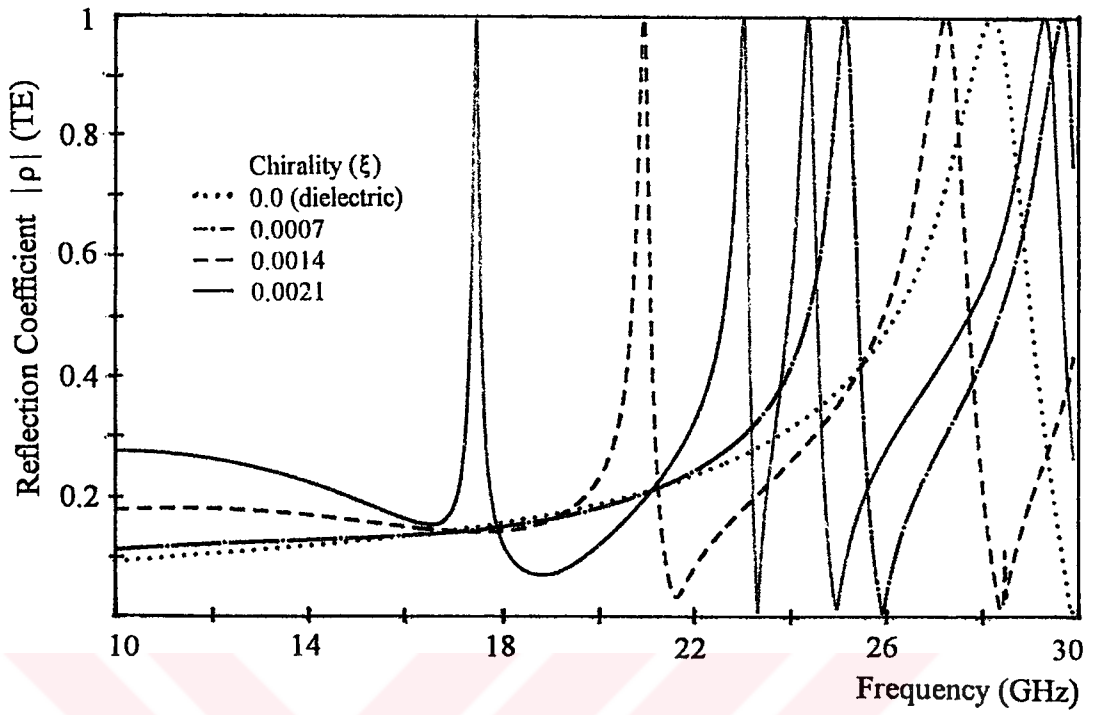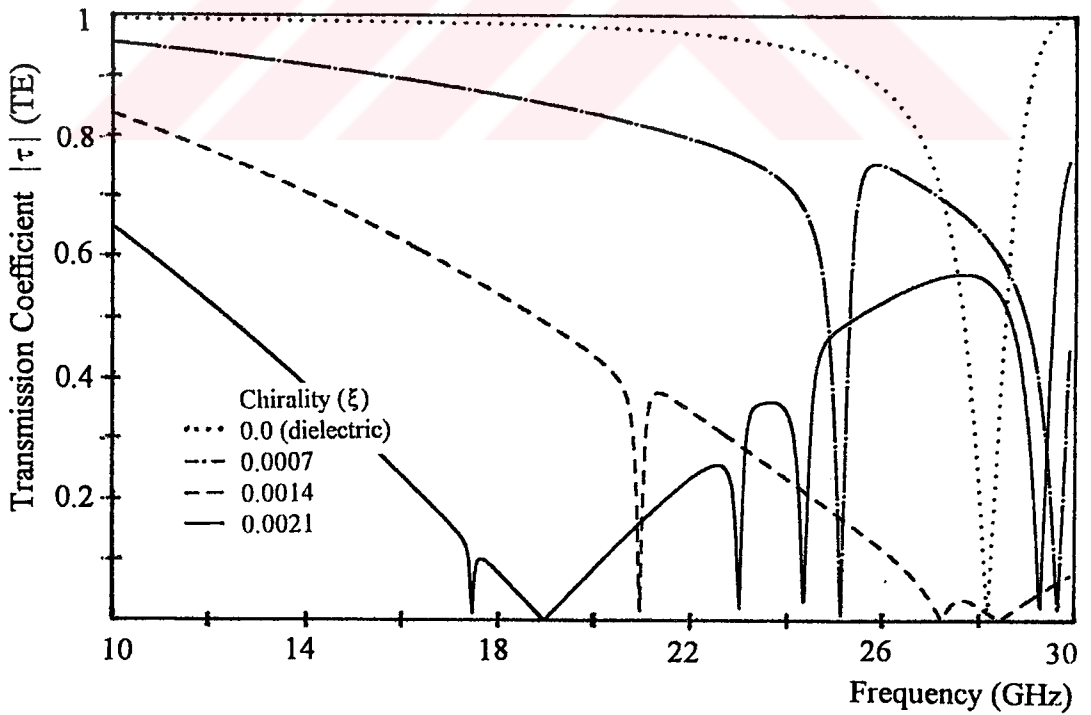
Figure 4.5.2   Spectral characteristics of Chiro-FSS with square patches; TE incidence
($\phi = 0°$, $\theta = 0°$), square lattice ($\alpha = 90°$), $D_1 = D_2 = 10$ mm, $L_x = L_y = 4$ mm,
$\epsilon_r = 1.06$, t = 5 mm. a) Reflection coefficient (TE), b) Transmission
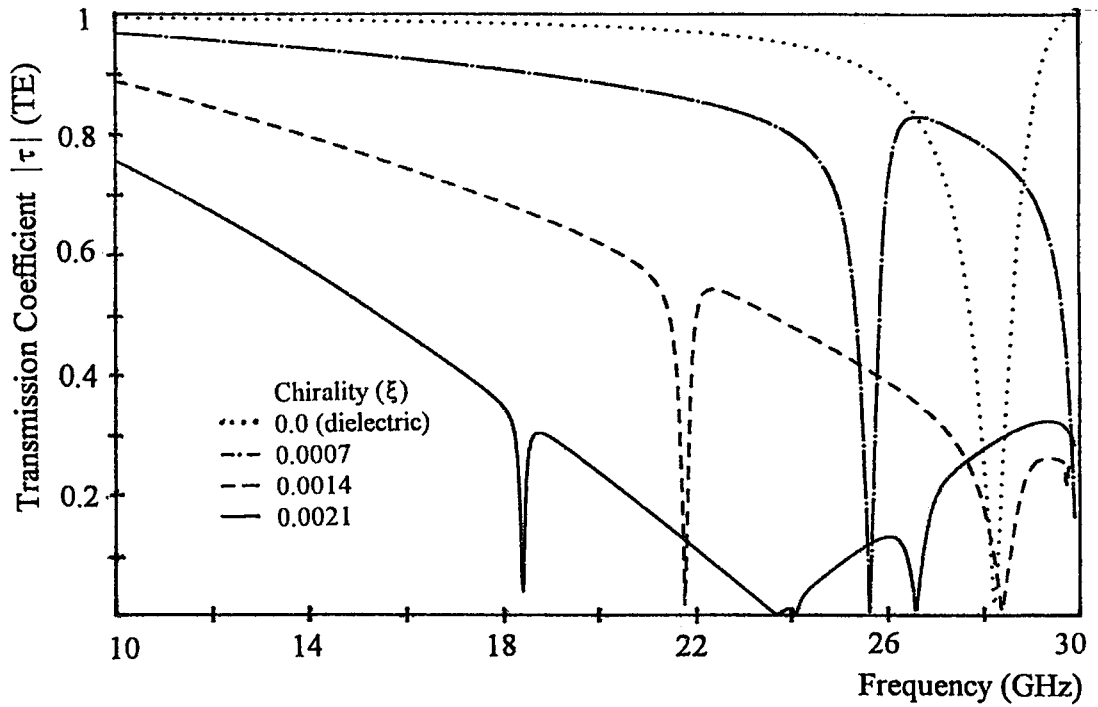coefficient (TE), c) Transmission coefficient (TM).

Figure 4.5.3   Spectral characteristics of Chiro-FSS with square patches; TE incidence
($\phi = 0°$, $\theta = 0°$), square lattice ($\alpha = 90°$), $D_1 = D_2 = 10$ mm, $L_x = L_y = 4$ mm,
$\epsilon_r = 1.06$, $t = 4$ mm. a) Reflection coefficient (TE), b) Transmission
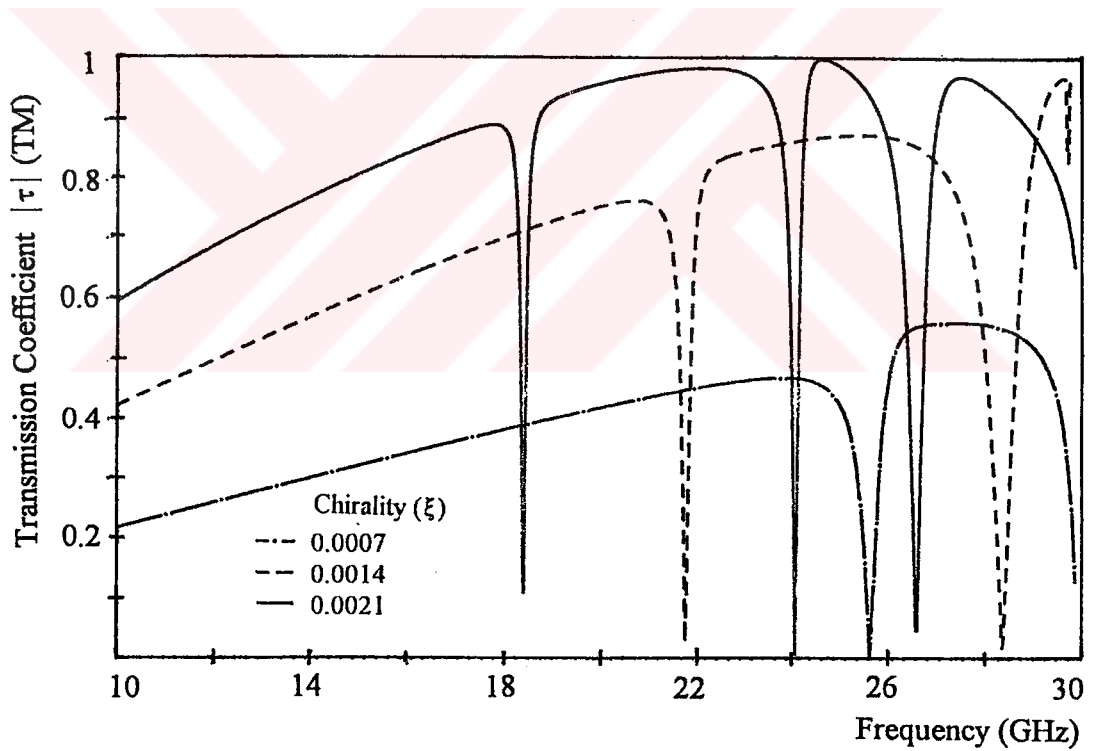coefficient (TE), c) Transmission coefficient (TM).

190

a

b

c

Figure 4.5.4   Spectral characteristics of Chiro-FSS with square patches; TE incidence
($\phi = 0°$, $\theta = 0°$), square lattice ($\alpha = 90°$), $D_1 = D_2 = 10$ mm, $L_x = L_y = 4$ mm,
$\epsilon_r = 1.32$, $t = 5$ mm. a) Reflection coefficient (TE), b) Transmission
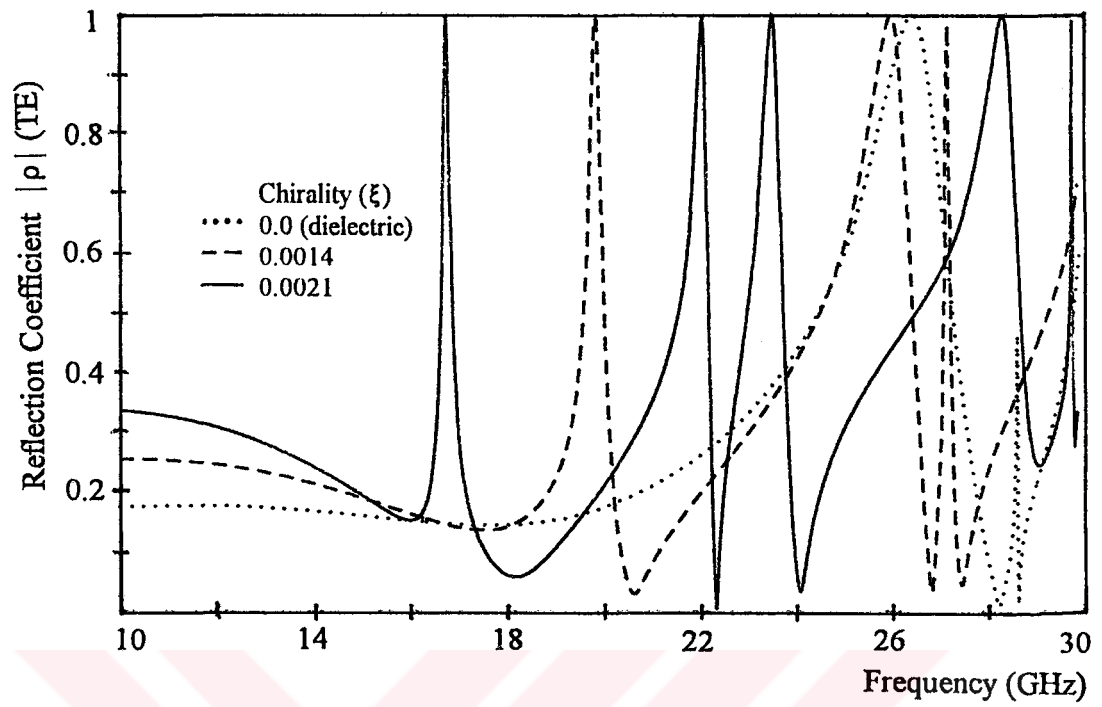coefficient (TE), c) Transmission coefficient (TM).

a

Figure 4.5.5 Spectral characteristics of Chiro-FSS with square patches; TE incidence
($\phi= 0°$, $\theta=0°$), square lattice ($\alpha= 90°$), $D_1=D_2=10$ mm, $L_x= L_y = 4$ mm,
$\epsilon_r=1.32$, t = 4 mm. a) Reflection coefficient (TE), b) Transmission
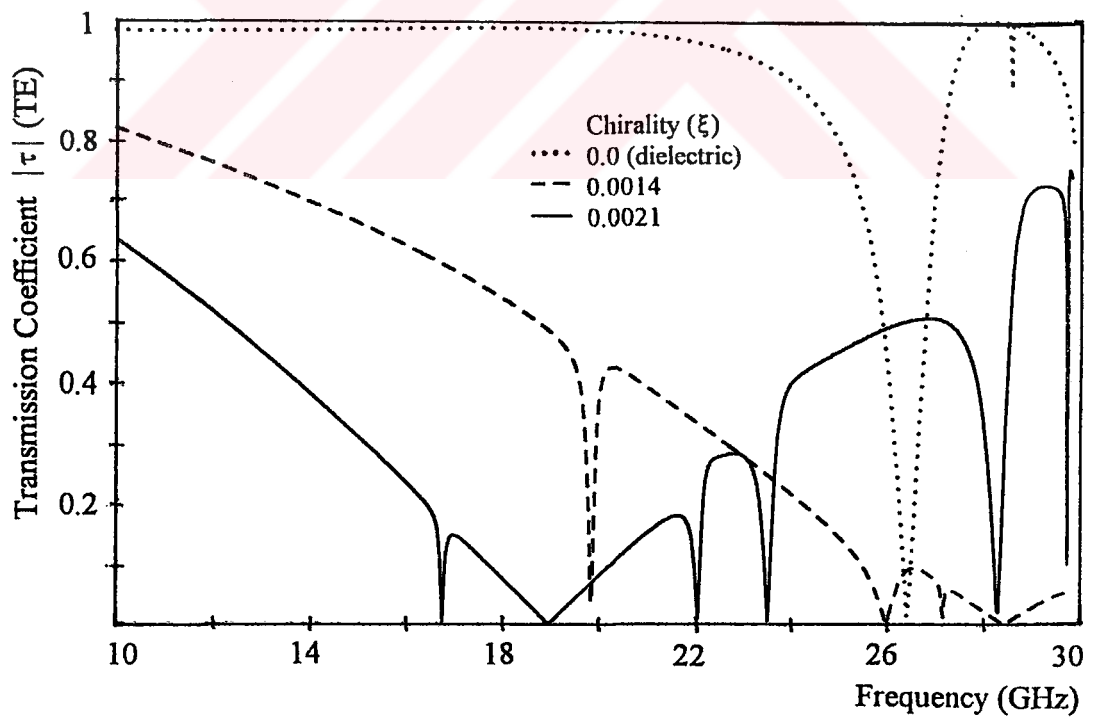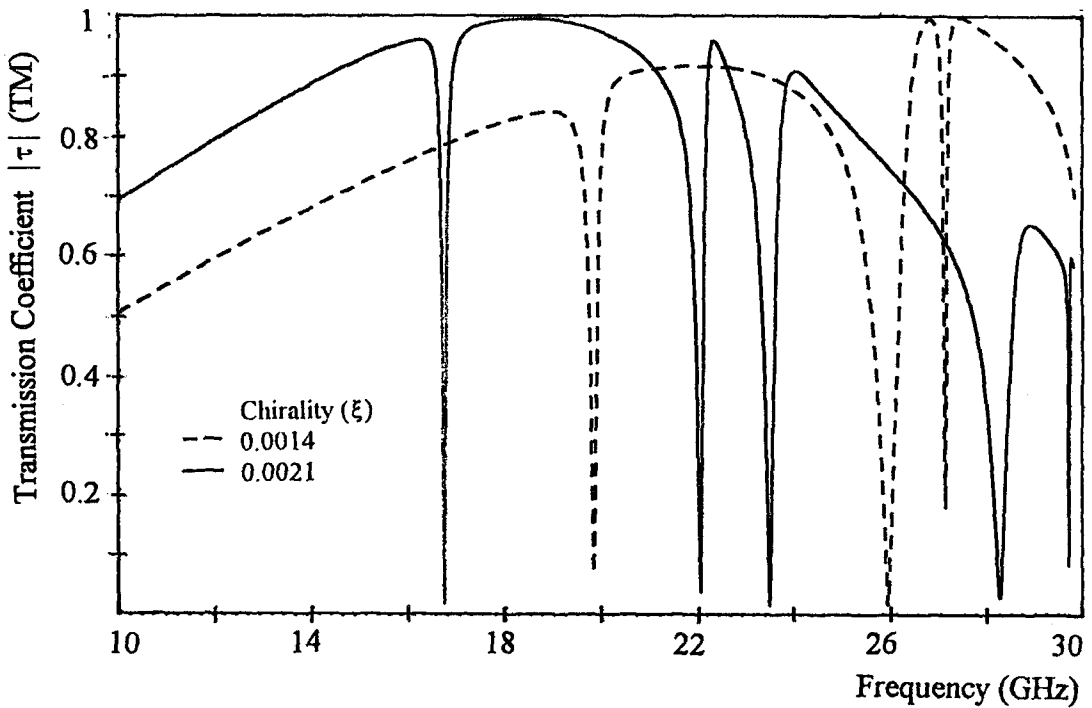coefficient (TE), c) Transmission coefficient (TM).

193

a

b

194

Figure 4.5.6   Spectral characteristics of Chiro-FSS with square patches; TE incidence ($\phi = 0°$, $\theta = 0°$), square lattice ($\alpha = 90°$), $D_1 = D_2 = 10$ mm, $L_x = L_y = 6$ mm, $\epsilon_r = 1.32$, $t = 5$ mm. a) Reflection coefficient (TE), b) Transmission coefficient (TE), c) Transmission coefficient (TM).
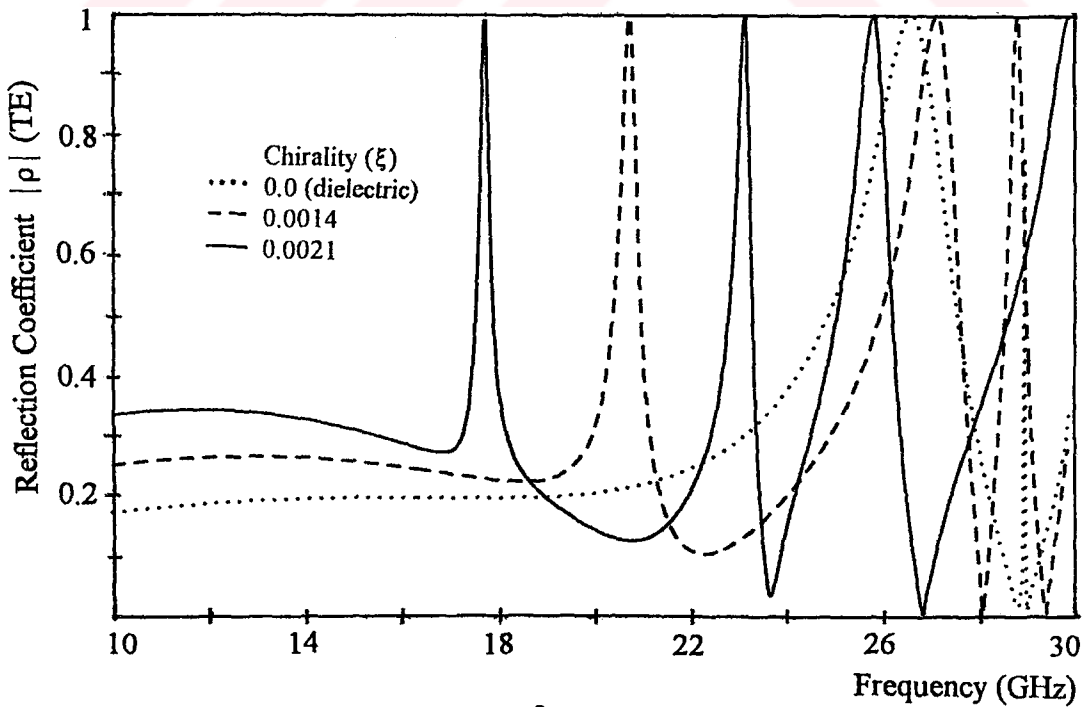

195

Figure 4.5.7 Spectral characteristics of Chiro-FSS with square patches; TE incidence (ϕ= 0°, θ=0°), square lattice (α= 90°), D_1=D_2=10 mm, L_x= L_y = 6 mm, ϵ_r=1.32, t = 4 mm. a) Reflection coefficient (TE), b) Transmission coefficient (TE), c) Transmission coefficient (TM).
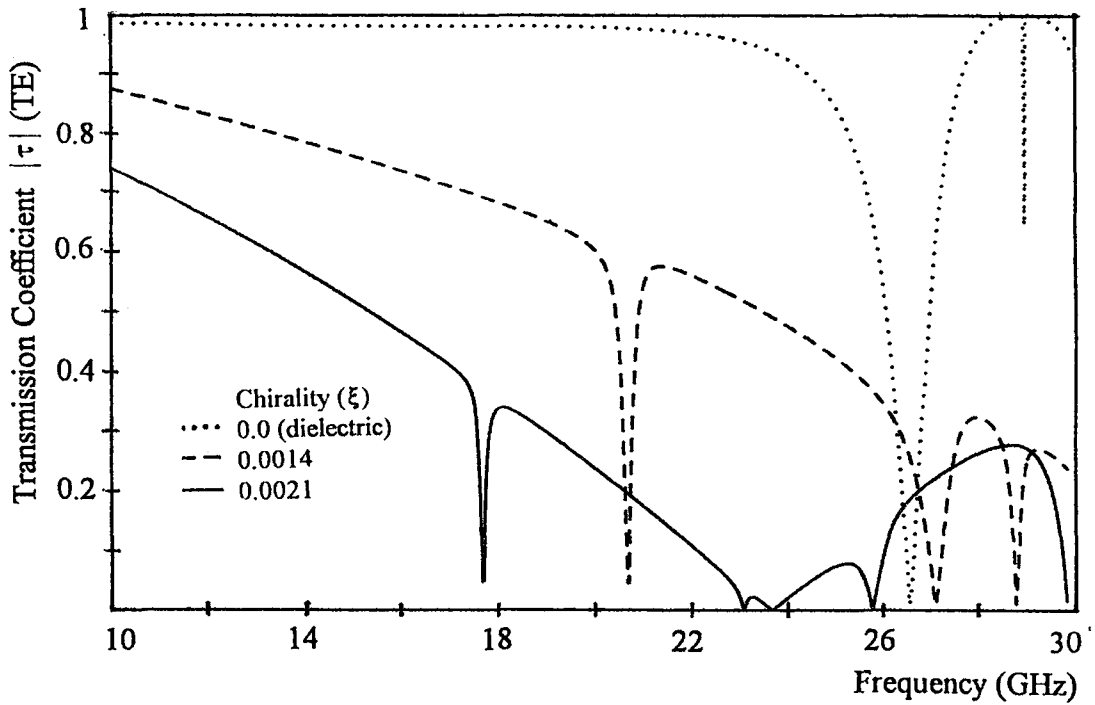
a

b
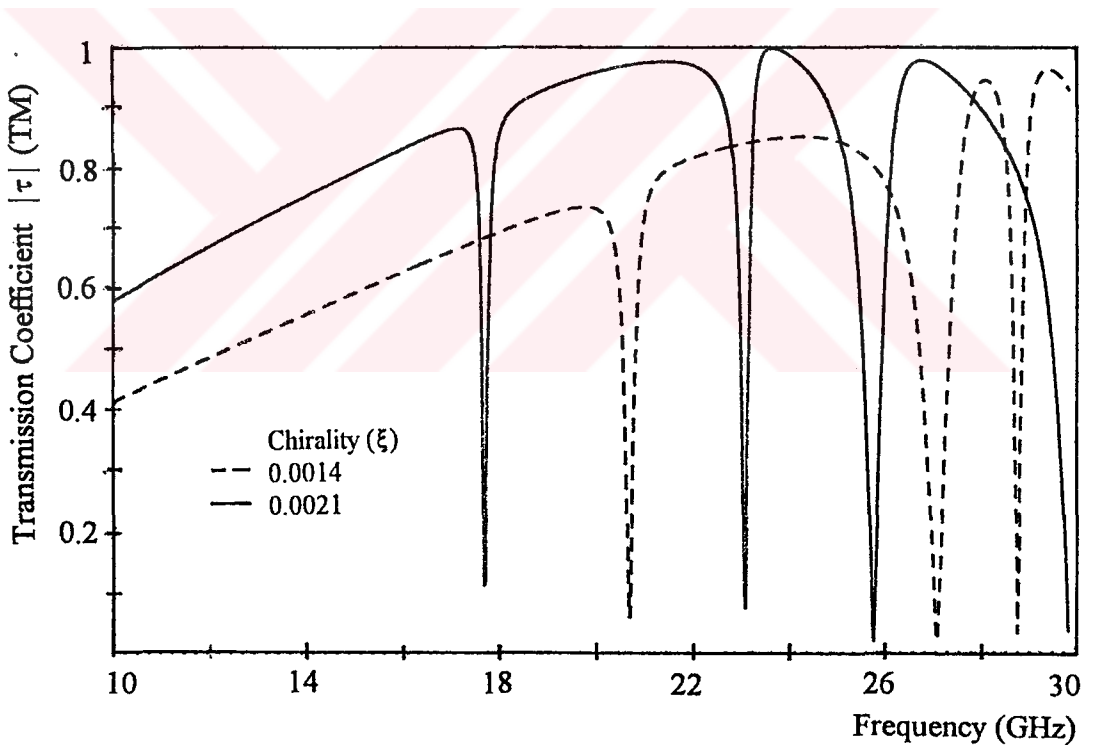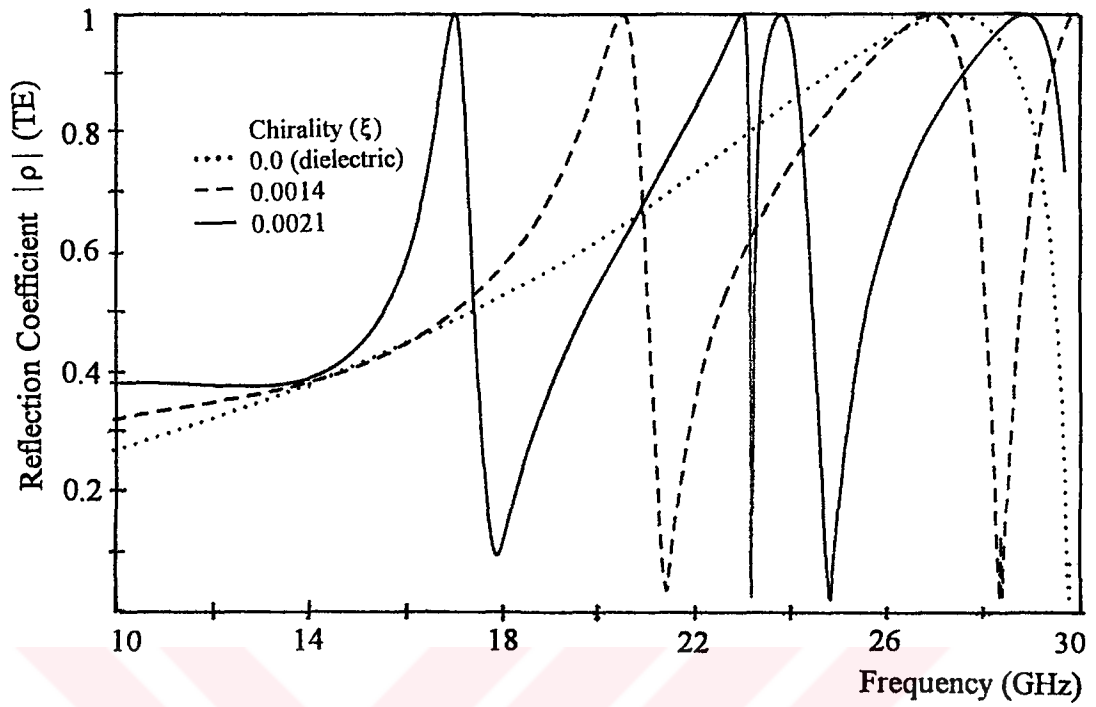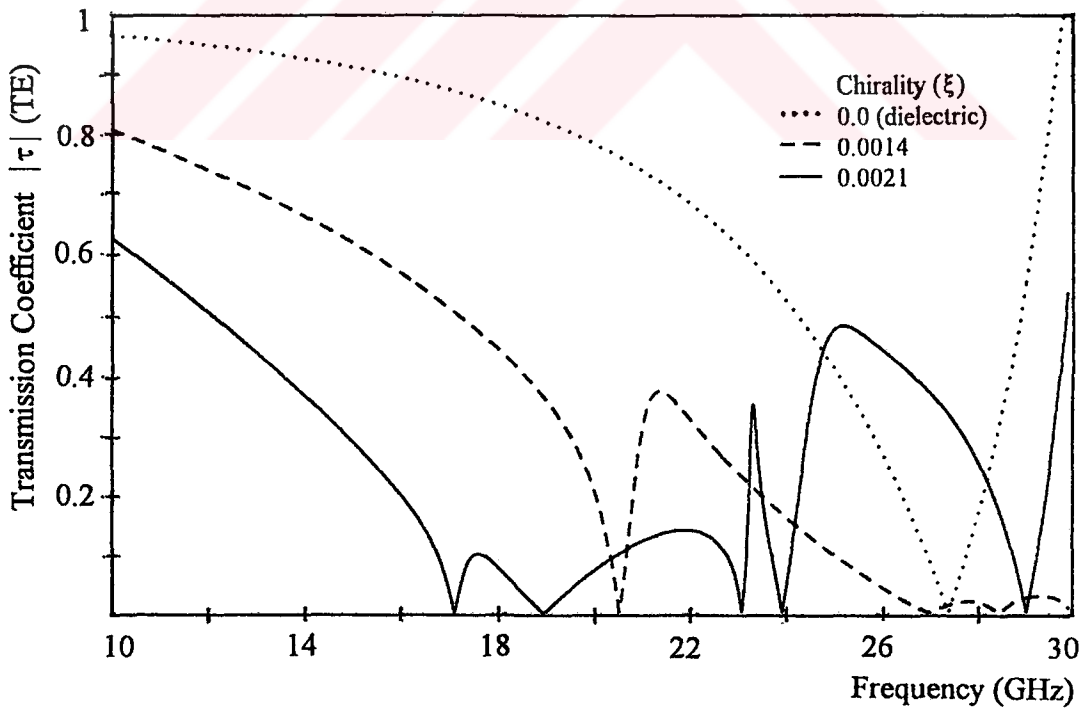
c

Figure 4.5.8   Spectral characteristics of Chiro-FSS with square patches; TE incidence
(ϕ= 30°, θ=0°), square lattice (α= 90°), D_1=D_2=10 mm, L_x=L_y= 6 mm,
ϵ_r=1.06, t = 5 mm. a) Power reflection coefficient (TE), b) Power
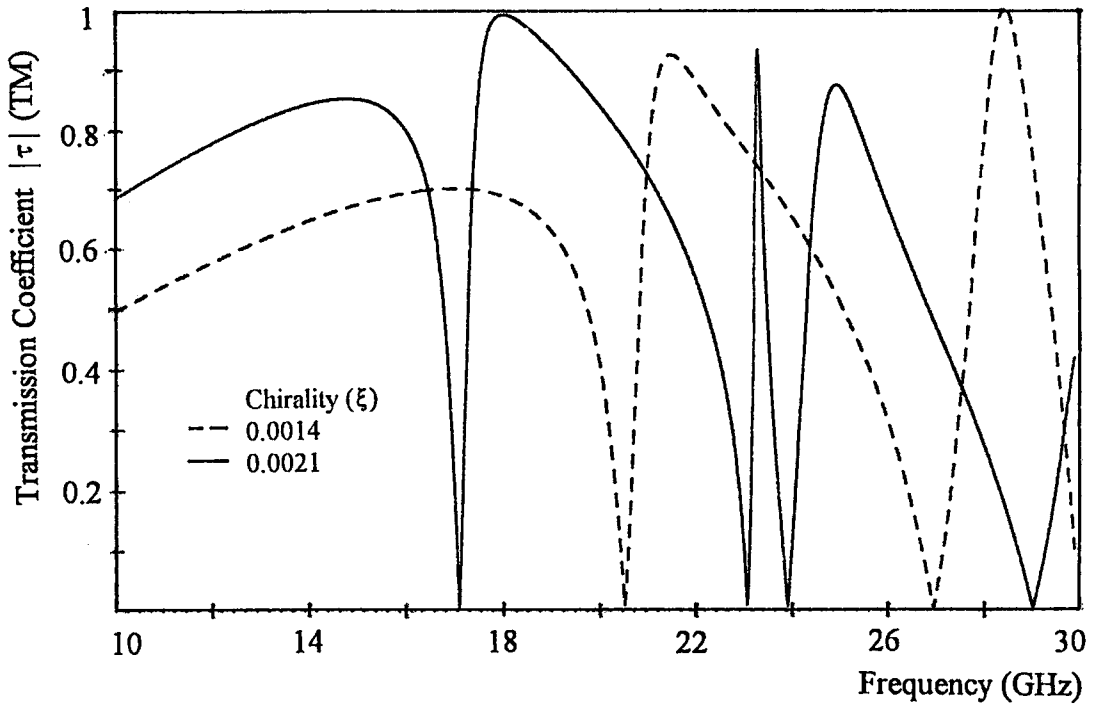transmission coefficient (TE), c) Power transmission coefficient (TM).

a

198

a

b

Figure 4.5.9   Spectral characteristics of Chiro-FSS with square patches; TM incidence
(ϕ= 30°, θ=0°), square lattice (α= 90°), D_1=D_2=10 mm, L_x=L_y= 6 mm,
ϵ_r=1.06, t = 5 mm. a) Power reflection coefficient (TM), b) Power
transmission coefficient (TE), c) Power transmission coefficient (TM).

199

a

b

200
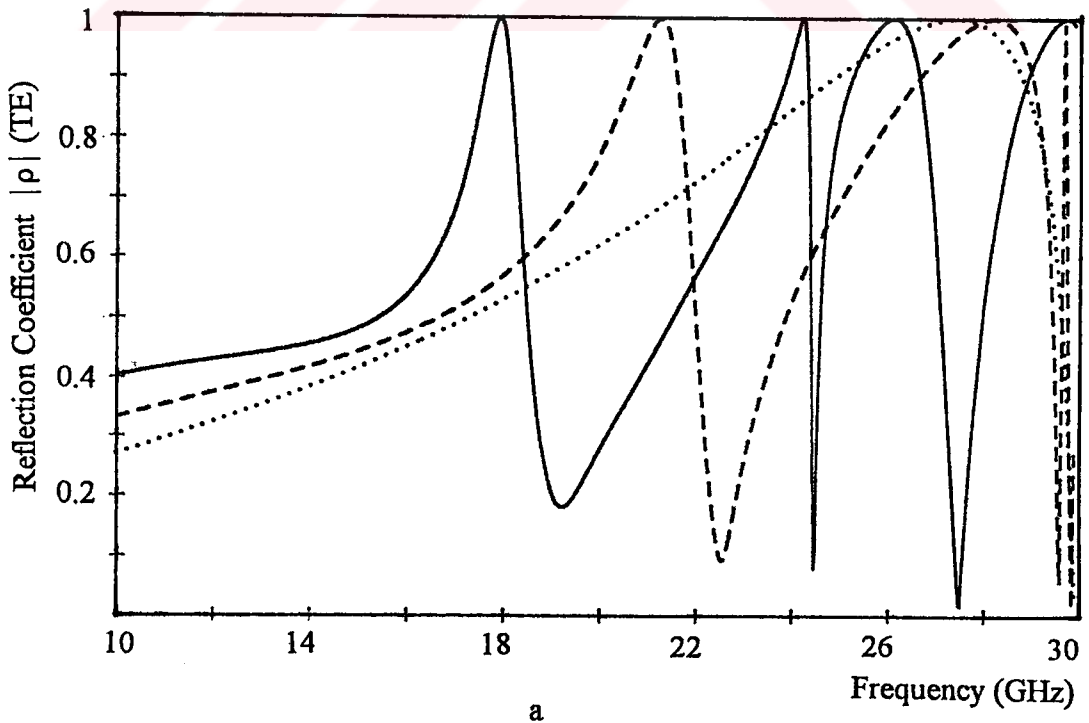
c

Figure 4.5.10   Spectral characteristics of Chiro-FSS with square patches; TE incidence ($\phi= 45°$, $\theta=0°$), square lattice ($\alpha= 90°$), $D_1=D_2=10$ mm, $L_x=L_y= 6$ mm, $\epsilon_r=1.06$, t = 5 mm. a) Power reflection coefficient (TE), b) Power transmission coefficient (TE), c) Power transmission coefficient (TM).

a

201

b
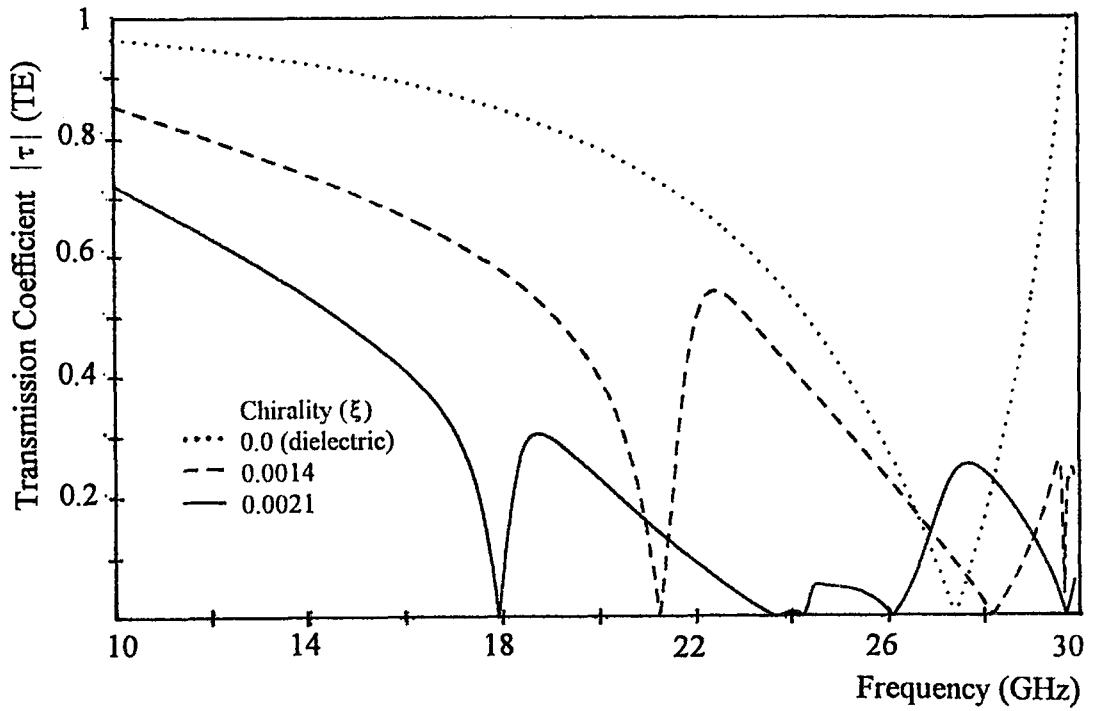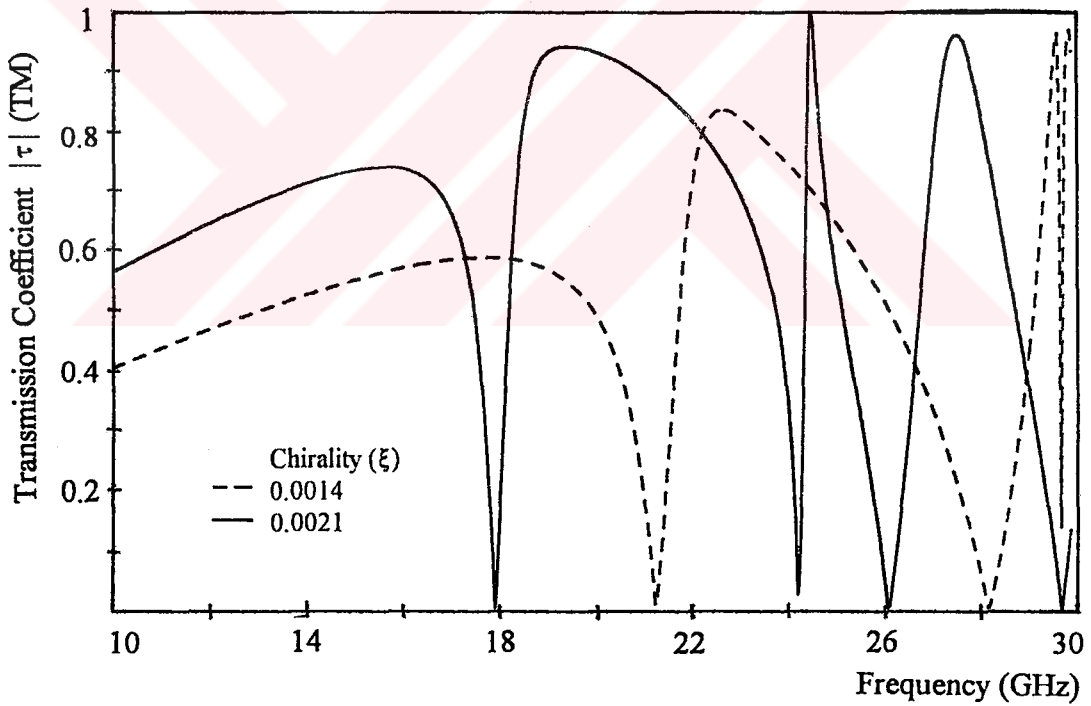

c

Figure 4.5.11 Spectral characteristics of Chiro-FSS with square patches; TE incidence
($\phi= 0°,\theta=30°$), square lattice ($\alpha=90°$), $D_1=D_2=10$ mm, $L_x=L_y= 6$ mm,
$\epsilon_r=1.06$, t = 5 mm. a) Power reflection coefficient (TE), b) Power
reflection coefficient (TM), c) Power transmission coefficient (TE),
d) Power transmission coefficient (TM).
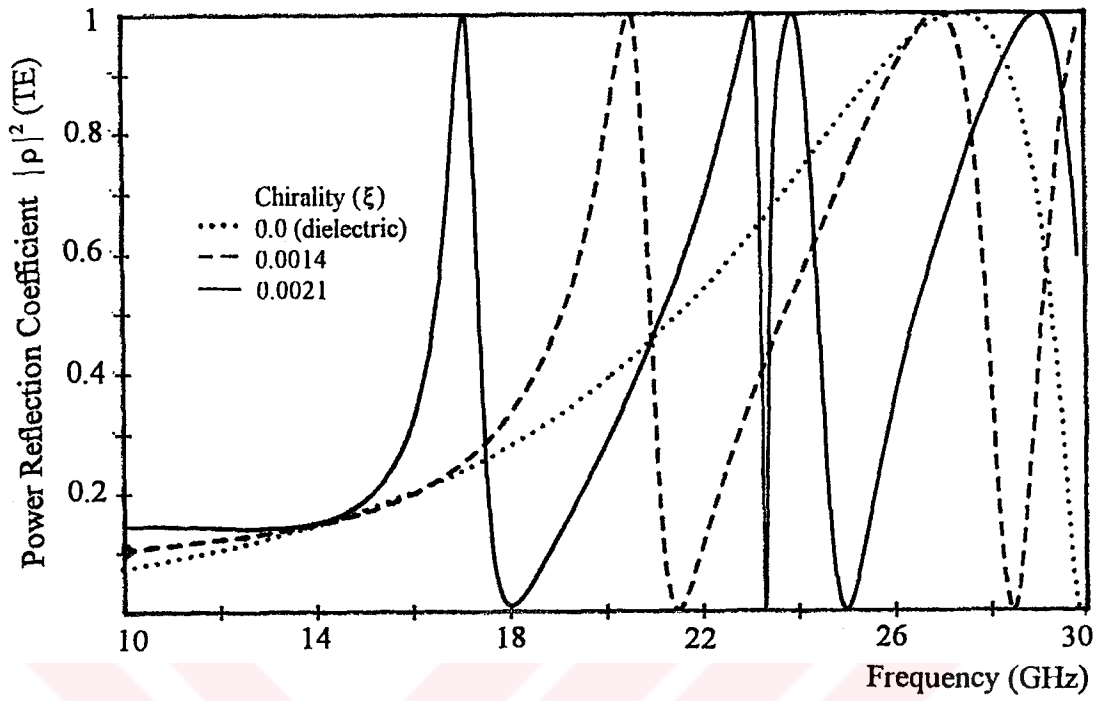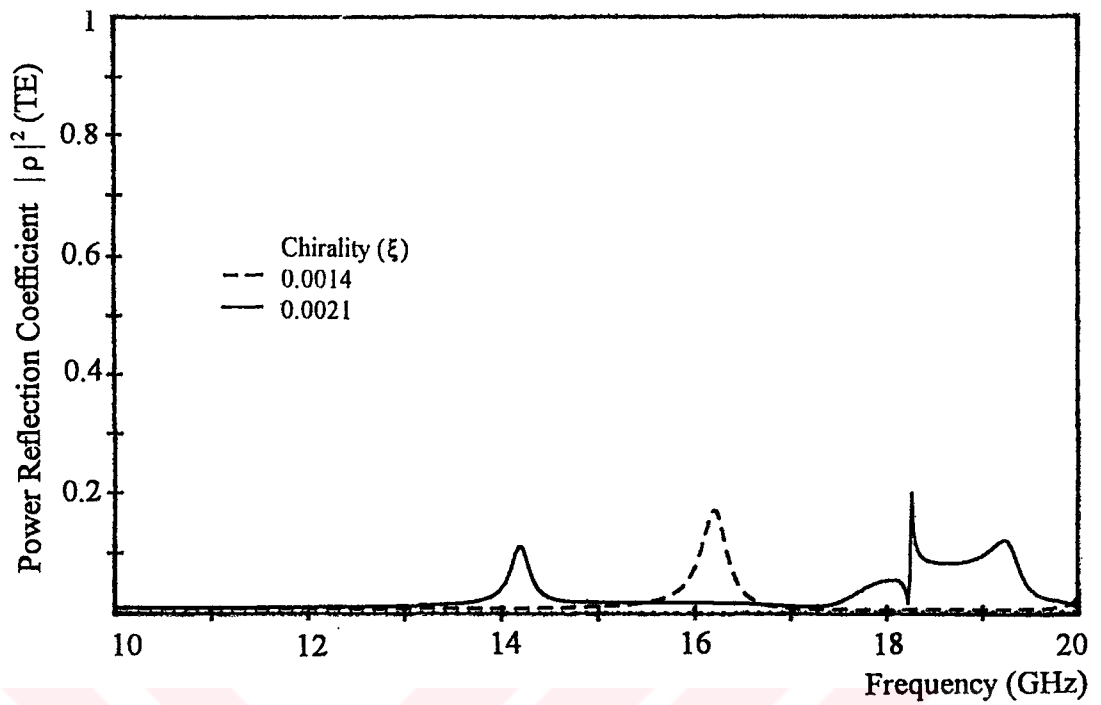
b
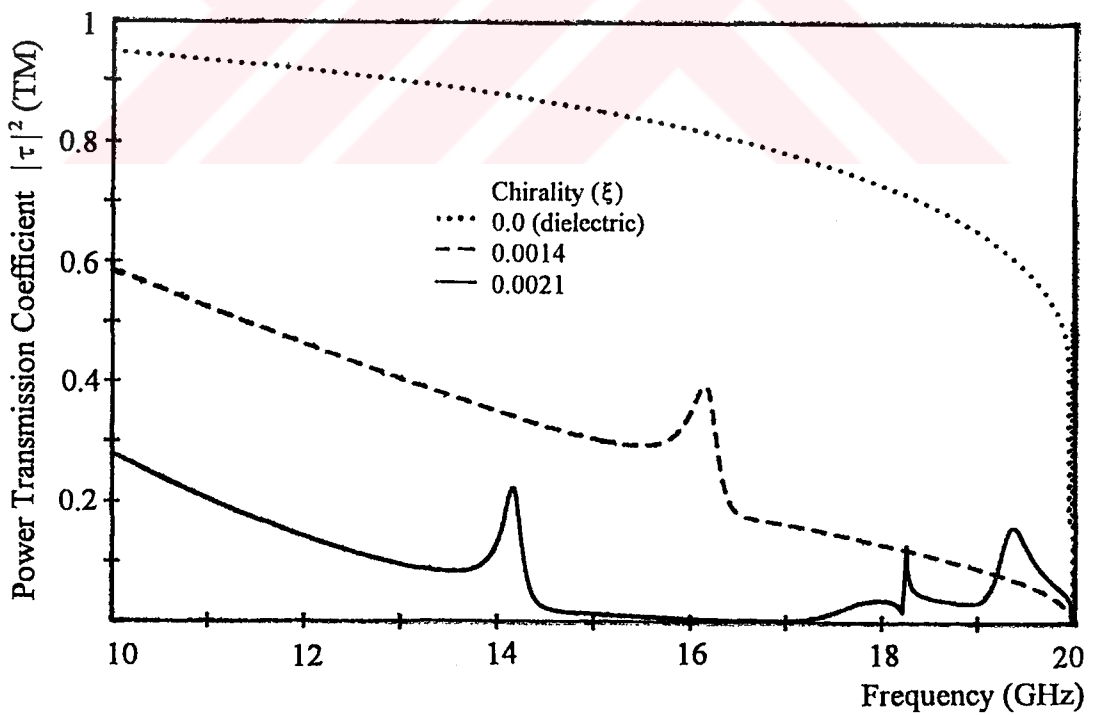
c
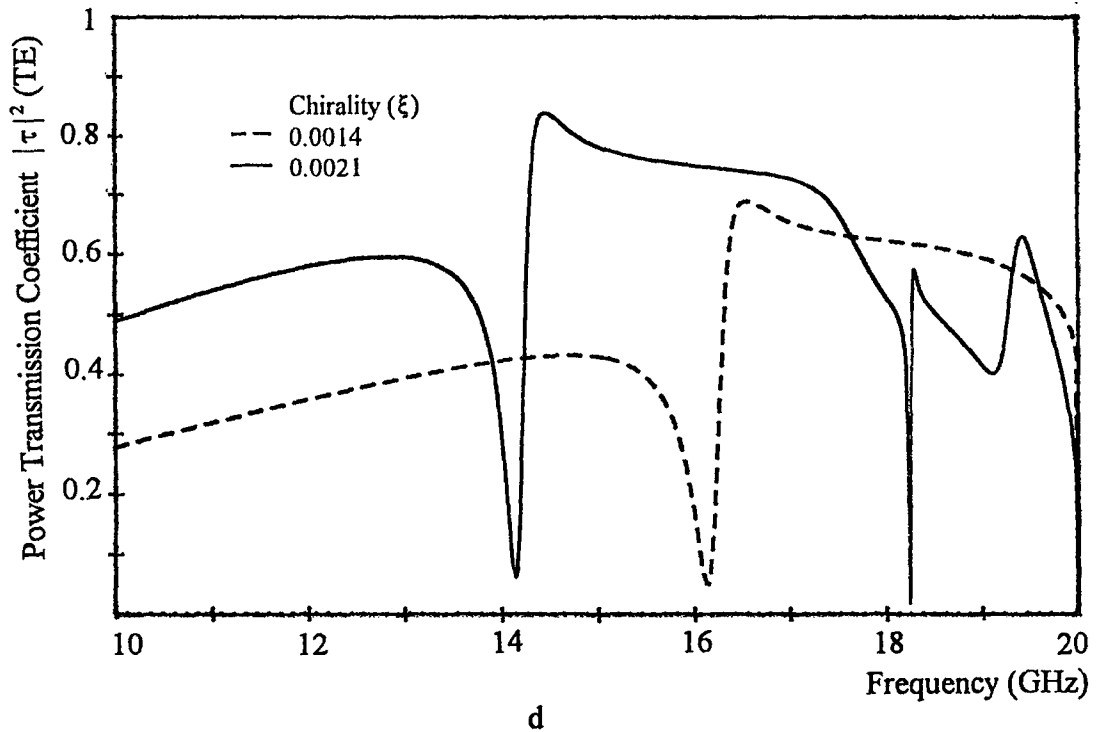
Figure 4.5.12 Spectral characteristics of Chiro-FSS with square patches; TM incidence ($\phi= 0°, \theta=30°$), square lattice ($\alpha=90°$), $D_1=D_2=10$ mm, $L_x=L_y= 6$ mm, $\epsilon_r=1.06$, t = 5 mm. a) Power reflection coefficient (TE), b) Power reflection coefficient (TM), c) Power transmission coefficient (TE), d) Power transmission coefficient (TM).
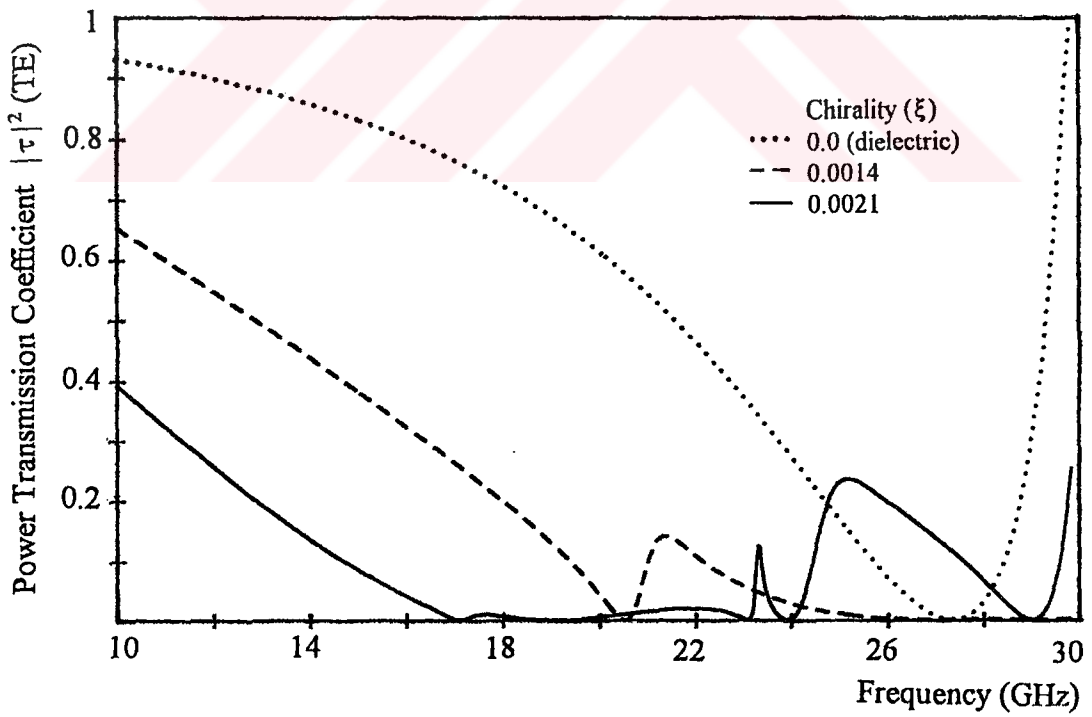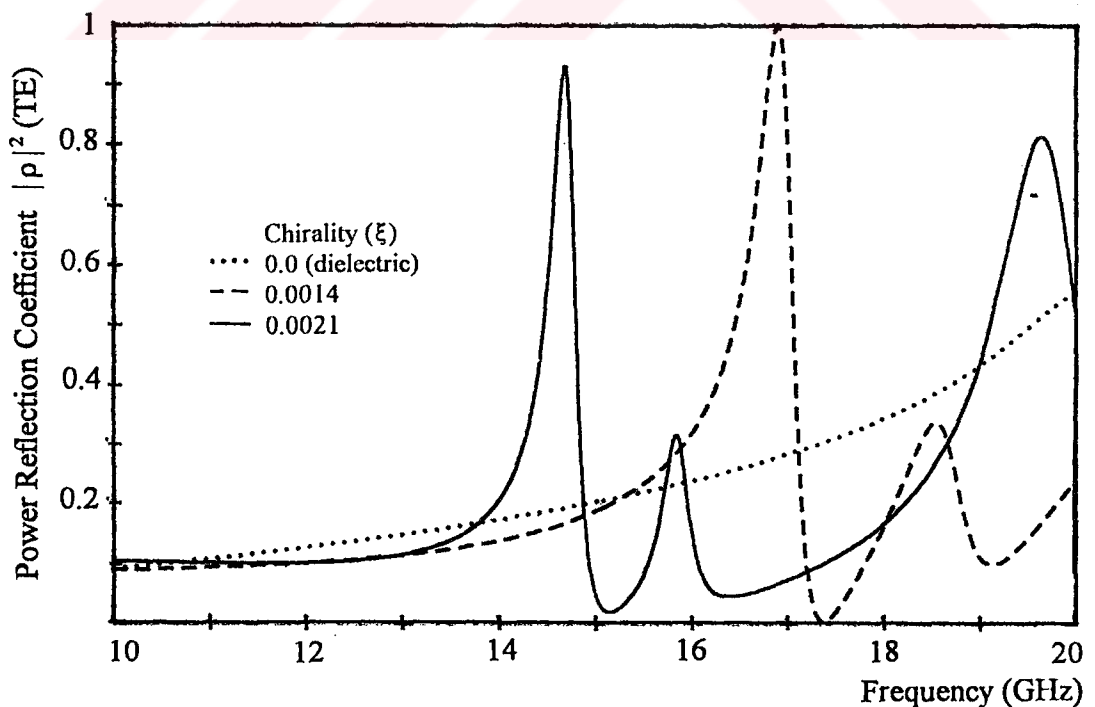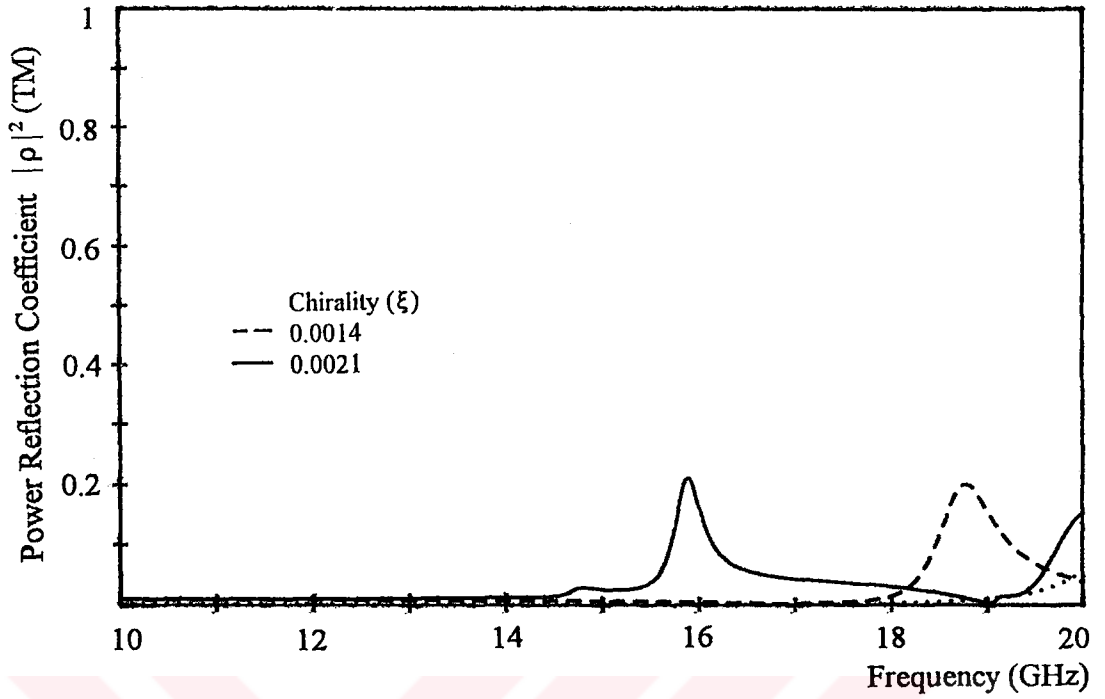
b
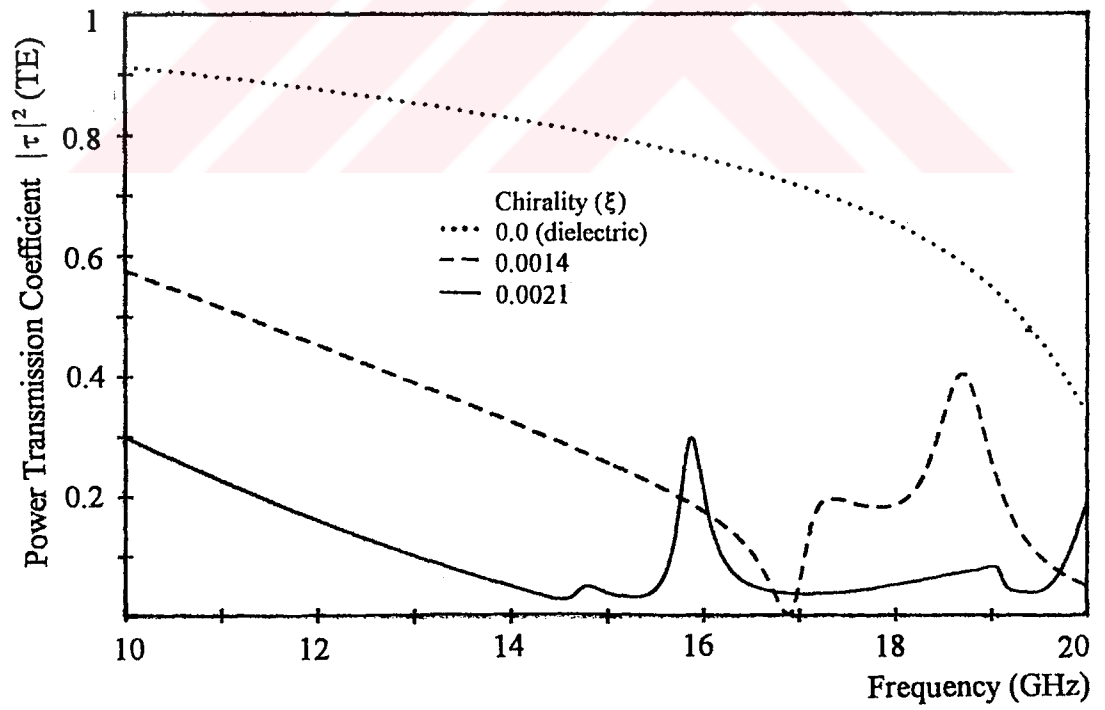
c
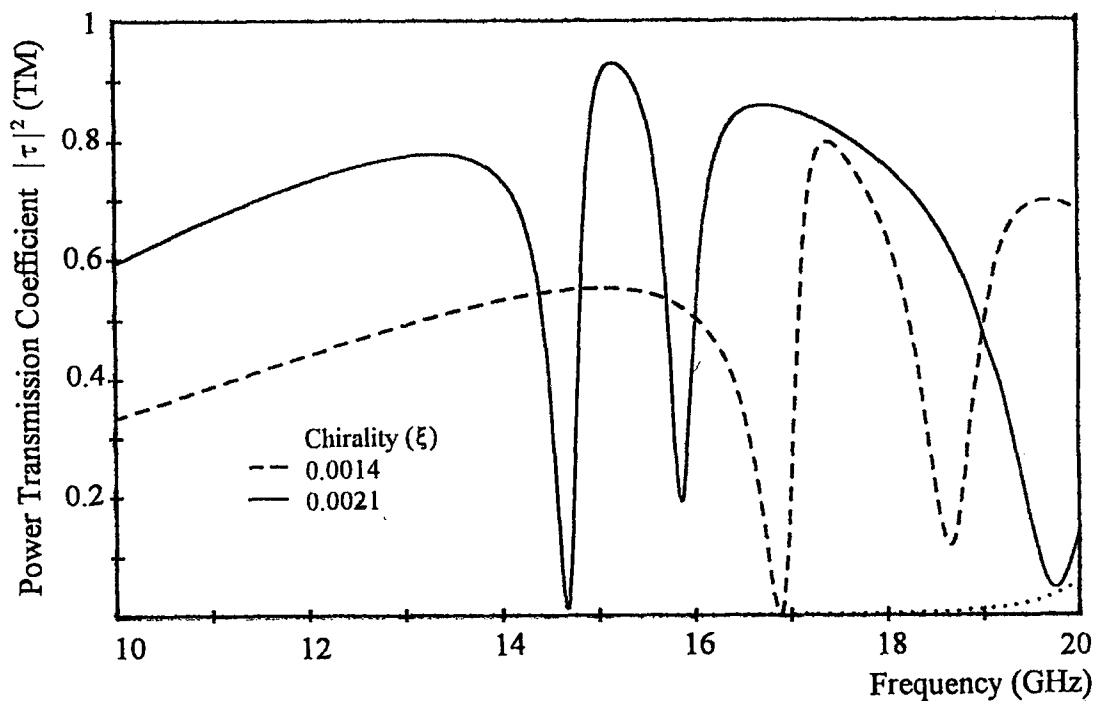
d
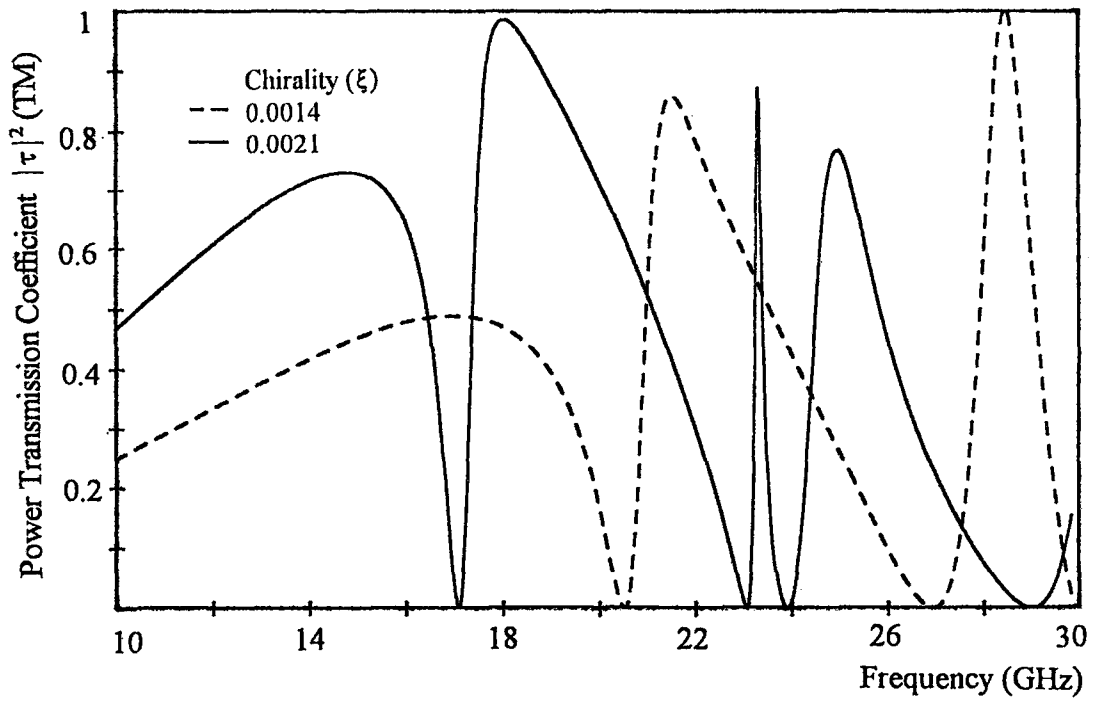
Figure 4.5.13 Spectral characteristics of Chiro-FSS with square patches; TE incidence ($\phi=30°,\theta=30°$), square lattice ($\alpha=90°$), $D_1=D_2=10$ mm, $L_x=L_y=6$ mm, $\epsilon_r=1.06$, t = 5 mm. a) Power reflection coefficient (TE), b) Power reflection coefficient (TM), c) Power transmission coefficient (TE), d) Power transmission coefficient (TM).
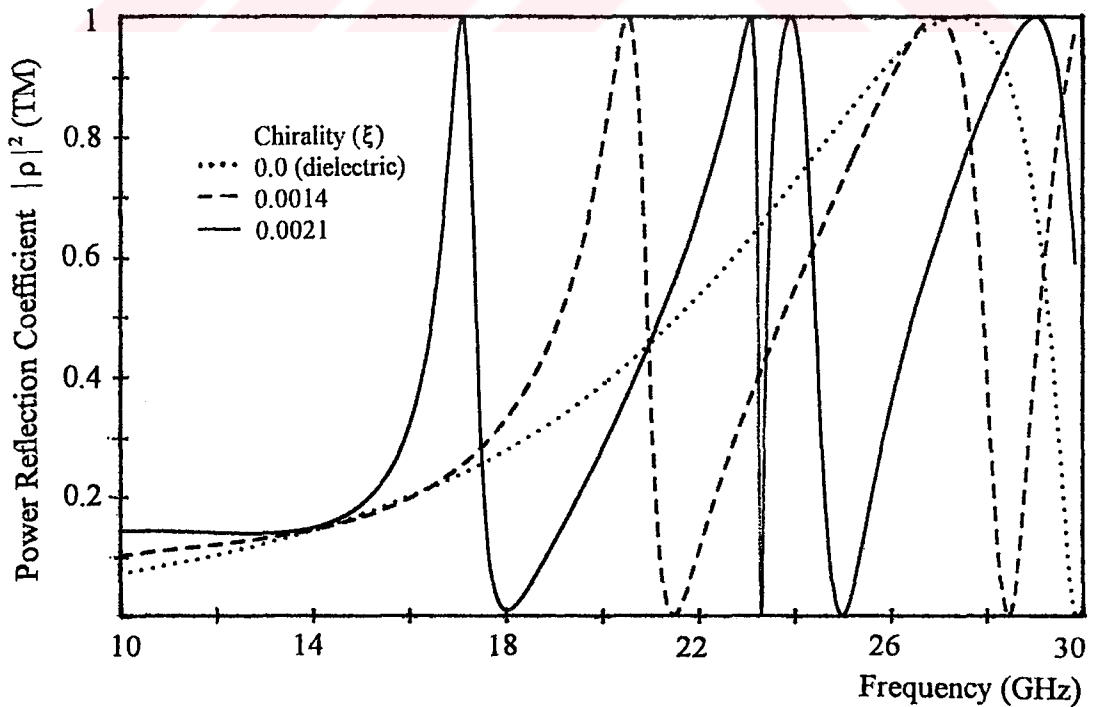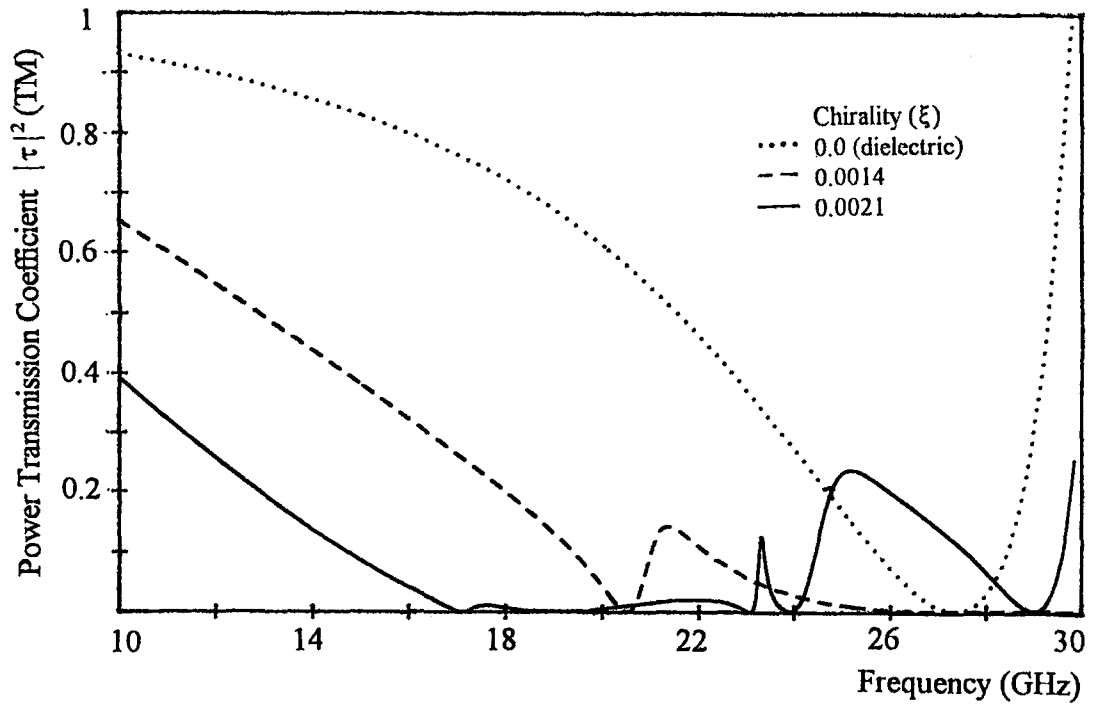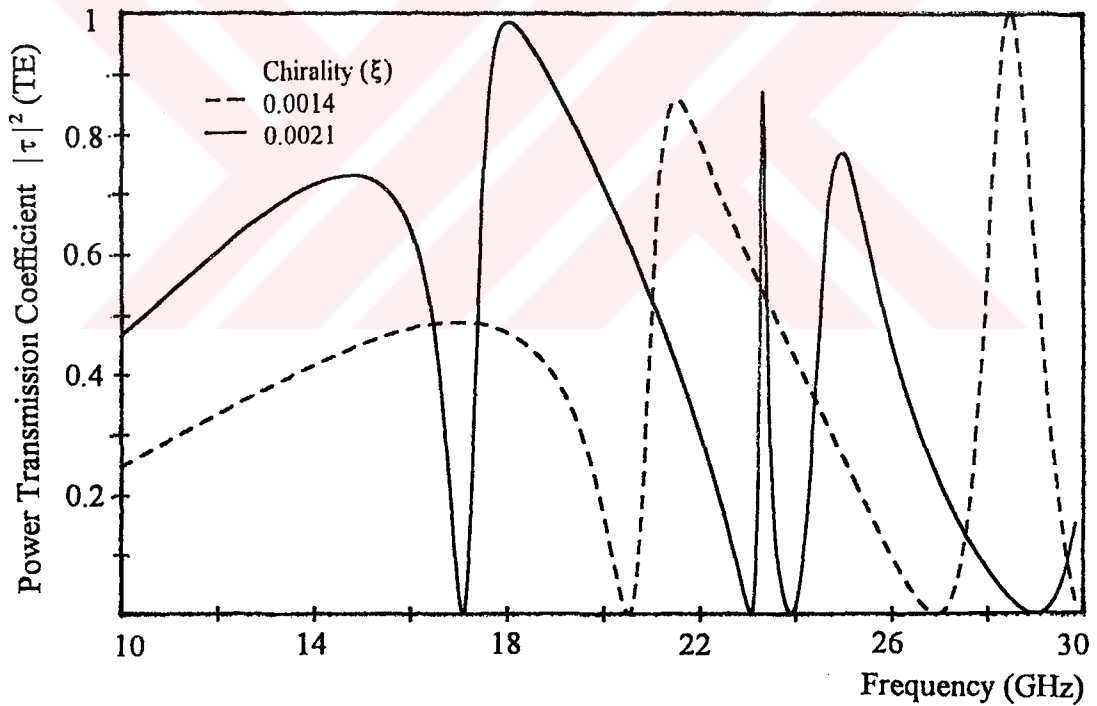

a

207

b

c

208
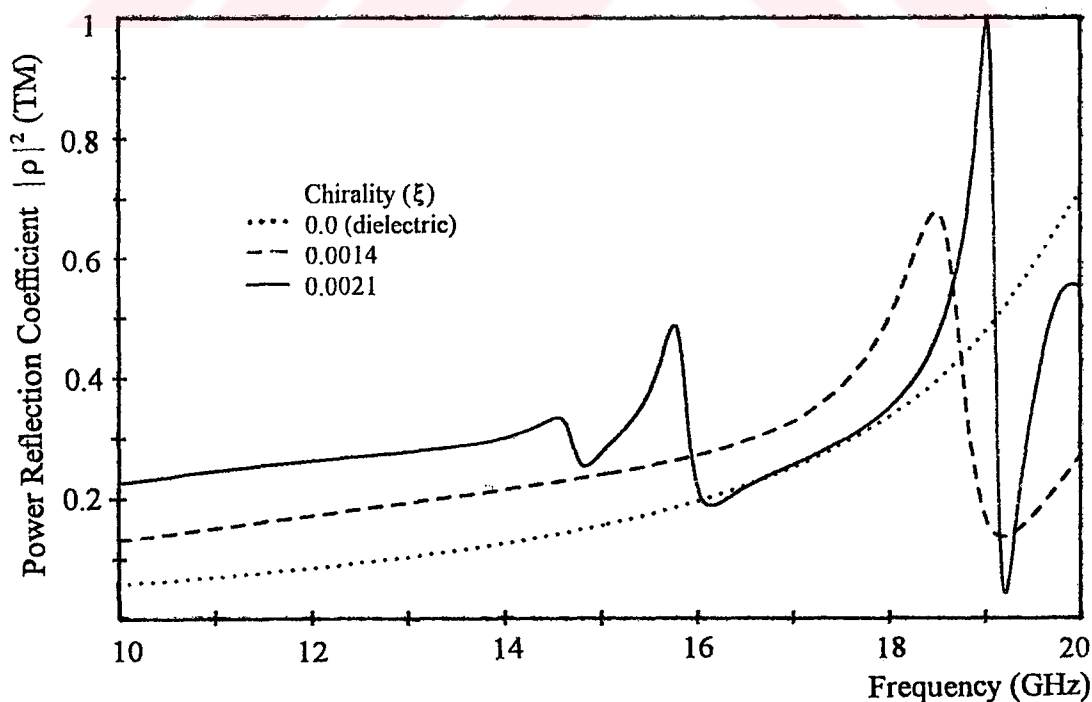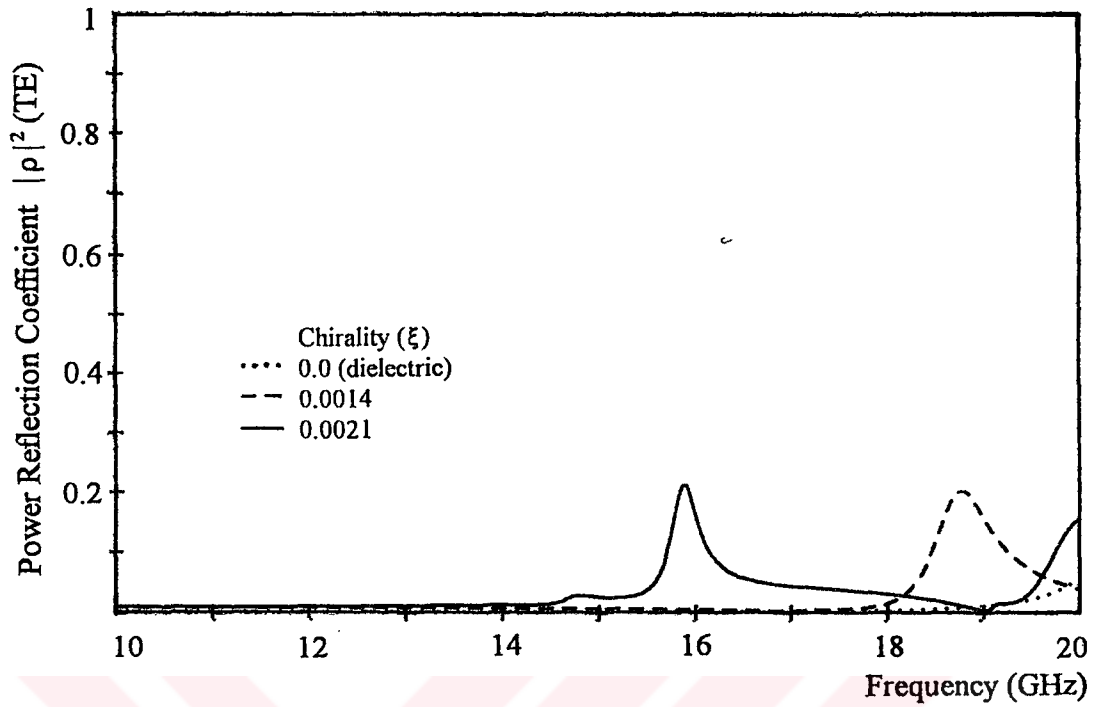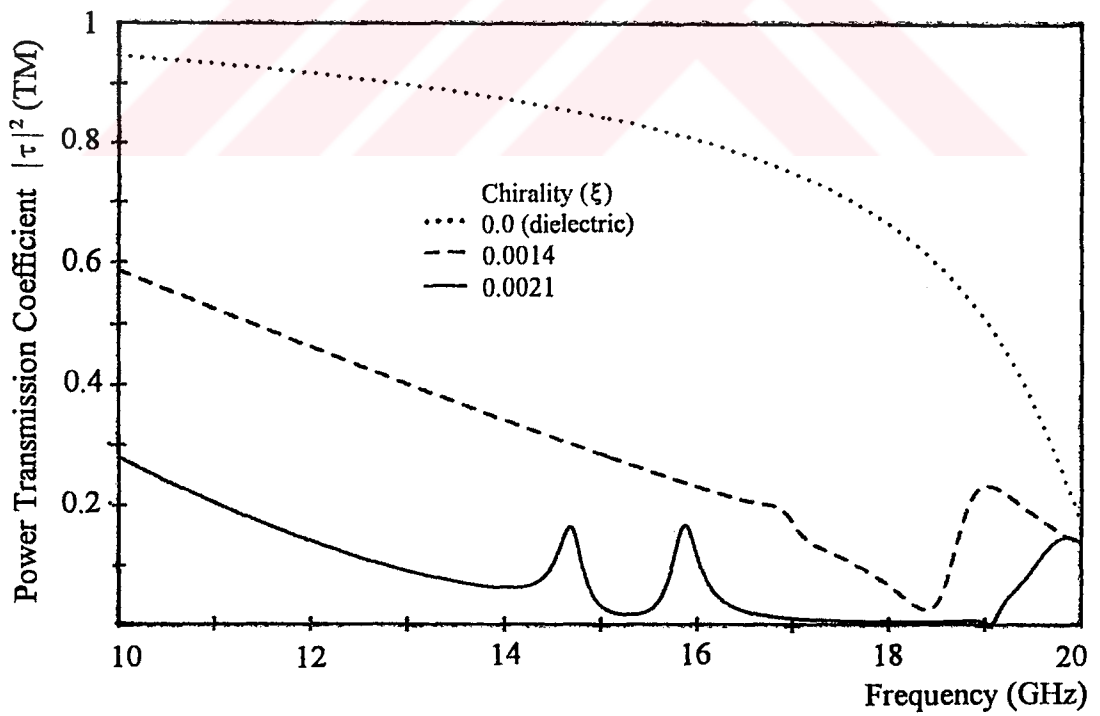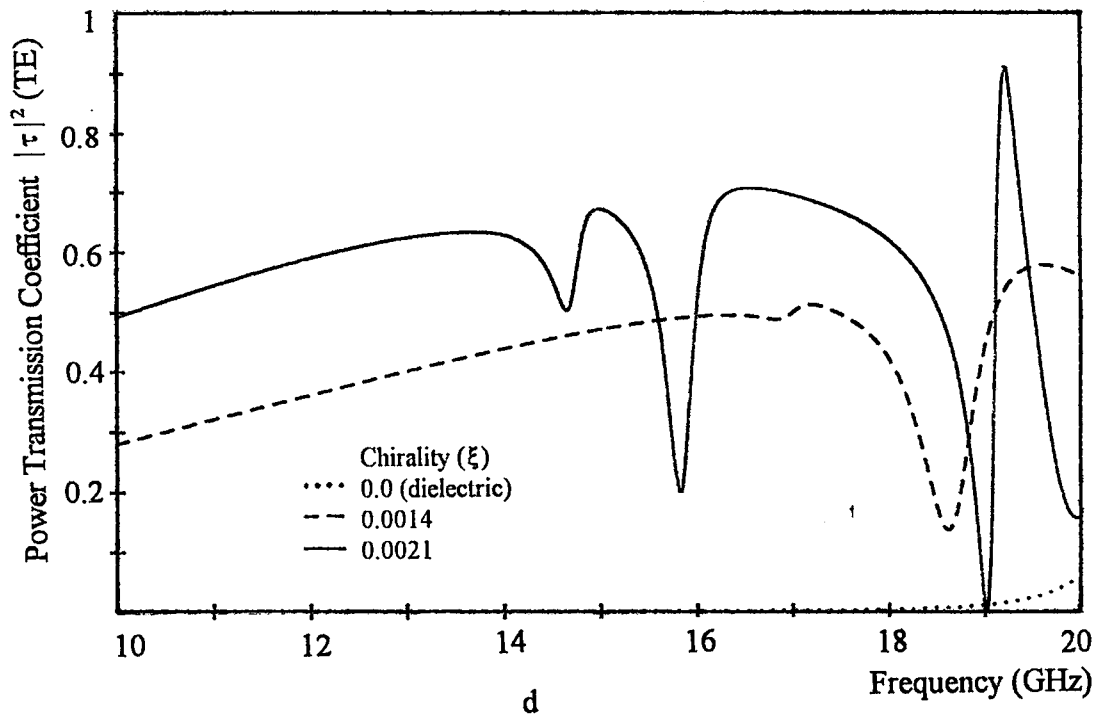
Figure 4.5.14   Spectral characteristics of Chiro-FSS with square patches; TM incidence
($\phi = 30°, \theta = 30°$), square lattice ($\alpha = 90°$), $D_1 = D_2 = 10$ mm, $L_x = L_y = 6$ mm,
$\epsilon_r = 1.06$, t = 5 mm. a) Power reflection coefficient (TE), b) Power
reflection coefficient (TM), c) Power transmission coefficient (TE),
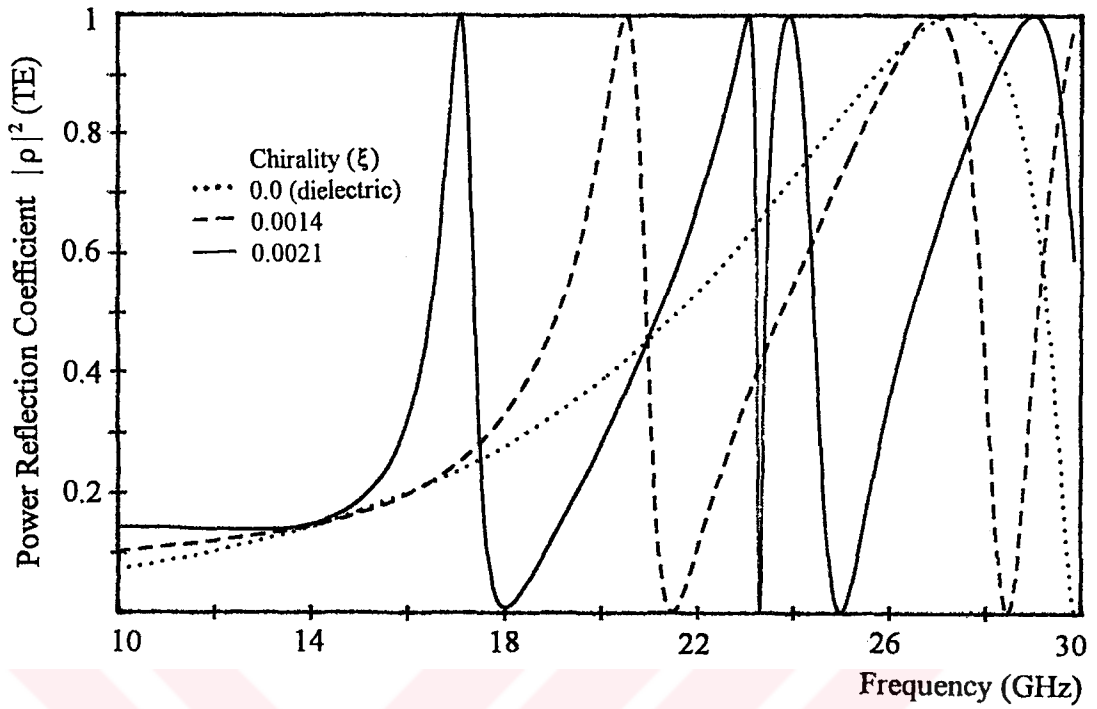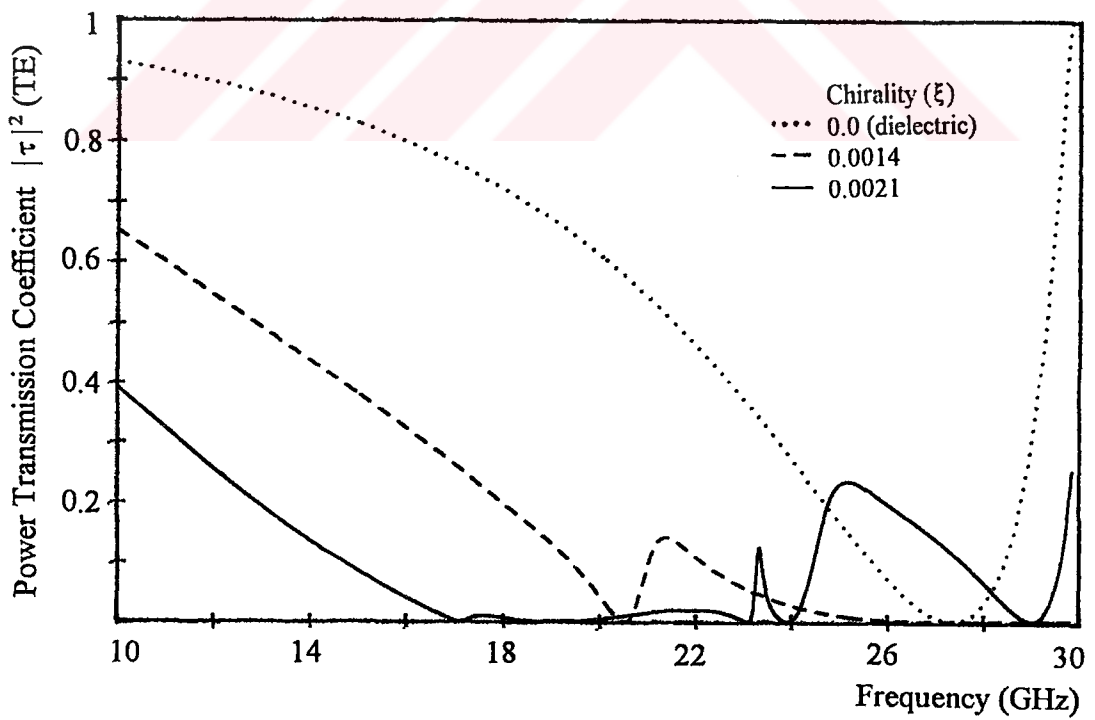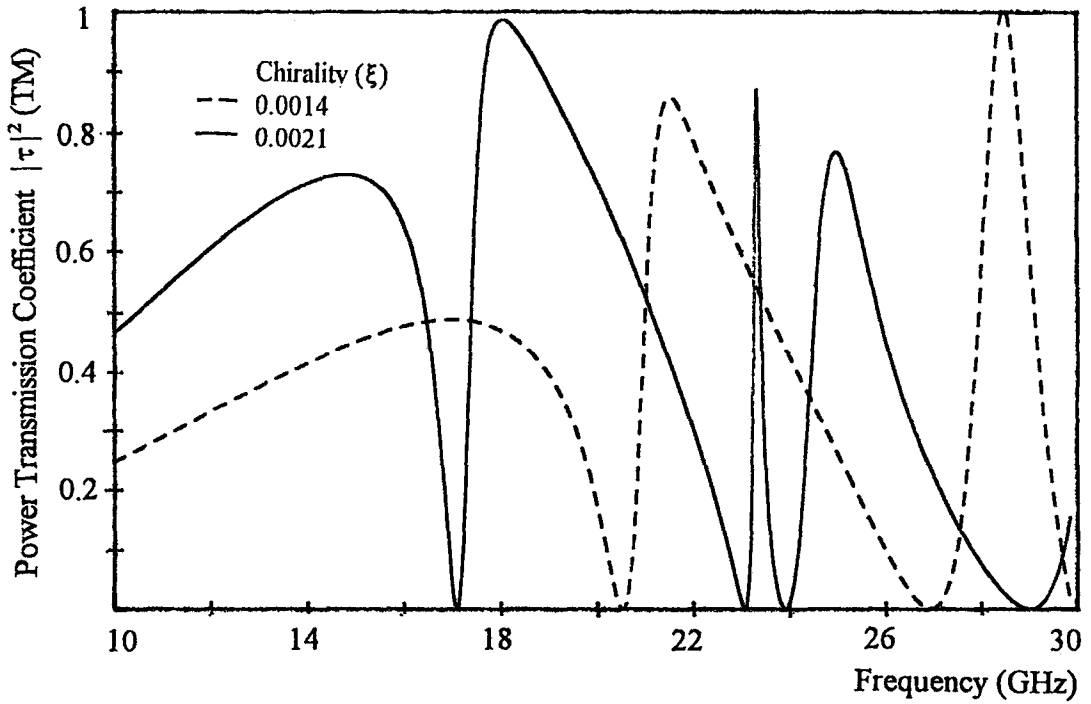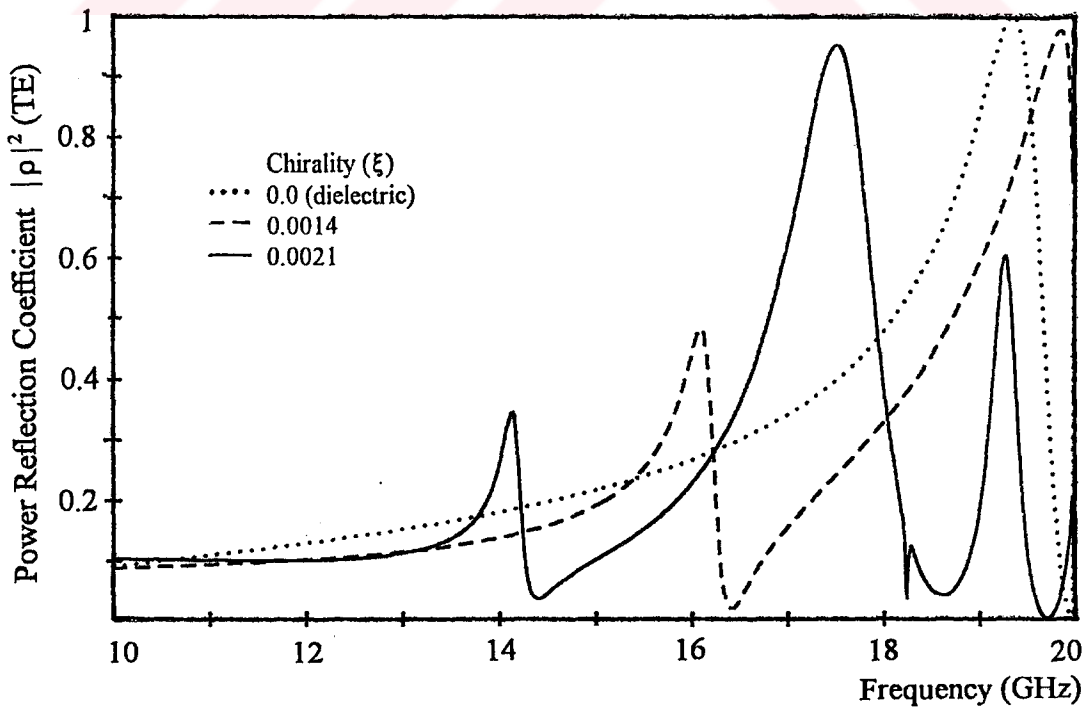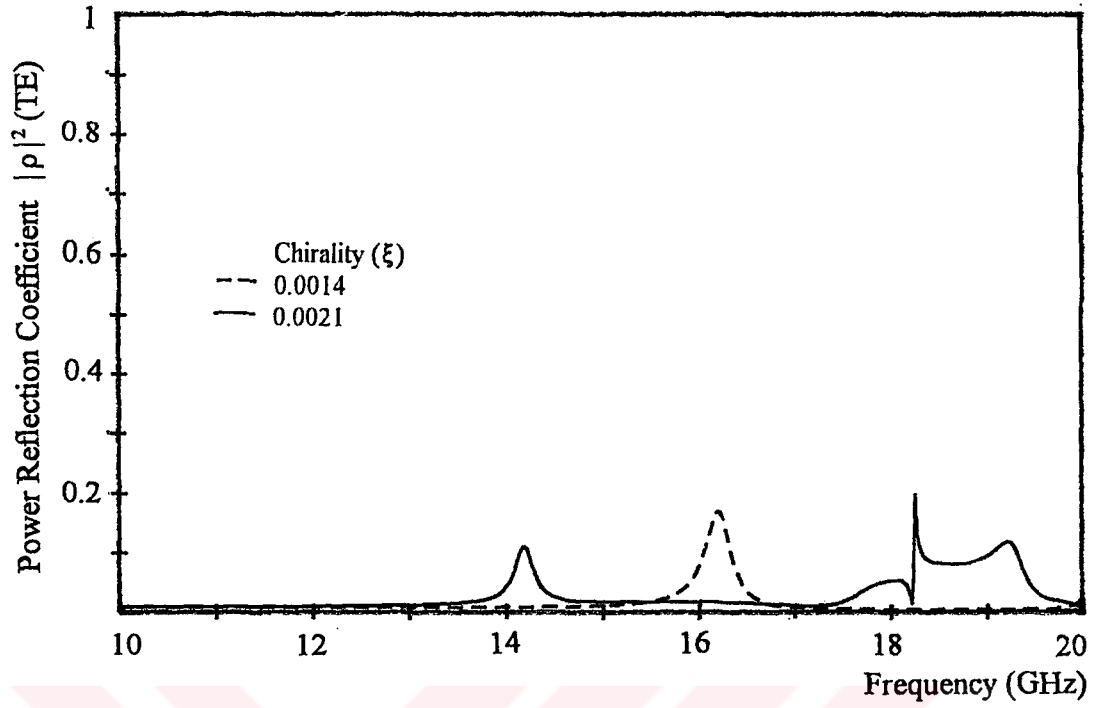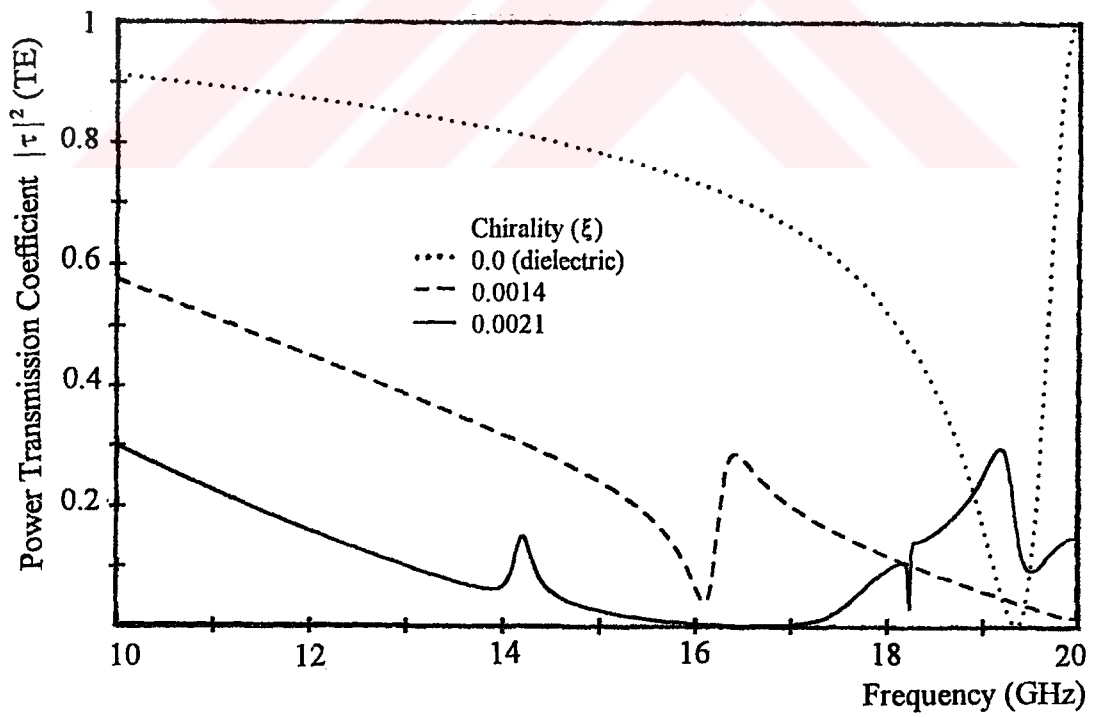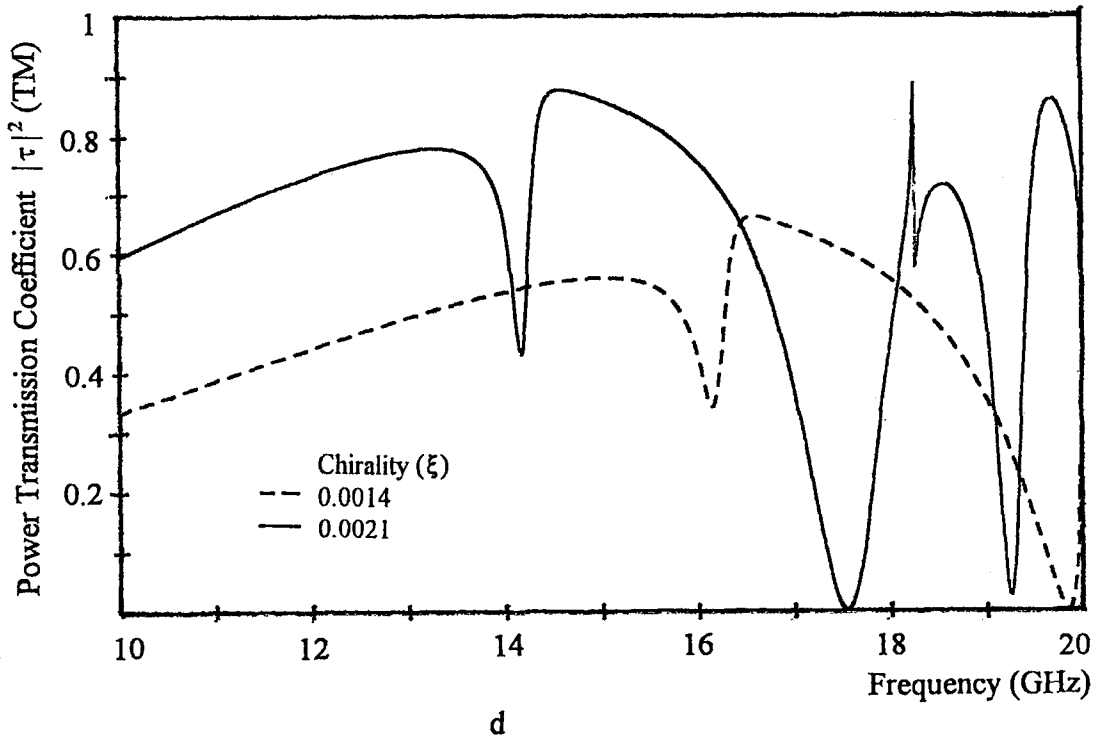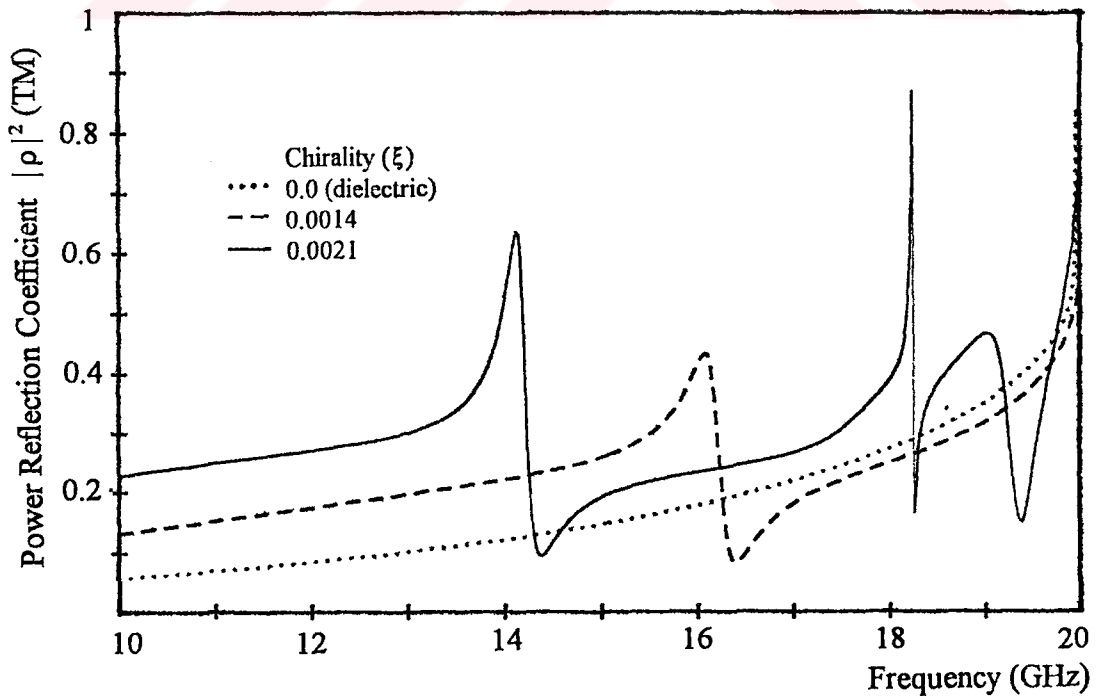d) Power transmission coefficient (TM).

CHAPTER 5

CONCLUSIONS

The analysis of an infinite FSS usually begins by reducing the formulation which holds for the infinite periodic surface to one which holds over a single periodic unit cell. This is accomplished by recognizing that a periodic structure producing a response which is also periodic, the period is that of the structure. Therefore the scattered fields and induced current on the conducting elements can be expressed by a superposition of the periodic functions- Floquet modes. The Floquet modes are the plane wave with propagation constant related to the surface periodicities and propagation constant of the incident field.

On the other hand, because of promising wide applications in microwave and antenna engineering, isotropic chiral media have been under extensive study during the last years. An isotropic chiral medium is an example of bi-isotropic medium, where cross coupling between electric and magnetic fields exist. The chiral media exhibit optical activity which differs from the Faraday rotation by the fact that the former is independent of direction of propagation whereas the later is not.

In this study, a new type of FSS, named as Chiro-FSS is proposed and analysed in detail. A Chiro-FSS consists of two dimensional periodic arrays of conducting elements loaded by an isotropic chiral slab. The motivation for this work is that, among other design parameters, using the chiral slab instead of dielectric slab allows us to get an extra design parameter (chirality) and degrre of fredoom. Therefore it is exploited to improve

210

the spectral characteristics of the FSSs.

It is seen that from the computed results of spectral characteristics of various type of Chiro-FSS, some important features and novel properties are obtained. In contrast to conventioanl FSSs (dielectric backed) comprised of a single narrow strip, cross dipole, circular ring, square loop and square patches within an unit cell, the computed results indicate that multiple resonances are obtained even at normal incidence in Chiro-FSS structure. Among other design parameters, chirality admittance of the slab is the most effective parameter such that any small change in its value alters the whole spectral response of the Chiro-FSS. The bandwidth of the resonances obtained in the reflection characteristics of the Chiro-FSS are rather narrow compared with the bandwidth of the resonance of conventional FSS. The isolations between the adjecent resonances are very good. In other words, for the Chiro-FSS case, there are sharp minimums, approximately zero, immediatelly after resonances in the reflection characteritics, while that is clearly not the case for the conventional FSS.

Results also indicate that, the reflection and transmission characteristics of the Chiro-FSS are very sensitive to the frequency of the incident plane wave. Another novel feature of these FSSs is that, polarisation conversion can be obtaind for the transmitted wave through the Chiro-FSS, that is, a TE (co-polar) wave incident on a Chiro-FSS can be converted into a TM (cross-polar) wave on the other side with total transmision. Almost full transmission of the co-polar components is posibble at some frequencies as well. The first resonance in the reflection characteristics occurs almost at the same frequency of the resonance obtained for conventional FSS but the higher resonance frequencies can be changed by varying the chirality admittance of the slab.

When the Chiro-FSS is illuminated by an obliquely incident plane wave, still multiple resonances can be obtained. But in the most of the cases considered the resonances occur at different frequencies for TE and TM polarisation case. This means that similar to the conventional FSS, Chiro-FSS are not too suitable for oblique incidence conditions.

The analysis method presented in this thesis can be extended for the analysis of cascade connections of chiro-FSSs. In this case, the analysis and formulation will be a bit more complicated than the analysis and formulation of the single Chiro-FSS.

Another future proposal is that anlysis of Chiro-FSS comprised of conducting elements having chiral (handedness) geometry. For example L (left handed) or ⌐ (right handed) shaped conducting elements can be used in forming the Chiro-FSS instead of cross dipoles, circular rings etc..

LIST OF REFERENCES

1. Arago, D. F. ,1881, 'Sur une modification remarquable qu'eprouvent les rayons lunineux dans leur passage a traverse certains corps diaphanes, et sur quelques autres nouveaux phenomenes d'optique', Mem. Inst. , Vol.1, pp. 93-134.

2. Biot, J. B., 1815, 'Phenomenes de polrisation successive, observers dans des fluides homogenes', Bull. Soc. Philomat. , pp. 190-192.

3. Fresnel, A., 1882, 'Memoire sur la double refraction que les rayans lumineux eprouvent on traversant les aiguilles de cristal de roche suivant des directions paralleles a l'axe', Deuvres Vol. 1, pp. 731-751.

4. Pasteur, L., 1848, 'Sur les relations qui peuvent exister entre la forme cristelline, la composition chimique et de sense de la polarisation rotatoine ', Ann. de. Chim et de Phy.Vol.24, pp.442-459

5. Lindman, K. F., 1920, ' Uber eine durch eine isotropes system von spiral formingen resonatonen erseugte rotations polarisation der elektromagnetichen wellen ' , Ann. de Phy., Vol. 63, pp. 621-624.

6. Jaggard, D. L. , Mickelson, A. R. and Papas, C. H., 1979, 'On Electromagnetic waves in chiral media ', App. Phy. Vol. 18, pp. 211-216.

7. Bassiri, S., Engheta, N. and Papas, C. H., 1986, ' Dyadic Green's function and dipole radiation in chiral media ', Alta Frequenza , Vol. LV, No. 2, pp. 83-88.

8. Lakhtakia, A., Varadan, V. K. and Varadan, V. V., 1985, ' Scattering and absorption characteristics of lossy dielectric, chiral, nonspherical objects ', App. Opt., Vol.24, No. 23, pp. 4146-4154.

9. Pelet, P. and Engheta, N., 1990, ' The Theory of Chirowaveguides ', IEEE Trans. Antennas Propagat., Vol. 38, No.1 pp. 90-98.

10. Bassiri, S, Papas, C. H and Engheta, N., 1988, ' Electromagnetic wave propagation through a dielectric-chiral interface and through a chiral slab ', J. Opt. Soc. Am. A , Vol. 5, No. 9, pp.1450-1459.

213

11. Lakhtakia, A., Varadan, V. V. and Varadan, V. K., 1994, 'Field equations, Huygen's principle, integral equationa, and theorems for radiation and scattering of electromagnetic waves in chiral media ', J. Opt. Soc. Am. A , Vol.42., No. 9, pp. 1690 - 1694.

12. Guine, T., Varadan, V. V. and Varadan, V. K., 1990, ' Influence of chirality on the reflection of EM waves by planar dielectric slab ', IEEE Trans. Electromag. Compat., Vol. 32, No. 4, pp. 300 - 303.

13. Jaggard, D. L., Engheta, N., Kowarz, M. W., Pelet, P., Lin, J. C. and Kim, Y., 1989, ' Periodic chiral structures ', IEEE Trans. Antennas Propagat. , Vol. 37, No. 11, pp. 1447 - 1452.

14. Saadoun, M. M. I., and Engheta, N., 1994, ' Theoretical study of varition of propagation constant in a cylindrical waveguide due to chirality : Chiro-Phase shifting ', IEEE Trans. Microwave Theory Tech., Vol. 42, No. 9, pp. 1690 - 1694.

15. Rittenhause, D., 1786, ' An optical problem, proposed by Mr. Hopkinson, and solved by Mr. Rittenhause ', Trans. Am. Phil. Soc. Vol. 2, pp. 201 - 206.

16. Anderson, I., 1975, ' On the theory of self-resonant grids ', The Bell Syst. Tech. J., Vol. 54, No. 10, pp. 1725 - 1731.

17. Compton, R. C. and Rutledge, D. , B., 1985, 'Approximation techniques for planar periodic structures ', IEEE Trans. Microwave Theory Tech., Vol. 33, No. 10, pp. 1083 -1088.

18. Montgomery, J. P., 1975, ' Scattering by an infinite periodic array of thin conductors on a dielectric sheet ', IEEE Trans. Antennas Propagat. , Vol. 23, No.1, pp. 70 - 75.

19. Agrawal, V. D. and Imbriale, V. A., 1979, ' Design of dichroic Cassagrain subreflector ', IEEE Trans. Antennas Propagat. , Vol. 27, No. 4, pp. 466 - 473.

20. Johansson, F. S., 1985, ' Analysis and design of double-layer frequency-selective surfaces ', IEE Proc. H., Vol. 132, No. 5, pp. 319 - 325.

21. Lee, S. W., 1971, ' Scattering by dielectric-loaded screen ', IEEE Trans. Antennas Propagat. , Vol. 19, No.5, pp. 656 - 665.

22. Ulrich, R., 1967, ' Far-infrared properties of metallic mesh and its complemantery structure ', Infrared Phy., Vol. 7, pp. 37 - 55.

23. Durschlag, M. S. and De Temple, T. A., 1981, ' Far-IR optical properties of freestanding and dielectrically backed metal meshes ', Appl. Opt., Vol. 20, No. 7, pp.1245 - 1253.

24. Arnaud, A. and Pelow, F. A., 1975, ' Resonant-grid quasi-optical diplexers ', Bell Syst. Tech. J., Vo. 54, No. 2, pp. 263 - 283.

25. Horwitz, C. M., 1974, ' A new solar selective surface ', Opt. Commun. ,Vol. 11, No. 2, pp. 210 - 212.

26. Ulrich, R. Rank, K. F. and Gerzel, L., 1963, ' Tunable submillimeter interferometers of the Fabry-Perot type ', IEEE Trans. Microwave Theory Tech., Vol. 11, pp. 363 - 371.

27. Rutledge, D. B. and Schwarz, S. E., 1981, ' Planar multimode detector array far infrared and millimeter-wave applications ', IEE J. Quantum Electron., Vol. 17, pp. 407 - 414.

28. Laun, W. W. et. al., 1988, ' Millimeter-wave diode-grid phase shifters ', IEEE Trans. Microwave Theory Tech., Vol.36, pp.902 -907.

29. Jou, C. F. et. al. , 1988, ' Millimeter-wave diode-grid frequency doublers ', IEEE Trans. Microwave Theory Tech., Vol. 36, pp.1507 - 1514.

30. Young, L., Robinson, L. A. and Hacking, C. A., 1973, Meander-line polarizer ', IEEE Trans. Antennas Propagat. , Vol. 21, pp. 376 - 378.

31. Tasi, L. L., Wu, T. K. and Mayhan, J. T., 1978, ' Scattering by multilayered lossy periodic strips with application to artificial dielectric ', IEEE Trans. Antennas Propagat. , Vol. 21, pp.257 - 260.

32. Cwik, T. and Mittra, R., 1987, ' The cascade connections of planar periodic surfaces and loosy dielectric layers to form an arbitrary periodic screen ', IEEE Trans. Antennas Propagat. , Vol. 35, pp.1397 - 1405.

33. El-Marsy, M. A. A. A, Parker, E. A. and Langley, R. J., 1983, ' Four layer inductive grid FSS at 45° incidence ', Electron. Lett., Vol. 19, pp. 602 - 603.

34. Wu, T. K. and Lee, S. W., 1994, ' Multiband frequency selective surface with multiring patch elements ', IEEE Trans. Antennas Propagat. , Vol. 42, No.11, pp. 1484 - 1490.

35. Chang, T. K., Langley, R. J. and Parker, E. A., 1994, ' Frequency selective surfaces on biased ferrite substrates ', Electron. Lett., Vol. 30, No. 15, pp. 1193 - 1194.

36. Zhang, D. et. al., 1993, ' Application to high T_c superconductors as frequency selective surfaces: Experiment and theory ', IEEE Trans. Microwave Theory Tech., Vol. 47, pp.1032 - 1035.

37. Kastner, R. and Mittra, R., 1987, ' Iterative analysis of finite sized planar frequency selective surfaces with rectangular patches or perforations ', IEEE Trans. Antennas Propagat. , Vol. 35, No.4, pp. 372 - 377.

38. Caroglanian, A. and Webb, K. J., 1991, ' Study of curved and planar frequency selective surfaces with non-planar illumination ', IEEE Trans. Antennas Propagat. Vol. 39, No.2, pp.211 - 217.

39. Ishimaru, A., 1991, Electromagnetic Wave Propagation, Radiation and Scattering , Prentice Hall, Englewood Cliffs, New Jersey.

40. Silverman, M. P., 1986, ' Reflection and refraction at the surface of a chiral medium: Comparision of gyrotropic constitutive relations invariant or noninvariant under duality transformations ', J. Opt. Soc. Am. A., Vol. 3, No. 6, pp. 830 - 837.

41. Wakabayashi, H., Kominami., Kusaka, H. and Nakashima, H., 1994, ' Numerical simulations for frequency selective screens with complementary elements ', IEE Proc. Microw. Antennas Propagat., Vol. 141, No. 6, pp. 477 - 482.

42. Jin, J. M. and Volakis, J. L., 1990, ' Electromagnetic scattering by a perfectly conducting patch array on a dielectric slab ', IEEE Trans. Antennas Propagat. , Vol. 38, No.4, pp. 556 - 563

43. Johansson, F. S., 1987, ' Convergence phenomenon in the solution of dichroic scattering problems by Galerkin's method ', IEE Proc. H., Vol. 134, No.1, pp. 87 - 92.

44. Tsao, C. H. and Mittra, R., 1984, ' Spectral domain analysis of frequency selective surfaces comprised of periodic array of cross dipoles and Jerusalem cross ', IEEE Trans. Antennas Propagat. , Vol.32, No.5, pp. 478 - 484.

45. Rubin, B. J. and Bertoni, H. L., 1983, ' Reflection from a periodically perforated plate using subsectional current approximation ', IEEE Trans. Antennas Propagat. , Vol. 31, No.6, pp. 829 - 836.

46. Hamdy, S. M. A. and Parker, E. A., 1982, ' Current distribution on the elements of a square loop frequency selective surface ', Electron. Lett., Vol. 18, No. 14, pp. 624 - 626.

47. Chen, C. C., 1970, ' Scattering by a two dimensional periodic array of conducting plates ', IEEE Trans. Antennas Propagat. , Vol. 18, No.5, pp.660 - 665.

48. Ott, R. H., Kouyoumjian, R. G. and Peters, L., 1967, ' Scattering by a two dimensional periodic array of narrow plates ', Radio Science, Vol. 2, No. 11, pp. 1347 - 1359.

49. CSELT, 1983, ' Frequency selective surface design capability programme, Final Report ', European Space Agency (ESA), Contract No. 4828/81/NL/MS(SC).

50. CSELT, 1984, ' Study of dichroic subreflectors for multifrequency antennae, Electrical Design, Final Report ', European Space Agency (ESA), Contract No. 5355/83/NL/GM(SC).

APPENDIX A

CURRENT DISTRIBUTION ON NARROW STRIPS AT RESONANCES

The spectral responses of the Chiro-FSS comprised of two dimensional infinite periodic array of narrow strips are given in Figure 4.1.2. The design parameters for this configuration are taken as; $\alpha=90°$(square lattice), $D_1=D_2=10$ mm, $L=9.2$ mm, $W=1$ mm $\epsilon_r=1.06$ and $t=5$ mm. The screen is illuminated by a normally incident plane wave of TE polarisation. As seen in Figure 4.1.2 for the case of $\xi=0.0025$ mho, various resonances appear in the reflection characteristics.

The current density induced on the strips for the first resonance which occurs at $f=13.69$ GHz is given in Figure A.1. As can be seen from this figure the current density has a regular and well-behaved distribution. Figure A.2 shows the current distribution for the second resonance which appears at $f=16.025$ GHz which has an extremely narrow shape. In contrast to the current distribution of the first resonance, the current distribution corresponding to the second resonance is quite different. In fact this resonance is due to the surface wave or traped wave propagating in the chiral slab. In other words, when the screen is illuminated by a TE polarised wave having frequency of 16.025 GHz, the incident plane wave is converted into a surface wave guided along the chiral slab. At this frequency the transverse wave number of the incident wave coincides with the propagation constant of the structure. Similar phenomenon has also been observed in the conventional FSS [41]. The current distribution corresponding to the third resonance ($f=17.3$ GHz) is plotted in Figure A.3. It can be seen from this figure that, the current distribution is very similsr to that of the first resonance given in Figure A.1.
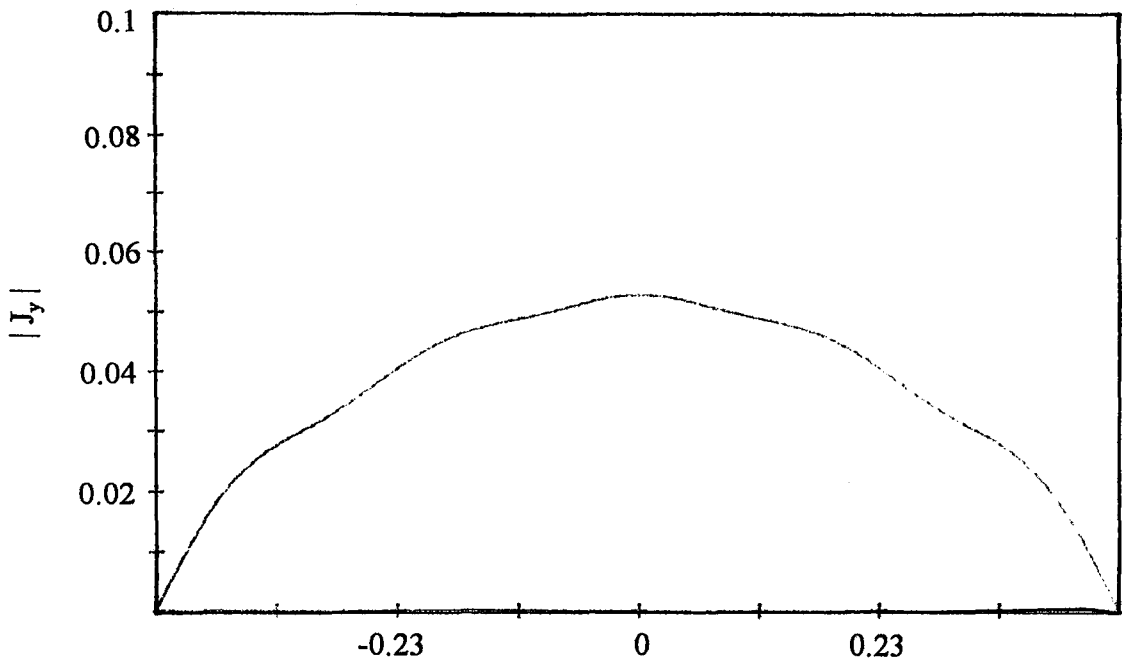
Figure A.1   Current distribution on narrow strips at f= 13.69 GHz; TE incidence
(φ= 0°, θ=0°), square lattice (α= 90°), $D_1=D_2$=10 mm, L=9.2 mm, W=1
mm, ϵ_r=1.06, t =5 mm, ξ=0.0025 mho.

Figure A.2   Current distribution on narrow strips at f= 16.025 GHz; TE incidence
(φ= 0°, θ=0°), square lattice (α= 90°), $D_1=D_2$=10 mm, L=9.2 mm, W=1
mm, ϵ_r=1.06, t =5 mm, ξ=0.0025 mho.

Figure A.3   Current distribution on narrow strips at f= 17.3 GHz; TE incidence ($\phi= 0°$, $\theta=0°$), square lattice ($\alpha= 90°$), $D_1=D_2=10$ mm, L=9.2 mm, W=1 mm, $\epsilon_r=1.06$, t =5 mm, $\xi=0.0025$ mho.

APPENDIX B

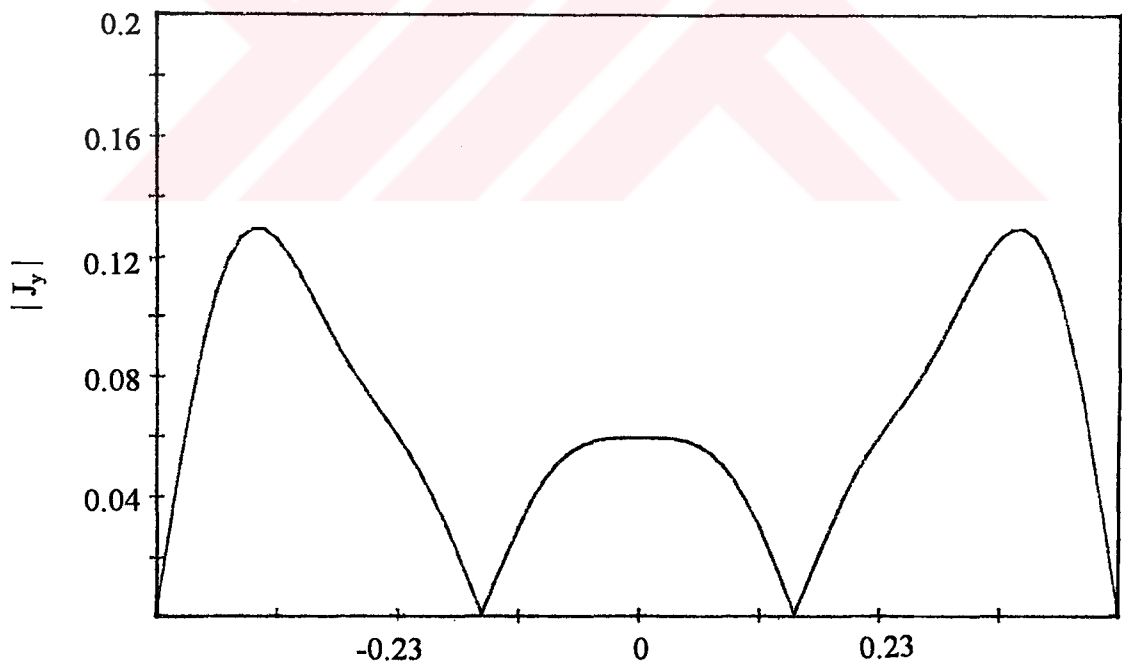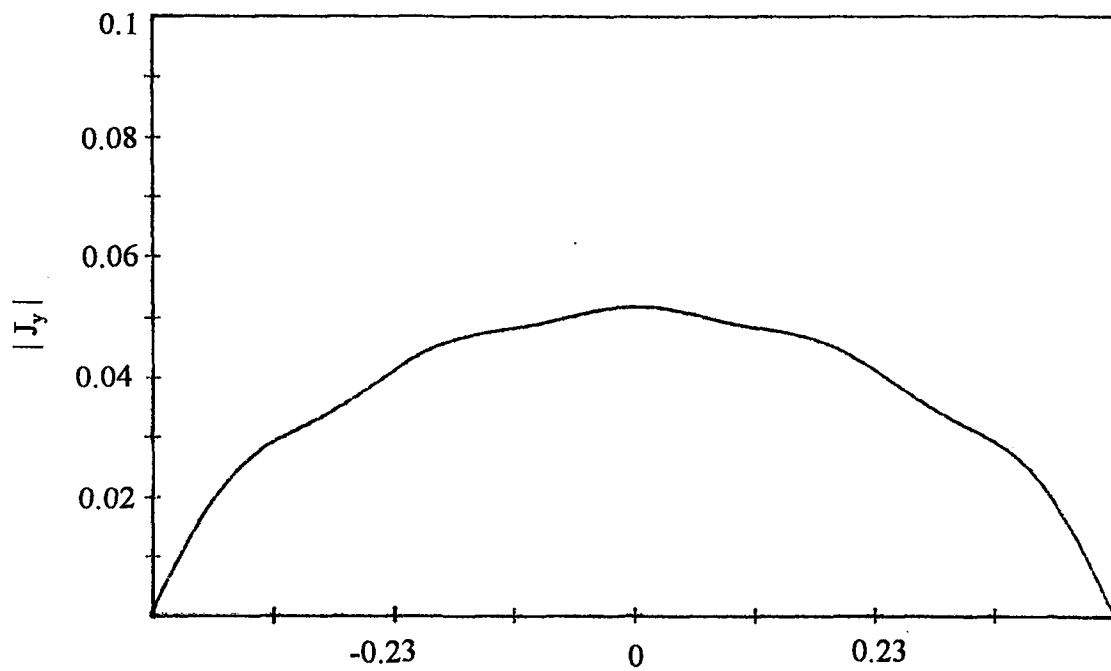## DEPENDENCE OF REFLECTION CHARACTERISTICS OF CHIRO-FSS COMPRISED OF CIRCULAR RINGS ON INCIDENCE ANGLE

The variations of the power reflection coefficient at the first resonance ($f=12.16$ GHz.) versus incidence angle for the Chiro-FSS which has the same design parameters as those of Figure 4.3.2, for $\xi=0.0015$ mho is given in Figure B.1. As shown in the figure, the reflection characteristics slightly vary between $\theta=0°$ to $\theta=45°$; TE and TM reflection characteristics are almost identical up to $\theta=45°$. For higher values of the incidence angle, TM reflection coefficient decreaes while the TE reflection characteristic remains almost unchanged.

Figure B.2 shows the dependence of the reflection coefficient on the incidence angle at the second resonance which occurs at 21.09 GHz. Figure B.2 reveals that the variation of TE and TM reflection coefficients are very sensitive to the incidence angle of the incoming wave. Perfect reflection is possible only from $\theta=0°$ to $\theta=3°$. When the incidence angle is greater than $3°$ the reflection characteritic of TE and TM cases differ considerably and thus this resonance can not be used in FSS applications.

The plot of power reflection coefficient as a function of incidence angle for the Chiro-FSS having the same geometry as in the previous example except where the chirality admittance is increased to $\xi=0.0025$ mho, is depicted in Figure B.3. In this case the first resonance occurs at 11.69 GHz. As seen from the figure, both TE and TM reflection characteristics have the same variation up to $\theta=40°$. However, when the incidence angle exceeds this value TE and TM responses of the screen exhibit different characteristics.

Figure B.4 shows the power reflection coefficient versus incidence angle at the second resonance which appears 16.55 GHz. It is seen from the figure that, the power

reflection coefficients for both TE and TM cases have the flat characteristics between θ=5° and θ=35° and are about 1.1 dB less than the perfect reflection. Contrary the results in case I discussed above this second resonance can be exploited in some FSS applications.

In the light of the results presented, one can conclude that, the first resonance in the reflection characteristics is not sensitive to the incidence angle. On the other hand, comparison of Figure B.2 to Figure B.4 yields that, depending upon the value of chirality admittance, the second or higher resonance in the reflection characteristics may or may not be strongly sensitive to the incidence angle.
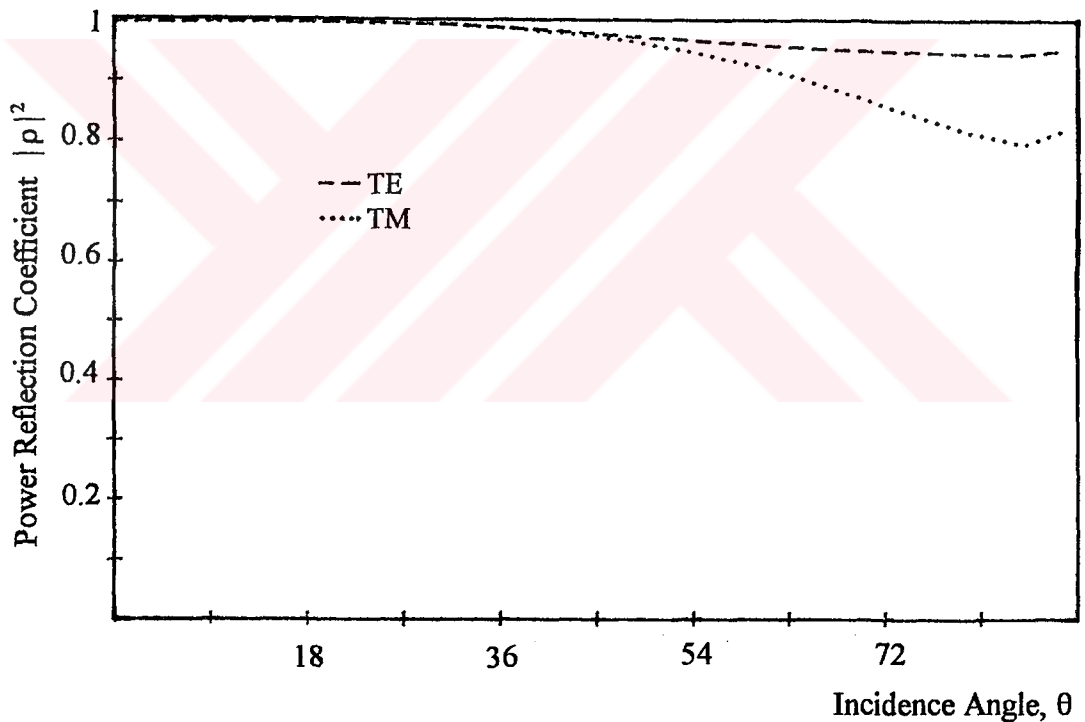

Figure B.1   Reflection characteristics of Chiro-FSS with circular rings; square lattice (α= 90°), R_i = 3.7 mm, R_o= 4.7 mm, ϵ_r=1.06, t = 5mm, ξ=0.0015 mho, f=12.16 GHz
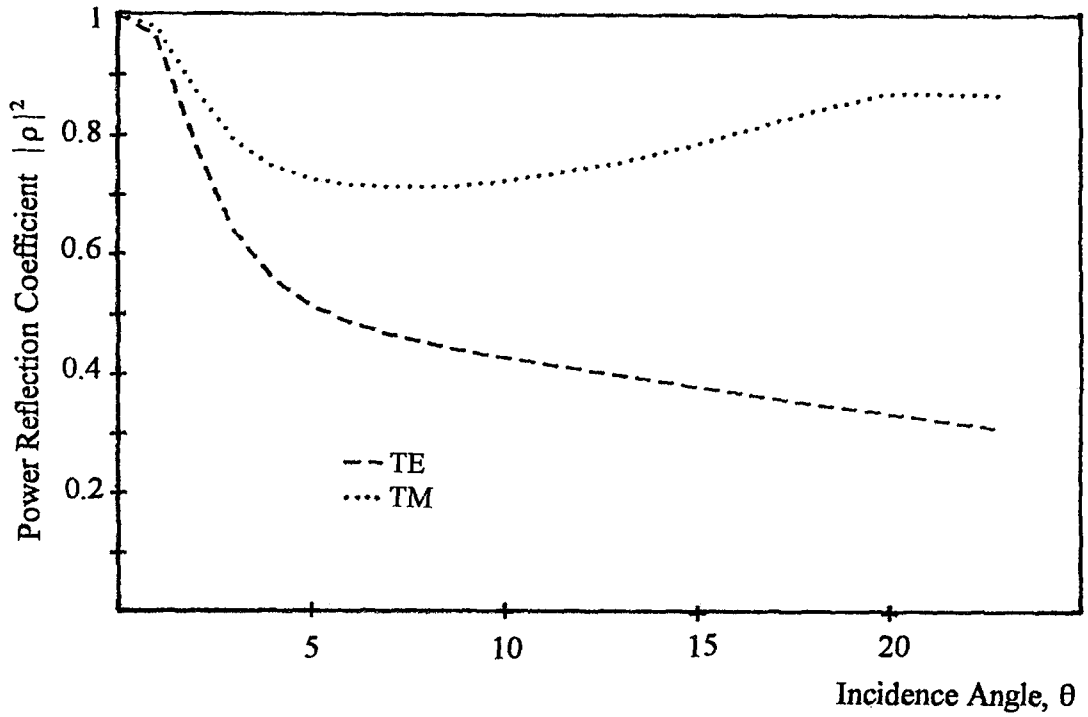
Figure B.2   Reflection characteristics of Chiro-FSS with circular rings; square lattice ($\alpha= 90°$), $R_i = 3.7$ mm, $R_o= 4.7$ mm, $\epsilon_r=1.06$, t = 5mm, $\xi=0.0015$ mho, f=21.09 GHz

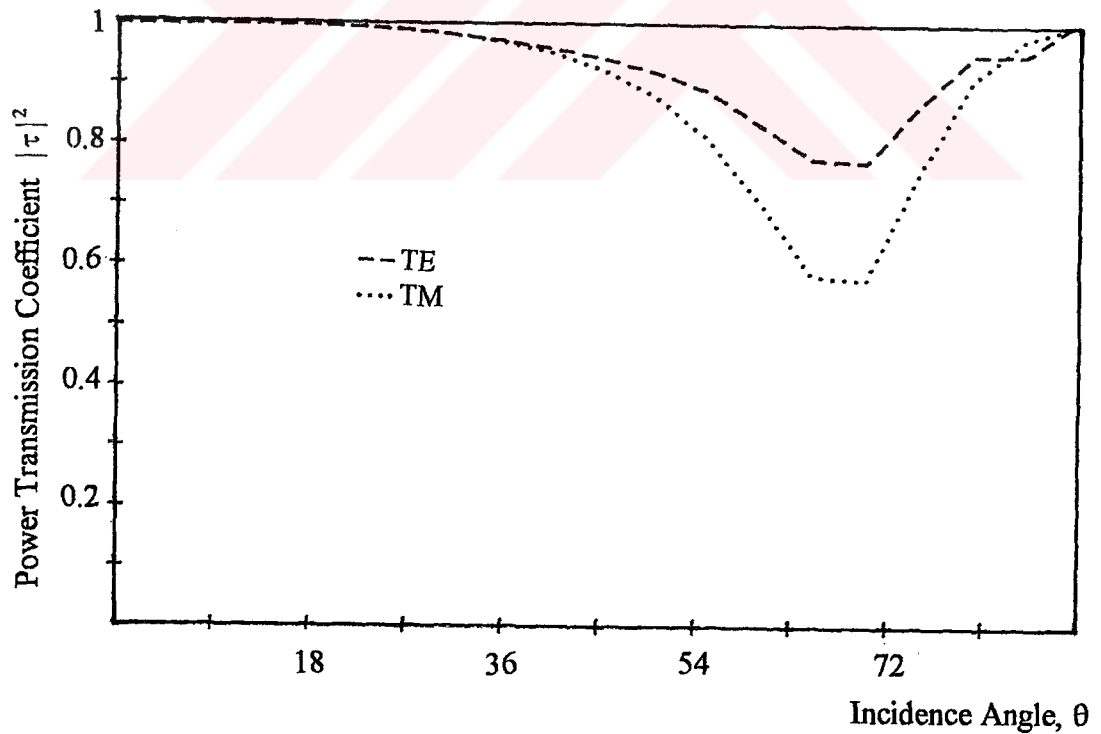Figure B.3   Reflection characteristics of Chiro-FSS with circular rings; square lattice ($\alpha= 90°$), $R_i = 3.7$ mm, $R_o= 4.7$ mm, $\epsilon_r=1.06$, t = 5mm, $\xi=0.0025$ mho, f=11.69 GHz .
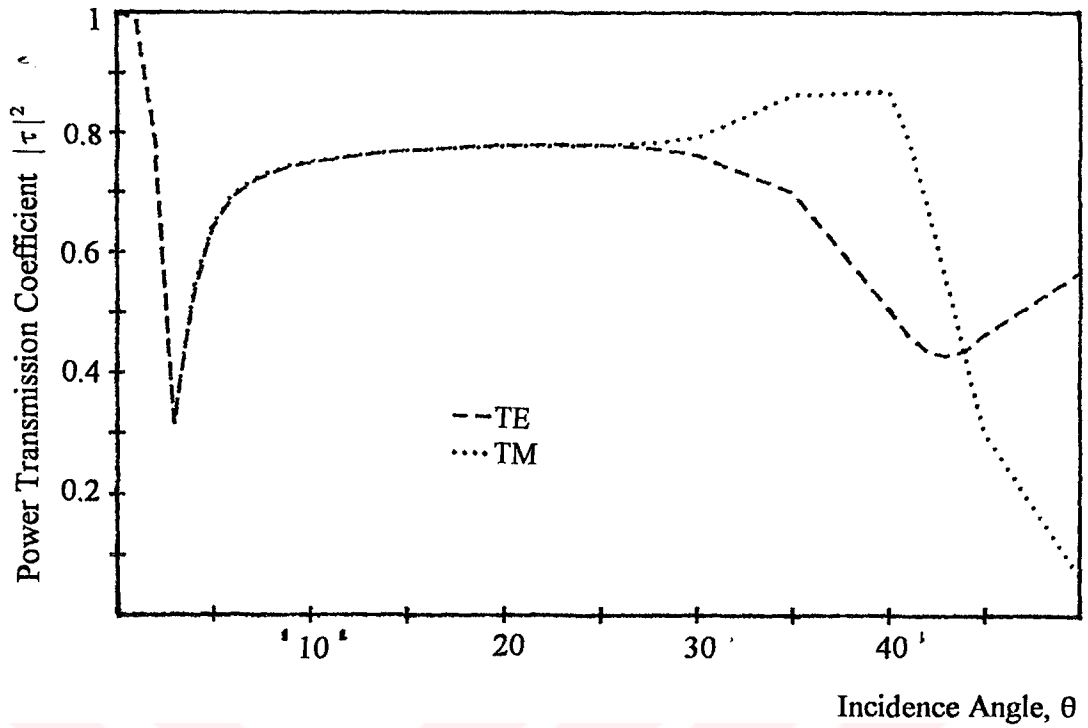
Figure B.4 Reflection characteristics of Chiro-FSS with circular rings; square lattice $(\alpha = 90°)$, $R_i = 3.7$ mm, $R_o = 4.7$ mm, $\epsilon_r = 1.06$, t = 5mm, $\xi = 0.0025$ mho, f=16.55 GHz

CURRICULUM VITAE

The author was born in Eskişehir, in December 3, 1966. He received his B. S. degree in 1989 in Electrical and Electronics Engineering, from Middle East Technical University, METU, Gaziantep Engineering Faculty. He received M. S. degree in 1992 in Electrical and Electronics Enginnering, University of Gaziantep with his thesis entitled ' Guided Waves Through Chiral Medium '. He has been with the electrical and Electronics Engineering Department in University of Gaziantep as a research assistant since October 1989.